Experimental Investigation of the Response of Turbulent Premixed Flames to Acoustic Oscillations

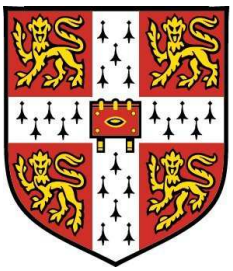

Ramanarayanan Balachandran

Department of Engineering

University of Cambridge

A thesis submitted for the degree of

Doctor of Philosophy

27 May 2005

Darwin College

Declaration

The work presented in this dissertation was conducted in the Hopkinson Laboratory, Department of Engineering between May 2002 and May 2005.

This dissertation is the result of my own work and includes nothing which is the outcome of work done in collaboration except where specifically indicated in the text. No part of this dissertation has already been, or is being concurrently submitted for any other degree, diploma or qualification.

This dissertation contains approximately 45000 words and 100 figures.

.....

Ramanarayanan Balachandran

27 May 2005

I would like to dedicate this thesis to my family and friends ...

Acknowledgements

I wish to express my gratitude to **Dr. E. Mastorakos**, for his continuous support and guidance throughout this study. I also wish to thank him for his help, his constructive criticisms, and above all for providing good lab. facilities and a wonderful atmosphere to work.

I am grateful to **Professor A. P. Dowling** for all her help and for her invaluable suggestions during critical moments. I am also thankful for the insightful discussions during the design phase and also during the problem definition.

I wish to thank, **Dr. C. F. Kaminski** for his help and his interest in my work. I would like to thank him for his useful suggestions and discussions during the PLIF measurements.

I would like to thank Babatunde Ayoola for all his help and the wonderful lunchtime discussions. I would like to express my sincere thanks to Mick Underwood, Trevor Parson, Robert Leroy, Roy Slater and John Harvey for all their help during the fabrication and installation of the test rig.

I would like to express my sincere thanks to Mr. Peter Benie for helping out with the computing facilities, and all his support and the extra work he put in during the critical moments.

I would like to thank Alex, Carol, Chang-wook, Christos, Ed, Ganapathy Subbu, KRV Subraminan, Giorgio, Ik Soo, James, Karthik, Haakon, Moncef, Marina, Omar, Pedro, Raj, Sara, Sameer, K. B. Senthil, Simon, Sohini and all the others in Hopkinson laboratory and heat gallery for their wonderful company, especially Mrs. Kate

Graham and Mrs. Karin Arnold for organizing 'Hopkinson Group Hug'.

I would like to express my thankfulness to Shamala for her deep thoughts, discussions, motivation and support during critical situations and also for the wonderful time spent.

The most important of all, I thank my parents (Mr. Balachandran Narayanaswamy and Mrs Vanaja Balachandran), my sister and brother-in-law (Mrs M. Revathi and Mr. R. Muralidharan) for being a source of constant moral courage and inspiration. I would also like to express my love to my two cute nephews (Ashwin and Srinivasan).

Finally, I would like to express my thankfulness to Department of Trade and Industry, UK and Rolls-Royce plc. for their financial support for my PhD.

Abstract

This thesis describes an experimental investigation of the response of lean premixed bluff-body stabilised flames to acoustic forcing that is relevant to understanding limit-cycle behaviour of realistic combustors.

The first part of the thesis describes an experimental investigation of forced lean fully premixed turbulent flames with special emphasis placed on the amplitude dependence of their response. The heat release rate estimates from OH*/CH* chemiluminescence, flame surface density (FSD) from OH Planar Laser Induced Fluorescence (PLIF), and reaction rate (RX) imaging using simultaneous CH_2O and OH PLIF were used.The heat release response became non-linear after inlet velocity amplitudes of around 15% of the bulk velocity. This value depended on the forcing frequency and the equivalence ratio. The non-linearity was found to occur when the shear layers rolled-up into vortices. These vortices not only generated flame area when the flame wrapped around them, but also caused large-scale flame annihilation events. The results suggest that the flame kinematics play the major role in the saturation mechanism in these flames.

The second part of the thesis describes the experimental investigation of the response of imperfectly premixed flames to acoustic oscillations. The results suggest that the flame response was controlled by two mechanisms, namely equivalence ratio perturbations and flame kinematics. The former mechanism dominated in low frequency conditions, under which the flame was compact, resulting in nonlinear amplitude dependence. The flame kinematics seemed to play an important role only when the flame length was comparable to the acoustic wavelengths.

The forced flame measurements were finally compared successfully with the response of self-excited flames which suggests that the mechanism of heat release variation investigated in the forced response studies is representative of the true limit-cycle behavior of self-excited flames.

Contents

List of Figures

Chapter 1

Introduction

This thesis describes an experimental investigation of acoustic responses of turbulent lean premixed flames that are relevant to understanding limit-cycle behaviour during combustion instabilities in low emission combustion systems such as lean-prevaporized premix combustors. In order to meet the stringent pollutant control measures, lean burn technology has been adopted in many industrial applications. Lean premixed combustion systems offer several advantages, including increased fuel economy and lower combustion temperatures leading to drastic reduction in NO_x, as well as reduced levels of soot and CO. However, these systems are often susceptible to acoustic combustion instabilities (Culick, 2002; Macquisten & Dowling, 1995).

Combustion instabilities are a consequence of the sensitivity of combustion processes to pressure and velocity fluctuations. Depending on the application, combustion instabilities are welcome, for example pulsating furnaces where the higher heat transfer rates and reduced pollutant formation are an advantage, or undesirable, for example combustion instability in rocket motors and gas turbines where they are dynamically and structurally detrimental to performance. However, the mechanisms driving combustion instability and pulse combustion are similar. Although the research in this field is spanning over decades, the prediction and control of combustion instability is still a great challenge.

Combustion instability generally refers to the sustained pressure fluctuations of acoustic nature in a chamber where unsteady combustion takes place. In most practical situations, it is essentially a self-excited oscillation, involving a

complex interplay between unsteady heat release, the acoustic fluctuation and the vorticity field. There are various experimental observations (Anning, 1999; Külsheimer & Büchner, 2002; Poinsot *et al.*, 1987; Schadow & Gutmark, 1992; Wu *et al.*, 2001; Yu *et al.*, 1991) from which the role of various phenomena involved in this complex process could be identified and understood. The role of vortices and the mechanism of instability from these studies can be described as follows. The presence of mixture and flow inhomogenities produce unsteady heat release. The unsteady heat release produces sound, which then triggers (Kelvin-Helmholtz) instability waves in the shear layer, which usually stabilises the flames. These waves amplify and roll up on the shear layer and finally break down into small-scale motions, thereby affecting flame surface and hence the heat release. The variation in heat release in turn affect the acoustics of the chamber. The whole process forms a closed cycle.

Many investigations on pulsating combustion indicate that the combustion process is the major source of the energy needed for maintaining the pressure oscillations. To sustain the oscillations, it is required that during the initial phase of the pulsations the energy provided by the combustion process per cycle be larger than the energy lost per cycle by the oscillation due to viscous dissipation, heat transfer, acoustic radiation and so on. In general, as the amplitude of the oscillation grows, the various energy addition and dissipation processes become amplitude dependent and a 'limit cycle' amplitude is reached at which these opposing processes balance one another during a cycle. The resulting amplitude remains unchanged as long as the operating conditions of the system do not vary.

When the pulsation starts spontaneously, as in the case of Rijke combustors (Zinn & Narayanaswami, 1982), the system is said to be linearly unstable; that is, the system is unstable with respect to any small amplitude disturbance, which might be present inside the combustor. It is also possible that a linearly stable combustor (i.e., one that does not pulsate spontaneously) could be 'triggered' into pulsating operation by the introduction of a finite amplitude disturbance, such as might be caused by a spark plug ignition or small explosion. Such a system will be stable with respect to all disturbances whose amplitudes are below a certain threshold value and it will transition into pulsating operation when the amplitude of the disturbance exceeds this threshold value. Practical pulsating combustors

could be nonlinearly unstable, requiring a finite amplitude disturbance to initiate oscillatory operation.

A necessary condition for achieving pulsating combustion operation is that the combustion processes respond to local flow oscillations by adding mechanical energy to the oscillation. This is not always possible to achieve and it depends upon the characteristics of the combustion process and the properties of the local flow oscillations. For situations, in which the effect of the combustion processes on the oscillations can be modelled by a heat addition process, the conditions under which pulsating combustion may occur have been stated by Rayleigh (1945), although without proof. Rayleigh stated that amplification or attenuation of the pressure oscillation by heat addition would occur if the periodic heat release occurs in or out of phase with the pressure oscillation, respectively. On the other hand only the frequency of the oscillation would change if the heat addition to the gas takes place 'instantaneously' when the amplitude of the pressure oscillation is zero.

Putnam & Dennis (1953) were probably the first to express Rayleigh's criterion for heat driven oscillations in a mathematical form. With a slight modification, the Rayleigh criterion was expressed in the following form:

$$\int_V \int_0^T p(x,t)Q(x,t)dtdV > \int_V \int_0^T \sum_i L_i(x,t)dtdV \tag{1.1}$$

where, p - pressure, Q - heat addition, x - location, t -time, L_i - ith wave energy dissipation process, T - period of the oscillation and V - Volume of interest. The left and right hand sides of Eq. 1.1 describe the total mechanical energy added to the oscillation by the heat addition process per cycle and the total energy dissipated by the oscillation per cycle, respectively.

The acoustic wave will be amplified in the system when the inequality expressed in the Eq. 1.1 is satisfied. The volume of integration should include all sections of the system where relevant processes which affect the growth and/or decay rates of the oscillation occur and the summation on the right hand side should include all the wave energy dissipation processes.

From the left hand side of the equation it can be concluded that to satisfy Rayleigh criterion for heat driven oscillations at a given location, a specific phase

relationship between p and Q must exist. If p and Q have a periodic time dependence, the sign of the time integral of the product pQ in the equation will depend upon the ratio (Φ/T) where Φ is the phase difference between p and Q. It is possible that the time integral on the left side of equation will be positive in some parts of the system and negative in others and the question of whether a net amount of mechanical energy will be added to the oscillation will depend upon the net effect of 'adding' these positive and negative contributions from the time integration during the space integration of the equation.

The above discussion indicates that in order to excite or eliminate combustion oscillations the ratio (Φ/T) must be within certain specified ranges. Thus, it is important to understand how the magnitude of this ratio can be controlled. In general, the period T is determined by the characteristics of the excited acoustic mode, the speed of sound and the geometry and dimensions of the system. Thus, T can be varied by changing the geometry of the system i.e., the length of the combustor. On the other hand Φ, which describes the phase difference between the pressure p and the heat addition Q oscillations, is controlled by the characteristics of the oscillatory combustion process (Neumeier & Zinn, 1996; Reuter *et al.*, 1986).

The difficulty in applying this criterion is that unsteady heat release is often part of the solution and thus not known a priori. By using available experimental data, some empirical relations between the heat release and sound fluctuation and extrapolated to convert this to a thermo-acoustic problem. This approach was employed by Bloxsidge *et al.* (1988) to describe 'reheat buzz' in a premix combustor (Langhorne, 1988). Dowling (1995) used this approach to calculate the thermo-acoustic oscillations in a simple geometry.

The determination of the mechanisms that are responsible for the establishment of an oscillatory combustion and heat addition processes in a combustor usually involves the determination of the responses of the various processes which affect the phase of the combustion process relative to the pressure oscillation. A given process is said to be responsible for the occurrence of pulsating combustion when its response to the combustor flow oscillations causes the heat release to take place in phase with the combustor pressure oscillations (Barr *et al.*, 1990).

The processes whose responses have been found to contribute to the occurrence of combustion oscillations include the flows in fuel and air feed systems (Lieuwen & Zinn, 1998a), periodic heating of the fuel by its oscillatory flow environment, enhanced diffusion and mixing caused by flow oscillations, periodic flame area variations, oscillations in equivalence ratio and so on (Dowling & Hubbard, 2000; Lieuwen & Zinn, 1998a; Marsano *et al.*, 1998; Reuter *et al.*, 1986; Sohn *et al.*, 1996; Torres *et al.*, 1999).

In addition to oscillatory heat addition, periodic mass addition to a gas is also capable of providing the energy needed for supporting gas phase oscillations. Heiser *et al.* (1996) had demonstrated the similarity between the influence of heat addition and mass addition. In a pulse combustor, unsteady mass addition to the gas flow may occur due to the response of the fuel feed line to the combustion chamber acoustics (Marsano *et al.*, 1998; Schimmer & Vortmeyer, 1977; Yu *et al.*, 1996).

However, at the heart of combustion dynamics is the coupling between the heat release and the pressure oscillations in the combustor. Accurate prediction of the effects of such coupling is especially difficult due to the unsteadiness of the driving processes (e.g., fuel injection) and the high nonlinearity of the interactions between turbulent mixing, acoustic wave propagation, and unsteady heat release. Large-scale flow structures play a key role in the coupling process by controlling the mixing of the essential ingredients of combustion: oxidizer, fuel, and heat. Realizing this, attempts have been made to control the vorticity both passively and actively. Combustion generated pressure pulses can enhance the formation of large vortices in shear flows created by splitter plates, bluff bodies, and rearward facing steps. This can also be created by external forces such as sirens or the cyclic movement of a piston to pulse the reactant flow, or the mechanical displacement of the splitter plate to modify vorticity coalescence in a mixing layer. Also, fluid dynamic strain can play a significant role in premixed turbulent flame propagation. Poinsot *et al.* (1987) have shown that vortices already present in the turbulence can locally quench the flame front.

In this thesis various phenomena that are important in determining the limit-cycle behaviour of premix combustors are investigated. In particular, we emphasize vortical structures and unsteady equivalence ratio. The following section

presents the background information needed for the present study. The specific objectives of the work are discussed in section 1.3, following a specific review of relevant work in section 1.2.

1.1 Literature Background

Since their discovery in 1777 by Higgins (Schimmer & Vortmeyer, 1977), combustion driven oscillations have gained great technical importance, be it to promote or to suppress them. Owing to the complex interplay between different processes involved in the onset and sustenance of such oscillations numerous investigations both experimental and theoretical have been performed to understand the underlying physics. In this section, some of these investigations are presented with special attention given to experimental methods.

1.1.1 Interaction of Flame, Flow-field and Acoustics

Since the advent of the advantages and the disadvantages of oscillatory combustion, many studies have been aimed at understanding the fundamental principles involved in these systems like interaction between flow field and flame, flame and acoustics, ignition and extinction of flames, and also on. This section reviews such investigations.

The instability problem can be considered as an energy transfer problem (Klein, 2000); if the flame adds more energy to the acoustic system than is dissipated, the amount of energy in the acoustic system will grow in time and the instability occurs. If the amount of dissipation equals (or exceeds) the energy transfer from the flame to the acoustic system, the system remains stable. The coupling between the chamber pressure and the heat release is a complex interaction of fluid dynamics, thermodynamics and chemistry. These energy transfer mechanisms can be due to either fluctuating mass flow through the burner system or fluctuations in equivalence ratio or flow instabilities or vortex shedding or due to oscillation in flame front area or all of the above.

In the case of combustion systems, where there is a coupling between the acoustic pressure in the combustion chamber and the fluctuating heat release of

the flame, the flame could act as an amplifier. In many situations, this is due to the interaction of acoustics with the fluid dynamics of the flame. For the flame to act as amplifier of sound, the role of interaction of the heat release as a function of acoustic pressure is vital, which can be explained through Rayleigh's Criterion. This coupling can be due to various mechanisms. Various mechanisms that are important in a gas turbine environment is summarized as follows (along with some literature that is relevant).

Oscillatory Inlet Mass flow: Velocity and density fluctuations at the inlet of the combustor could be induced if the acoustic pressure oscillations in the combustor are strong, which would result in the fluctuation of the mass flow of reactants at the inlet. The fluctuations of air mass flow at inlet may oscillate heat release either through flame front fluctuations or by varying equivalence ratio.

The response of sidewall stabilized, premixed, flat flames to imposed axial acoustic oscillations was studied by Sankar *et al.* (1990). They found that in the presence of acoustic field the flame displaced periodically with a frequency of the acoustic field relative to the sidewall. The oscillatory reaction rates within the flame and the oscillatory nature of the velocity of combustible mixture at the burner surface was found to be responsible for this oscillatory movement. These oscillatory reaction rates produced periodic expansion, which, in turn, generated velocity perturbations downstream of the flame region. The LDV velocity measurement showed that some sections of the flame tended to drive the acoustic field whereas the others tended to damp. These experiments showed that the flame driving/damping tendencies depended upon the acoustic admittance of the sidewall burner. It was also suggested that the oscillatory flame displacement, if present, could produce oscillatory heat transfer, which, in turn, might be an instability driving mechanism.

Theoretical and experimental investigations were performed by Baillot *et al.* (1992) to investigate conical premixed laminar flames. Their flame was found to respond to flow modulations for frequencies less than 200 Hz and their model predictions were in good agreement with their experiments. Later a detailed investigation on the same type of flame by Bourehla & Baillot (1998) threw more light on acoustic response of quasi-conical premixed flames and the parametric

response was further reported in detail (Baillot *et al.* (1999)). The recent work of Schuller *et al.* (2002) on modelling these flames suggested that the response of these flames are mainly through the flame surface area modulations. The kinematic model for the response of bluff body stabilised premixed flame proposed by Dowling (1997) assumed that the flame surface was proportional to the heat release and the predictions based on the model agreed well with the experiments (Langhorne, 1988).

Flow Instability/Vortex Shedding: The flow instability or vortex shedding present in the practical flow situations can amplify the fluctuations in the inlet mass flow. If this frequency matches with the one of the acoustic eigen frequencies of the combustion system, a strong coupling between the flow and acoustics may occur. This may result in strong variation of flame shape and thus heat release distribution. Such mechanism was observed by McManus *et al.* (1990) while investigating the effects of periodic flow excitation on the performance of a two-dimensional dump combustor for lean premixed flames. Gutmark *et al.* (1991) investigated the interaction between fluid-dynamic and acoustic instabilities in combusting flows within ducts. Their results showed substantial increases in the amplitude of the instability when the fluid dynamic frequency associated with large-scale coherent structures in the near field of the duct matched the acoustic mode frequency of the confining duct.

Schadow & Gutmark (1992) reviewed the research related to the driving mechanism of dump combustor instability, with gaseous fuels. They summarized that vortex shedding is an important driving mechanism for combustion instabilities in dump combustors. They concluded that the development of coherent vortices and their breakdown into fine-scale turbulent structures could lead to periodic heat release, which when in phase with the pressure oscillations, can drive the oscillations as stated by the Rayleigh criterion.

Savin (1996) studied the interaction of a subsonic plane jet with a Helmhotlz resonator and found that within defined ranges of parameters, self-oscillations were induced with an amplitude of pressure pulsation that was close to the dynamic pressure of the jet. He also reported the increase in the frequency of self-oscillations with the increase in jet velocity and the amplitude was found

to be its maximum when the frequency of oscillations was equal to the natural frequency of the resonator and he was also able to show that the finite amplitude of oscillation was determined primary by a convolution of vortices in the jet.

Results from all the studies presented above suggest that vortex interactions with the flame play a key role in driving a large class of combustion instabilities. Apart from controlling the combustion instabilities, vortical flows of various types are also employed to enhance mixing, organize the flame, and improve the flame stabilization process. The problem has been investigated extensively in recent years a complete review of which was given by Renard *et al.* (2000).

Equivalence ratio fluctuation: A common instability mechanism in lean prevaporized premixed (LPP) combustion systems is fluctuations in inlet equivalence ratio (ϕ). Usually this occurs when the pressure/velocity fluctuations interact with the fuel/air supply line. If the mass flow of air and/or fuel fluctuates, the equivalence ratio (reactant composition) at the flame front will oscillate. This will influence the heat release. The role of this mechanism in the lean premixed combustion systems was investigated by many investigators theoretically and experimentally (Hubbard & Dowling, 2001; Lieuwen & Zinn, 1998a,b; Menon, 1991; Sattelmayer, 2000; Yang & Culick, 1986)).

Apart from the prior discussed phenomena, there were other notable parameters, which were found to influence the pulsating combustion. For instance, during (Macquisten & Dowling, 1993) an experimental investigation with a confined flame stabilized in the wake of a conical gutter with inlet conditions representing that of engine afterburner, the frequency of the buzz mode was found to increase with increasing (a) temperature and (b) Mach number of the approach flow. When the Mach number was low, the frequency of the mode increased gradually with the equivalence ratio and the amplitude of the pressure oscillation was found to increase with rising equivalence ratio, even at higher Mach numbers.

These investigations show that the flame plays a major role in the onset of combustion instability either by being a source or as an amplifier. However, from a careful observation of the review we can see that the flame acoustic response were investigated mostly on premixed combustion system and in many cases with simple geometries. Investigation of flame dynamics in complex geometries and

operating conditions that simulate realistic conditions are not yet explored fully. However, these studies suggest that there are two important mechanisms through which the heat release modulation occur in gaseous flames: flame front oscillations and fluctuations in the fuel/air composition.

1.1.2 Experiments in Pulse Combustors

While in pulse combustors the sustenance of the oscillations is the objective, the oscillations in other practical combustors are not welcome and thus control and suppression of the oscillation have been tried. Investigation in pulse combustors have helped greatly in understanding the role of different phenomena affecting the combustion instability. The limit cycle behavior of the combustion devices could be understood from these studies.

A large number of investigators (Clark & Humphrey, 1986; Crump *et al.*, 1986; Hegde *et al.*, 1987; Yang & Culick, 1986; Yu *et al.*, 1991) report on combustion instabilities particularly in dump combustors. Poinsot *et al.* (1987) investigated the combustion instabilities in a multiple inlet dump combustor. They concluded that low-frequency instabilities are acoustically coupled and occur at the eigen frequencies of the system. Theoretical and experimental work concerning pulse combustors, and the phenomenon of acoustic instability in combustion chambers has always been the subject of interest to the combustion and propulsion community. Since the underlying physics behind the combustion instability and pulse combustors are the same, this section is devoted to the state of art of pulse combustor technology.

Reuter *et al.* (1986) provided experimental data, describing the mixing of the reactants, the time dependence of the combustion process heat release rate, its phase relationship with the combustor pressure, and the spatial characteristics of the combustion processes. They used high speed shadow and Schlieren photography and also captured C_2* and CH* radiations. Their data showed that the reaction was periodic and that it remained nonzero throughout the entire cycle. Furthermore, the reaction rate was found to be in phase with the combustion pressure oscillations, satisfying the Rayleigh criterion for wave driving by heat addition.

Studies by Keller *et al.* (1989) examined the influence of characteristic times on the performance of a Helmholtz type pulse combustor. Under varying conditions, it was found that the pressure oscillations and frequency were strong functions of the phase relationship between the resonant pressure wave and the instantaneous energy release rate. They concluded from their results that the total delay time is an important factor in determining the response of a pulse combustor. They suggested that P_{rms} a parameter to measure the behaviour of pulse combustor since it exhibited same trend as that of Rayleigh efficiency.

Time resolved gas temperature measurements also provide insight into the magnitude and importance of cyclic temperature fluctuations (fluctuations of the gas temperature through the combustor cycle) in the pulse combustor tail pipe. Dec & Keller (1990) investigated the cyclic behavior of the gas temperature in the oscillating turbulent flow in a pulse combustor tail pipe using two-line atomic fluorescence. Spatially resolved temperature measurements were made providing cycle-resolved profiles of temperature. Random temperature fluctuation intensity, velocity, and combustion chamber pressure were compared. Velocity field effects dominated the cyclic behavior of the gas temperature, over the effects of isentropic compressive heating and the convection of hot pockets of gas from the combustion chamber. Cycle-resolved profiles were found to show the gas temperature to be constant across the tail pipe, except for the boundary layer region, at all times during the cycle.

The results of numerical experiments by Keller *et al.* (1989) showed that changing the phase relation between pressure and energy release could vary the operating frequency and pulsation magnitude and changing the temperature field could vary the acoustics. They also found that changes to the injection geometry or the kinetics affected the time delay between injection and reaction. Studies showed that the operating frequency was not very sensitive to changes in the heat transfer coefficient. Since the sound speed affected the phase relation between pressure and the energy release, the pulsations magnitude was more sensitive to heat transfer. They claimed that fluid mixing of the cold reactants with hot products provided control of the time varying energy release profile and so they suggested that the mixing could be adjusted by changes in the injection geometry.

An experimental investigation into the details of mixing, combustion and ignition processes occurring in a flow field under the influence of resonant acoustic perturbations in a Helmholtz type pulse combustor was done by Keller *et al.* (1994) by using detailed cycle resolved measurements of the velocity field, which was determined combined with cycle-resolved single-shot images of both chemiluminescence and Schlieren photographs. Tang *et al.* (1995) used flow visualization, LDV, and radical radiation imaging phase locked with the pressure to understand the fluctuating heat release mechanism in a non-premixed Helmholtz type pulse combustion system. Kushari *et al.* (1996) studied the effect of fuel composition on pulse combustor performance and they found that hydrogen in the fuel advanced timing of the heat release, leading to reduction of driving and higher frequency of the combustor. Apart from that, they reported that hydrogen in the fuel also lead to lower decibel levels and higher heat contents and their tests indicated that changes in combustion chemistry rather than mixing rates were responsible for these observations. It was also observed that addition of hydrogen extended the rich limit of operation of the combustor while reducing the amplitude of pulsations.

Marsano *et al.* (1998) presented several variations of a spatially averaged phenomenological model to predict trends observed in pulse combustors with aero-valved inlets. They could report that the frequency of inlet supply was coupled to the combustor's frequency, which induced a more stochastic oscillatory behavior consistent with experimental results.

These investigations are very useful not only because of the realistic geometries and flow conditions that were employed, but also because the underlying phenomena of the operation of these devices are similar to that of the combustor during the limit-cycle combustion oscillations. In the case of investigations where systems with simple configurations were considered the use of advanced diagnostic methods has revealed very important information on driving mechanism and also on mixing, ignition and stability.

1.1.3 Transfer Function of a Burner System

In many premixed gaseous flames the coupling between the heat release fluctuations and the pressure is mainly due to the fluctuating mass flow through the burner. These fluctuations are mainly because of the fluctuations in inlet velocity. Thus the coupling between the pressure in the combustion chamber and the heat release by the flame can be split into two parts 1) the relationship between the pressure in the chamber and the velocity fluctuations at the burner inlet (admittance of the burner) 2) the relation between the velocity fluctuation in the burner mouth and the fluctuating heat release. The second relation is generally called 'flame transfer function' (Merk, 1956). To determine the flame transfer function from measurements, the heat release from the flame should be correlated to the fluctuating inlet velocity. The most common method to measure the flame transfer function is to impose a fluctuation on the inlet velocity and to measure the response in heat release on these fluctuations.

Mastui (1981) used a speaker driver unit to excite a premixed, laminar methane-air flame and measured the pyro-acoustic amplification. He used a mathematical model of an axially symmetric premixed flame and he also used the concept of transfer function which was in good agreement with the experiments.

Lang (1991) also studied the flame transfer function by exciting the flame with speakers. It was observed in that study that at low amplitudes there was only the frequency of excitation but at high amplitudes, harmonic frequencies appeared. He suggested that their appearance could be correlated with a specific change in the flame front movement. On the basis of the results obtained by his experiments he proved that there was interaction between the flame front movement and the acoustic resonance.

Dowling & Hubbard (2000) using a kinematic model described the unsteady combustion in premixed ducted flames and in a typical lean premixed industrial turbine. Their flame transfer function measurements were in good agreement with their theory.

Dynamic behaviour of a laminar premixed flame was investigated by Ducruix *et al.* (2000). They characterized their flame response to incident perturbations with a transfer function with a constant flame speed approach as that of Fleifl

et al. (1996). The response of burner stabilized flat premixed flames to acoustic perturbations was done in this way by Rook *et al.* (2002). Recently, Zähringer *et al.* (2003) developed an experimental setup and a method for the determination of the transfer function of practical heating systems.

For lean premixed flames the flame transfer function for a combustion zone describes its response to small flow perturbations as a function of frequency (Cheung *et al.*, 2003). They assumed that the flow was one-dimensional, and also the flow to be composed of a steady mean flow and a small disturbance. If the fuel flow is choked, the fluctuations in equivalence ratio are due to fluctuations in flow modulations. Thus

$$\frac{\hat{Q}}{\bar{Q}} = -H_\phi(\omega)\frac{\hat{m}_i}{\bar{m}_i} \tag{1.2}$$

where, $H_\phi(\omega)$ denotes the flame transfer function, Q the heat release and m is the mass flow rate of reactants. Here cap denotes the fluctuating component and bar denotes the mean value.

Most of the studies related to experimental determination of flame transfer functions probe the response of the flames as a function of frequency. These studies have helped modelling the frequency response of the flames in the linear regime (i.e. at low perturbations). However in order to model the limit-cycle behaviors, there is a need for experiments at these non-linear regimes. The transfer function measurement studies generally employ chemiluminescence measurement technique to quantity heat release. Recently, there are a number of studies (see review by Lee & Santavicca (2003)) suggesting the possibility of ambiguity in the interpretations of the results from these measurements in these non-linear regime. Use of advanced laser based diagnostic methods are proposed for such studies in the same study. One such study was by Pun (2001), who developed a diagnostic technique based on phase resolved OH Planar Laser Induced Fluorescence (PLIF) measurements to study the burner behavior subjected to cyclic instabilities. Phase resolved OH PLIF and OH* chemiluminescence images were used to determine the heat release and the measurements were processed to obtain a flame transfer function.

In order to predict combustion instability, knowing the response of the combustion system to inlet flow conditions is necessary. Transfer functions that were

defined and determined by various investigators are all capable of evaluating the combustion dynamics of their respective systems. The transfer functions also help in determining the performance of a combustion system and in many cases leading to a better design for maximum fuel economy and with very low level pollutant production. However, it can be concluded that measurements in the nonlinear regime of flame response are yet to be explored to improve the capacity to predict the amplitudes of oscillations during limit-cycle behavior.

1.2 Motivation and Scope

The theoretical description of combustion-induced oscillations, a problem of significant theoretical and practical importance, necessitates a quantification of the response of the flame to the unsteady inlet velocity and/or equivalence ratio caused by the pressure waves that may be set up in the combustor. This is usually done by the flame transfer function (H) (Baillot *et al.*, 1992; Bloxsidge *et al.*, 1988; Brookes *et al.*, 2001; Candel, 2002; Dowling, 1997; Dowling & Stow, 2003; Ducruix *et al.*, 2000; Külsheimer & Büchner, 2002; Langhorne, 1988; Lawn & Polifke, 2004; Lawn *et al.*, 2004; Lieuwen, 2003; Lieuwen & Neumeier, 2002; Schuller *et al.*, 2003b; Zähringer *et al.*, 2003; Zhu *et al.*, 2001). As discussed previously, most of these investigations have been devoted to understanding the response of the flames in linear regime, and mostly quantified by flame transfer functions, H (see 1.2). If we include the dependence of the transfer function on the amplitude of the velocity fluctuations, which would result in understanding the limit cycle behavior, the transfer function can be rewritten as follows.

If the instantaneous flow velocity at the burner exit is U, then $U(t) = \langle U \rangle + u'(t)$, where $\langle\rangle$ and primes represent the mean and the fluctuating components, respectively. Similarly, if Q is the heat release rate, $Q(t) = \langle Q \rangle + Q'(t)$. For completely premixed mixtures, the non-linear flame transfer function or non-linear frequency response function can then be defined as $H(f, A)$:

$$H(f, A) = \frac{Q'(f)/\langle Q \rangle}{u'(f)/\langle U \rangle} \tag{1.3}$$

where $\langle Q \rangle$ is the time-averaged heat release rate, $\langle U \rangle$ is the bulk velocity of the mixture entering the combustor, $Q'(f)$ and $u'(f)$ are their corresponding

amplitudes at frequency f (i.e. the amplitudes of the Fourier transforms of Q and U, narrow-band filtered around f) and A is the magnitude of $u'(f)/\langle U \rangle$. If H were available, then reduced-order models (for a recent review of this concept, see Dowling & Stow (2003)) could be advantageously deployed to predict the onset of instabilities. H has been determined by theoretical models (Baillot *et al.*, 1992; Candel, 2002; Dowling, 1997; Dowling & Stow, 2003; Ducruix *et al.*, 2000; Lawn *et al.*, 2004; Lieuwen, 2003; Schuller *et al.*, 2003b) and CFD (Brookes *et al.*, 2001; Zhu *et al.*, 2001), but very few direct measurements of H are available (Bloxsidge *et al.*, 1988; Külsheimer & Büchner, 2002; Langhorne, 1988; Lawn & Polifke, 2004; Lieuwen & Neumeier, 2002; Zähringer *et al.*, 2003) due to the difficulties involved in estimating the heat release rate. Although the earlier linear models (Dowling & Stow, 2003; Lieuwen, 2003) for predicting combustion instabilities could predict the phase relationships well even with rough estimates of H, more accuracy is required on the amplitude dependence of H for limit-cycle amplitude predictions, which essentially fall in the non-linear regime. In these non-linear regimes the difficulties in measuring heat release rates are much more pronounced, prohibiting the understanding of such processes.

Until now, most heat release measurements have been based on narrow-band OH*, CH*, C_2* and broadband CO_2* chemiluminescence emission (Bernier *et al.*, 2003; Bloxsidge *et al.*, 1988; Külsheimer & Büchner, 2002; Langhorne, 1988; Lawn, 2000; Lawn & Polifke, 2004; Lieuwen & Neumeier, 2002; Pun *et al.*, 2003; Zähringer *et al.*, 2003). Langhorne (1988) used light emission from C_2* to quantify the heat release and investigated 'Reheat Buzz' in a premixed flame stabilised by V-gutter. The measurements were used to obtain heat release-pressure transfer function, which was later used for theoretical predictions successfully (Bloxsidge *et al.*, 1988). OH* chemiluminescence was used to measure the transfer function to understand the combustion dynamics of turbulent swirling flames (Külsheimer & Büchner, 2002) and was also used later successfully by Zähringer *et al.* (2003) to measure the transfer function in a practical industrial burner. Further, Lieuwen & Neumeier (2002) measured non-linear transfer function in a gas turbine combustor using OH* chemiluminescence. Lawn (2000) developed a cross-correlation technique based on OH* chemiluminescence to measure the distributed heat release in unsteady flames. Pun *et al.* (2003) used OH* as well as OH PLIF to

measure the flame response and Bernier *et al.* (2003) used CH* to quantify the heat release for their study in a model premixed, prevaporized swirl-stabilised combustor. In all the above studies, the chemiluminescence signals have been observed to scale linearly with fuel consumption rates and have thus been assumed to correlate with global heat release rates. CH* was used to understand also the response of forced non-premixed flames by Hardalupas & Selbach (2002). In a recent study with opposed jet flames (Hardalupas & Orian, 2004), the authors conclude that OH*, CH* and CO_2* are better heat release measures as opposed to the C_2* chemiluminescence, which was reported to fail at high strain conditions.

In earlier experimental studies with CH PLIF it was found that CH disappears in regions of high curvature and rates of strain (Nguyen & Paul, 1996). By inference, both CH* and OH* must be questioned for their reliability as heat release or flame front markers, because both are products of the CH reaction pathway. Similar problems exist for CO_2* chemiluminescence. A thorough recent review of related theoretical and experimental work by Lee & Santavicca (2003) with relevance to instability research also suggests that chemiluminescence data must be interpreted with care. However, very few investigations were dedicated to compare the dynamic response of the flame chemiluminescence with other advanced optical measurements.

In parallel to theoretical models that use a calculation of flame surface area to build the flame transfer function (see Dowling (1999) and the reviews Candel (2002); Lieuwen (2003)), measurements of the flame area have been performed for laminar flames (Baillot *et al.*, 1992; Ducruix *et al.*, 2000; Schuller *et al.*, 2003b) but not extensively yet for turbulent flames. Various techniques can be used to visualise the flame contour and hence flame area. For premixed flames, OH PLIF is very powerful since OH gradients are generally found to correlate well with the position of the local flame front (Haq *et al.*, 2002; Kaminski *et al.*, 2000; Knikker *et al.*, 2002; Lee & Santavicca, 2003). Knikker *et al.* (2002) performed OH PLIF in a bluff body stabilised, ducted premixed turbulent flame to identify the two-dimensional flame contours and hence to estimate heat release rates from them. To get an estimate of heat release from the flame area, one must assume that the flame speed does not change along the flame contour. In addition, the total flame area is difficult to estimate from two-dimensional image slices because

no information on the effects of wrinkling in the third dimension is available. Hence, there are ambiguities in estimates of the total heat release from such data. Despite these reservations, Lee & Santavicca (2003) reported measurements of two-dimensional flame contours, which were identified from OH PLIF images in an unstable flame in a gas turbine combustor and the resulting estimated total flame area was found to be in phase with CO_2* emission. Since flame surface density (FSD) has already been proven a very useful tool for turbulent combustion in general (Chew *et al.*, 1990; Shepherd, 1996) and can be captured equally well by tomography (Chew *et al.*, 1990; Shepherd, 1996; Veynante *et al.*, 1994) and OH PLIF (Descamps *et al.*, 1996; Lee *et al.*, 2000), this technique can be used for flame instability studies, provided that the burning rate along the flame contour does not change significantly.

A more direct measurement of local heat release rate can be accomplished by simultaneous PLIF imaging of formaldehyde (CH_2O) and OH. The pixel-by-pixel product of such images has been shown to correlate well with the local heat release rate in studies of laminar flame-vortex interactions (Najm *et al.*, 1998b; Paul & Najm, 1998). Böckle *et al.* (2000) have demonstrated the technique in turbulent premixed flames stabilised on a Bunsen burner and Fayoux *et al.* (2005) used it in laminar counterflow premixed flames. It was suggested in Najm *et al.* (1998a) that this technique predicts the heat release better than chemiluminescence in the presence of strong vortex, which makes this technique a better candidate for conditions where the flame-acoustics interaction is dominated by vortex shedding mechanisms. However, this measurement method has been proved to work only for completely premixed flames.

In the thesis, we apply the above methods of heat release measurement to derive flame transfer functions for acoustically forced fully-premixed and partially premixed turbulent flames. The difficulties discussed above are expected to be more pronounced when large-amplitude oscillations are present, with resulting high strain rates and possible localised extinctions. Very few experimental investigations of this so-called 'non-linear' regime are available (e.g. Bellows *et al.* (2003); Lieuwen & Neumeier (2002)), although it is a condition that may occur in combustion-induced oscillations in realistic combustors and is related to the combustor's limit-cycle behaviour. The saturation of the flame response to

flow velocity fluctuations is challenging to describe theoretically (Dowling, 1997) and little is known about its physical origin, although its presence has been observed in naturally-unstable combustors (Huang & Yang, 2004; Poinsot *et al.*, 1987; Schadow & Gutmark, 1992). There have been numerous investigations on small-amplitude perturbations both by experimental determination and by modelling (see Baillot *et al.* (1992); Ducruix *et al.* (2000); Lieuwen (2003); Schuller *et al.* (2003b)), however the information about finite amplitude effects on frequency response of flame is very scarce. Dowling (1997) modelled the non linear coupling between inlet velocity fluctuations and heat release based on the fact that the chemiluminescence cannot become negative during the flow reversals, leading to conditions where the saturation happens when the flow velocity fluctuations are of the order of mean velocity, i.e. $A \sim 1$. The measurements in a lean turbulent premixed flame by Bellows *et al.* (2003) showed a saturation in their flame chemiluminescence at a velocity amplitude of $A \sim 0.2$-0.3. They speculated that the non-linear response could be due to non-linear flame sheet kinematics, but suggested further optical studies of the flame front dynamics to better understand the mechanism present in their study. Theoretical and experimental determination of transfer function in laminar flames (Baillot *et al.*, 1992; Bourehla & Baillot, 1998) showed that the flame area evolved non-linearly with increase in amplitude. In a recent work (Schuller *et al.*, 2003a), it was shown that the cyclic flame surface destruction during the neighbouring flame front interaction was an important mechanism in self-excited oscillations. Preetham & Lieuwen (2004) suggest a similar kinematic restoration process as a possible mechanism for non-linear frequency response of flame.

In the case of premixed flames with time varying equivalence ratio, the role of kinematics and the fluctuations in equivalence ratio (Armitage *et al.*, 2004) is yet to be understood fully for their role in non-linear response during the self-excitation. Though the role of equivalence ratio fluctuations was identified in the combustion instability mechanisms, most of the theoretical and experimental methods till now have been dealing with the frequency responses of the flames (Lieuwen & Zinn, 1998a,b; Sattelmayer, 2000). The lack of experimental measures to quantify the heat release reliably in this scenario adds to the complexity for the interplay of different physical processes involved. The nonlinearity in these

flames is yet to be understood fully. There is hence a need for detailed experiments to understand the amplitude dependence of flame responses to equivalence ratio perturbations, which can then improve the prediction capabilities (Lieuwen, 2003).

It is clear that various possibilities exist as to the origin of a flame's non-linear response and that various techniques, with different associated uncertainties, are available for measuring the heat release rate that determines this non-linear response. In an effort to understand this phenomenon better, in this thesis, two series of experiments were performed. First, a relatively simple turbulent fully-premixed flame was forced at high amplitudes and its response was quantified by chemiluminescence, FSD and direct local heat release imaging (RX). The results provide both a comparison on the heat release measurements and some data on non-linearity. Second, the response of a flame to oscillating equivalence ratio and inlet velocity was investigated using conventional chemiluminescence technique and FSD measurements.

Table 1.1 summarizes the key experimental investigations performed to understand the flame acoustic interaction. It can be seen from the literature, that albeit the exhaustive research on premixed combustion system, the investigations of system in the nonlinear regime and also on partially premixed flames have been very few.

Table 1.1: Summary of literature pertaining to experimental investigations on processes related to combustion dynamics.

	configuration/geometry	operating condition	excitation	freq/amplitude	probing technique
Laminar					
Schimmer & Vortmeyer (1977)	encl. flat flame	P, $0.6 < \phi < 1.4$;	speakers		
Joos & Vortmeyer (1986)	encl. flat flame	P,$0.8 < \phi < 1.3$	self+speakers	50-200 Hz; multiple freq	OH* chemi; LDV
Sankar *et al.* (1990)	encl. flat flame	p ,0.8¡$\phi < 1.3$	speakers	200-1250 Hz 135 dB	2 component LDV
Baillot *et al.* (1992)	burner stab. coni.	P, ϕ=1.05;	speakers	$< 200Hz$	2 comp. LDV
Bourehla & Baillot (1998)	burner stab. coni.	P,ϕ=1.06;	speakers	20-1000 Hz; $0 < u'/U < 1.5$	LDV, luminosity
Mueller *et al.* (1998)	encl flat	P, ϕ=0.585	speakers		PIV
Durox *et al.* (1998)	burner stab coni.	P,ϕ=1.05;	speakers	880,950 Hz	LDV
Samaniego & Mantel (1999)	encl. V flame	P,$0.55 < \phi < .61$;	speakers		CO2* chemi; smoke;schn
Baillot *et al.* (1999)	quasi-coni.	P,ϕ=1.05	speakers	880,950 Hz;152dB	Laser tomo.
Ducruix *et al.* (2000)	burner stab. coni.	P,ϕ=0.95	speakers	5-300 Hz	CH* chemi;Schn; LDV
Najm *et al.* (2001)	encl. V flame	ϕ=1.0,1.2	speakers		PLIF CH, OH, HCO,CH3O
Turbulent					
Reuter *et al.* (1986)	helmholtz comb	P,	speakers	40 Hz	CH*,C2* chemi;high speed shad;schn
Poinsot *et al.* (1987)	dumb comb.	P, ϕ around 0.8	self	440-590 Hz	C2* chemi, Schn.
Langhorne (1988)	con. gutter stab	P, $0.65 < \phi < .708$	self	73-109 Hz	C2* chemi
Dec & Keller (1989)	Helmholtz combustor	P, ϕ=1.0	self	101-54 Hz; 7.35kPa	LDV
Gutmark *et al.* (1989)	coannular	D, Re, 7000	speakers	100, 200 Hz	OH PLIF thermometry
Dec & Keller (1990)	Helmholtz comb	p,ϕ=1.0	self	67-101 Hz,upto 500%	cycle resolved TLAF tempr
Barr *et al.* (1990)	Helmholtz comb	p, $0.4 < \phi < 1.5$	self	65-80Hz	
McManus *et al.* (1990)	2D dump	P,ϕ =0.63	speakers	35-400 Hz u'=0 - 10m/s	CH* chemi;smoke,schn LDV
Macquisten & Dowling (1993)	enclosed gutter stab.	P;$0.8 < \phi < 0.62$	siren	120-200 Hz	C2* chemi; LDV
Keller *et al.* (1994)	Helmholtz comb	p,ϕ=0.68	self+speakers	100 Hz	Schn,cycle resol OH* chem., LDV
Macquisten & Dowling (1995)	twinstream afterburner	P, ϕ=0.7/.88	self	109,240 Hz	C2* chemi
Tang *et al.* (1995)	Helmholtz comb	P	self	47 Hz	CH* chemi; LDV,high speed shad
Hardalupas & Selbach (2002)	sw stab. open/diff.	D,$0.2< \phi <4$	speakers	200,920 Hz	CH* chemi; LDV
Ratner *et al.* (2002)	bluffbody/aerodyn stab (encl)	P,Re=8000	speakers	22-55 Hz	NO, OH PLIF
Cala *et al.* (2002)	bluffbody stab,open	P, ϕ=0.6	speakers	600 Hz	shad; LDV
Lieuwen & Neumeier (2002)	sw, dump comb	P,ϕ=0.8	self+speakers	157,235 Hz	OH/CH* chemi
Paschereit *et al.* (2002)	sw,dump comb	P	speakers	40-200Hz Hz	OH* chemi
Pun *et al.* (2003)	bluffbody/aerodyn stab (encl)	P, Re=20,000, U=30m/s	speakers	< 55 Hz	OH PLIF
Cheung *et al.* (2003)	LPP	P, $37.5 < AFR < 41.8$;	siren	50-1000 Hz	CH* chemi
Giezendanner *et al.* (2003)	swirl stab	D,ϕ=0.8	speakers		OH* chemi; OH,CH, H2CO PLIF
Bernier *et al.* (2003)	swirl stab encl	ϕ=0.9	sec. air	400 Hz	CH* chem
Bellows & Lieuwen (2004)	model GT	P, ϕ=0.95	actuator	250-330 Hz	CH*/OH* chemi

1.3 Specific Objectives

The main objectives of this thesis are therefore:

- to develop a bluff-body combustor which can be operated under different acoustic modes with capacity to vary amplitude & frequency of the forced oscillations and combustion modes (premixed and partially premixed) (to introduce spatial and time variation in premixedness);
- to compare the various techniques for estimating the heat release rate and to apply them to an acoustically-forced premixed/partially premixed flame stabilised by a bluff-body;
- to explore how the flame response measured by these techniques behaves as a function of large excitation amplitudes;
- to understand the origin of the phenomenon of saturation of the heat release response of premixed flames to inlet velocity and also to the equivalence ratio perturbations in the case of partially premixed flames.

1.4 Outline of the Thesis

This dissertation describes the experimental investigation of the response of the premixed flames to acoustic forcing, with main aim to understand the amplitude dependence of the flame response. Experiments have provided data on the acoustic response of flames at various conditions, which could serve as input to acoustic analysis and also serve as a validation database for CFD and other prediction methods.

Chapter 2 describes the experimental apparatus and the various experimental methods employed during the present study. The data processing procedure is also described in detail in this chapter. The results from cold flow smoke visualization measurements and the behaviour of the steady flames are presented in Chapter 3. Chapter 4 presents the results from the study of fully premixed flames, while Chapter 5 presents the response of premixed flames to time-varying equivalence ratio and velocity at the inlet. In Chapter 6, self-excited flames are

studied to show to what extent the high-amplitude forced flames are representative of limit-cycle combustion induced oscillations. Chapter 7 summarizes the conclusions reached in all the above chapters.

Chapter 2

Experimental Methods

This chapter describes the experimental apparatus, the flow configurations and also the experimental techniques employed during the present work.

2.1 Development of a Bluff-body Combustor

The experimental apparatus used for the present investigation is a 10 kW acoustically excited bluff body combustor. The combustor was designed to facilitate excitation of different acoustic modes inside the combustor using external acoustic drivers.

Figures 2.1 and 2.3 show the schematic and photograph of the burner assembly. The burner is designed to facilitate external acoustic forcing and can be operated in the absence or presence of strong acoustic oscillations. The burner consists of two concentric circular ducts of length 300 mm. The inner diameter (ID) of the outer duct was 35 mm, which also housed pressure taps for acoustic pressure measurements. The inner and outer diameter of the inner duct were 8 mm and 6 mm respectively. One end of the inner duct had a conical bluff body of diameter 25 mm, giving a blockage ratio of 50%, which stabilised the flame.

In order to achieve a completely premixed condition at the bluff-body, the air and fuel were mixed far upstream ($\sim$2 m) of the combustor. During the present work, ethylene and methane were used as fuel. The annulus between the outer and inner ducts served as the passage for the reactant mixture. The premixed reactants before entering the annulus of the pipes, flow through a 200 mm long

plenum chamber of inner diameter 100 mm. The plenum had a divergent and convergent cross-sections at the inlet and the exit, which helped to avoid the flow separation during the expansion and contraction. The flow was streamlined inside the plenum chamber by flow straighteners.

There are several ways in which the flame may be perturbed, so that the heat generation will oscillate (Schimmer & Vortmeyer, 1977):

1. Oscillating input mass flow rate of reactants
2. Oscillating the mixture ratio
3. Oscillating heat transfer to the burner
4. Oscillating turbulence generation or by vortex shedding
5. Oscillating change of reaction rate by adiabatic compression

The experimental work in this thesis deals with (1), (2) and (4). Acoustic perturbations were imposed using two loudspeakers with the peak power of 80 W. These two loudspeakers were mounted diametrically opposite to each other on the circumference of the plenum chamber at a location 100 mm downstream of the plenum inlet. The loudspeakers were excited by sinusoidal signals generated using a TTi 40 MHz Arbitrary waveform generator. The wave form generator had two channels which could be operated independently to generate two waveforms of different frequencies and amplitudes. The signal from a single or that from two channels after superimposition, was amplified by a 80 W amplifier, and sent to the speakers. The forcing amplitude (peak-to-peak voltage to the speakers) and the frequency of forcing were varied independently to understand the dependence of the flame response on amplitude and frequency of forcing. The forcing achieved was as high as 70% of the mean velocity (i.e., $A = 0.7$) for certain forcing frequencies (details of the acoustic characteristics of the combustor are presented in Chapter 3, Figs. 3.1 and 3.2).

In the case of fully premixed conditions, the acoustic forcing by the loudspeakers effected velocity oscillations at the bluff body. In order to obtain a time-varying equivalence ratio at the flame-front, the combustor was also operated in an imperfectly premixed mode, where the flame-acoustic interactions

would closely mimic the oscillations in gas turbine combustor. In this case, the fuel (ethylene) was injected radially through six choked injectors along the circumference of the central pipe 55 mm upstream of the bluff body and air through the outer pipe (see Fig. 2.2). This resulted probably in an imperfectly premixed condition at the flame, which when imposed with acoustic oscillation would also result in a time varying equivalence ratio.

The flame was enclosed using a 80 mm long fused silica quartz cylinder of inner diameter 70 mm which provided optical access for the imaging and also avoided equivalence ratio (ϕ) variations due to possible air entrainment from the surroundings. In order to reduce the interference from the acoustics of the downstream geometry on upstream forcing, the length of the enclosure was chosen to be small so that its resonant frequency was much higher than the frequency of forcing. For the present study, the forcing frequency was varied between 20 to 400 Hz while the fundamental frequency of the downstream duct is around 1000 Hz, hence the resonant effects of the downstream geometry are minimized. However, longer tubes were used for certain experiments aimed to study self-excited oscillations (details in Chapter 6).

Different swirl conditions were achieved by introduction of static swirl vanes along the flow passage between the inner and outer ducts (see Fig. 2.1). The swirls with vane angles 45^o and 60^o with respect to the flow axis were employed to induce a medium and high swirl in the flow. Figure 2.4 shows the swirlers used for the study. The height of the 45^o and 60^o swirlers are 16.6 mm and 14.6 mm respectively. The swirler is located at 50 mm upstream of the bluff body plane (see Fig. 2.2).

The burner was built for understanding flame, acoustic and flow field interactions relevant to practical combustors and hence, the various geometrical parameters where chosen very carefully. The basic burner design was based on liquid fuelled ramjet combustor design guidelines (Zelinski *et al.*, 1960). The geometry of the flame holder and its blockage may affect the stabilization process. The flame structure not only depends on the fuel characteristics, but also on the characteristics of the recirculation zone. The confinement would also be a deciding parameter due to the resulting blockage ratio of the bluff body; walls constrain the flow field and influence the recirculation zone. Increasing the blockage ratio

of the bluff body would increase the length of the recirculation zone and increase in bluff-body cone angle would lead to an increase in the intensity of the circulation in the bluff body wake (Esquiva-Dano *et al.*, 2001). However, with a flame model for combustion instability studies, Dowling (1999) showed the blockage of the bluff body could be neglected without degrading the agreement between the theory and the experiments in a low Mach number flow (see Langhorne (1988)), which implies that the drag exerted by the gutter/bluff-body has negligible effect on combustion oscillations. Bearing all the aforementioned points, the enclosure dimensions, bluff body shape and diameter were chosen. The conical shaped bluff body with 45° half cone angle and with a blockage ratio of 50% was used for the present study. The aspect ratio of the enclosure diameter to that of the combustor inlet was chosen based on a scaled model of a RB211 Rolls-Royce combustor (Armitage *et al.* (2004)).

2.2 Instrumentation

In this section, various measurement techniques employed for the current study are discussed in detail, outlining the reservations and strengths of these measurements wherever appropriate. Estimates of error for these techniques are also provided in this section.

2.2.1 Flow-rate Measurements

The air input to the combustor was supplied from a reservoir with a capacity of 0.57 m^3 at a constant pressure of $10x10^5$ Pa. The fuel was supplied from commercial cylinders fitted with appropriate gas regulators, which can supply the gas at constant pressure. The mass flow rates of the air and fuel were controlled and monitored with BRONKHORST Hi-Tech mass flow controllers with measurement ranges of 12-600 liters per minute (lpm) for air and 1.2-60 lpm for ethylene, with an accuracy of 0.5% of the Full Scale Deflection.

2.2.2 Acoustic Pressure/Velocity Measurements

Three Kulite high sensitivity pressure transducers (Model XCS -093 with sensitivities of 4.2857x10^{-3} mV/Pa) were flush mounted to the flow passage in order to measure pressure perturbations accurately. The two-microphone technique reviewed in Seybert & Ross (1977) was used to determine the bulk velocity fluctuations at the combustor inlet from these pressure measurements. Direct measurements of velocity fluctuations were performed under cold flow conditions with a Dantec hot-wire anemometer located at a radial distance of 15 mm from the bluff body center to calibrate the two-microphone technique. The signal from the transducers and the hot-wire anemometer were amplified, digitised and saved using a digital data acquisition system with an analog to digital (A/D) convertor. National Instruments PCI 6034E DAQ card with 16 bits resolution and with an input voltage range of 10 $\pm$ 0.05 V was used for this purpose, the maximum sampling rate at which data can be acquired with this unit was 200 KHz. In order to digitize analog signals with minimum distortion, the sampling of an analog signal should be performed with a sampling frequency twice that of the maximum value of expected frequency, called Nyquist frequency. The range of forcing frequencies employed for this investigated was between 20-400 Hz. Data were acquired at a sampling rate of 10,000 Hz and time series lasting 2 seconds were collected and stored for post-processing. This resulted in a frequency resolution of 0.5 Hz.

2.2.3 Smoke Visualisation

General properties: A common way to visualize a flow-field is to use laser tomography. This technique consists of lighting the flow seeded with fine particles by means of a laser sheet. The light is scattered by different types of markers incorporated in the flow, for example particles, fine droplets or smoke. The word "smoke" is commonly used in wider sense, including combustion products, steam, vapor, aerosols, mists and some tracer gases (such as CO_2) which becomes visible without need of special optical techniques (Merzkirch, 1987). In general, the smoke refers to neutrally buoyant tracer. The particles, liquid or solid in the smoke are usually of very small diameters, of the order of 1 μm and hence the buoyancy effects are negligible.

Smoke generation: The basic types of producing smoke are burning or smoldering tobacco, wood or straw, or incense sticks; vaporizing mineral oils; producing mist from various chemical reactions and condensing steam to form a visible fog (Merzkirch, 1987). During the present work, a commercially available *ProSound MFX-700 Fog machine* was used to produce smoke. The smoke generator uses a water based, non-toxic fog liquid. The smoke generated by the fog machine was contained in a rectangular chamber. This smoke reservoir had an inlet into which a small amount of bleed air was passed, which carried the smoke through an outlet into the combustor. Figure 2.5 shows the schematic of the smoke visualization unit used during the present study.

Introduction into the flow: The smoke was introduced into the central recirculation by injecting the smoke through the central bluff body. Figure 2.6 shows the bluff body used for smoke injection. The holes provided along the radius and the holes on the circumference introduced smoke into the recirculation zone. The amount of air carrying the smoke into the flow was kept to a minimum, so that the shape and size of the central recirculation zone was not affected.

Illumination: The smoke filled recirculation was illuminated using a thin sheet of laser light. Beam from a 20W copper vapor laser (Manufacturer: Oxford Lasers) was used to make a 1.5 mm thick laser sheet. The green laser light emitted at 510 nm was transported to the interrogation point using a fiber optic cable and at the point of interrogation the beam was made into a sheet using optics consisting of concave and convex cylindrical lens combinations.

Imaging: The use of cameras allow one to record the smoke visualizations for quantitative analysis. During the present study, the laser illumination of the recirculation zone was recorded using a high speed, mono CMOS Phantom v4.2 camera. The images where taken at 2500 frames per second. The individual frames had an exposure time of about 200 μs. The interrogation area was focused on to a 256 x 512 pixel area. These images were saved for post processing.

2.2.4 Chemiluminescence Measurements

In order to study the unsteady dynamics of a flame, a reliable technique to visualize the combustion process and its response to an oscillating flow field is required. Two common methods that are used to perform these measurements are chemiluminescence and Planar Laser Induced fluorescence (PLIF) techniques.

Chemiluminescence is radiation emitted from electronically excited molecules, while returning to a lower energy state. The wavelength of this radiation is characteristic of the particular molecule and the particular transition the molecule undergoes. For simple diatomic molecules, the spectrum exhibits one major peak and relatively few, weak secondary peaks. For complicated molecules, the radiation spectrum is broader. OH* and CH* are examples of molecules exhibiting a simple spectrum with major peaks at 308 nm and 431 nm respectively. The reason for which chemiluminescence from flames is interesting is that the concentrations of excited molecules seen in flames exceed the equilibrium concentrations expected at the same temperature without chemical reaction by several orders of magnitude. It can be deduced from this fact that excited molecules are not only produced by thermal excitation but also are produced as the products of reactions. Because the amount of radiation observed in the flame at particular wavelength is proportional to the concentration of the associated excited molecule, the intensity of the measured radiation can be directly related to the concentration of the excited molecule (Haber, 2000).

The idea of using chemiluminescence in dynamic measurements was explored early on by Price *et al.* (1968) who found a good correlation between the noise from turbulent flames to oscillation in the strength of the chemiluminescence signal. Later, Samaniego *et al.* (1995) showed that the heat release rate had a linear correlation with CO_2 chemiluminescence in their numerical investigation. In combustion dynamics research, oscillating heat release is often assumed to be proportional to the oscillating strength of a chemiluminescence signal from the reaction zone. Paschereit *et al.* (1998) used OH* chemiluminescence measurements to understand the dynamic behaviour of the flame in their experimental study. Langhorne (1988) assumed C_2* chemiluminescence to be proportional to heat release rate in their studies. Langhorne's work gave a calibration of C_2 heat

release, which was later used to model unsteady pressure oscillation by Bloxsidge *et al.* (1988). However, one major draw back of the chemiluminescence is the inability of the measurements to provide high spatial resolution, since it essentially involves a line of sight integration at the detectors. Assumptions generally made during the flame chemiluminescence measurements were that the chemiluminescence can be considered diffuse and that there is no chemiluminescence trapping, in other words, the flame is transparent to the chemiluminescence (i.e. the flame does not absorb any of the emitted radiation) (Haber, 2000).

The chemiluminescence experiments can be categorized into two groups; measurements using Photomultiplier tubes (PMT) with a slit obscuring a portion of the flame to obtain some spatial (typically axial) resolution and full planar view imaging using charge coupled device (CCD) based cameras. The chemiluminescence measurement facility used during the current investigation involves measurements with both these systems. It essentially consists of collection optics, which transports the signal to the PMT through appropriate filters. The photomultiplier tubes used to measure the global OH* and CH* chemiluminescence during the present work were Hamamatsu (R3788) side-on PMTs, both fitted with interference filters of 10 nm bandwidth centred at 307 nm and 435 nm respectively. The signal collection optics used for OH* and CH* chemiluminescence measurement were identical and were designed to collect light from the entire combustion zone and it was ensured that both the PMTs viewed the same region. The PMT measurements were recorded simultaneously with the acoustic pressure measurements using the data acquisition system described earlier. During the current study, along with the PLIF images (described in the next section), the OH* chemiluminescence was also recorded simultaneously by using the double frame double exposure option of the ICCD-1 camera (Fig. 2.8), for which the intensifier was gated at 50 μs. The collection wavelength of OH* chemiluminescence images taken with the camera was broad (from 305 nm to 400 nm), while that of PMT measurements was a 10 nm wide band around 307 nm.

While chemiluminescence measurements are more readily obtained, they have several disadvantages. The problem of low resolution (when captured using collection optics and PMT) can be circumvented by using an ICCD camera. However, these measurements cannot capture fine structures in flames, since the signal is

integrated through the depth of the flame, whereas PLIF images are obtained of only a very specific plane where the laser sheet illuminates the flame. Another disadvantage of chemiluminescence is that the signal is several orders of magnitude weaker than PLIF. This decreases the temporal resolution of measurements, since longer integration times are required to obtain a sufficiently strong signal. Najm *et al.* (1998b) performed a thorough study on indicators of heat release rate. Their studies concluded that HCO (among other observables studied such as CH* chemiluminescence, CH LIF, HCO fluorescence) is an excellent indicator of heat release rate everywhere. CH* and CH LIF particularly are poor indicators of heat release rate in areas of high flame strain and curvature immediately prior to extinction. They also reported that the assumption that chemiluminescence is proportional to heat-release rate, breaks down in regimes of very high strain and curvature, near extinction. The conclusion of their study was that in highly strained and curved flames, chemiluminescence of any sort is not a good indicator of heat-release rate.

2.2.5 Laser Induced Fluorescence Measurements

The advantage of laser diagnostics techniques is the ability to provide non-intrusive, in-situ measurements. The introduction of a physical probe will inevitably disturb the flow field, distorting the physics of the experiment. Another problem to note is the difficulty for a physical probe to survive in a high temperature, high pressure combustion environment. Laser diagnostics have been proven to be suited to acquiring chemical species data. Especially, laser-induced fluorescence (LIF) is capable of resolving minor species concentrations at low parts-per-million (ppm) levels Crosley (1993). Planar laser-induced fluorescence (PLIF) can be performed by spreading the laser beam into a sheet, yielding species concentration/number densities information as a 2-D planar image, contrast to LIF that resolves only a single point with each pulse. PLIF and LIF operate on essentially the same principles, with the difference being the way in which fluorescence signal is collected. In a LIF system, a photomultiplier can be used as a detector, whereas PLIF requires either a CCD or an intensified CCD (ICCD) camera or some other detector that provides two dimensional imaging.

Laser-induced fluorescence is performed by first, bringing the species of interest to an excited electronic state. Generally using lasers, (in the present work a tunable-dye laser, pumped by an Nd:YAG is used). The excited molecules then fluoresce, by emitting photons to attain lower energy states. The emitted photon can be at the same wavelength as the excitation source. It is more convenient if it is not, since detection can take place without interference from the laser source. The photon emitted through this process is detected using PMT or using an imaging system. Figure 2.7 outlines schematically this process.

In order to obtain an accurate LIF measurement, the quenching (or collisional quenching) rate is of primary importance. Quenching represents energy loss of the molecule by some pathways other than the fluorescence. The different possibilities include dissociation, collision with other molecules, ionization, chemical reaction, or transitions to unmonitored molecular energy states. To avoid errors introduced by unknown quenching rates generally saturated LIF is performed, which involves excitation with high intensity laser so that the quenching rate is small compared to absorption and stimulated emission rates. This also has the advantage of maximizing the fluorescence signal strength.

Generally, LIF measurements are done in the linear fluorescence regime, which allows for the use of comparatively low powered lasers. However, this does not eliminate the quenching dependence. The quenching rates are generally modelled if the the precise state of the system, such as temperature and concentrations of all other species are available. The primary purpose of applying the quenching correction is to determine quantitative species concentration information. During the present study, planar laser induced fluorescence of OH and formaldehyde was performed in the linear regime. The details of which are presented in the next section.

2.2.5.1 Spatially-resolved Heat Release Measurements

Figure 2.8 shows the layout of the laser diagnostic facility employed during the present work to measure spatially resolved heat release rate from simulatenous OH and formaldehyde (CH_2O) PLIF. The technique is described in more detail in Balachandran *et al.* (2005) and Ayoola *et al.* (2005). The technique has been

developed at Hopkinson Laboratory, Department of Engineering, University of Cambridge in collaboration with Mr. B. O. Ayoola of Chemical Engineering Department (University of Cambridge).

Laser system: The laser system consists of a cluster of 4 Nd:YAG lasers (Continuum Surelite), 2 dye lasers (Sirah Cobra-Stretch) and 2 high-resolution double-pulsed ICCD cameras (Lavision Nanostar). The Nd:YAG laser outputs 660 mJ/pulse at 1064nm (IR) and is equipped with a secondary harmonic generation system to provide beam at 532 nm (green). The 532 nm beam pumps the dye laser. The ICCD camera used during the current investigation is LaVision Nanostar with spectral response from 190-900nm, whose sensitivity is more than 80 counts/electron. The camera can be operated from 8 to 30 frames/s with a pixel rate of 12.5 MHz. The camera uses a 1280 x 1024 CCD array with pixel size equal to 6.7 mm and the minimum exposure time around 1.5ns. Digitization is done with 12 bit intensity resolution.

For OH PLIF, the frequency-doubled output from one dye laser (marked as Dye laser -1 in Fig. 2.8) was tuned near 283 nm to pump the $Q_1(4.5)$ transition of the $A^1\sum - X^2\prod$ (1,0) band. OH fluorescence from the (0,0) and (1,1) bands near 310 nm was captured on the ICCD camera (labelled ICCD 1 in Fig. 2.8) fitted with a UV f/4.5 Nikkor lens and a combination of UG 11 and WG 305 Schott glass filters. For CH_2O LIF excitation, the frequency-doubled output from the second dye laser (marked Dye laser -2) was tuned to pump the band $\tilde{A}^1A_2 - \tilde{X}^1A_1 4_0^1$ of CH_2O near 353 nm. The two counter-propagating laser beams were formed into overlapping sheets of 55 mm width, which intersected the axis of the bluff-body burner.

The thickness of the laser sheet was measured by the scanning knife-edge technique (Hornak, 2002). This was accomplished by placing a knife edge (here, a razor blade) normal to the laser sheet and traversing across it so that the beam was blocked progressively by the movement of the knife edge. The power of the transmitted laser beam was measured by a power meter while the knife edge was traversed. The derivative of the power versus distance curve is the mean sheet intensity profile. Figure 2.9 shows the power measured and its derivative, during such a knife-edge traverse. The thickness of the laser sheet, defined as twice the

distance from the center of the beam to where the light intensity dropped to $1/e^2$ of its maximum value was found to be 0.1 mm at the focal point (burner axis), increasing to not more than 0.2 mm at the confinement radius.

The CH_2O fluorescence was recorded on the other ICCD camera (i.e., ICCD 2) fitted with an f/1.2 Nikkor camera lens and filters (GG 375 (Schott) and 550 nm short pass), which provided broadband collection of the LIF signal and rejected out-of-band interference. The lasers were tuned off resonance to verify that the laser-generated interference was not an issue. The temporal separation of the laser pulses ensured that there was no cross talk between the two LIF measurements. In order to investigate local heat release fluctuations, the measurements were performed with a projected pixel resolution of 35 μm per pixel. For the FSD estimation, the OH LIF signals were recorded with a projected pixel size of 50-70 μm, which was enough to give both high resolution and large imaging areas so that the whole flame was viewed.

Measurement scheme: Numerical results have established an excellent correlation of HCO production rate with heat release and burning rates in N_2-diluted premixed methane/air flames (Najm *et al.*, 1998a; Paul & Najm, 1998). The major pathways leading to the production of CO and CO_2 in the lean combustion of hydrocarbon fuels proceed via HCO (Paul & Najm, 1998). The direct imaging of HCO is difficult due to the low levels of HCO present and hence HCO was imaged through simultaneous OH and formaldehyde imaging, which can be expressed through the following the reaction:

$$CH_2O + OH \rightarrow HCO + H_2O \tag{2.1}$$

The production rate of HCO directly dependent on the CH_2O concentration which in turn depends on the reaction $CH_3 + O \Leftrightarrow CH_2O + H$, which was shown to exhibit the largest fractional influence on the heat release rates (Paul & Najm, 1998). The forward rate of reaction 2.1 can be written as $k(T)[CH_2O][OH]$, where k is the rate constant, T is temperature and $'[\ ]'$ denotes number density. Since LIF signals are related to species densities, this provides an avenue to measure the reaction rate via the concentrations of CH_2O and OH. However, LIF intensities depend also on the temperature through the collisional quenching

and the Boltzmann population fraction (Paul & Najm, 1998). The product of simultaneously recorded LIF signals of CH_2O and OH can therefore be expressed as:

$$(CH_2O\ LIF)(OH\ LIF) \propto f(T)[CH_2O][OH] \tag{2.2}$$

Over a limited range of temperatures, it is possible to select transition lines such that $f(T)$ closely mimics the forward reaction rate $k(T)$ in Eq. 2.1 (Paul & Najm, 1998). The excitation lines chosen during this work are the same as that of Najm *et al.* (1998b); Paul & Najm (1998), which satisfy this criterion.

In atmospheric flames the fluorescence quantum yield is dominated by the quenching rates. In the case of OH PLIF, from judicious choice of excitation and detection wavelengths, the temperature dependence can be cancelled out and thus the PLIF images would essentially represent mole fraction (Paul & Najm, 1998). However, with CH_2O molecules, there is a strong temperature dependence from the Boltzmann fraction. This temperature dependence was modelled in Paul & Najm (1998) and the formaldehyde LIF signal was represented by $(CH_2O\ LIF) \propto X_{CH_2O}T^{-\beta}$, where X denotes mole fraction, with $2.2< \beta <3$ over the temperature range 800-1800 K, thus the functional dependence for $f(T)$ (Eq. 2.1) is between $T^{-0.2}$ and T^{-1}. In the work by Paul & Najm (1998) it was shown that in the range of temperatures expected in the region of overlap of the OH and CH_2O, the primary dependence in the product of LIF signals is through the product of number densities. Thus, the product of the two LIF signals provided a measure of a quantity that correlated with local heat release rate. In the present study, a similar approach as that of Najm *et al.* (1998b); Paul & Najm (1998) and Böckle *et al.* (2000) was followed, i.e. the product of LIF signals of OH and CH_2O was used to obtain a quantity which correlates with the heat release rate. More details are given in Ayoola *et al.* (2005).

Despite the fact that the numerical study in Paul & Najm (1998) was performed for methane, the same conclusion applies to ethylene that gives higher quantities of CH_2O and hence better signal to noise ratios. Steady laminar flame calculations also indicate that this reaction contributes significantly to the heat release in a lean ($\phi = 0.6$) premixed ethylene/air flame (Ayoola *et al.*, 2005), which

suggests that the simultaneous OH and CH_2O technique should be applicable also to the ethylene flames used here. In a recent work (Fayoux *et al.*, 2005), it was shown that the measurements from this technique in a laminar counterflow premixed flame of propane were in good agreement with computations with detailed chemistry, hence giving extra credence to the technique.

The laser imaging was phase locked with the reference signal. The TTL component of the forcing signal (the reference signal) triggered the CH_2O laser. After a delay of 500 ns, the OH laser was subsequently triggered. With respect to the flow and combustion timescales, this delay renders the laser measurements quasi instantaneous. Both OH and CH_2O fluorescence signals were captured with the respective image intensifiers gated at 350 ns. The acoustic cycle was divided into 18 phases and at every phase angle 75-100 images were taken and saved for post-processing and statistical analysis. The stored instantaneous images were processed and then averaged to obtain phase-averaged quantities (more details given later).

2.2.5.2 Time-resolved OH PLIF Measurements

For the time-resolved OH PLIF measurements, both dye lasers (1 and 2 in Fig. 2.8) were tuned near 283 nm to pump the $Q_1(6)$ transition of the $A^1\sum - X^2\prod$ (1,0) band. The four Nd:YAG lasers which pumped these dye lasers were triggered in sequence at a time interval of 1 ms. The images were captured using the double frame, double exposure option of the cameras resulting in four OH-PLIF images separated by 1 ms. This duration is not short enough to track the quickest transients of the turbulent flame. For example, using an advection speed of about 10 m/s, 1 ms gives a distance of 10 mm, which is about half a bluff-body diameter. However, some very useful insights can still be drawn on the dynamics of larger scale structures, as will become evident later.

2.3 Data Processing

2.3.1 Determination of the Flame Response

2.3.1.1 Based on OH* and CH* Chemiluminescence

Figure 2.10 shows an example time series of simultaneously performed reference signal, acoustic pressure and OH* chemiluminescence measurements. Such traces were analysed spectrally for different forcing frequencies and amplitudes using the Fast Fourier transform (FFT) technique. From such power spectra, the complex amplitude of the quantities $OH^{*\prime}$ and $CH^{*\prime}$ at the forcing frequency f, were determined. These values were normalised using the time mean values of OH* and CH* respectively to obtain $OH^{*\prime}(f)/\langle OH^{*}\rangle$ and $CH^{*\prime}(f)/\langle CH^{*}\rangle$ which are used as estimates of $Q'(f)/\langle Q\rangle$. The two quantities, $Q'(f)/\langle Q\rangle$ and $u'(f)/\langle U\rangle$ determined from the simultaneous acoustic pressure measurements using the two-microphone method were used to determine the flame transfer function $H(f, A)$ defined by Eq. 1.3. The reference point at which $u'(f)/\langle U\rangle$ is measured for the transfer function is critical to obtain a reliable H value. In a recent work by Truffin & Poinsot (2005), it was shown that if the reference point is not close to the inlet of the combustion chamber, it would result in uncertainties in H estimation. During this work, the reference point was located at the inlet of the combustion chamber.

2.3.1.2 Based on Flame Surface Density

The phase locked instantaneous OH PLIF images were used to estimate the flame surface density. The OH PLIF intensity images were corrected for the background noise and also for the beam profile in-homogeneities. These images were then filtered with a Gaussian filter of width 3 pixels to remove the high frequency noise. The filtered intensity images were subsequently resized by 2x2 binning, which resulted to a projected pixel size of 150 μm and were then converted into binary images by an intensity thresholding procedure. Here, the pixel value of 1 corresponds to progress variable equal to 1 (burnt gases) and pixel values of zero indicate progress variable 0 (fresh mixture). The instantaneous flame contour was obtained from the instantaneous map of progress variable. The

flame surface density (FSD) was computed with a procedure similar to the one mentioned in the Veynante *et al.* (1994). The measurement domain was divided into overlapping square boxes of 5 pixel x 5 pixel, thus the interrogation box dimension chosen for the FSD computations was about 0.5 mm x 0.5 mm. The box dimension was kept to this small value to avoid the artificial diffusion that would be introduced if larger box dimensions were chosen. In each box, the arc length of the flame was computed. The results are averaged over the available number of images (generally around 75-100 images). These computed values when divided by the box surface resulted in flame surface density (FSD) at the center point. During these tests, an increase in the number of images did not alter the calculations significantly. The dependence of box size on the FSD computation was investigated as mentioned in Donbar *et al.* (2000) and it was found that the results were independent of the box size for the chosen values during these computations.

Figure 2.11 shows the natural emission of an unforced flame captured using a digital camera. The figure suggests that the flame is symmetric and is also compact within the short enclosure. Figure 2.12(a)-(i) shows a typical instantaneous OH PLIF image and the corresponding instantaneous flame trace (image (iv) in the sequence). By averaging the instantaneous progress variable and flame surface density images taken at the same phase, phase-averaged progress variable and phase-averaged flame surface density images are obtained. In order to compare the evaluated quantity with measured global heat release measurements, such 2D FSD phase averaged images were revolved around the central burner axis to obtain a 3D surface. In order to compare the OH* chemiluminescence and FSD, 2D slice of time averaged OH* image obtained using Abel inversion is presented in Fig. 2.13 along with the corresponding FSD image. It can be clearly seen from these images that the spatial heat release distribution evaluated from these two techniques agree very well, which also implies that the axisymmetric assumption is true for this flame. The axisymmetric assumption was further verified by horizontal OH PLIF measurements performed on an open flame under similar flow conditions. This phase averaged quantity obtained for every phase over the full cycle at each forcing condition was used to compare with the corresponding quantity determined from chemiluminescence. Despite the fact that the flame

surface area estimate obtained in this way may differ from the true flame surface area due to the presence of fine scale wrinkles along the flame circumference in turbulent flames, the flame surface area fluctuations reported in Lee & Santavicca (2003) were found to correlate well with CO_2* chemiluminescence, a conclusion also reached here and discussed in later chapters.

2.3.1.3 Reaction Rate Evaluation Based on OH and CH_2O PLIF

In order to obtain heat release rate from the OH and CH_2O PLIF images, a number of corrections were made on the raw fluorescence images. As mentioned earlier, the images were corrected first for the background noise. Secondly, images were corrected for the beam profile variations. Finally, both the OH and CH_2O images were overlapped on a pixel-by-pixel basis. In order to do this, a target image was aligned in the measurement plane defined by the laser sheets and in the field of view of both cameras. From the coordinates of the target images, polynomial warping coefficients were extracted and used to geometrically transform one of the images to overlap with the other (Ayoola *et al.*, 2005). The precision of the image matching was in the sub-pixel range. The corrected images were resized by 2x2 binning, which resulted in an effective spatial resolution of 100 μm and then multiplied on a pixel-by-pixel basis to obtain the local heat release image.

Figure 2.12(a)-(ii) shows a typical instantaneous CH_2O image and the reaction rate (RX) image (iii) along with the corresponding flame trace determined from the OH image (iv). These instantaneous images were averaged to obtain time averaged reaction rate image shown in Fig. 2.12(b) to indicate the width of the flame brush in this unforced flame. Figure 2.12(b) shows typical time-averaged distributions of OH, CH_2O and heat release rate along with their flame brush. From these images it can be seen that the flame contour obtained from OH PLIF essentially marks the flame, while the reaction rate imaging technique has also captured the local heat release variation along the flame.

2.4 Error Estimates

The uncertainties in the values of heat release fluctuations Q' over the mean value $\langle Q \rangle$ arise from many sources. First, there is broadening due to the FFT processing, which is estimated to cause an uncertainty of about 0.1% in the reported $Q'/\langle Q \rangle$. Secondly, there is statistical uncertainty due to the finite number of samples taken for all techniques. This is estimated to be around 0.4% for the PMT data, 10% for the FSD and 15% for the heat release imaging. Thirdly, reproducibility of the whole system (e.g. setting of flow rates, forcing, alignment of optics etc.) was checked by performing identical experiments on different dates and it was found that $Q'/\langle Q \rangle$ was different by not more than 1% for the PMT data and 10% for the FSD. Hence these can be used as final estimates of the accuracy of these techniques for the relative magnitude of heat release fluctuations.

The heat release imaging technique has not been used in a fully quantitative manner yet and it is difficult to estimate its precision. Uncertainties in the simultaneous OH and CH_2O PLIF may arise due to variation in the quenching cross sections through temperature dependence. It was reported in Giezendanner *et al.* (2003) that the calculated error in quantum yield in the temperature range where OH can be detected could be as high as $\pm 35\%$. These uncertainties do not affect the FSD calculation, which relies only in the large difference between OH in the unburnt and the burnt gases. No quenching data are available for CH_2O and hence such corrections are not possible. Hence, the RX measurements in this thesis are not quantitative, as also suggested by Fayoux *et al.* (2005). Despite this, measurements in laminar premixed flames (Ayoola *et al.*, 2005) show that the heat release as a function of equivalence ratio, divided by the corresponding measurement at $\phi = 1$, has a trend to within 20% of laminar flame computations. The reaction rate along turbulent premixed flames as a function of local flame curvature, normalized by the reaction rate at no curvature, also followed the expected trend from Direct Numerical Simulations (Ayoola *et al.*, 2005), with the reaction rate decreasing as the flame switched from negative to positive curvatures. This shows that the RX technique produces reasonable results concerning the local heat release rate, if the data are suitably normalized. In this work, we

use the RX data only for the ratio $Q'/\langle Q \rangle$, which should not be affected by these uncertainties.

2.5 Figures for Chapter 2

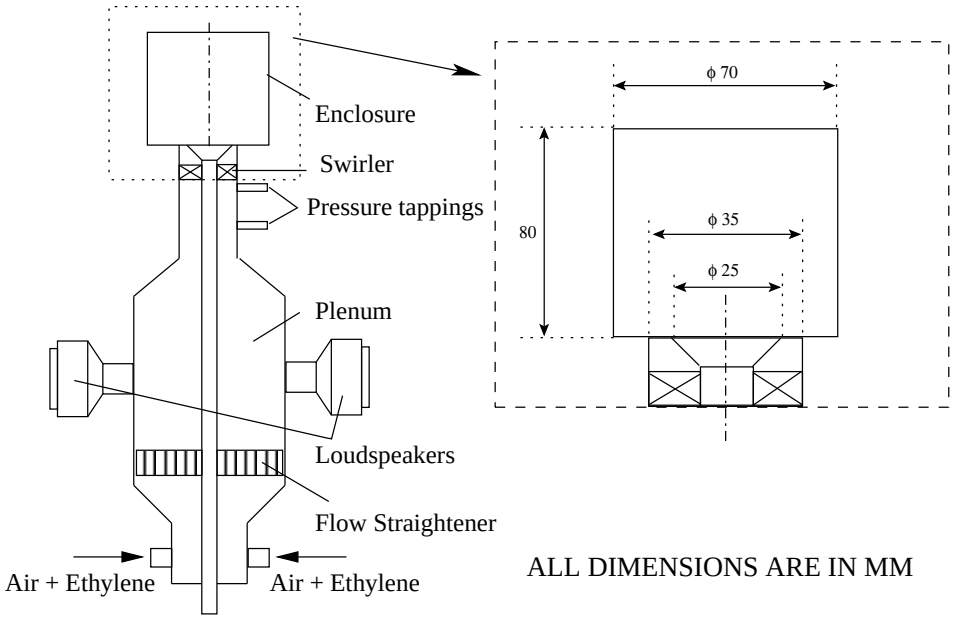

Figure 2.1: Schematic of the premix burner.

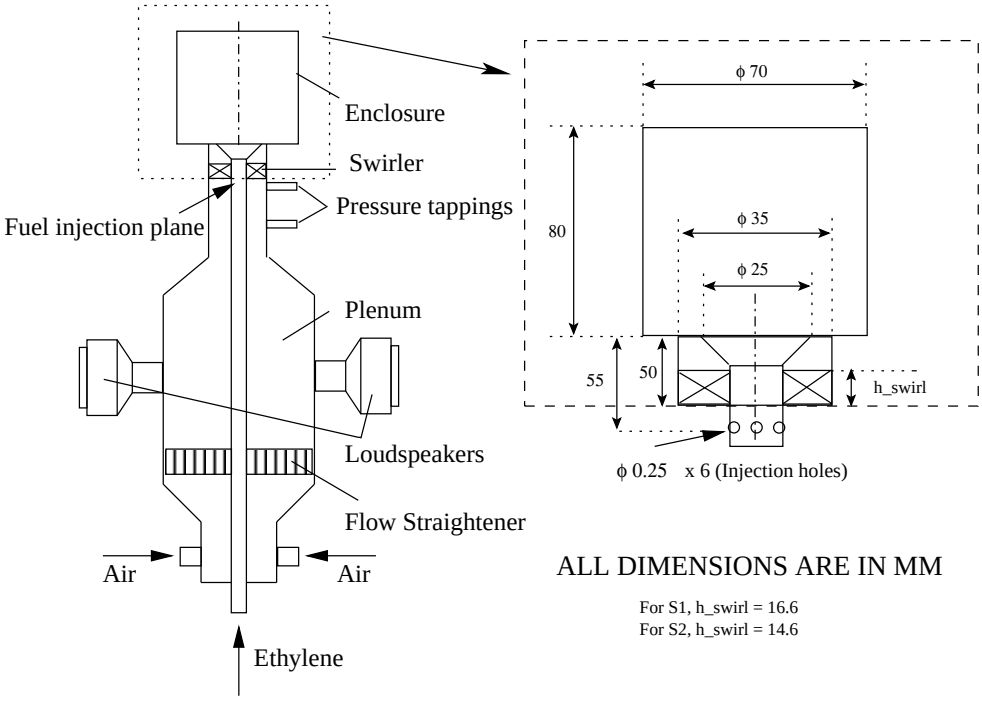

Figure 2.2: Schematic of the burner used for imperfectly premixed combustion.

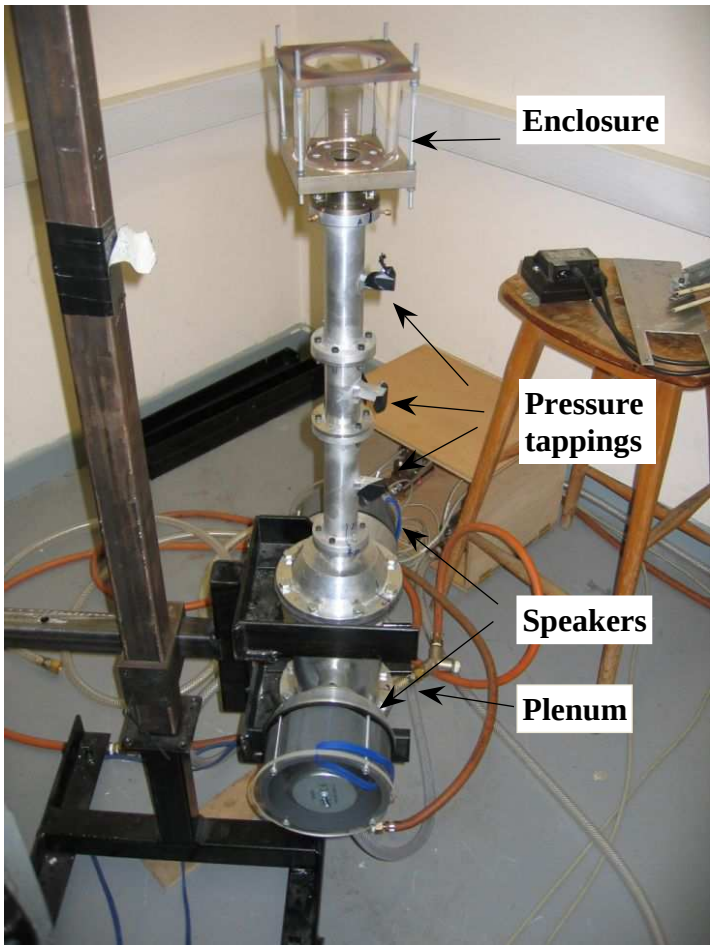

Figure 2.3: Photograph of the burner assembly.

Figure 2.4: Swirlers with (a) 45° vanes and (b) 60° vanes.

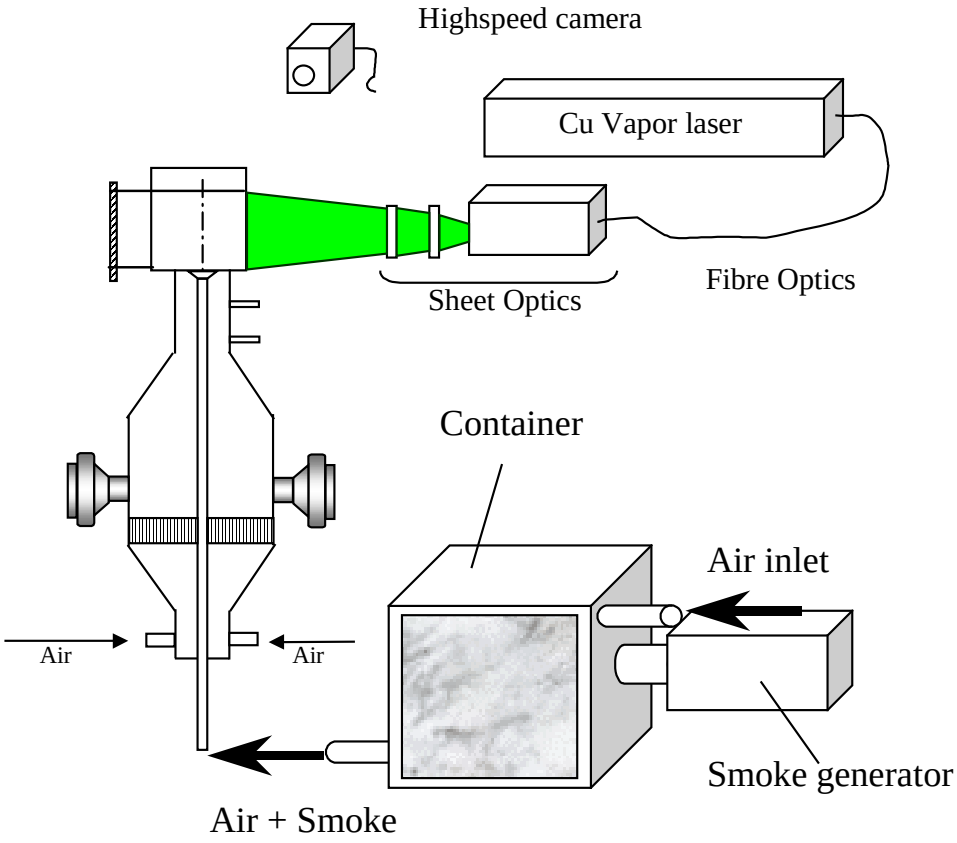

Figure 2.5: Schematic of the smoke visualization setup.

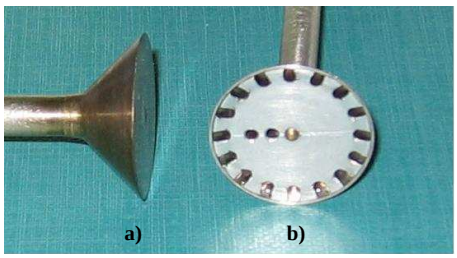

Figure 2.6: (a) The sideview of the bluff body used for all the test conditions and (b) the bluffbody used for smoke visualization.

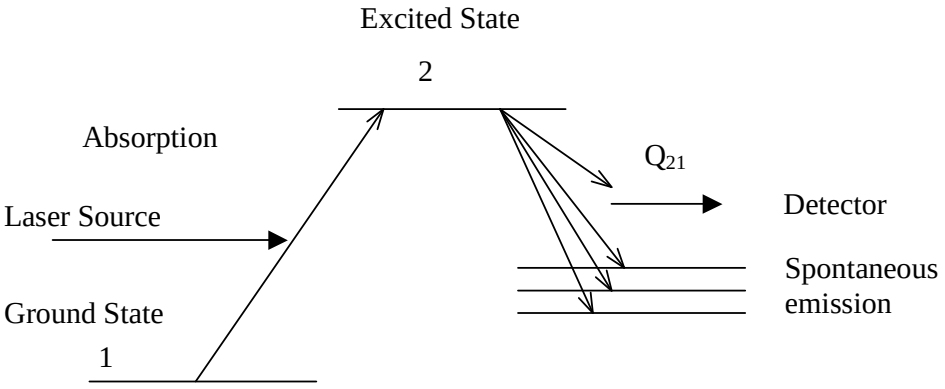

Figure 2.7: Simplified energy level transfer diagram for LIF.

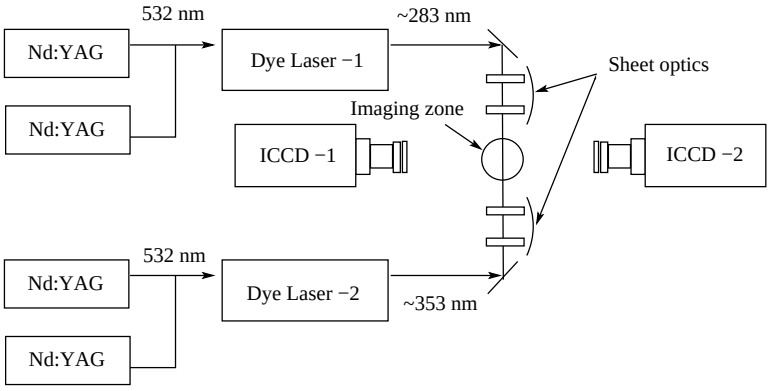

Figure 2.8: Schematic of the laser layout used for simultaneous OH, CH_2O and OH* imaging.

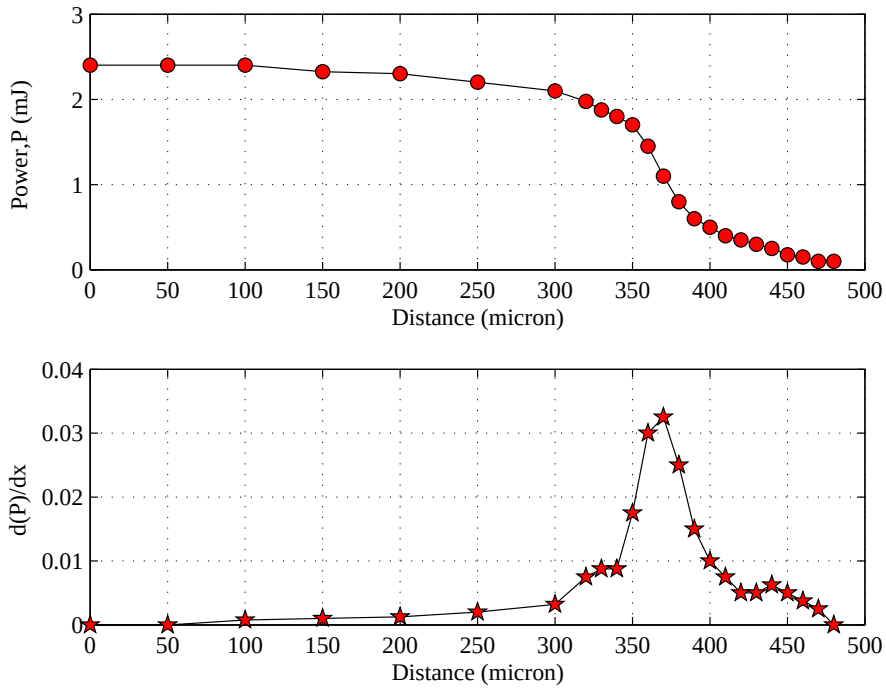

Figure 2.9: A typical mean laser power profile and its derivative during a knife-edge scanning experiment, performed at the center of the burner.

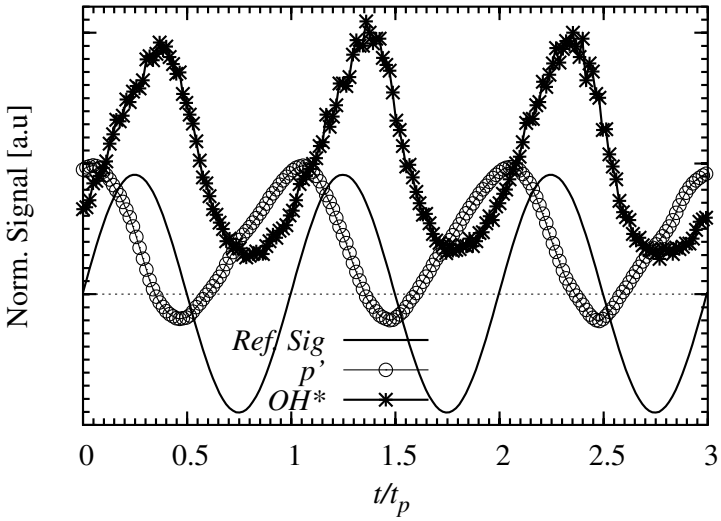

Figure 2.10: Time series of normalized reference signal, acoustic pressure and OH* chemiluminescence signal; Conditions are: $\langle U \rangle = 9.9$ m/s, $\phi = 0.55$, $f = 160$ Hz and $A = 0.45$.

Figure 2.11: Photograph of an unforced fully premixed flame. Conditions are: $\langle U \rangle = 9.9$ m/s, $\phi = 0.55$.

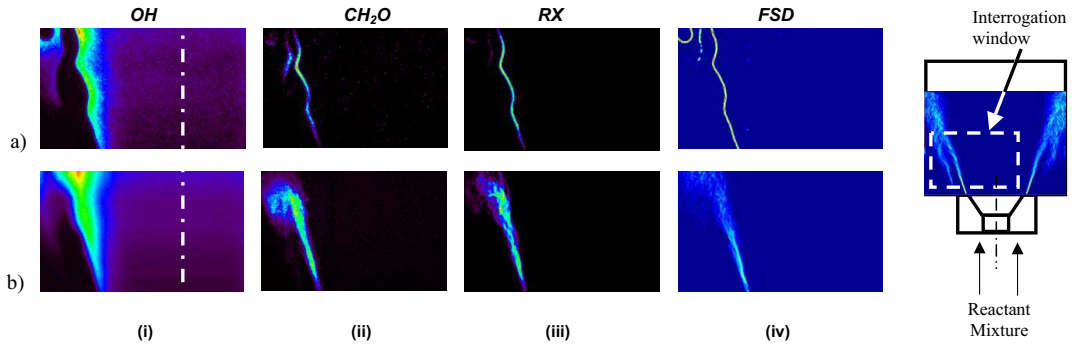

Figure 2.12: Simultaneous instantaneous (a) and time-averaged (b) images of OH, CH_2O and the heat release rate (RX) and flame contour. (The field of view is 40 mm x 36 mm, lower side of image is 10 mm above the bluff body.)

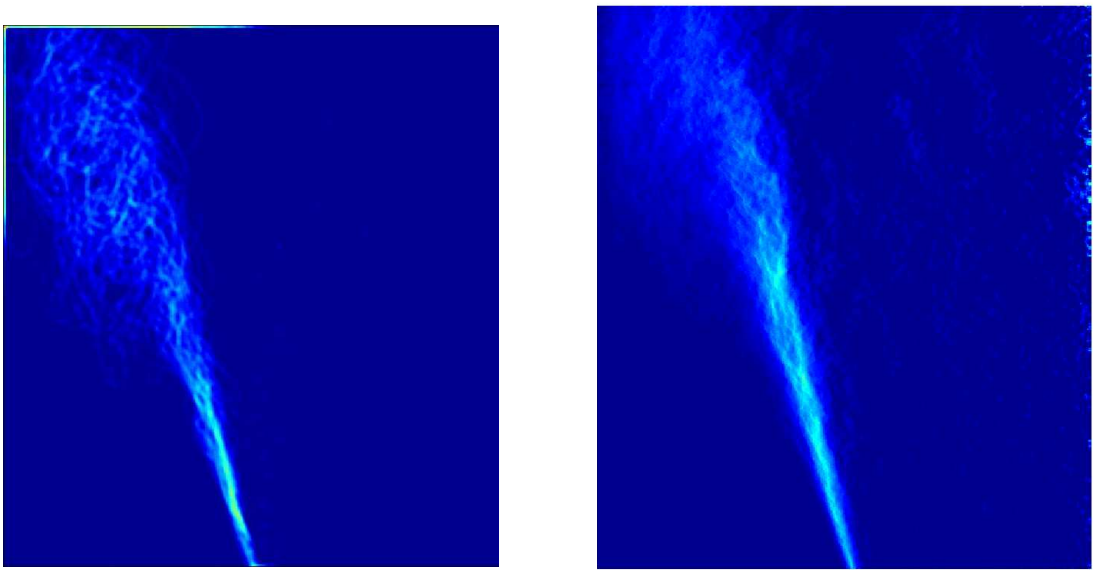

(a) (b)

Figure 2.13: Comparison of time-averaged (a) FSD and (b) Abel inversion of OH* chemiluminescence image, for the data presented in Fig. 2.12.

Chapter 3

Characterization of the Combustor

This section summarizes the acoustic and flow characteristics of the burner under cold isothermal conditions. The bulk behaviour of the completely premixed and imperfectly premixed flames is also discussed in detail.

3.1 Cold Flow

3.1.1 Acoustic Characteristics

Understanding of acoustic characteristics of the combustor under cold flow conditions is important, especially for forced flame studies, since the requirement is to obtain a high forcing amplitude, which are generally obtained by forcing at the resonant frequencies (Hardalupas & Selbach, 2002).

A constant mean flow of air at 280 lpm (i.e., bulk velocity of 9.9 m/s at the combustor inlet) was established in the burner. The airflow was perturbed by the loudspeakers mounted on the plenum circumference (see Chapter 2). The frequency of the input signal to the amplifier from the signal generator was swept from 10 to 400 Hz. The acoustic response of the combustor was determined using simultaneous velocity and acoustic pressure measurements. As explained in Chapter 2, the acoustic pressure measurements were used to calculate the velocity fluctuations using the two-microphone technique. The Dantec hot-wire

was placed at the center of the inlet flow passage (15 mm from the center of the bluff body) to measure the acoustic velocity fluctuations during this external excitation. The acoustic velocity obtained from this measurements was used to understand the acoustic boundary conditions of the combustor system, which could serve as input to the acoustic-network models (Dowling & Stow, 2003).

These experiments were performed for two configurations, i) with the short tube enclosure, which was used for flame-transfer function measurements through external excitation and ii) with long enclosure, which was employed to obtain self-excitation. In both the above cases, the flow conditions were kept the same. Figure 3.1 shows the A value that was obtained during experiments with short tube, by the external excitation using an input signal of constant peak to peak voltage value, as a function of forcing frequency, and Fig. 3.1 also shows the phase difference (normalized using π), with reference to the forcing signal. It can be clearly seen from the figure that there are three resonant peaks, they are at around 40 Hz, 160 Hz and 320 Hz. These results suggest that the combustor plenum chamber with the air supply line act like a resonator with peak responses around 40 Hz, 160 Hz and 320 Hz respectively, thus resulting in high A values around these frequencies. The first peak corresponded to the eigen mode of the combustor including the plenum and the air supply line, while the other frequencies were that of the geometric modes of the combustor including the plenum chamber. It can be seen from Fig. 3.1 that the two-microphone method slightly over estimates the magnitude of the velocity fluctuation but the trend of the variation is captured well. This discrepancy is due to the fact that in the two-microphone calculations an area-averaged velocity was used. Similarly, the phase of the velocity fluctuations relative to the input-forcing signal is very similar from both techniques. Despite the good agreement, the two-microphone estimate was corrected based on the hot wire measurement at the cold flow conditions to provide accurate velocity fluctuation amplitude for characterization of the hot flow condition.

With the increased length of the enclosure from 80 mm to 350 mm the self-excitation acoustic oscillation was achieved during the hot flow for the same combustion condition as that of forced case with short tube, as described in Chapter 2. Since, the resonant peaks obtained with short enclosure were mainly

longitudinal acoustic modes, the change in the enclosure length would affect the acoustic characteristics of the combustor by altering the acoustic boundary conditions and hence the resonant responses. Figure 3.2 shows the variation of the A values measured by the two microphone method as a function of frequency for acoustic excitation with constant input peak-to-peak voltage to speakers. Definite changes in the acoustic characteristics are clearly observed from this figure. It can be seen that the first two peaks (at around 40 Hz and 160 Hz) remained nearly unaffected. However, the third peak around 320 Hz was suppressed. A new peak at 380 Hz was observed and between the peaks at 160 Hz and 380 Hz, there existed a small peak at around 260 Hz. This kind of complex acoustic resonant characteristics is due to the interaction of the modes of the downstream (enclosure) and that of the upstream chamber.

3.1.2 Flow-field Visualization

The non-reacting smoke visualization experiments under unforced and forced conditions were performed to understand qualitatively the flow-field, which is important in understanding the flame stabilization and flame response mechanisms. The details the facility used for smoke visualization were described in detail in the previous chapter.

The schematic of the flow field of the configuration used for the present work is given in Fig. 3.3. The recirculation zone formed by the wake of the bluff body is referred to as central recirculation zone (CRZ) and that formed by the rearward-facing step (dump plane) is called side recirculation zone (SRZ). The shear layers produced by these recirculation zones are very important for flame stabilization. The primary recirculation produced by the bluff body was investigated in detail using smoke visualization. The recirculation was seeded with fine smoke particles as described in Chapter 2 and then a thin laser sheet was used to illuminate the central plane using a continuous copper vapor laser. The laser light scattered by the smoke particles was captured using a high-speed camera. The images were captured at the rate of 2500 frames per second; with an exposure of 200 μs. These images can be considered as quasi-instantaneous, since the flow time scales are much greater than the exposure time (of the order of ms, for the experimental

conditions). Typical instantaneous and time-averaged smoke visualization images are presented in Fig. 3.4 showing the CRZ of an unforced flow field. The images suggest that the width and height of the recirculation zone were about 1 and 1.5 bluff-body diameters respectively.

The influence of acoustic perturbations on the shear layer has been dealt in detail in many investigations. It has been shown in earlier investigations that when a shear layer is subjected to pulsation, it may roll up to form a coherent vortex ring (Cala *et al.*, 2002; Cho *et al.*, 1998; Zhou & Wyganski, 2001). In the present study, similar shear layer roll up was observed for certain forcing frequencies. As described earlier in this section, the amplitude of pulsation was high for frequencies around 40 Hz, 160 Hz and 320 Hz. Hence, the experiments were performed for these frequencies. Figure 3.5 shows the evolution of the vortex ring during pulsation of the flow for a forcing frequency of 160 Hz with $A = 0.64$. It can be seen from the figure that the recirculation width was increased slightly and then a small deformation formed at the base of the recirculation, which then evolved into an inward rolling vortex ring. Though the smoke was seeded only at the central recirculation zone, it can be seen from the images that while the inner shear layers of CRZ showed an inward rolling vortex, the outer shear layer at SRZ also rolled-up outwardly from the bluff body. Thus a pair of counter rotating vortex rings were formed. The formed vortex rings grew in size and moved downstream with the speed of bulk fluid velocity. Subsequently, this vortex ring moved far downstream from the combustor inlet, after which a new vortex pair formed at the base of the recirculation zones and this process repeated itself for every forcing cycle. It can be observed from Fig. 3.6 that the variation in mass flow and the counter rotating vorticity field generated by forcing brought the two shear layers very close to each other. These shear layers which stabilized the flame during the hot flow experiments, due to turbulent motion of the flame front resulted in annihilation of flame fronts. The evidence for occurrence of such events was observed during the hot flow experiments and the details will be presented in the next chapter using PLIF measurements.

Figure 3.6 shows the sequences of vortex ring formation when the flow was forced at 320 Hz with $A = 0.61$. It can be observed from these images that the dynamics of the vortex ring was similar to that of the 160 Hz forcing case.

However, it should be noted that before one vortex ring moved away completely from the shear layers, a new vortex formed, increasing the possibility of complex interaction between the vorticity field generated by the two vortex rings.

Figure 3.7 shows the forced dynamics of the pulsed flow at 40 Hz. It is clearly evident from the figure, that the central recirculation zone (CRZ) was affected greatly during excitation. The CRZ became much wider and the height of the recirculation was reduced to a very small height at some point during the cyclic variation, while the CRZ was found to be longer and with a small width at some part on the cycle. However, it has to be noted from these experiments that there was no shear layer roll up even at the highest forcing amplitudes during the forcing at 40 Hz. The images in Fig. 3.7 also suggest that the instances during which the two shear layers were brought very close during the cyclic flow variation were shorter for forcing at 40 Hz than that at 160 Hz and 320 Hz.

The introduction of swirl was found to affect the structure of both recirculation zones CRZ and SRZs greatly. The size of CRZ increased while the size of SRZs decreased. Figure 3.8 shows the instantaneous image of recirculation for swirl cases, S1 and S2 (with swirl vane angles of 45°, 60° respectively). It was observed that the flow impinged on the sidewall at around a distance of 1.5 and 1 bluff-body diameter for cases S1 and S2 respectively.

Figure 3.9 shows the dynamics of pulsed swirl flow of moderate swirl intensity i.e. case S1, when forced at 160 Hz. The figure suggests that the pulsation has changed the structure of recirculation zones, however the vortex evolution and the dynamics are very similar to that of no swirl case. However, the pulsation in high intensity swirl flows did not change the recirculation structure, the flow impingement angle remained the same at that of no forcing case, shown in Figure 3.10. In both the swirl cases, it was observed that the smoke injected in the CRZ mixed thoroughly with the flow and reached the SRZs.

These results suggest that the flow field was affected greatly by the acoustic forcing. The effects of forcing on the recirculations zones were frequency and amplitude dependent as previously suggested by Külsheimer & Büchner (2002). During the excitation with low frequency, even at highest amplitudes there was no shear layer roll up, however the recirculation size was modulated to a greater extent during this case. With the increase in forcing amplitude during high

frequency forcing the shear layer rolled up to form vortex rings. The introduction of swirl in the flow affected the recirculation shape and the flow impingement angles.

3.2 Reacting Unforced Flow

Although the main objective of this research work is to investigate the forced response of the flames, understanding the static stability of the combustor is very important. The static stability of the combustors operated with completely premixed reactants, pertains to the physical flame attachment and its response to small flow fluctuations, while for the combustors with spatial and temporal variation in equivalence ratios the mixing of the fuel and air stream dictates the static stability. The main objective of this section is to investigate the characteristics of fully premixed turbulent flames and that of partially premixed or imperfectly premixed turbulent flames (here referred to the flames with spatial variation in premixedness) approaching the lean blowout limits.

3.2.1 Bulk Behaviour of Premixed Flames

In premixed combustion systems, the fuel and air are premixed upstream of the flame stabilization point and the recirculation zone generated by the aerodynamic design (bluff body, baffle or dump plane etc) where the hot products are trapped, serve as an ignition source for the incoming combustible mixture. In these fully premixed combustors, the flame surface will appear at the point where the local mixture velocity matches the local flame speed. If the flow velocity at the stabilization point is high, the flame may blow off. On the other hand, if the mixture velocity is smaller than the local turbulent flame speed, the flame can travel upstream of the combustor (flash back). Flash back is not desirable in premixed systems, because it may lead to flame stabilization at the locations inside the system. Meanwhile, flame blow off is not desirable especially during high altitude flight conditions, since the relight of the mixture is more difficult to achieve.

In this section, the investigation of flame stabilization and blow out characteristics of the premixed flame is described. During these experiments, the air mass

flow rate was kept at a fixed value, the value at which most of the flame response studies were performed. The flow rate of fuel was adjusted to vary the equivalence ratios. The equivalence ratio was decreased from a higher value in steps, till flame blow-out was achieved. The flame stabilization characteristic at each equivalence ratio was investigated using OH* chemiluminescence and PLIF based measurements. Three different measurement approaches, described in Chapter 2, were employed to investigate the structure of the flames approaching lean blow-off limit, namely the conventional UV-chemiluminescence from the flame, the flame surface density FSD computed from the OH PLIF instantaneous images, and the local reaction rate computed from simultaneous OH and formaldehyde PLIF measurements.

Figure 3.11 shows a typical instantaneous OH PLIF image of a lean premixed flame stabilised on the bluff body without swirl (Case S0). It can be seen from the figure that the flame is primarily anchored at the shear layer formed by the central recirculation (CRZ) generated by the bluff body. The recirculation formed by the dump plane brought the hot products and mixed with the reactants, the secondary recirculation also had flame elements occasionally stabilised on the shear layer formed by the dump plane.

The FSD was computed from instantaneous OH PLIF images (see Chapter 2). During these experiments, 100 realizations were recorded for each condition; the FSD computations performed on each image when averaged resulted in the time-averaged flame surface density images. Since the OH concentration decreases with decreasing equivalence ratio, the threshold values for computation was adjusted for each conditions based on a trial and error basis. In addition, with decreased OH number densities the intensity of light captured reaches very low values, resulting in the decreased signal to noise ratios, which makes the thresholding procedure more difficult (Lee & Santavicca, 2003). The local heat release images obtained from simultaneous OH and CH_2O PLIF and the OH* chemiluminescence where used to verify the FSD computation. Figure 3.12 shows such FSD images captured as function of equivalence ratio. The color scale used for presenting these images is the same for all the cases presented in the figure. It can be seen from these images that although the flame stabilization location seems to be the same, the value of FSD seems to be decreasing with decreasing equivalence ratio.

The heat release rate evaluated from OH and formaldehyde PLIF measurements performed for the case of Fig. 3.12 presented in Fig. 3.13. Fig. 3.13 shows that the flame was mainly stabilized at the inner shear layer, with flame elements occasionally trying to stabilise along the outer recirculation zone. Both Figs. 3.12 and 3.13 show that the latter events increased with decreasing equivalence ratio at first, but then the stabilization was achieved only by the central recirculation zone. From Figs. 3.12 and 3.13 it can also be seen that the variation in the flame structure and the decreasing trend in heat release rate captured by the FSD computations and RX measurements agree very well. The OH* chemiluminescence measurements performed along with the PLIF are presented in Fig. 3.14, which also showed a similar variation in the flame structure with decreasing equivalence ratio. Fig. 3.14 also shows the decreased heat release with decreasing equivalence ratio.

Figure 3.15 shows the variation of heat release measured by OH* chemiluminescence, RX imaging technique and the FSD computations, normalized by the value of heat release at ϕ =0.65. The product of the FSD and the laminar flame speed S_L (referred as $FSD.S_L$ in the figure) was also presented in the graph. It is clearly evident from the figure that both OH* chemiluminescence and the heat release rate from RX imaging measurement technique show a similar variation. The FSD values first decreased with different rate up to a point and after which decreased rapidly, however the product of the laminar flame speed and the FSD agreed very well with OH* and RX measurements. These results improve the confidence in FSD computations in predicting the mean heat release rate.

The variation in flame structure by decreasing equivalence ratios in the presence of swirl was further investigated and reported here. Figure 3.16 shows the time-averaged flame surface density images of flames with moderately swirled flows, obtained for various equivalence ratios. It can be clearly observed that the flame was primarily anchored at the central recirculation zone, with some flame elements weakly stabilised on the side recirculation zones, SRZs. With a decrease in equivalence ratio, the heat release was distributed more evenly than at the higher equivalence ratio case. With further decrease, the flame elements in the SRZs disappeared and the flame anchoring was only at the CRZ. The heat release obtained from FSD evaluations and OH* chemiluminescence are presented

in Fig. 3.17 for the case presented in Fig. 3.16. The initial increase in flame surface density values are due to the fact the flame becomes more distributed (with more flame elements in SRZ) with decrease in equivalence ratio initially. It can be further explained from two instantaneous images taken at two equivalence ratio conditions. Typical instantaneous OH PLIF and OH* chemiluminescence taken at two equivalence ratios ϕ =0.61 and 0.45 are presented Fig. 3.18. It is clearly evident from this figure that for a slighty higher equivalence ratio (ϕ=0.61) the flame surface is positioned primarily on the CRZ, with few flame elements on the SRZ. However, with a decrease in equivalence ratio, events of pockets of isolated flame zones trapped in the SRZ appeared which gives a distributed appearance to the flame zone. The presence of these isolated flame pockets has increased the flame area and thus the FSD values, shown in Fig. 3.17. It should also be noted from these figures that the amount of heat released decreased up to $1/5^{\text{th}}$ of the value at ϕ=0.61. However, the product of FSD and S_L doesn't seem to agree, for this case (Case S1 presented in Fig. 3.17), suggesting an ambiguity in the FSD estimation during these experiments with swirl.

The time-averaged flame surface density images for a highly swirled premixed flame is presented in Fig. 3.19. It can be seen from these images, that the flame is more compact and the flame brush thickness has increased with comparison to no swirl and moderately swirled cases. As in the case of moderate swirl, the flame structure changed to become more distributed first and then the flame was stabilised only on the inner shear layer. Figure 3.20 shows the variation of heat release as a function of equivalence ratio (normalized using the max. value, ie the value at the highest equivalence ratio). These results also suggest that the results from FSD estimations should be interpreted carefully.

3.2.2 Bulk Behaviour of Imperfectly Premixed Flames

The stability of the flames with spatial variation in premixedness was predominately dominated by the mixing between the streams. Figure 3.21 shows the flame surface densities of imperfectly premixed flames with moderate swirl for various equivalence ratio conditions. It can be seen from these images that the flame anchored on both the shear layers. With decrease in equivalence ratio the

flame brush thickness increased as in the case of completely premixed flames. The flame stabilised on the SRZs became weaker and weaker with decreasing equivalence ratio and before extinction, the flame was anchored only on the CRZ. Figure 3.22 shows the variation in flame structure for a highly swirled imperfectly premixed flames. The increased swirl increased the mixing between the hot products and cold reactants and resulted in high distributed heat release, thus resulting in increased flame brush thickness. With a decrease in equivalence ratio, before extinction, as in other previous cases, the flame anchoring was only at the CRZ.

3.3 Summary

In this chapter, the details of acoustic characteristic of the combustor was described. The results suggest that there are peak frequencies around 40 Hz, 160 Hz and 320 Hz that could be exploited to achieve high forcing amplitudes. The cold flow smoke visualization revealed the variation in flow field in the presence of strong acoustic forcing. The images taken during these experiments suggested that during low frequency forcing, the recirculation zones were affected greatly, while the shear layer seemed to be oscillating without any roll up process. In contrast the high frequency forcing resulted in shear layer roll up, which was depended on the strength of the forcing.

The experiments investigating the flames in the absences of acoustics helped to identify the lean limits for a particular mass flow, which was used commonly during this study. Three different measurement approaches to measure mean heat release was found to agree very well in predicting the heat release variation as function of equivalence ratio in non-swirling flames. The flame structure alterations when the flame approaches extinction was identified, which was found to agree with earlier investigations.

3.4 Figures for Chapter 3

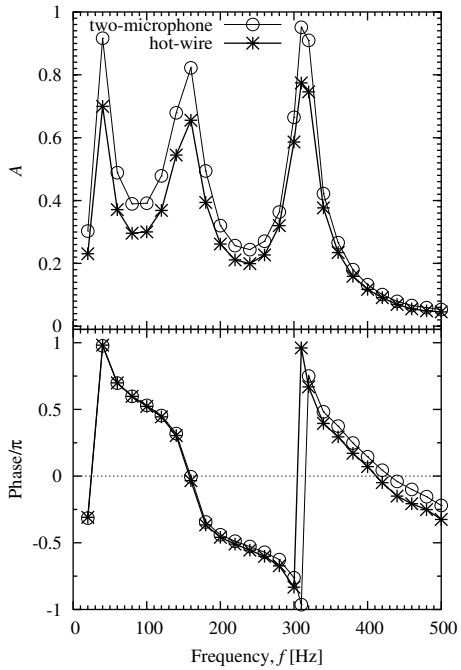

Figure 3.1: Comparison of amplitude and the phase of the velocity fluctuation measured by the two-microphone method and a hot-wire located at a radial location 15 mm from the bluff body under cold flow conditions, as a function of forcing frequency for a constant peak-to-peak input voltage to the speakers. Length of the enclosure, $L_e = 80$ mm, $\langle U \rangle = 9.9$ m/s.

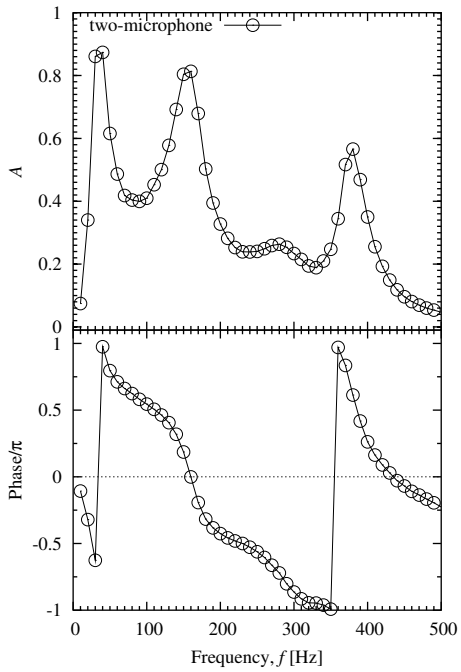

Figure 3.2: Amplitude and the phase of the velocity fluctuation measured by the two-microphone method under cold flow conditions, as a function of forcing frequency for a constant peak-to-peak input voltage to the speakers. Length of the enclosure, $L_e = 350$ mm, $\langle U \rangle = 9.9$ m/s.

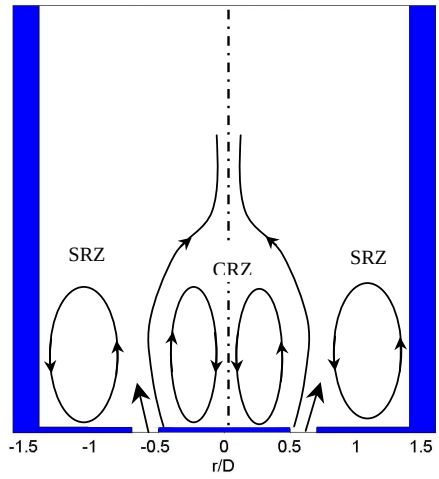

Figure 3.3: Schematic of the flow field in a bluff-body combustor.

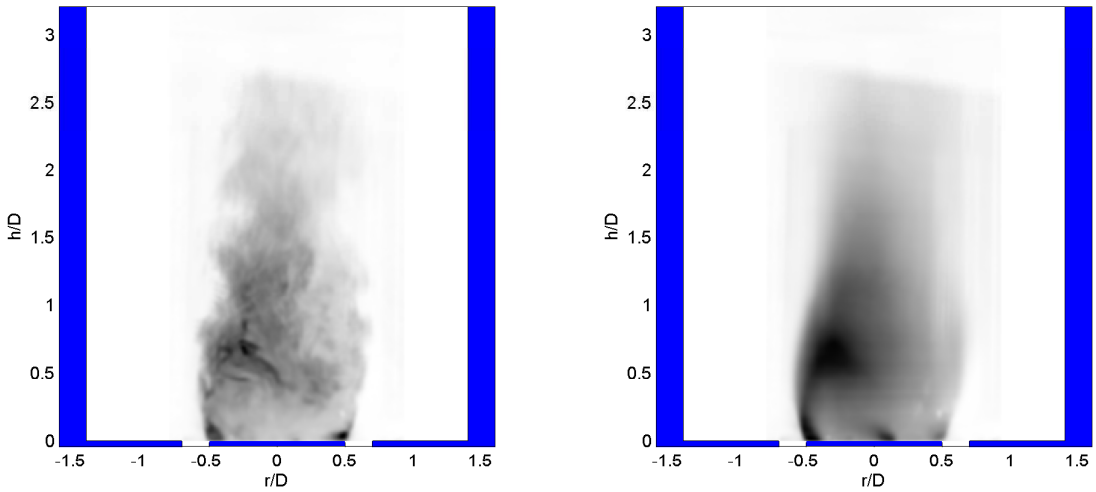

(a) (b)

Figure 3.4: Typical instantaneous (a) and time-averaged (b) smoke visualization images, with smoke seeded through the central bluff body. Images taken at rate of 2500 frames per second, with exposure of 200 μs.

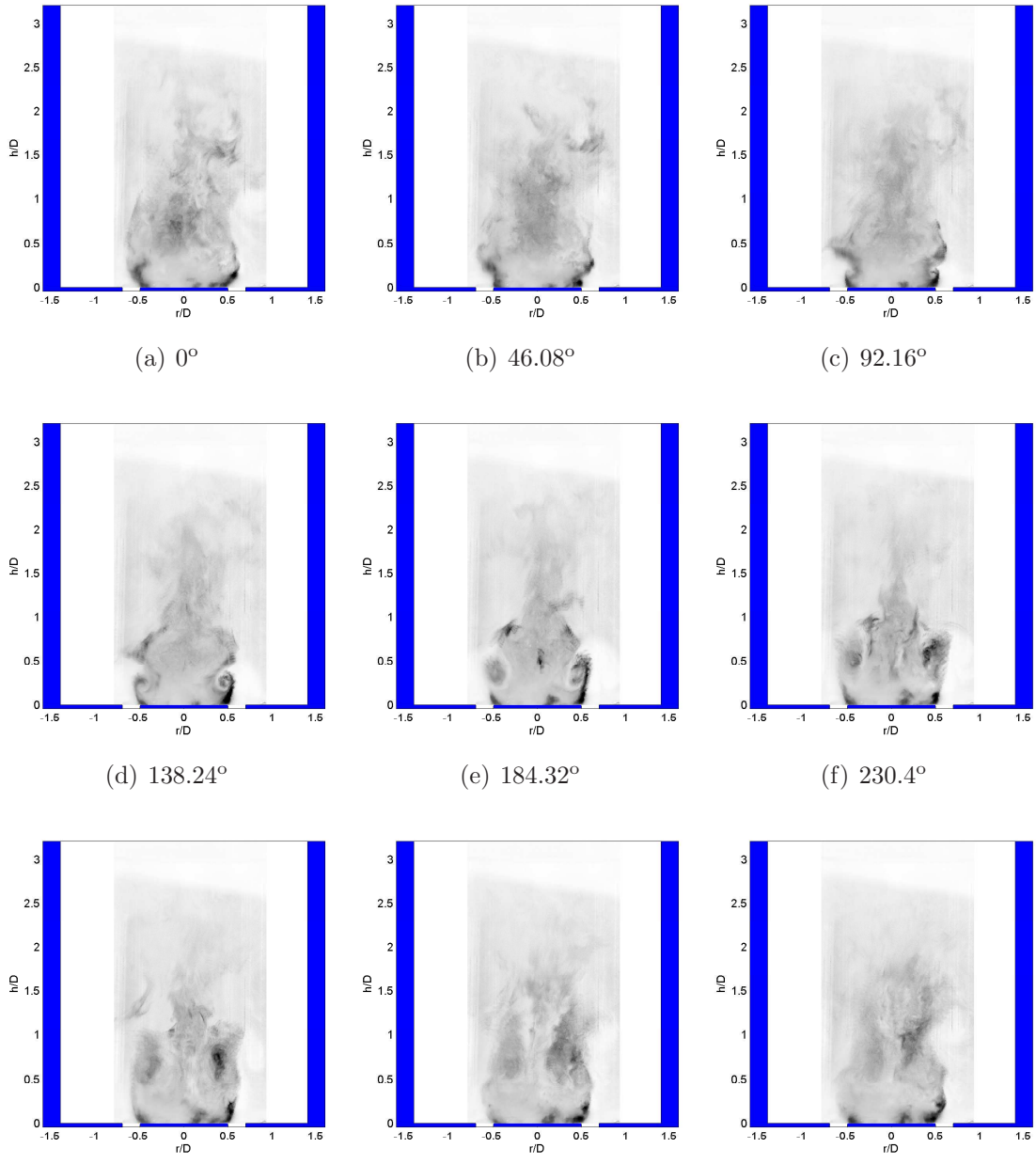

(a) 0° (b) 46.08° (c) 92.16°

(d) 138.24° (e) 184.32° (f) 230.4°

(g) 276.48° (h) 322.56° (i) 368.64°

Figure 3.5: Sequence of instantaneous smoke visualization images showing the vortex evolution and dynamics of a pulsed isothermal flow. Case S0, $\langle U \rangle = 9.9$ m/s, $f = 160$ Hz, $A = 0.65$.

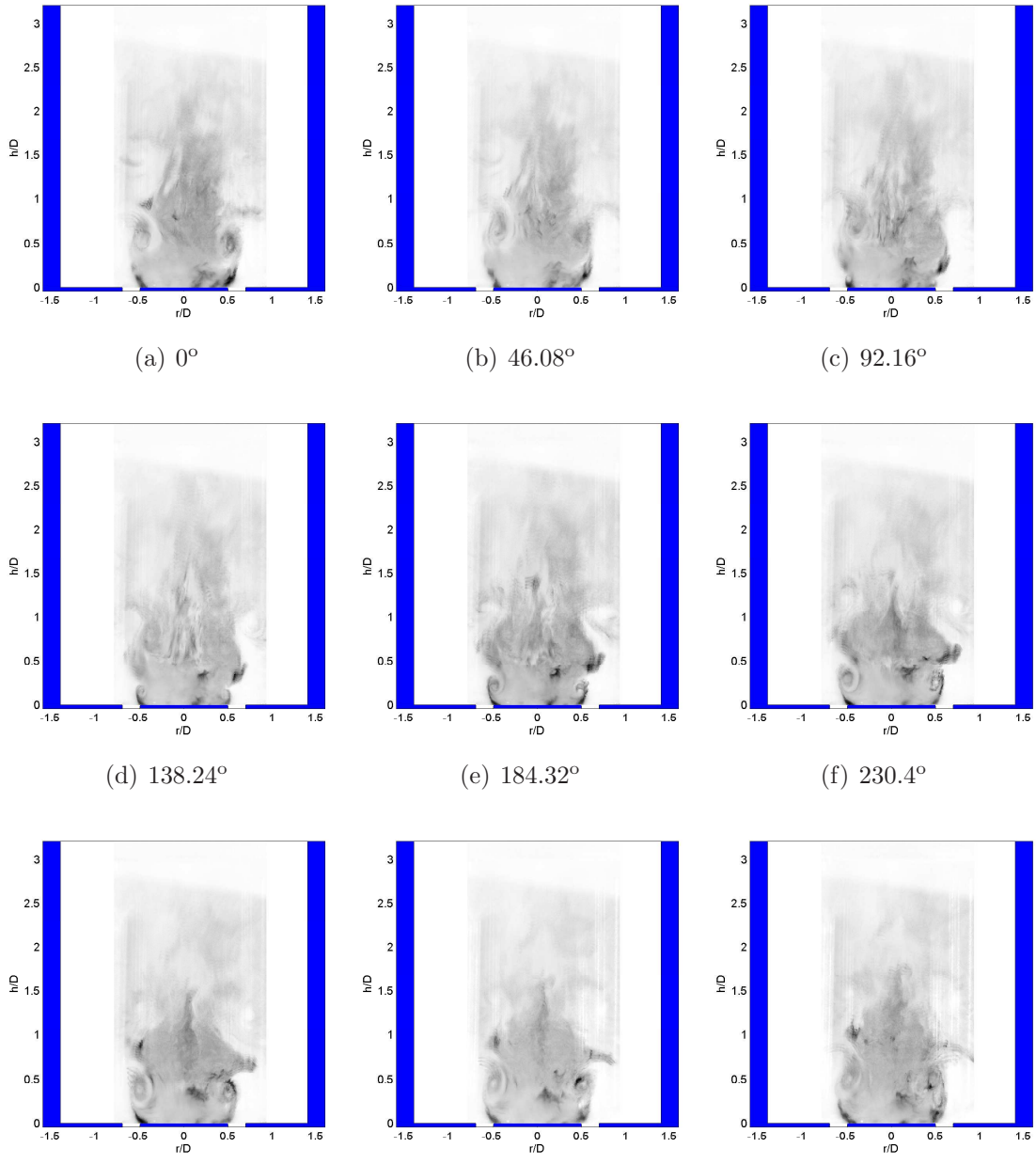

(a) 0° (b) 46.08° (c) 92.16°

(d) 138.24° (e) 184.32° (f) 230.4°

(g) 276.48° (h) 322.56° (i) 368.64°

Figure 3.6: Sequence of instantaneous smoke visualization images showing the vortex evolution and dynamics in a pulsed isothermal flow. Case S0, $\langle U \rangle = 9.9$ m/s, $f = 320$ Hz, $A = 0.62$.

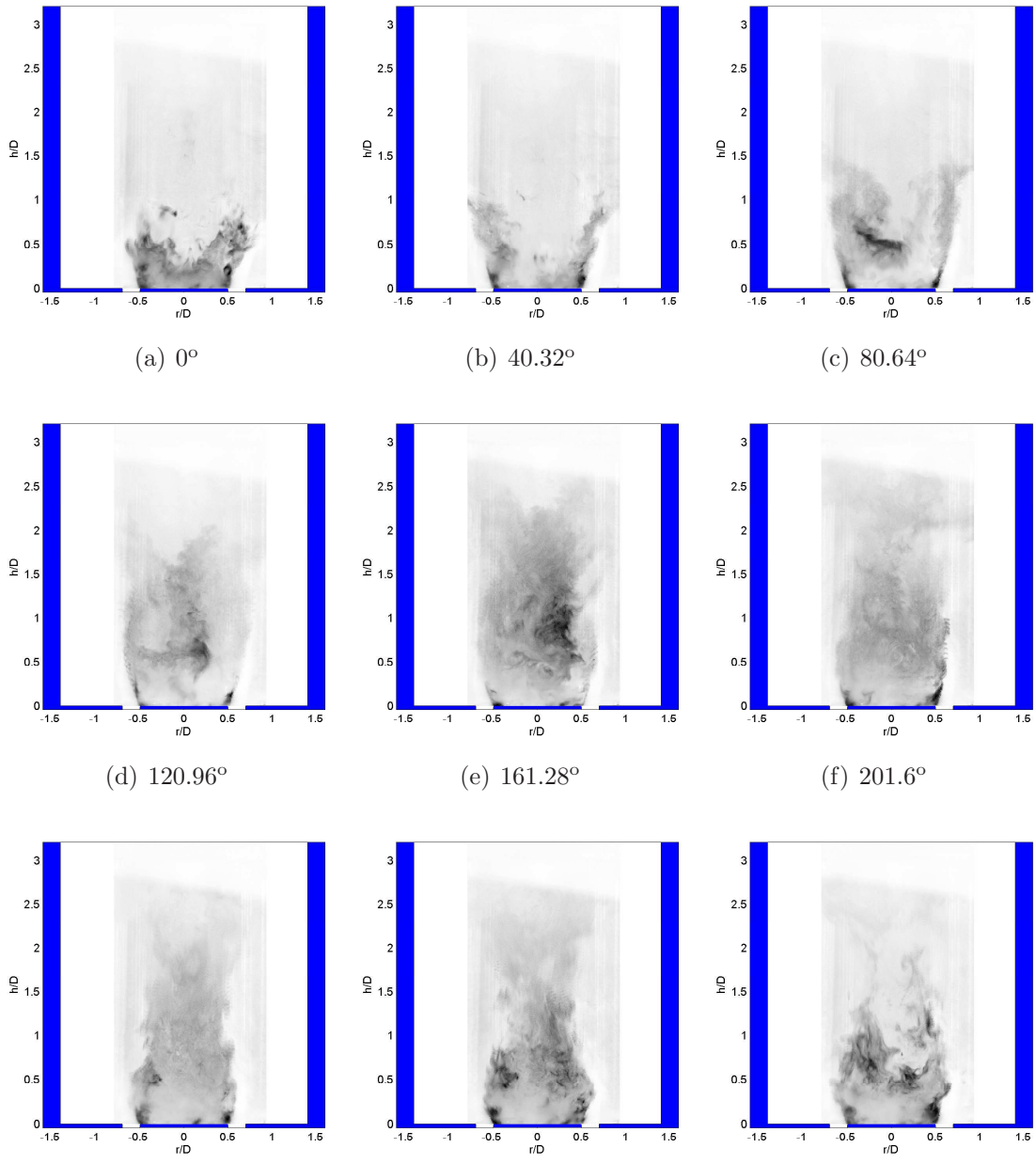

(a) 0° (b) 40.32° (c) 80.64°

(d) 120.96° (e) 161.28° (f) 201.6°

(g) 241.92° (h) 282.24° (i) 322.56°

Figure 3.7: Sequence of instantaneous smoke visualization images showing the variation in recirculation in a pulsed isothermal flow. Case S0, $\langle U \rangle$ = 9.9 m/s, f = 40 Hz, A = 0.60.

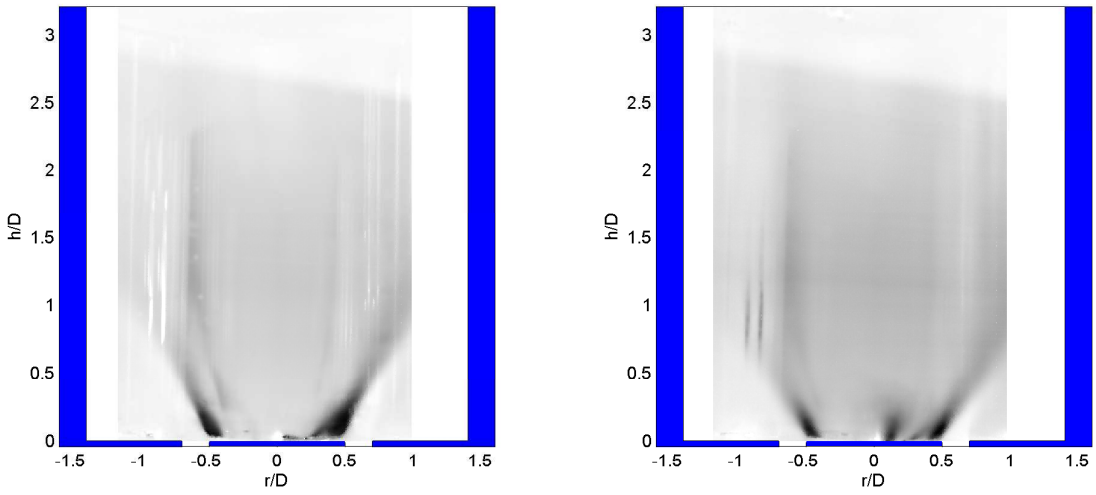

(a) (b)

Figure 3.8: Time averaged smoke visualization images of (a) moderately swirling flow, case S1 and (b) that of highly swirled flow, case S2. Images taken at the rate of 2500 frames per second, with exposure of 200 μs.

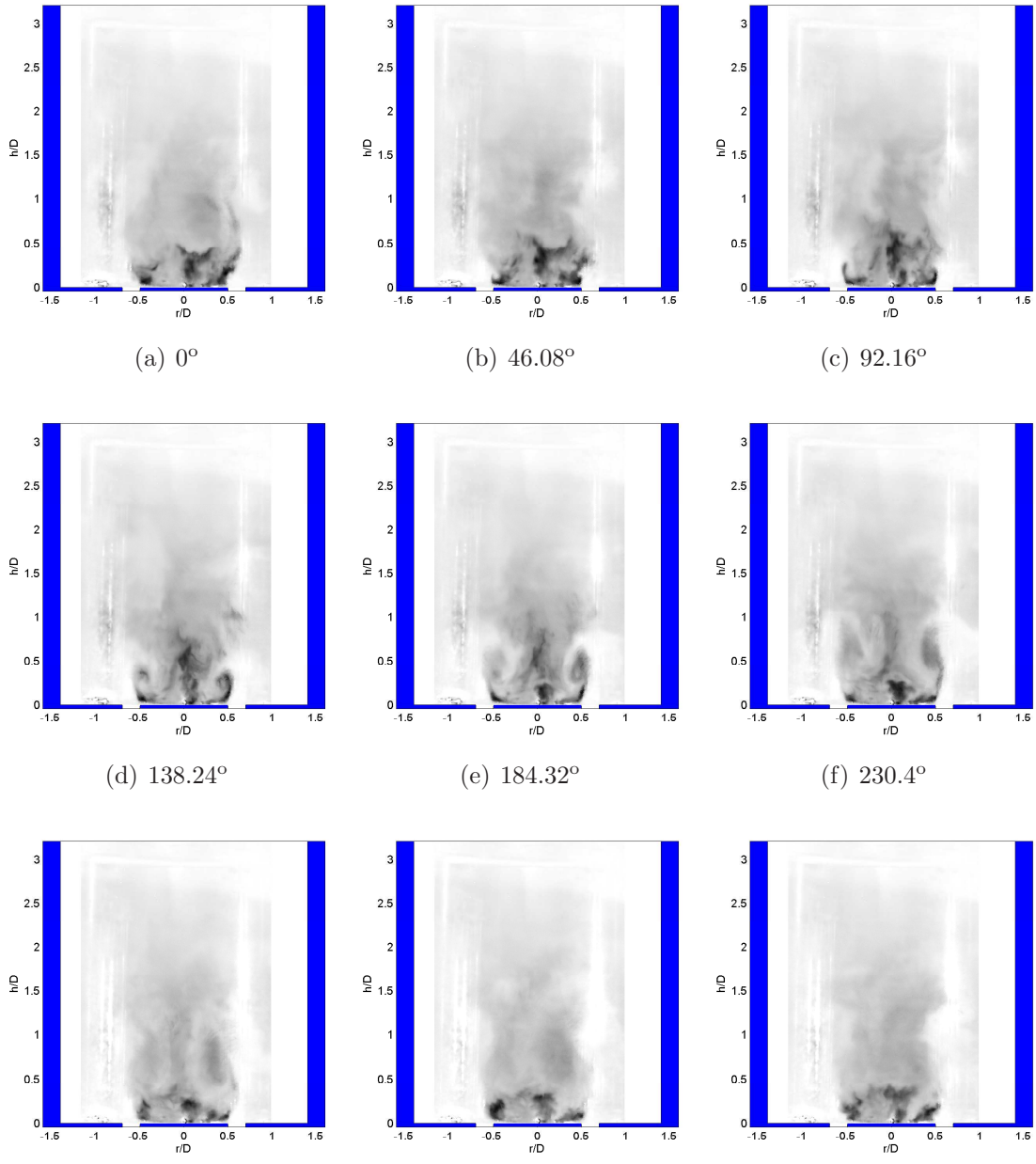

(a) 0° (b) 46.08° (c) 92.16°

(d) 138.24° (e) 184.32° (f) 230.4°

(g) 276.48° (h) 322.56° (i) 368.64°

Figure 3.9: Sequence of instantaneous smoke visualization images showing the vortex evolution and dynamics in a pulsed isothermal flow. Case S1, $\langle U \rangle = 9.9$ m/s, $f = 160$ Hz, $A = 0.64$.

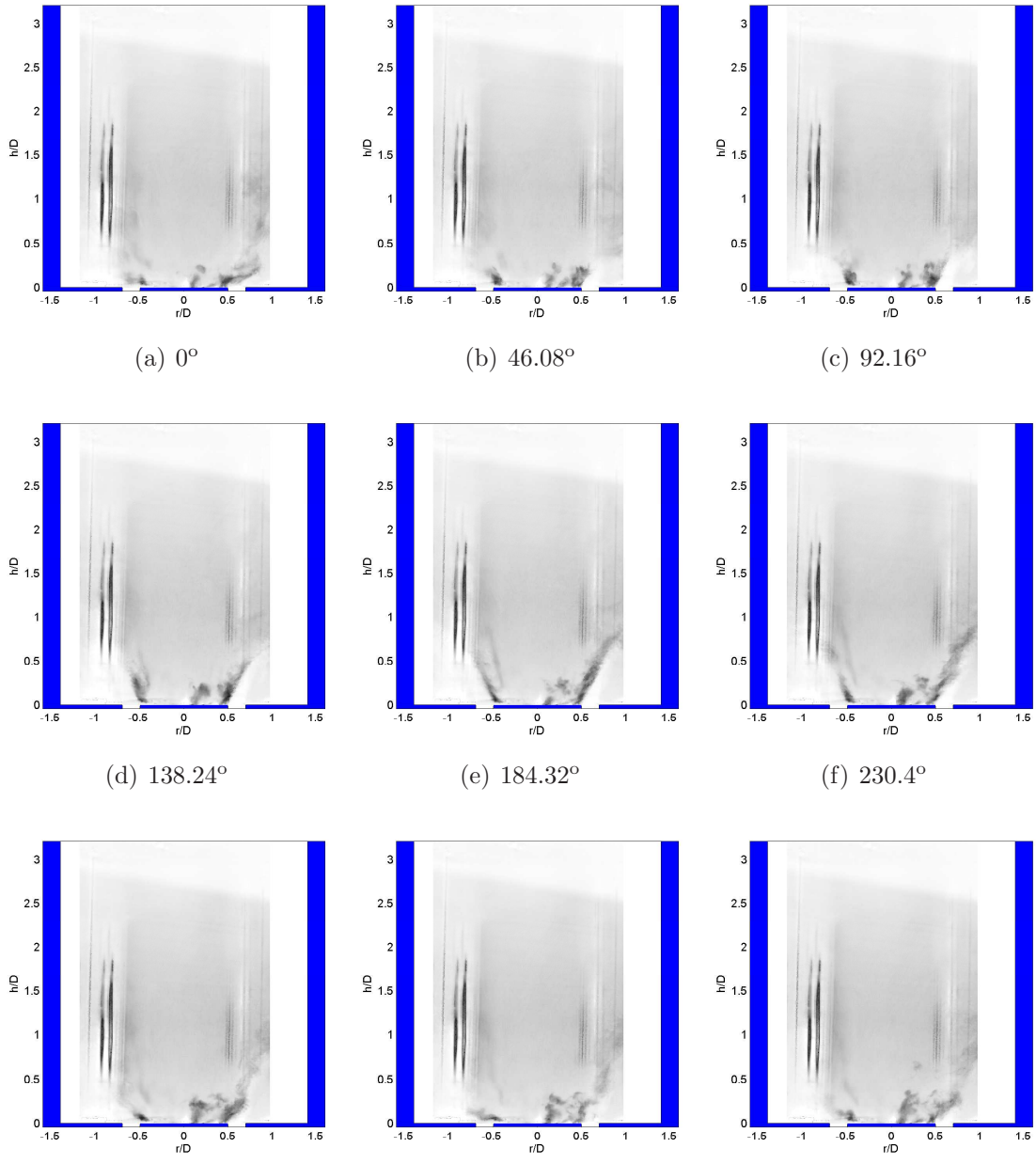

(a) 0° (b) 46.08° (c) 92.16°

(d) 138.24° (e) 184.32° (f) 230.4°

(g) 276.48° (h) 322.56° (i) 368.64°

Figure 3.10: Sequence of instantaneous smoke visualization images showing the vortex evolution and dynamics in a pulsed isothermal flow. Case S2, $\langle U \rangle = 9.9$ m/s, $f = 160$ Hz, $A = 0.62$.

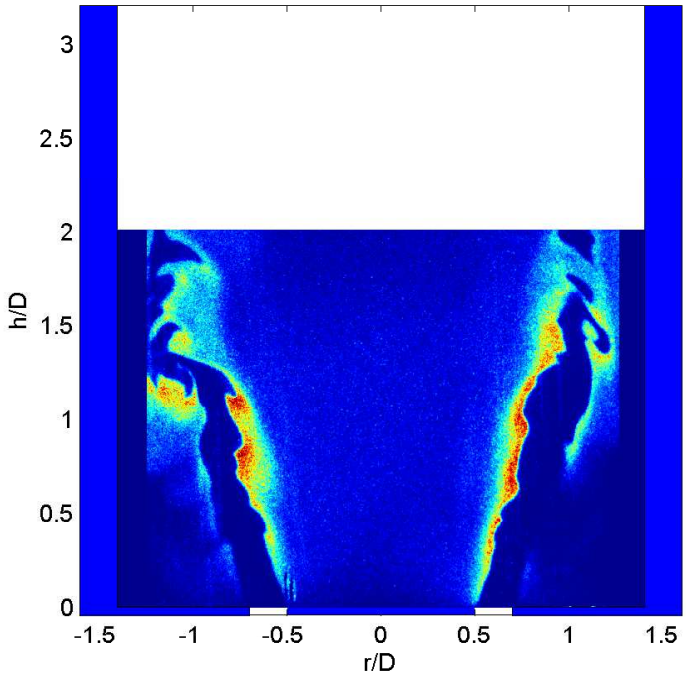

Figure 3.11: Typical instantaneous OH PLIF image of a bluff-body stabilised lean flame with no swirl. Case S0, ϕ =0.55.

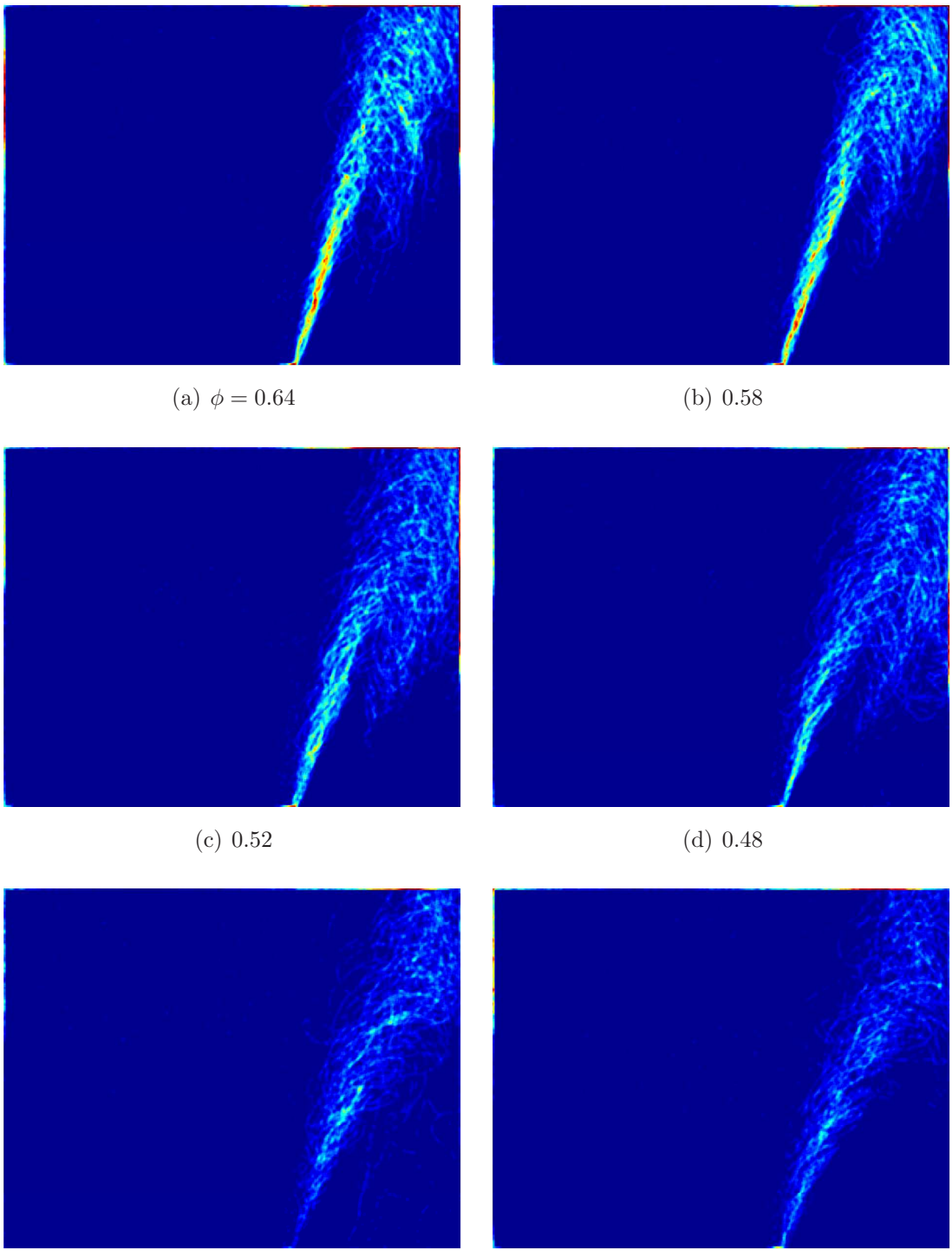

(a) $\phi = 0.64$ (b) 0.58

(c) 0.52 (d) 0.48

(e) 0.45 (f) 0.44

Figure 3.12: Time-averaged FSD images obtained from OH PLIF images showing flame structure variation with decreasing equivalence ratio (ϕ). Case S0, $\langle U \rangle$ = 9.9 m/s. Color scale for these images are the same.

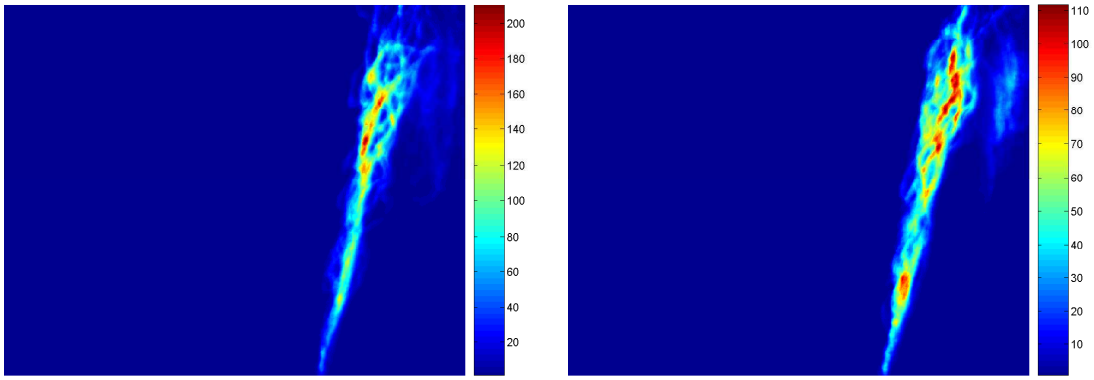

(a) $\phi = 0.64$ (b) 0.58

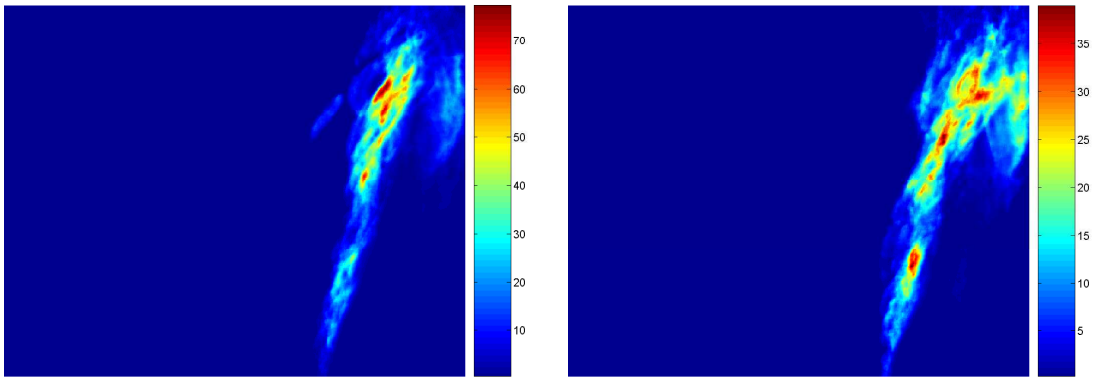

(c) 0.52 (d) 0.48

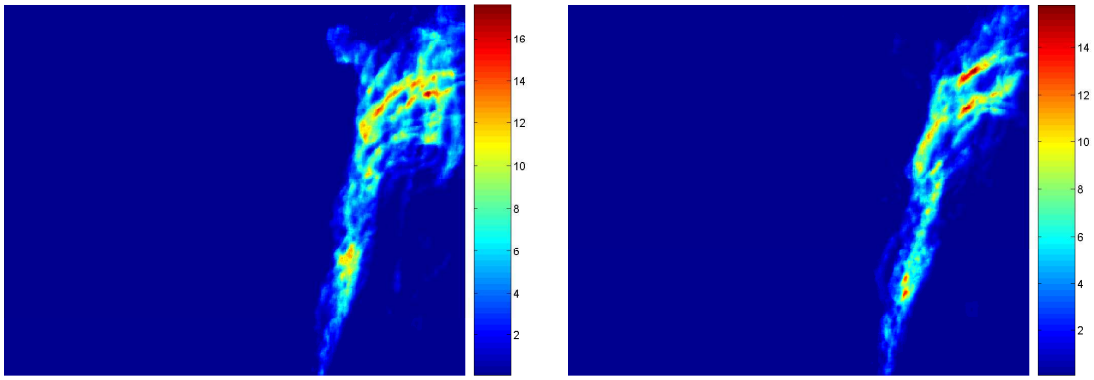

(e) 0.45 (f) 0.44

Figure 3.13: Time-averaged RX images obtained from simultaneous OH and formaldehyde PLIF images. Case S0, $\langle U \rangle = 9.9$ m/s.

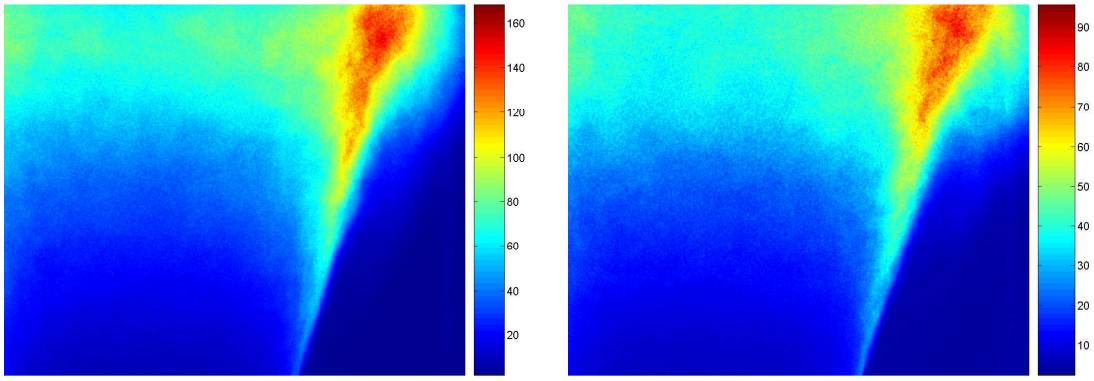

(a) $\phi = 0.64$ (b) 0.58

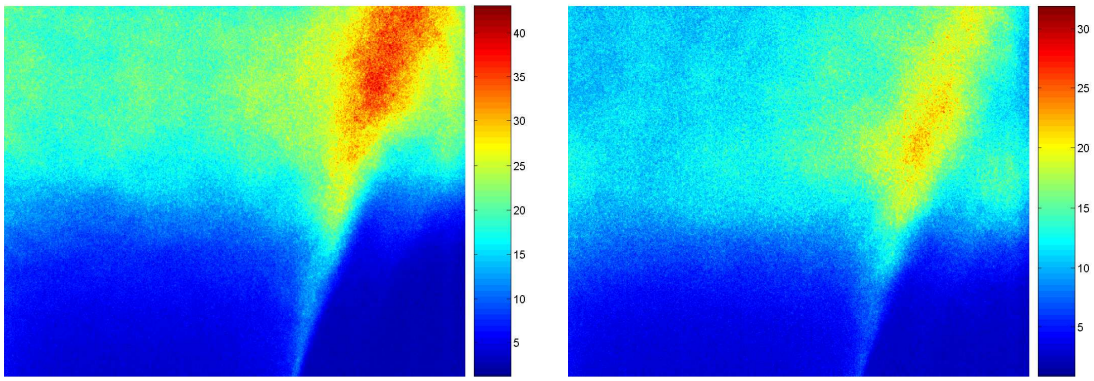

(c) 0.52 (d) 0.48

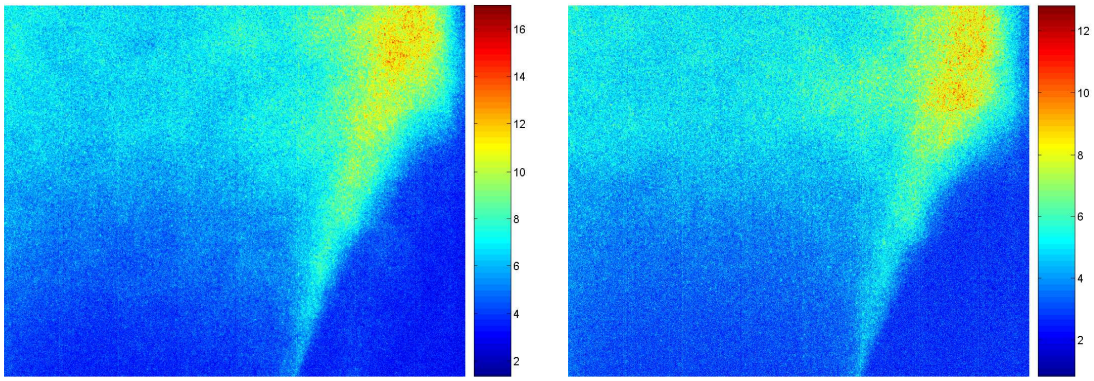

(e) 0.45 (f) 0.44

Figure 3.14: Time-averaged OH* chemiluminescence images as a function of equivalence ratio. Case S0, $\langle U \rangle = 9.9$ m/s.

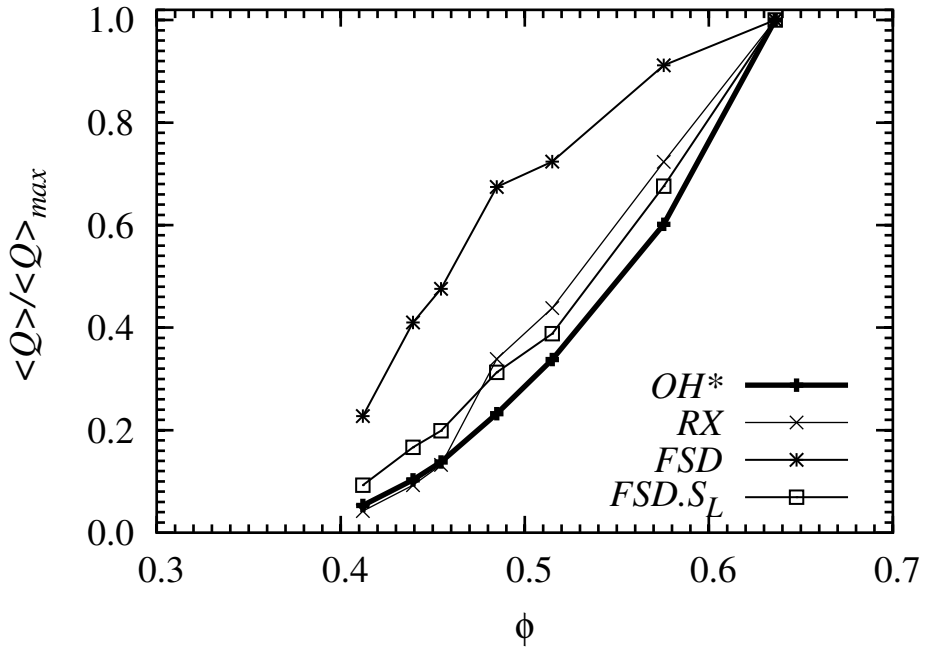

Figure 3.15: Variation of mean heat-release computed from different measurement approaches as a function of equivalence ratio from the data presented in Figs. 3.12, 3.13 and 3.14.

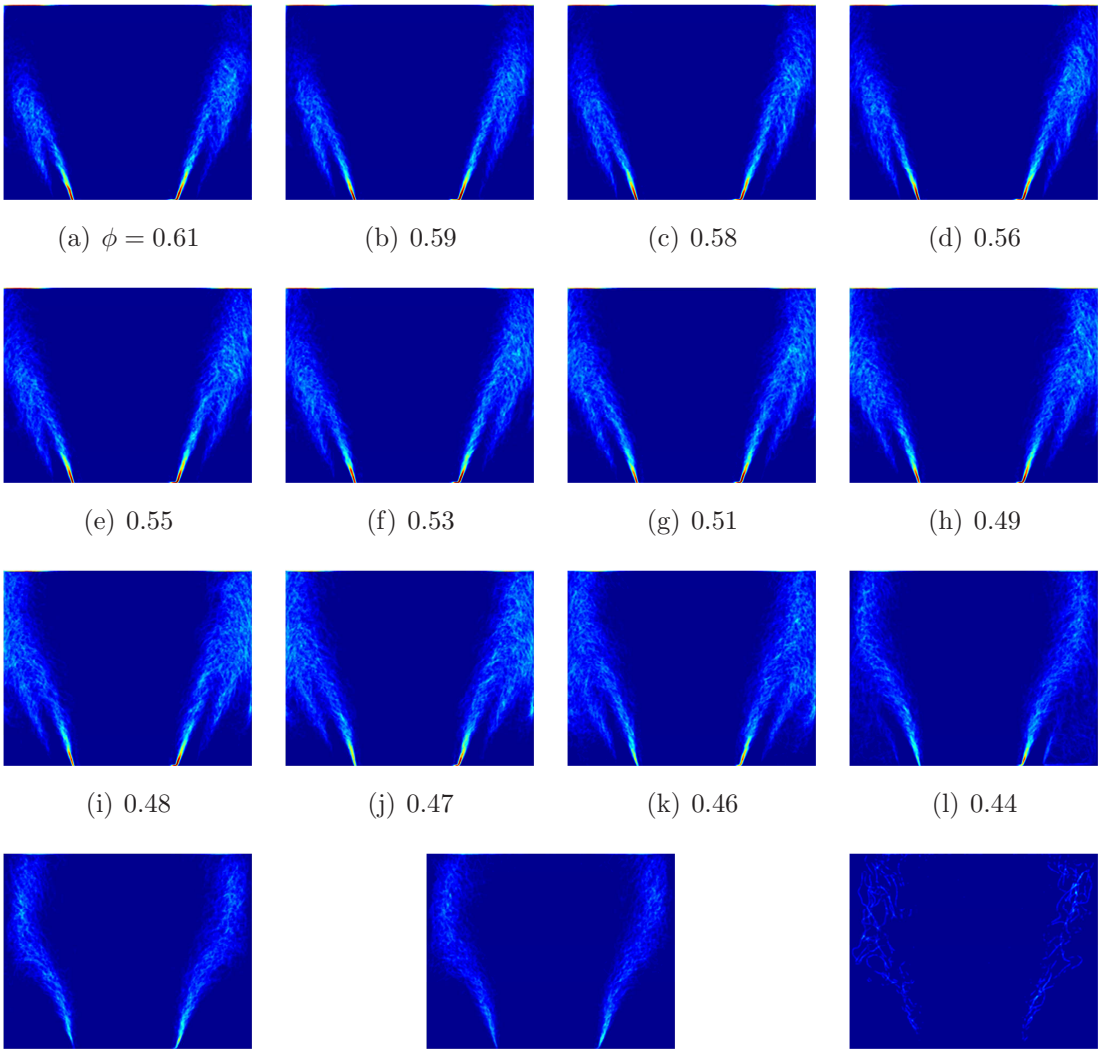

(a) $\phi = 0.61$ (b) 0.59 (c) 0.58 (d) 0.56

(e) 0.55 (f) 0.53 (g) 0.51 (h) 0.49

(i) 0.48 (j) 0.47 (k) 0.46 (l) 0.44

(m) 0.42 (n) 0.41 (o) 0.39

Figure 3.16: Time-averaged FSD images of flame with moderate swirl for the indicated ϕ. Case S1, $\langle U \rangle = 9.9$ m/s.

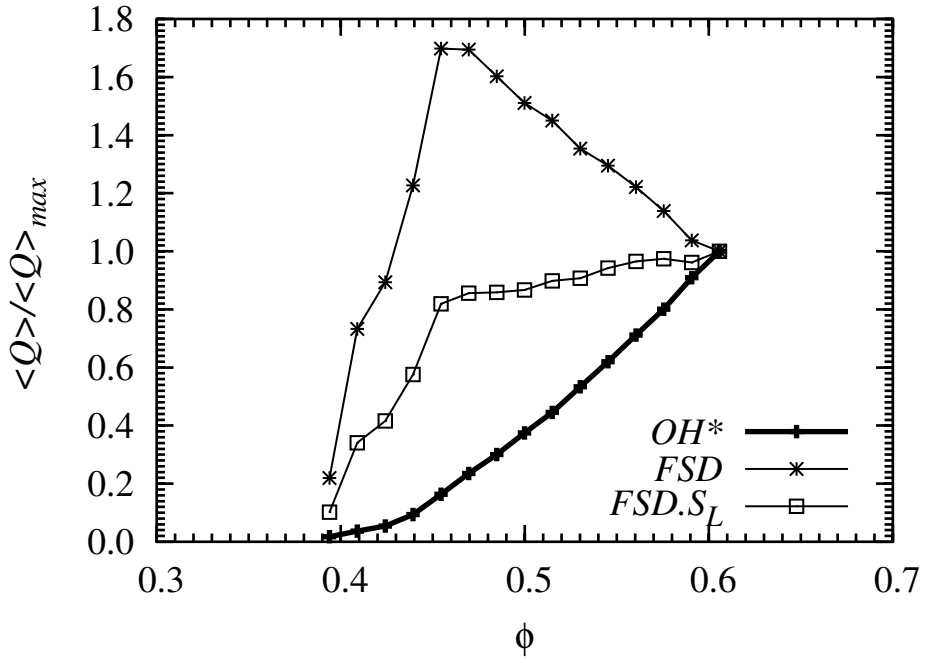

Figure 3.17: Variation of mean heat-release computed from different measurement approaches as a function of equivalence ratio. For the case presented in Fig. 3.16.

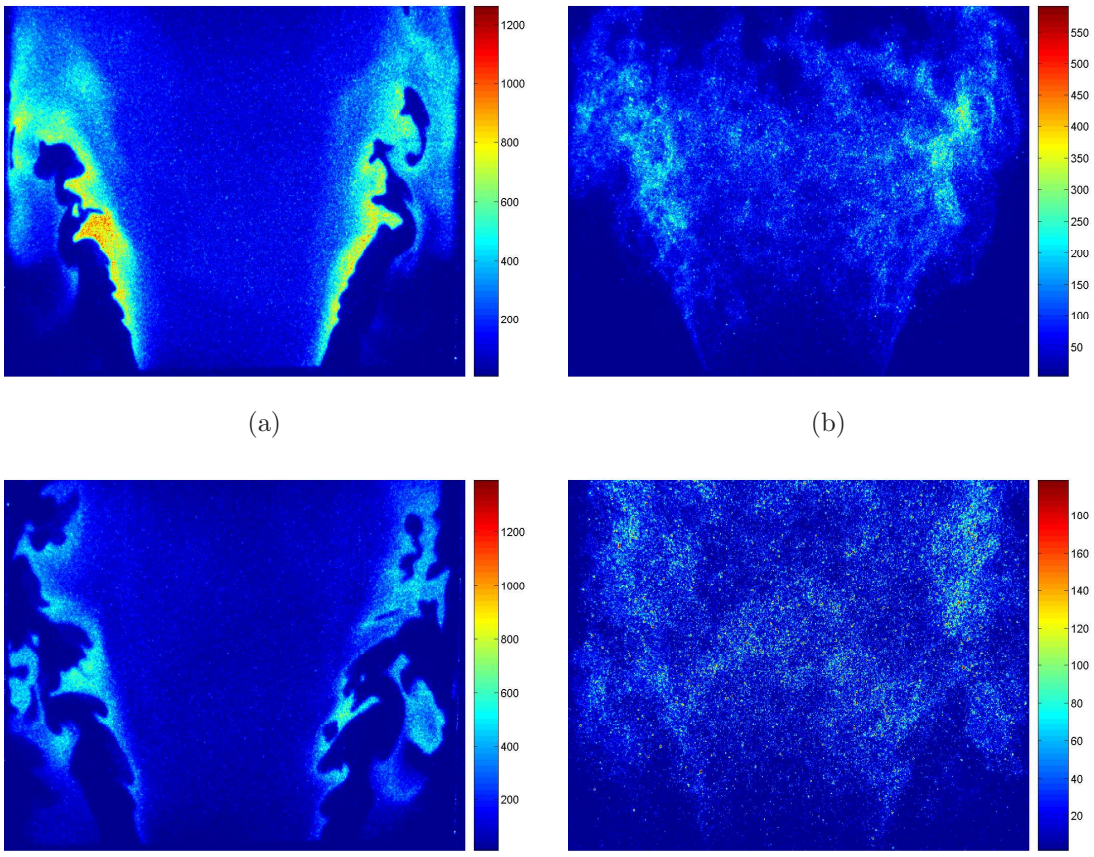

(a) (b)

(c) (d)

Figure 3.18: (a) Instantaneous OH PLIF and (b) Chemiluminescence image of flame with $\phi = 0.61$, (c) and (d) that of $\phi = 0.45$. Case S1.

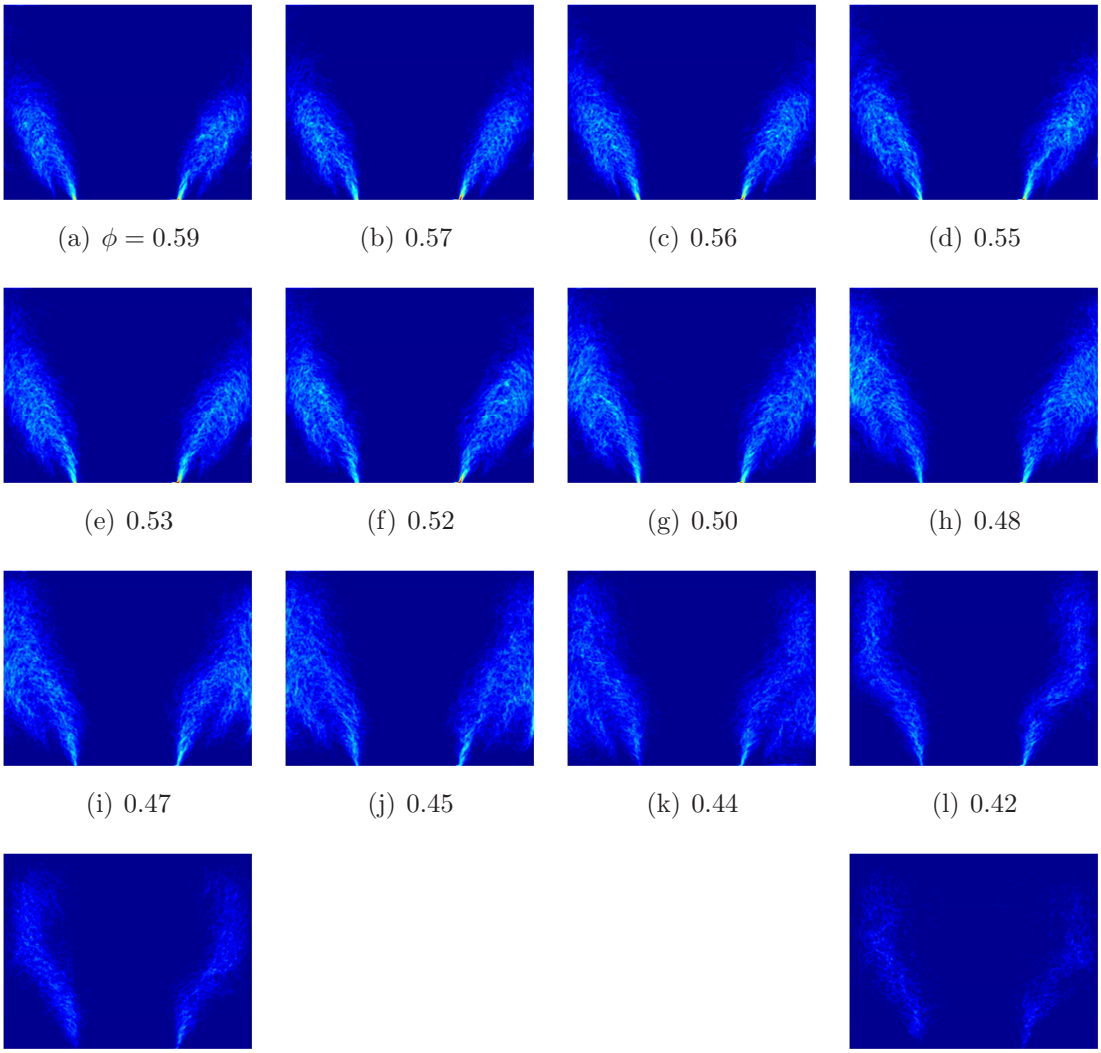

(a) $\phi = 0.59$ (b) 0.57 (c) 0.56 (d) 0.55

(e) 0.53 (f) 0.52 (g) 0.50 (h) 0.48

(i) 0.47 (j) 0.45 (k) 0.44 (l) 0.42

(m) 0.41 (n) 0.40

Figure 3.19: Time-averaged FSD images of flame with high swirl for the indicated ϕ. Case S2, $\langle U \rangle = 9.9$ m/s.

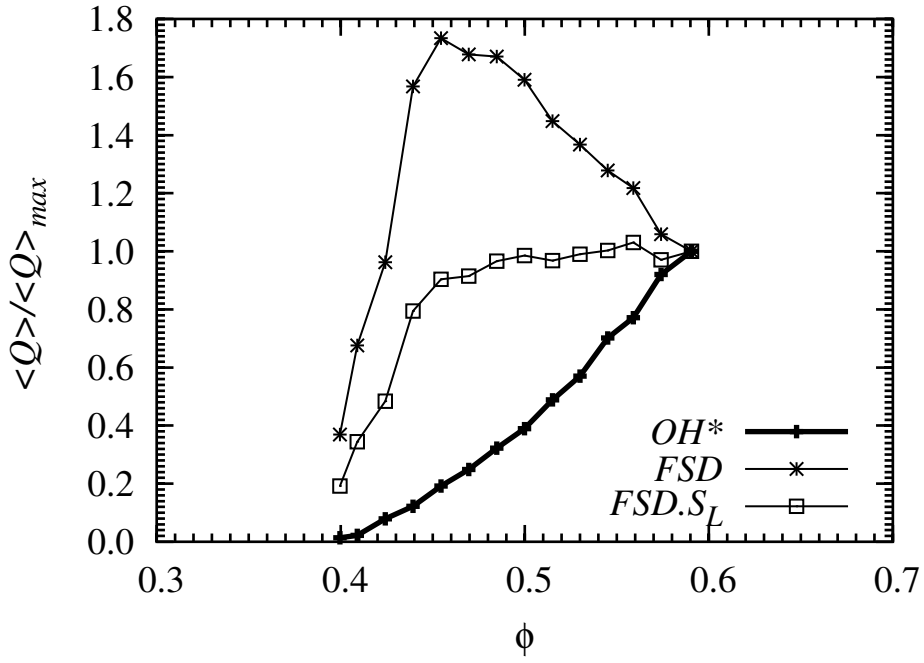

Figure 3.20: Variation of mean heat-release computed from different measurement approaches as a function of equivalence ratio. For the case presented in Fig. 3.19

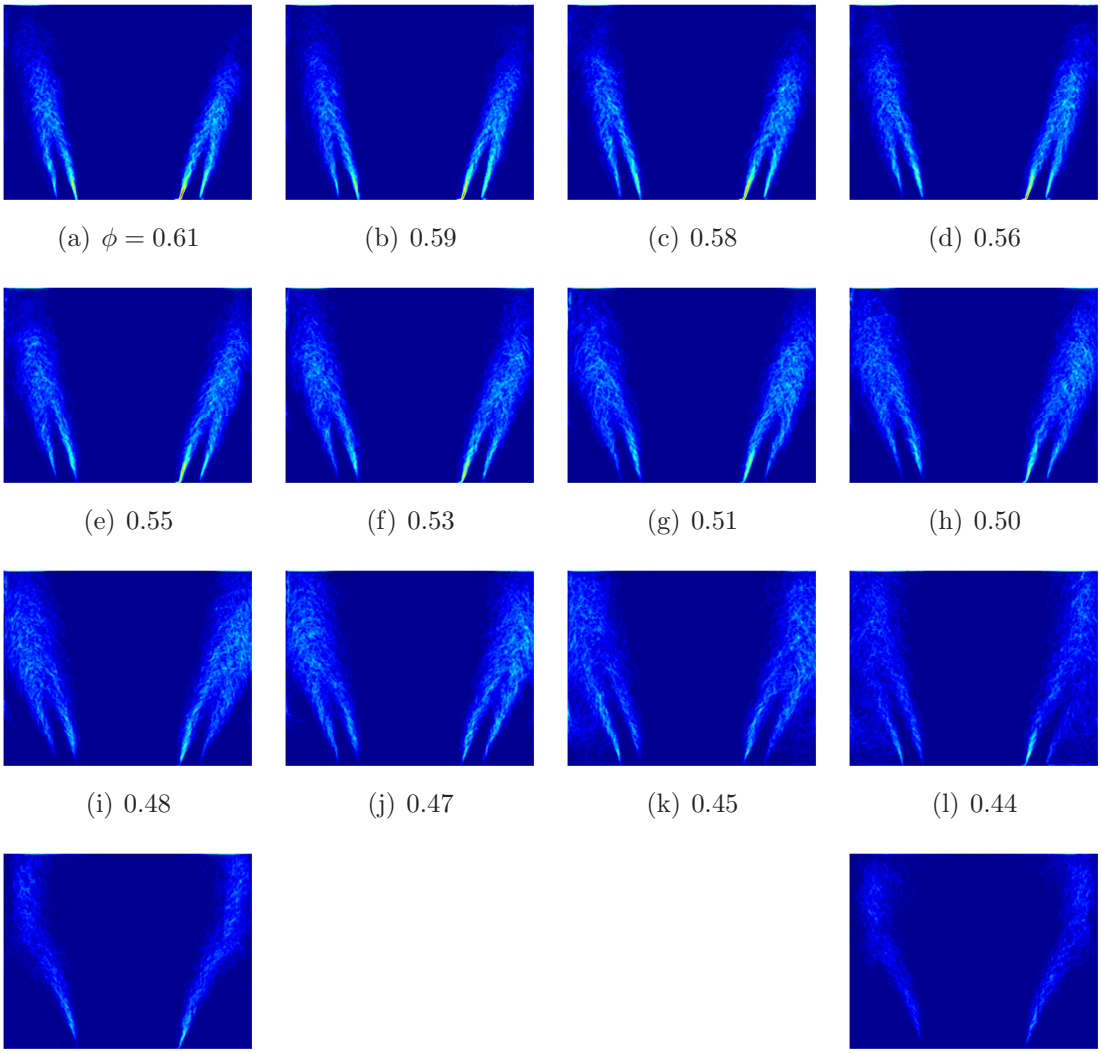

(a) $\phi = 0.61$ (b) 0.59 (c) 0.58 (d) 0.56

(e) 0.55 (f) 0.53 (g) 0.51 (h) 0.50

(i) 0.48 (j) 0.47 (k) 0.45 (l) 0.44

(m) 0.42 (n) 0.41

Figure 3.21: Time-averaged FSD images of imperfectly premixed flame with moderate swirl for the indicated global ϕ. Case S1, $\langle U \rangle = 9.9$ m/s.

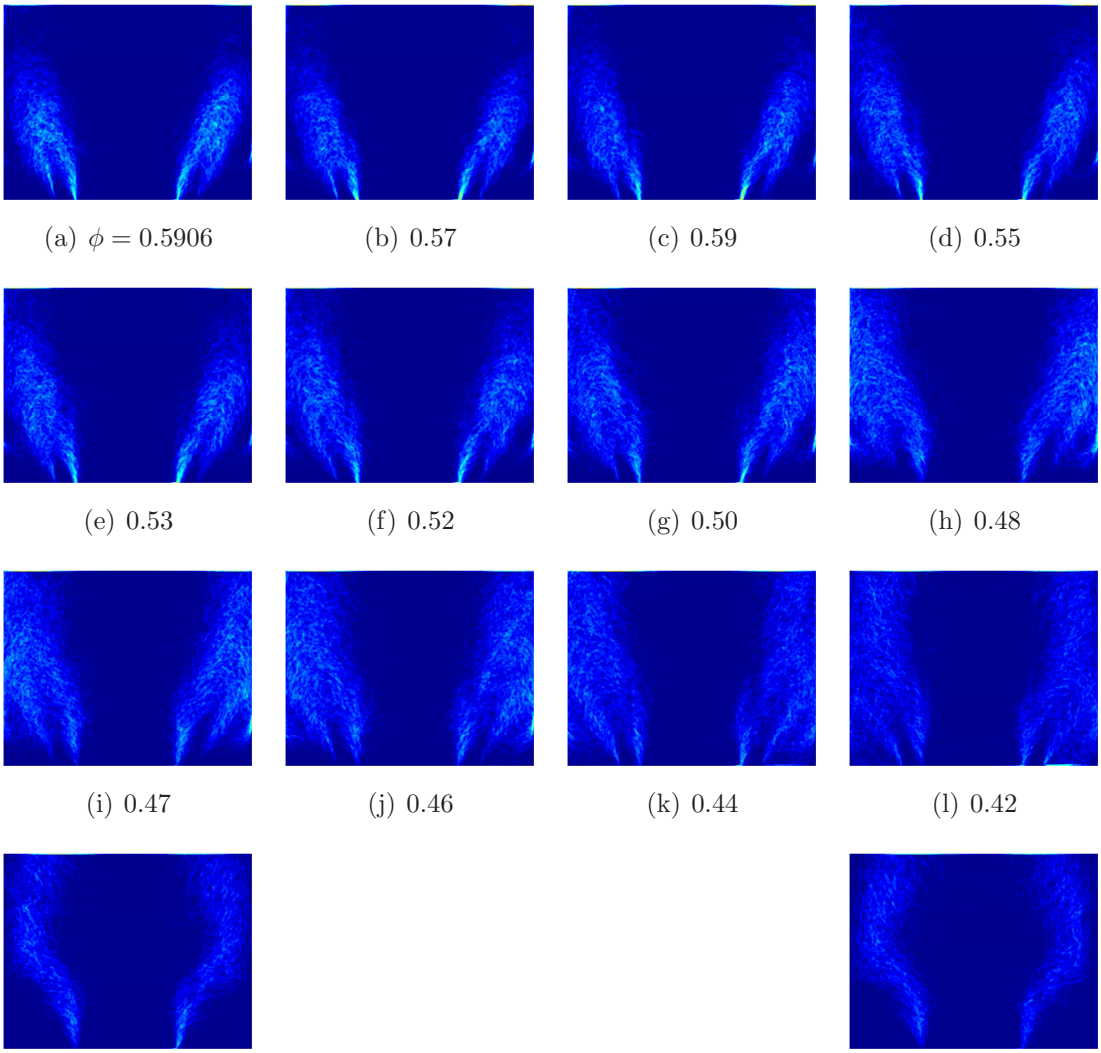

(a) $\phi = 0.5906$ (b) 0.57 (c) 0.59 (d) 0.55

(e) 0.53 (f) 0.52 (g) 0.50 (h) 0.48

(i) 0.47 (j) 0.46 (k) 0.44 (l) 0.42

(m) 0.41 (n) 0.40

Figure 3.22: Time-averaged FSD images of imperfectly premixed flame with high swirl for the indicated global ϕ. Case S2, $\langle U \rangle = 9.9$ m/s.

Chapter 4

Response of Fully Premixed Flames

This chapter describes the results of experiments on the response of fully premixed flames to acoustic forcing. Section 4.1 presents briefly the background on the response of fully premixed flames. From section 4.2, the results of the experiments performed with various measurement techniques presented in Chapter 2 used to measure the heat release response of forced lean premixed flames are presented. A comparison of the variation of heat release rate evaluated from these techniques are presented in section 4.3. Furthermore, in section 4.4, the dynamics of the local flame structure and the non-linear response of the flames to forcing as function of various parameters such as forcing amplitude and frequency, equivalence ratio, swirl, are elucidated in detail. The non-linear response of flames when forced with two frequencies is also described. Finally, this section closes with a discussion about the mechanism of heat release modulation and the origin of saturation in forced fully-premixed flames.

4.1 Brief Background

As described in Chapter 1, various mechanisms have been suggested for oscillatory heat release in a combustion induced by pressure oscillations. The common mechanisms by which unsteady combustion may occur include a pulsating fuel supply (introducing fuel/air ratio ie equivalence ratio variations (Lieuwen & Zinn,

1998a)) or oscillating flame front, convective entropy and vorticity waves, and vortex driven instabilities. It has been shown by previous investigators (Cala *et al.*, 2002; Külsheimer & Büchner, 2002; Poinsot *et al.*, 1987; Schadow & Gutmark, 1992) that in bluff body and dump stabilised combustors, the presence of acoustic oscillations resulted in formation of vortices in the shear layer between the high speed fuel stream and the low speed wake and the recirculation formed by the rearward facing step (or dump). The formation of a vortex ring in these flow play significant role in combustion process. The overall flame surface area could be greatly affected by such vortices. In flames under large velocity fluctuations, dominated by these large-scale coherent vortices, the variation in flame displacement speed due to fluctuation in strain rate could also be very important for variation in global heat release rate. There are numerous investigations on the flame response where the heat release fluctuation was modelled using flame kinematics. Also, the abundant laminar flame response experimental data base could not give enough information about the role of flame speed variation that could occur in realistic turbulent flames. Moreover, owing to the difficulties in measuring the heat release in vortex-dominated, highly-strained flow, there are not many systematic experimental investigation to elucidate the role of vortices in turbulent premixed flame response. This section deals with the issues mentioned above. Hence, this section is devoted to the formation and dynamics of large-scale vortices and their role in variation in heat release rate in turbulent premixed bluff-body flame using chemiluminescence and laser based measurements (described in Chapter 2). The origin of nonlinearity in premixed flame was studied closely and the section closes with a clarification on role of flame speed variation in turbulent flames. Further, the effect of parameters such as swirl and equivalence ratio is also presented here.

4.2 Experimental Conditions

The data presented in this section were performed on a configuration with completely premixed flames. As mentioned in chapter 2, the fuel (ethylene) was mixed upstream of the combustor ($\sim$ 2m). The flame of equivalence ratio ϕ equal to 0.55 with a bulk velocity of 9.9 m/s at the burner plane was commonly used in this section. Two swirlers blocks with vane angles 45^o and 60^o were employed to

introduce swirl in the flow. The no-swirl, 45° and 60° cases are referred to as S0, S1 and S2. The amplitude and frequency velocity perturbation effected at the burner plane was varied; frequencies from 20-400 Hz and amplitudes A up to 70% at resonant frequencies. (See Fig. 3.1 that show the variation of maximum amplitude that could be excited for the selected flow condition). In order to excite multiple frequencies, combination of two harmonic frequencies with maximum values were chosen i.e., in this case 160 Hz and 320 Hz.

4.3 Dynamics of a Forced Premixed Flame

Figure 4.1 shows a typical time-averaged FSD image of an unforced flame. The image shows that the flame was primarily anchored at the shear layer generated by the bluff body, with some flame elements at the outer shear layer generated by the rearward facing step (dump plane). Due to lower local temperatures in the outer recirculation caused by the dump plane, stabilization of such flame elements was not achieved. When the reactant mixtures were forced with sufficiently large amplitude, these shear layers roll up to form a counter rotating vortex pair (Cala *et al.*, 2002). The inner shear layer rolls inwards and the outer shear layer rolls outwards. The shear layer roll up as a result of acoustic forcing was investigated in the cold flow case and was presented in Chapter 3. Figure 4.2 shows the evolution of the flame using phase-averages of FSD when the flame was forced at 160 Hz (a condition selected to give high A value, from Fig. 3.1) with the value of forcing amplitude, A equal to 0.63, a relatively high value. The 18 images show the flame surface evolution at every 20 degree phase angle. The image sequence shows clearly the deformation of the flame base, later resulting in roll up of the flame front stabilised at the inner shear layer, radially inwards while the flame stabilised on the outer layer rolled up outwards. It can be observed that the rolled-up flame front grew in size and was convected with the flow and impinged on the wall. Once this disturbance moved out of the imaging region, a new vortex started forming at the base of the flame. This phenomenon was cyclic following the imposed velocity fluctuations. Figure 4.3 shows the phase-averaged OH* chemiluminescence images taken simultaneously with the PLIF measurements for the case presented in Fig. 4.2. The details of cold flow corresponding to the

flow conditions presented in Figs. 4.2 and 4.3 was presented in Fig. 3.5. The roll-up of the reacting shear and the dynamics of the vortex ring formed are found to be similar to that of the cold flow.

The phase averaged FSD images obtained from the PLIF images (as described in Chapter 2) were revolved around the burner central axis and were used to obtain the normalized cyclic heat release fluctuation and this was compared with the quantity obtained from OH* chemiluminescence imaging. Figure 4.4 shows the heat release variation evaluated from spatial integration of each of the phase-averaged FSD images in Fig. 4.2 and the OH* chemiluminescence images in Fig. 4.3 captured simultaneously during the experiments. From Figs. 4.2, 4.3 and 4.4, it can be noticed that the heat release decreased with the beginning of the roll up and decreased further to attain the lowest value around 100-120 degrees, which corresponded to the case where the flame surface area was at the lowest value due to the vortex roll up. The vortex while moving downstream towards the wall increased in size, increasing the flame area. The heat release evaluated from these measurements increased during this phase to attain a peak value around 280 degrees, which corresponded to the highest flame surface area.

The heat release variation captured by both FSD and OH* are in agreement with a small difference in magnitude and phase. The agreement between FSD and chemiluminescence was also noted earlier by Lee *et al.* (2000) and in Chapter3 as well (Fig. 3.15). It was observed that the difference in the magnitude between the two measurements techniques increased with increase in forcing amplitude, but was about 20% at the most. These measurements suggest that the FSD can capture the global heat release variation well in spite of the reservation of it being a planar measurement and that the flame speed can vary along the flame.

The FSD technique was further compared with high-resolution heat release images under different forcing conditions in an effort to evaluate its accuracy. These experiments were performed to image the vortex-dominated region only. During these measurement cases, the forcing cycle was resolved into 13 phase bins and OH and CH_2O PLIF images were taken at every phase and stored. As described earlier, these instantaneous images were processed to obtain RX and FSD image and then these instantaneous images were averaged to obtain phase averaged RX and FSD images respectively. The heat release variation

over the forcing cycle was obtained from these phase-averaged RX and FSD images. Figures 4.5(a) and (b) show typical instantaneous and phase averaged distributions of OH, CH_2O, OH* and the corresponding RX and FSD images respectively. These images were phase locked at a phase angle of 40 degrees with reference to the forcing signal. It can be seen clearly that the flame, stabilised at the shear layers, has rolled up into a counter rotating vortex pair due to the strong acoustic forcing. From the images it can also be seen that the FSD marked the flame very well, in full agreement with the RX imaging. However, the instantaneous RX image shows a smaller heat release at the vortex region formed at the outer shear layer (marked as A in Fig. 4.5) than at the flame region inside the bluff body generated recirculation zone (marked B in Fig. 4.5), something that an FSD - based heat release measurement cannot capture. The phase-averaged images reflect these facts clearly. It can also be observed from the instantaneous and averaged OH* images, in spite of longer integration times (50 μs), that the heat release was not captured well in the outer re-circulation regions due to weaker emissions from these regions. Both OH* and RX images show higher heat release in the region A marked in Fig. 4.5. This is due to the fact that the acoustically excited inner shear layer when rolled into a vortex brought reactants between the flame surfaces resulting in higher heat release at the point of focus.

We should finally noted that even at high forcing amplitudes, the RX imaging always showed a connected reaction zone without any evidence of localised extinctions, which may have been expected because the images cover the vortex-dominated region close to the bluff-body where high strain rates are possible. The absence of localised extinctions seems to suggest that this is not a key mechanism determining the flame response in this flow.

Figure 4.6 shows the cyclic evolution of heat release directly evaluated from RX imaging and that estimated from the FSD, for the case presented in Fig. 4.4. It can be clearly seen from this figure, that when the vortex appeared, the heat release evaluated from both the measurements increased, but the heat release evaluated from RX peaked ahead of that computed from FSD. The magnitude of heat release fluctuation over its mean evaluated from RX is around 10-15% higher than that evaluated from the FSD technique and this difference increased

up to 20% with increase in forcing amplitude. The increase in local heat release rate captured by both techniques in the vortex dominated region and the fact that global heat release decreased with the appearance of the vortex (Fig. 4.4) suggest that the flame annihilation in the regions above the vortex region could be playing a significant role in heat release modulation.

It has to be noted that the accuracy of the RX imaging is critically dependent on the geometrical transformation procedure. Hence, the RX imaging technique if used to image a larger interrogation window has to be interpreted with care due to the increased error in estimations. The error in FSD estimates is mainly due to the noise in the images. The fact that the FSD in the current study is based on OH PLIF which has high signal to noise ratio, makes FSD a better choice for determination of local mean reaction rate while performing global imaging (i.e., bigger interrogation window size).

Figures 4.4 and 4.6 suggest that FSD underestimates the heat release rate by not more than 20% at the highest forcing amplitudes. This difference may be attributed to the burning rate fluctuations along the flame as seen in Fig. 2.12(a)-(iii) and Fig. 4.5(a)-(iv), although we cannot be certain at this stage as the RX technique is not fully quantitative. We can conclude, however, that tracking the evolution of the flame front with FSD and measuring global chemiluminescence are probably sufficient tools to understand flame response even at high amplitudes. Details on the non-linear response are given next.

4.4 Heat Release Response

The spectral analysis of the heat release measured by chemiluminescent techniques and that evaluated from flame surface density (FSD) and RX imaging were used obtain the complex amplitude of the cyclic heat release variation. These measurements together with the acoustic velocity calculated from the two-microphone technique was used to understand the nonlinear heat release velocity coupling. The effects of various parameters affecting the nonlinear flame response are presented in this section.

4.4.1 Amplitude and Frequency Dependence of the Flame Response

Figure 4.7(a) shows the dependence of the OH* and CH* chemiluminescence upon the inlet forcing amplitude at the same forcing frequency. It can be clearly seen from the figure that the heat release response saturates at an amplitude of around 15% marked as x in the figure. In this thesis, the deviation from linearity is termed as saturation. With further increase in amplitude the flame response levelled off which is marked as x'. Figure 4.7(c) shows the transfer function (i.e., the y-axis of Fig. 4.7(a) divided by A) and the corresponding phase information calculated from the data presented in Fig. 4.7(a). A linear response would be a straight horizontal line. The transfer function measurements show clearly a non-linear amplitude dependence: at lower amplitudes the transfer function drops rapidly with increase in amplitude and once the magnitude reached a certain value, with further increase in amplitude there was little change in transfer function. At the point corresponding to x', the transfer function again starts decreasing. It can be seen from Fig. 4.7(c) that the phase of the transfer function was nearly independent of the amplitude of forcing up to the point x, after which the phase increased with increasing forcing amplitude. From these data it is also clearly evident that the magnitude and phase of the heat release response measured by both the OH* and CH* chemiluminescence techniques are in good agreement. It should be noted that Samaniego *et al.* (1995) showed that the chemiluminescence signal scaled with heat rate linearly, which implies that the nonlinearity observed here, might not be due to the measurement method. Bellows et al. (Bellows & Lieuwen, 2004; Bellows *et al.*, 2003) observed saturation similar to the 'x' (marked in Fig. 4.7(a)) in their experiments with forced turbulent premixed flames. They speculated this saturation to be due to a non-linear evolution of the flame surface area. However, they insisted on the need for optical measurements to confirm this, and such measurements are discussed below.

Figure 4.7(b) shows the heat release response evaluated from FSD as a function of forcing amplitude. The figure shows two saturation points similar to that of OH* and CH* measurements. However, the magnitude of the normalised response measured from FSD technique has lower values compared to that of

chemiluminescence measurements, which may be due to local burning rate fluctuations along the flame contour. These measurements confirmed that the level of contribution of flame surface modulation to the total heat release response is significant and that the flame area evolution is playing a key role in the observed saturation. This is consistent with results obtained by Schuller *et al.* (2003b) for laminar flames.

Figure 4.8 shows averaged FSD images for the same case presented in Fig. 4.7 at a particular phase angle (120 degrees w.r.t. forcing signal), at different forcing amplitudes. It can be seen that as A increases from 0.23 (corresponding to point x marked in the Fig. 4.7) the flame surface is increasingly curved. It can also be seen that the vortex rollup has shortened the flame, which in turn reduced the total flame area non-linearly, despite the fact that the flame area is expected to be increased by flame elements wrapping around the vortex. It can be observed from these images that the intensity of the flame elements above the vortex region decreases with an increase in amplitude of forcing, suggesting possible flame surface destructions in these regions. Further increase in amplitude shows decreased response in FSD and it can be seen in Fig. 4.7(b) that the response levelled off around $A = 0.59$, marked as x'. It can be seen that the flames at $A = 0.59$ and 0.64 are virtually identical, which explains why the last two points in Fig. 4.7(b) show identical $Q'/\langle Q \rangle$.

Figure 4.9 shows the cyclic variation of heat release evaluated from FSD images for different amplitudes of forcing. It can be seen from this figure that with an increase in forcing amplitude, the increase in the peak-to-peak amplitude of heat release up to A=0.12 was linear. With A values, reaching higher values, the cyclic variation in heat-release seemed to saturate, in Fig. 4.9 it can be seen that for the cases A=0.59 and A=0.65, the cyclic variation was nearly the same in magnitude and phase.

The finite amplitude response of the flame was investigated further for different forcing frequencies between 20-400 Hz. However, only three frequencies other than 160 Hz are presented here, selected so that they give relatively high magnitude of inlet forcing (see Fig. 3.1). Figure 4.10 shows the amplitude dependence of heat release response of the flame at 40 Hz, 240 Hz and 310 Hz,

with the corresponding magnitude of transfer function and the phase information measured using OH* and CH* chemiluminescence. It is evident from Fig. 4.10(a) that the chemiluminescence response was linear throughout the forcing conditions. The magnitude of transfer function shows a nearly linear dependence on the amplitude while the phase seemed to be independent of the amplitude of forcing. Figure 4.11 presents the phase-averaged FSD images for the highest forcing case presented in Fig. 4.10(a). It can be seen from these FSD images that there was no shear layer rollup, and the flame area modulation was only by the oscillatory motion of the flame.

Figures 4.10(b) and (c) show the amplitude dependence of the heat release response and the corresponding transfer function calculations when the flame was forced at 240 Hz and 310 Hz. As in the case of 160 Hz forcing, the appearance of the saturation point x was consistent with the appearance of the flame roll up during the 240 Hz forcing. The phase-averaged FSD images showing the variation in flame surface when forced at 240 Hz and 310 Hz at the highest amplitudes corresponding to the forcing frequencies, are presented in Figs. 4.12 and 4.13. In the case of 240 Hz forcing, the roll up of the flame front was not prominent due to the low level of forcing amplitude achieved by the excitation system at that frequency. For the forcing at 310 Hz with relatively higher amplitude than that at 240 Hz, the flame front roll up was very prominent. In both cases, the non-linearity in the flame response was observed only when the flame front started to roll up. However the amplitude at which the non-linearity started for 240 Hz and 310 Hz forcing conditions was found to be lower than that of the 160 Hz forcing. This could be due to the fact that the amplitude of inlet oscillation required to achieve excitation of the shear layer to roll up into vortex has strong frequency dependence also noted in Chapter 3.

It was showed in the work by Külsheimer & Büchner (2002) that the required amplitude to excite the shear layer to roll up decreases with increasing frequency. It can also be seen that the phase dependence for forcing at 310 Hz has a linear dependence upon the amplitude up to the point of saturation, while beyond that point the phase increased with increase in forcing amplitude. This could be due to the fact that at this forcing frequency the flame might not be acoustically convectively compact. (A flame whose length is much less than an acoustic

convective wavelength is referred to as acoustically convectively compact, see Lieuwen (2003).) From Figs. 4.13 and 4.14 showing the response of flame at 310 Hz, using phase-averaged FSD and OH* images, it can be seen that before one vortex moves out of the combustion zone, a new vortex appeared at the base of the flame. The interaction of these two vortices could be causing this non-linear dependence of phase on the amplitude. Figure 4.15 shows the variation of heat release evaluated from Fig. 4.14. The images presented in Fig. 4.14 suggest that the heat release was at the lowest value at around 120^o which corresponded to a case where the the flame was fully rolled up into a vortex. The highest value of the computed heat release corresponded to the phase where there was two vortices in the imaging area resulting in highest flame surface area. Of the two vortex rings, one, laminar like was at the base at the formation stage while the other was at the top of the image with increased heat release resulting from fine mixing between the reactants and the products. Figure 4.16 shows that the variation of heat release response measured from FSD has trend similar to that measured using OH* presented in Fig. 4.10(c). In both Figs. 4.16 and 4.10(c), it can be noted that the normalized heat release response on the amplitude was nearly linear up to the level of input forcing achieved. This could be due to the increased flame area due to presence of vortex, the contribution of which (expected to increase proportionally with forcing) is larger than the flame loss due to the flame annihilation events. These results further prove that the heat release variation in this flame is through surface area modulation.

In an effort to understand further the response of the flame to acoustic forcing, the transfer functions measured at different forcing frequencies for a range of amplitudes are consolidated in Fig. 4.17. Figure 4.17(a) shows the magnitude of the transfer function at different forcing frequencies for different amplitudes, and Fig. 4.17(b) shows the phase between the heat release and the velocity fluctuations. The magnitude of the transfer function was found to decrease with increasing amplitude for all forcing frequencies (better represented in Fig. 4.18). However, at lower frequency ranges this scatter was very low when compared to that of high frequency forcing conditions.

The phase plot (Fig 4.17(b)) shows the variation in phase of the transfer function as the function of forcing frequency, which suggests a definite time delay.

This time delay was referred to as "fuel convection delay time" in Dowling & Stow (2003). From the data presented in Fig. 4.17(b) it was calculated to be of the order of 8 ms. This delay time along with the mean velocity of 9.9 m/s would translate into a convection distance of ∼80 mm, which correspond to the length of the region of measurement. It can be observed from the figures that the phase measured above 280 Hz had more scatter than at the lower frequencies; this could be again due to the fact that the flame was not acoustically convectively compact. These are the conditions where the spread in time delay (Armitage *et al.*, 2004) has to be modelled with care.

To better understand the effect of forcing amplitude on the frequency response of the flame, the data presented in Fig. 4.17 were reconstructed for constant amplitude of forcing from the interpolation between the magnitude of transfer function and amplitude of forcing for every frequency using a bilinear fit. Figure 4.18 shows the reconstructed flame transfer function measurements for constant forcing amplitude. It can be observed that with an increase in forcing amplitude the magnitude of the transfer function decreases, this decrease being greater for higher frequencies than for the lower frequencies. During these experiments, it was observed that up to nearly 100 Hz, there was no significant flame surface modification irrespective of the magnitude of the forcing amplitude. For the higher forcing frequencies, flame surface roll up was observed. Since this is amplitude dependent, significant difference in the amplitude dependence of the flame responses at low and high frequency forcing occurs.

4.4.2 Effect of Equivalence Ratio

Figure 4.19(a) shows the effect of equivalence ratio on the non-linear heat release response of the flame forced at 160 Hz with different forcing amplitudes. The equivalence ratio was varied from 0.55 to 0.7 and the OH* chemiluminescence and acoustic pressure measurements were performed simultaneously to obtain the global heat release response of the flame. Figure 4.19(b) shows the magnitude of transfer function and phase for the case presented in Fig. 4.19(a). As suggested earlier, the saturation was determined by the flame front roll up. The amplitude required for this roll up was higher for higher equivalence ratios possibly because

the corresponding increase in laminar burning velocities shifts the flame position relative to the vortex. The phase of the transfer function was also found to increase with increase in equivalence ratio. However the trend in variation as a function of amplitude was the same for all cases.

It is interesting to also note that for the equivalence ratios 0.67 and 0.7 and after the saturation, an increase in amplitude of forcing resulted in a sudden drop in heat release response, marked as x' in the figure. The time series measurement of OH* and the corresponding cold flow inlet velocity measurements before and after the point of saturation x' are shown in Figs. 4.20(a) and (b) respectively. The velocity measurements show relatively small harmonic contents, however the OH* clearly shows a disproportionately larger distortion of the waveform after the saturation, suggesting a strong response at a harmonic frequency. The amplitude required to obtain this saturation x' was also found to decrease with increase in equivalence ratio.

In order to better understand this non-linear behaviour, the inlet velocity measurements were analyzed to determine the amount of harmonic content under cold flow. It was observed that there was a linear increase in harmonic content during forcing (Fig. 4.21). However, the ratio of fluctuation of heat release at the first harmonic frequency to that of the forcing frequency showed a highly non-linear variation against the forcing amplitude (see Fig. 4.22). For a particular equivalence ratio this relative response to the first harmonic frequency was found to increase linearly up to the saturation point x (marked in Figs 4.19 & 4.22), after which this relative response stayed constant. This suggests that with the appearance of the flame roll up, the response to the harmonic frequency was suppressed. This proportional harmonic response increased suddenly with further increase in amplitude (for certain equivalence ratio conditions, here 0.67 and 0.7). This behaviour could be due to a complex interaction between flame, harmonic content present in the velocity and the upstream geometry. An analysis of the response of laminar flames to monochromatic velocity forcing (Schuller *et al.*, 2003b) also suggested that the flame surface fluctuations contained harmonics of the forcing frequencies. To understand this non-linear flame response to multiple frequencies in inlet velocity fluctuations further detailed investigation with optical measurements is necessary, which will be presented later in the chapter. However,

the data presented up to now, suggest an additional reason why transfer functions can be non-linear.

4.4.3 Effect of Swirl

In this section, the results from the experiments on response of the flame with swirling inlet flow are presented. Figure 4.23 shows the unforced swirl flames with two swirl conditions, Fig. 4.23(a) corresponding to the moderate swirl S1, and Fig. 4.23(b) that of high swirl at the inlet, case S2; both flames were at the same bulk velocity $\langle U \rangle$ = 9.9m/s and same equivalence ratio, ϕ=0.52. Increasing swirl resulted in decreased overall flame height and also increased flame brush thickness. When the moderately swirled flame was forced at 160 Hz with sufficiently large amplitude, the flame front rolled up into vortex ring as in the case of non-swirling case. Figure 4.24 shows the evolution of the vortex ring in moderately swirled flame (case S1). The phase-averaged OH* chemiluminescence images taken with the PLIF measurements are presented in Fig. 4.25. Figures 4.24 and 4.25 suggest that when the flame wrapped up by the vortex, the flame elements were annihilated in the region above the vortex. With an increase in the vortex size and during the convection downstream, the vortices become more and more turbulent and the mixing between the reactants and the products increased, resulting in increased heat release. The variation of the heat release through the cycle is presented in Fig. 4.26, the figure also shows comparison of the two techniques (OH* chemiluminescence and FSD evaluation) for this swirled case (data presented in Figs. 4.24 and 4.25). The figure suggests that the heat release modulation in this flame is through flame surface area modulation, while the slight difference in the phase and the magnitude can be attributed to increased wrinkling in the third dimension due to the presence of swirl.

The heat release response as function of forcing amplitude at 160 Hz is presented in Fig. 4.27. The normalized global heat release response presented in Fig. 4.27(a) suggests that the amplitude dependence of the flame response was nonlinear at around 20%, the two measurement techniques both capturing the trend correctly while the magnitude of FSD was slightly lower than the OH*

measurements. The magnitude of transfer function and its phase presented in Fig. 4.27(b) also suggest that the trend was captured well by both techniques.

As in the forced response of a no-swirl flame (case S0) at 40 Hz (Fig. 4.10(a)), the amplitude dependence of heat release response at 40 Hz forcing for moderately swirled flame S1 was linear for the range of measured amplitudes of forcing (see Fig. 4.28). The magnitude and phase of the transfer function measured by OH* chemiluminescence also shows a linear dependence on the amplitude of forcing. When the flame with swirl S1 was forced at 330 Hz, the response varied nearly linearly with the forcing amplitude (see Fig. 4.29(a) and (b)). However, the phase was highly nonlinear, increased with increase in the forcing amplitude, which, as explained earlier for no-swirl flames, could be because the flame was not acoustically convectively compact. The magnitude and phase of the transfer function for a range of frequencies, presented in Fig. 4.30 suggests that, as in the case of flame with no swirl (S0), the magnitude of flame response first increased with frequency and then started to decrease after 160 Hz. The phase as a function of frequency, presented in Fig. 4.30(b) again suggests that the variation is due to a simple time delay. The increased scatter around 300 Hz could again be due to the fact that flame was longer than the acoustic-convective wavelength.

Figures 4.31 and 4.32 show the response of a flame forced at 160 Hz with increased swirl, using phase-averaged FSD and OH* image sequence. Figure 4.33 shows the comparison of heat release evaluated from the two techniques (data from Fig. 4.31 and 4.32). These figures suggest that the FSD and OH* techniques agrees very well, further confirming the role of flame surface modulation in the heat release response. The slight increased FSD values when the vortex is very close to the base could be due to the increased error in the FSD algorithm arising because of increased OH pockets in the recirculation zone introducing difficulty estimating the true flame area. Furthermore, the amplitude dependence captured by the two techniques presented in Fig. 4.34 agree fairly well. The linear dependence of the response to the amplitude can be explained from the Fig. 4.35, which shows the variation of the FSD over the forcing cycle for various forcing amplitudes. The figure suggests that peak-to-peak variation between the trough of the heat release cycle, caused by the flame annihilation events when the vortex was at the base of the flame and the peak value, when the vortex was at

the top of the image, increased continuously with increase in forcing amplitude, thus resulting in a linear amplitude dependence. These results from the swirled flames improved the confidence in FSD measurements and further proves the important role played by the flame area modulations in the heat release response and saturation in premixed flames.

Furthermore, the response of swirl flames to different forcing frequency was studied. The results presented in Figs. 4.36, 4.37 and 4.38 suggest that the flame response at this high swirl condition was nearly linear for most of the forcing frequencies. However, the magnitude of the transfer function was very small when compared to that of the other swirl conditions. With a decrease flame height, the flame was closer to being acoustically convectively compact than the previous cases and hence the scatter in the phase at around 300 Hz is less compared to the cases S0 and S1.

4.4.4 Simultaneous Excitation by Two Frequencies

The external excitation of the shear layers and control of mixing had been investigated by various investigators (see review Renard *et al.* (2000)), including the excitation of shear layers with two frequencies of which one of them was fundamental and the other was subharmonic of the forcing frequency (Cho *et al.*, 1998; Zhou & Wyganski, 2001). It was shown that the forcing at two frequencies could greatly affect the coherent vortex formation (Zhou & Wyganski, 2001). The use of external excitation to actively control the instability was also found to be successful (Candel, 2002). In practical combustion systems, there are many cases where there could be more than one oscillatory frequency. Furthermore, in predicting the instabilities using acoustic analysis methods, one would require to measure the transfer functions using external excitation methods, the use of the data obtained critically depends on the amount of other harmonics present in the inlet flow. There have been no rigorous, systematic study of role of the presence of harmonics in the inlet on the transfer function measurements. In this section, the results from an investigation of the effect of the presence of two frequencies on the vortex evolution and on the amplitude dependence of the measured flame response are presented.

The two channels from the waveform generator were utilized to generate two signals of two different frequencies and amplitudes. The data presented here were obtained by forcing the flame S0 with equivalence ratio ϕ =0.55, with two frequencies, the primary frequency was 160 Hz and the secondary frequency was 320 Hz. The variation in the cyclic variation of the heat release by increasing the amplitude of one of the frequencies, by keeping the amplitude of input signal at the other frequency constant are presented in Figs. 4.39 and 4.40. The fundamental (primary) and harmonic (secondary) frequencies are referred by symbols f_1 and f_2, while A_1 and A_2 denotes the amplitudes at these frequencies respectively.

The amplitude of the input signal to the speakers at the secondary frequency (f_2 = 320Hz) was kept constant and the amplitude of forcing at f_1 = 160 Hz was varied. It was observed that the heat release response was first following the 320 Hz forcing and with increase in amplitude at 160 Hz, the variation in the heat release drastically changed and at highest forcing, the response was nearly fully at 160 Hz (see Fig. 4.39). In the case of forcing at 160 Hz at maximum amplitude, introduction of oscillation at 320 Hz resulted in drastic change in the shape of the cycle. However, the time period of oscillation remained that of the primary forcing (that of 160 Hz). It should be noted that the peak value of the variation nearly remained the same while the trough became broader and decreased in the amplitude. Since the amplitude of trough region of the heat release variation was found to be associated with the flame annihilation event, one could speculate that there is a decrease of flame annihilations events due to the presence of harmonics in the flow at the inlet.

The variation in the normalized heat release response measured using OH* chemiluminescence as function of primary forcing amplitude A_1 is presented in Fig. 4.41(a). From the figure it can be clearly seen that the introduction of secondary oscillations has changed the amplitude dependence of the response from highly nonlinear to linear. The transfer function obtained from the data in Fig. 4.41(a), presented in Fig.4.41(b) shows that the magnitude of the variation in response was reduced up to $1/3^{\text{rd}}$ from monochromatic forcing conditions. The phase of the transfer function in Fig. 4.41(c) shows an increase in the phase with increase in amplitude of harmonics. The data presented in these plots in Fig. 4.41

are presented with peak-to-peak voltage into the speakers, which was kept constant, however this did not result in constant velocity conditions. The variation in amplitude of secondary velocity amplitude is presented in Fig. 4.42(a). This figure suggests that even at very low amplitude of secondary forcing or without any secondary excitation imposed on the flow, there were velocity contents in the secondary frequency (as presented in Fig. 4.21). The response of the flame at the secondary frequency as a function of primary forcing amplitude is also presented in 4.42(b). The presence of 320 Hz forcing did not affect the flow greatly above the primary forcing amplitude value of around 20% (the point at which the flame front was wrapped around by the vortex).

The phase averaged FSD images at two forcing conditions are presented here to understand the role of these frequencies in the formation of vortex rings. Figure 4.43 shows that with low primary forcing, and high secondary forcing, the flow was dominated mainly by the secondary forcing. It can be seen that there was two cyclic variations in heat release, which correspond to the secondary frequency 320 Hz, while the measurements were phase locked with the primary frequency 160 Hz. In the case of increase in primary forcing, the vortex evolution was due to the primary excitation (see Fig. 4.44). The OH* chemiluminescence for the case presented in 4.44 is presented in Fig. 4.45 and the comparison of the heat release evaluated from the data presented in the two figures is presented in Fig. 4.46. The comparison made in Fig. 4.46 further proves that the flame area modulation was through the primary forcing in this case.

In order to understand the variation of the response characteristics with increase in primary forcing amplitude, the data obtained from phase-averaged FSD for these cases are consolidated in Fig. 4.47(a). The figure shows clearly that at low primary forcing amplitude, the flow was dominated by secondary forcing and with increase in primary forcing amplitude, the heat release response changed from 320 Hz to 160 Hz. The flame response measured using FSD is presented in Fig. 4.47(b). The linear dependence found in Fig. 4.47(b) is in good agreement with the case presented in Fig. 4.42(a). The variation in response of heat release evaluated from FSD as a function of amplitude presented in Fig. 4.47(b) shows a sudden change in the response at $A_1 = 11\%$, which corresponded to variation in dominant frequency of the fluctuations.

4.5 Discussion

In this chapter, chemiluminescence measurements (from OH* and CH*) both measured continuously (using PMT) and by phase-averaged (using ICCD) imaging along with laser based measurements, flame surface density (FSD) based on OH PLIF and reaction rate (RX) imaging based on simultaneously OH and CH_2O PLIF, were used to investigate the heat release modulation and to understand the non-linear response of a turbulent premixed flame to high amplitude inlet velocity fluctuations. The reaction rate (RX) imaging has been proved to correlate well for some hydrocarbon fuels (methane, propane and ethylene) both computationally and experimentally for laminar flame at lean conditions (Fayoux *et al.*, 2005; Najm *et al.*, 1998a,b; Paul & Najm, 1998). However, the technique is yet to be used extensively as a quantitative measure of heat release. During the present study with turbulent fully premixed flames, the reaction rate imaging was found to capture the local heat release variation well in the vortex dominated regions, hence extending previous results from laminar flame-vortex interactions (Najm *et al.*, 1998b; Paul & Najm, 1998). This suggests the potential of the technique in exploring combustion instability in the non-linear regime where strain and curvature may play an important role. It has been found here that such local effects are not very large contributors to the global heat release modulation with the forcing.

The flame surface density (FSD) based on OH PLIF was found to agree well with chemiluminescence in the works by Lee et al. (Lee & Santavicca, 2003; Lee *et al.*, 2000) and also during the present study. Furthermore the FSD measurements agreed reasonably well with RX imaging. Apart from the fact that the FSD evaluation is less expensive compared to RX imaging, the data from the present study prove the ability of the FSD technique to capture the non-linear heat release response of the flame. This implies certain confidence in using FSD in evaluating local mean reaction rate for fully premixed flames. However for the cases with high swirl, the determination of a quantity proportional to true heat release was difficult due to increased wrinkling in the third dimension and the algorithm may also introduce error due to difficulties in identifying the flame front at the side recirculation zone (details of which presented in Chapter 3).

It was observed that the flame response measured using OH* and CH* are in very good agreement (Fig. 4.7). However, care must be taken while measuring CH* (which lies in visible region), due to possible interference from the ambient light. If this happens, it would result in higher mean signal thereby affecting the magnitude of the transfer function greatly. During the present investigation, the OH* and CH* chemiluminescence measurements were found to capture the non-linear flame response well. Furthermore the agreement between the techniques OH* and FSD and the later with RX imaging even in the vortex dominated regime increases the confidence in chemiluminescence emission measurements.

For the transfer function measurement, estimating the global response is more critical than the local variation. The fact that the chemiluminescence technique is cheaper and requires no additional skills for computation or measurements and the ability to monitor fluctuations continuously in time, makes the chemiluminescence measurements a reasonably good choice of instrument. The chemiluminescence can also be used to evaluate heat release from imperfectly premixed flames with some limitations in interpretation, although recently spatially resolved instruments that can also estimate local ϕ have been developed (Hardalupas & Orian, 2004).

The dynamics of the flame to imposed inlet velocity oscillations was captured using OH*, FSD and RX imaging techniques. All these measurements, when using data only from the vortex dominated region, showed a definite increase in phase averaged heat release rate when the vortex appeared. However, the global heat release measurements (i.e. including data from the whole domain) showed a decrease in heat release at the same phase relative to the forcing. The phase-averaged FSD and OH* imaging also showed a decreased heat release in regions above the vortex when the vortex was close to the bluff body. The measurements hence suggest the possibility of flame surface destruction or flame annihilation away from the bluff body, downstream from the vortex. Thus, the balance between the fluctuations in local heat release by vortex roll up and by cusp formation and flame annihilation resulted in the global heat release modulation.

This conjecture was tested with examination of time-series of OH PLIF. Figure 4.48 is a typical time-sequence of four OH PLIF images separated by 1 ms. It shows the flame surface evolution with time when subjected to strong inlet

velocity perturbations. It was observed from these measurements that the vortex induced by velocity fluctuations was convected with a velocity approximately equal to the bulk velocity at the dump plane and the vortex grew in size. The important observation during this measurement is that the vortex brought together the flame elements stabilised on the inner and outer shear layer (at the interface of inner and outer recirculation zone respectively) and this interaction resulted in flame surface destruction (marked with circle labelled "A" in Fig. 4.48). Similar flame annihilation events were observed when different flame elements interacted close to the vortex (marked by square labelled as "B" in Fig. 4.48).

These measurements along with the phase-averaged FSD measurements, suggest that the flame surface modulation plays a major role in heat release magnitude. It seems that the flame burning rate fluctuations along the flame surface, despite being present (e.g. account for the difference in FSD and OH* data in Figs. 4.4 and 4.7 and the difference in FSD and RX data in Fig. 4.6) are of smaller importance than the magnitude of the flame surface density and how this is altered by the vortices. The latter effect depends conceivably on the laminar burning velocity and hence the difference in the point of saturation in Fig. 4.19. The former interaction is mostly due to the strain and flame curvature affecting the local burning rate. Laminar strained premixed flames of ethylene have Le>1 and hence a burning rate reduction is expected (Rutland & Trouve, 1993). It would be interesting to examine mixtures with Le=1, where strain and curvature effects would be less important.

In an effort to explore this point, measurements with a methane flame at $\phi = 0.7$ that give Le$\sim$1 (Mizomoto & Yoshida, 1987) were also taken. This equivalence ratio was selected so that the laminar burning velocity of the flame was the same ($\sim$0.18 m/s) as the ethylene flame studied here ($\phi = 0.55$). Figure 4.49 shows that the methane flame also saturates at approximately the same A value. The $Q'/\langle Q \rangle$ value from OH* in ethylene is higher than that of OH* in methane. The difference of the two curves in Fig. 4.49 is of similar magnitude to the difference between the OH* and FSD in ethylene flames (Fig. 4.7) and both differences should be due to local strain and curvature effects. The measurement in swirl flames with different swirl intensities further proved that the heat release variations were mainly due to the flame area variations. We may conjecture hence

that the flame area modulation is the most important phenomenon affecting the global heat release fluctuations, with localized variations being less important.

4.6 Summary

Detailed experimental investigations were performed to measure the response of lean fully premixed turbulent bluff-body stabilised flames to imposed inlet velocity perturbations. Special attention was given to the amplitude dependence of the transfer function, since the flame response to high amplitudes is relevant to the emergence of limit-cycle combustion-induced oscillations. Three different heat release measurement approaches were followed during the present work, namely OH* and CH* chemiluminescence using photo-multiplier tubes and ICCD, flame surface density (FSD) based on OH PLIF, and local heat release (RX) rate evaluated from simultaneous OH and CH_2O PLIF measurements. The imaging system comprised four Nd:YAG lasers, two dye lasers, and two double-exposure cameras. It was also used to provide a sequence of four OH PLIF images separated by 1 ms, which assisted in showing the time evolution of the flame front during the forcing cycle.

Concerning a comparison of the above techniques used to evaluate the flame transfer function, the following conclusions were reached. First, the global heat release evaluated from OH* and CH* chemiluminescence agreed very well both in magnitude and in phase. Second, the magnitude of the heat release response captured by chemiluminescence measurements and by FSD showed a similar trend with forcing amplitude in all the measurement conditions. Finally, the local heat release evaluated from high resolution reaction rate imaging was higher than that estimated from the FSD measurement by 10-20% in magnitude and the latter had a phase lag of about 40 degrees. These results show that the heat release estimation through measurement of the flame surface density is adequate for flame instability studies, despite the large amplitudes of forcing used here. This implies that the local effects of strain and curvature in reducing the burning velocity probably do not cause large variations in the global heat release rate.

Concerning the detailed flame response with forcing amplitude, it was found that the heat release increased non-linearly after inlet velocity amplitudes of

around 15% for flames without swirl, a value that depended on the forcing frequency and the equivalence ratio. This non-linearity was found to occur when the reacting shear layers rolled-up into vortices and was captured with all heat release measurement techniques. The vortices induced by the inlet velocity fluctuations not only generated flame area when the flame wrapped around them, but also caused cusps and even large-scale flame annihilation events, as observed in time-resolved OH-PLIF images, when parts of the flame stabilised on the inner shear layer close to the recirculation zone collapsed on parts of the flame stabilised on the outer recirculation zone, a phenomenon that was made more prominent with increasing forcing amplitude. A further non-linearity occurred at high amplitudes and at some equivalent ratios, where a significant leakage of energy to higher harmonics was observed, despite the fact that the inlet velocity fluctuation had a correspondingly small content at the harmonic frequency.

The measurements of heat release response of swirl flames further proved the role of flame area modulation. With moderate swirl (produced by 45° swirl vane), the flame response was very similar to the no-swirl flame with saturation occurring from 20% forcing. However, for high swirl (produced by 60° swirl vane), the response was found to have a nearly linear dependence on the amplitude of the forcing. This is attributed to the smaller coherence of the vortex even at the highest forcing amplitudes, as also shown by the flow visualization experiments of Chapter 3 (see Fig. 3.10). The phase variation in all the cases studied were found to depend on the amplitude only when the flame was not acoustically convectively compact.

The measurement concerning the presence of harmonics suggest that the transfer function measurement is unaffected only up to a level of presence of harmonics, above which the transfer function values were greatly affected. We attribute the effect of the secondary frequency to the break up of the coherence of the vortex. The results suggest that the interpretation of the transfer function measured in any system should be done carefully based on the amount of other harmonics present in the flow at the inlet. The reduced flame response by introduction of secondary frequency also suggest the possibility of active control of the instability by carefully chosen external excitation.

The present results suggest that the flame sheet kinematics play the major role in the saturation mechanism of lean completely premixed flame response, hence extending previous experimental and analytical results from laminar to turbulent flames. Heat release fluctuations due to local fluctuations of strain rate and curvature had a smaller effect, while no localised extinction has been observed even at large forcing amplitudes.

4.7 Figures for Chapter 4

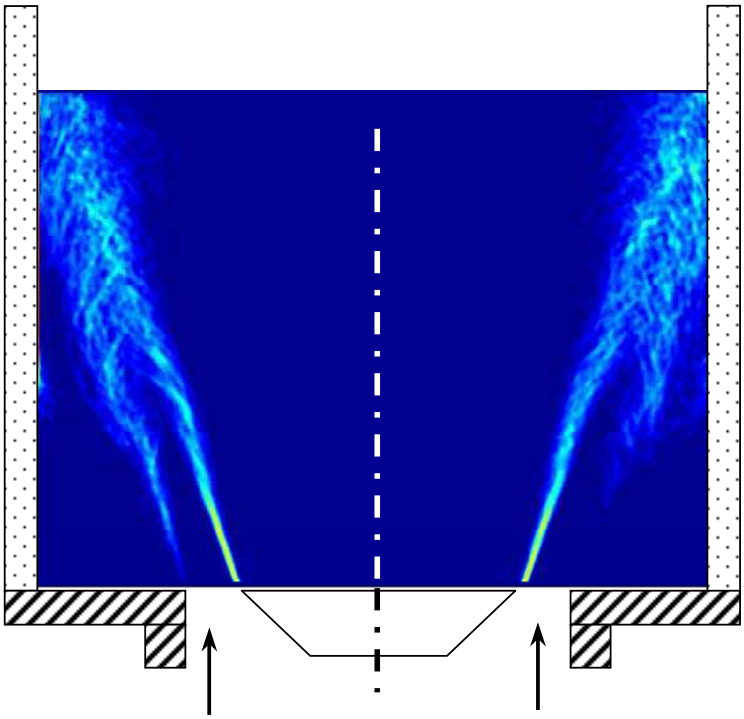

Figure 4.1: Time-averaged FSD image of an unforced flame. Conditions are: ϕ = 0.55, $\langle U \rangle$ of 9.9 m/s. (The field of view is 70 mm x 55 mm, lower side of image is 0.5 mm above the bluff body.)

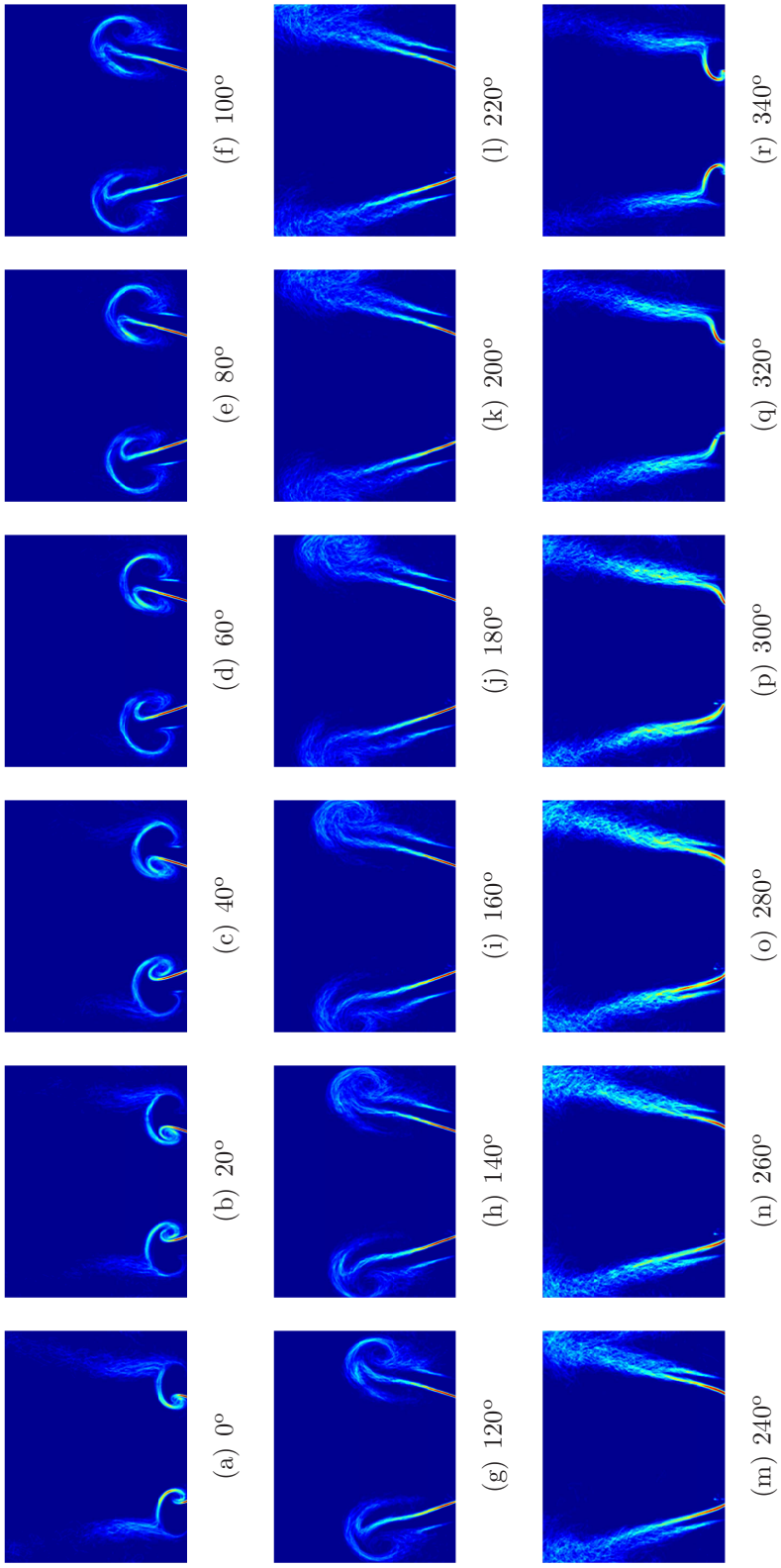

Figure 4.2: Phase-averaged FSD image sequence under strong acoustic forcing: $\langle U \rangle = 9.9$ m/s, $f = 160$ Hz, $A = 0.64$, $\phi = 0.55$.

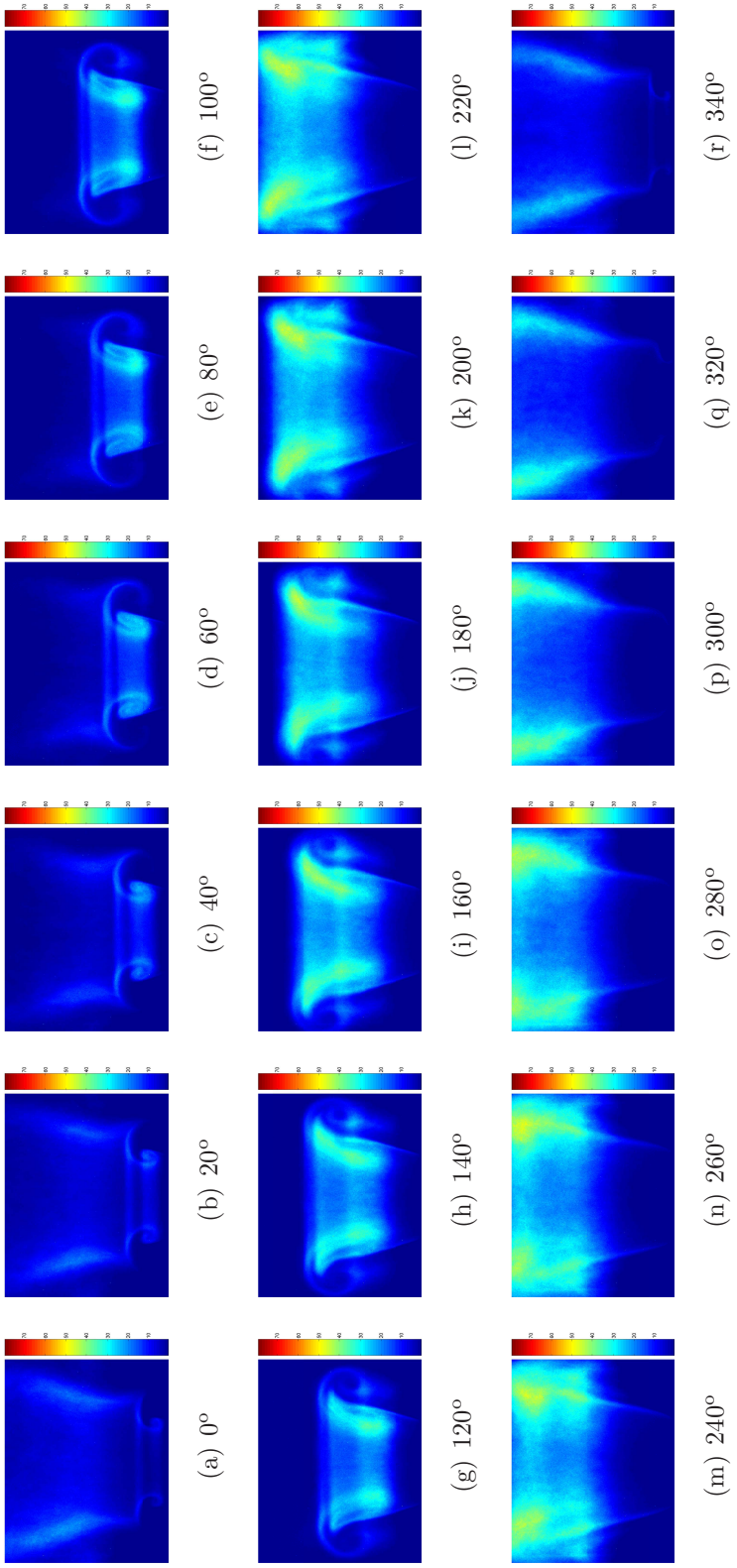

Figure 4.3: Phase-averaged OH chemiluminescence image sequence of flame forced at $f = 160$ Hz, imaged simultaneously with OH PLIF for the case presented in Fig 4.2: $\langle U \rangle = 9.9$ m/s, $A = 0.65$, $\phi = 0.55$.

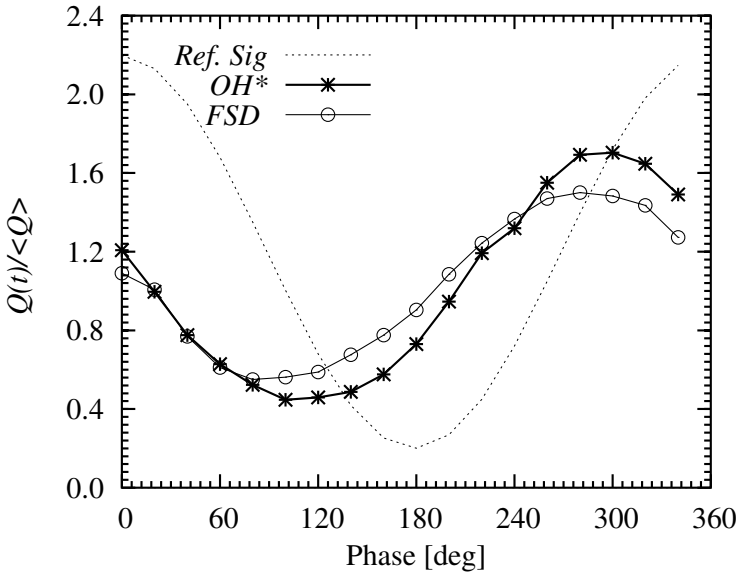

Figure 4.4: Comparison of the global heat release fluctuations evaluated from phase-averaged FSD and from OH* chemiluminescence images (both imaged simultaneously, with estimated resolution of 50μm): $\langle U \rangle$ = 9.9 m/s, ϕ = 0.55, f = 160 Hz and A = 0.64.

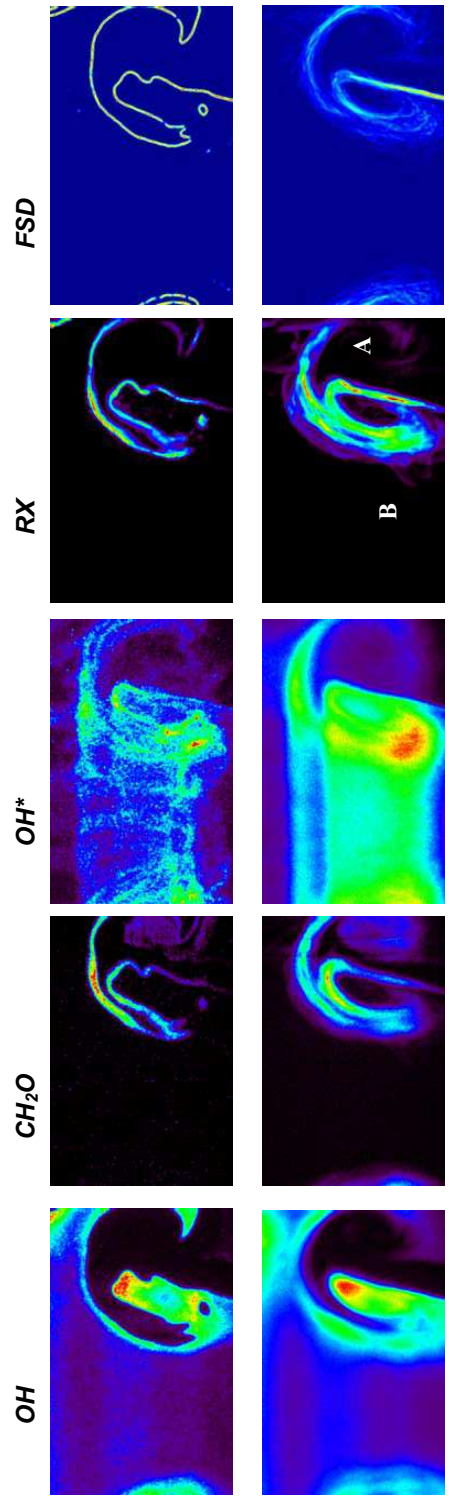

Figure 4.5: Simultaneous instantaneous (a) and phase averaged (b) images of OH, CH_2O, the heat release rate (RX) and flame contour at 40 degrees phase angle with reference to the forcing signal: $\langle U \rangle = 9.9$ m/s, $\phi = 0.55$, $f = 160$ Hz and $A = 0.64$.

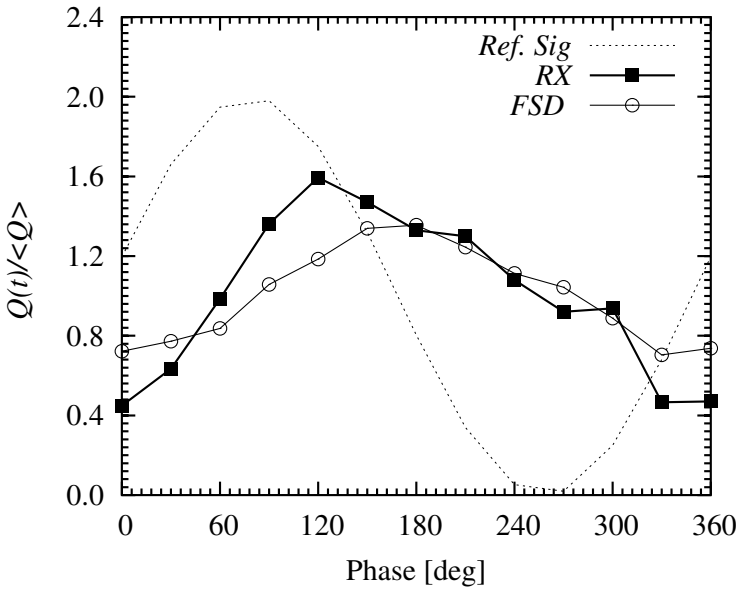

Figure 4.6: Comparison of the heat release fluctuations evaluated from phase-averaged RX and FSD images: $\langle U \rangle = 9.9$ m/s, $\phi = 0.55$, $f = 160$ Hz and $A = 0.64$.

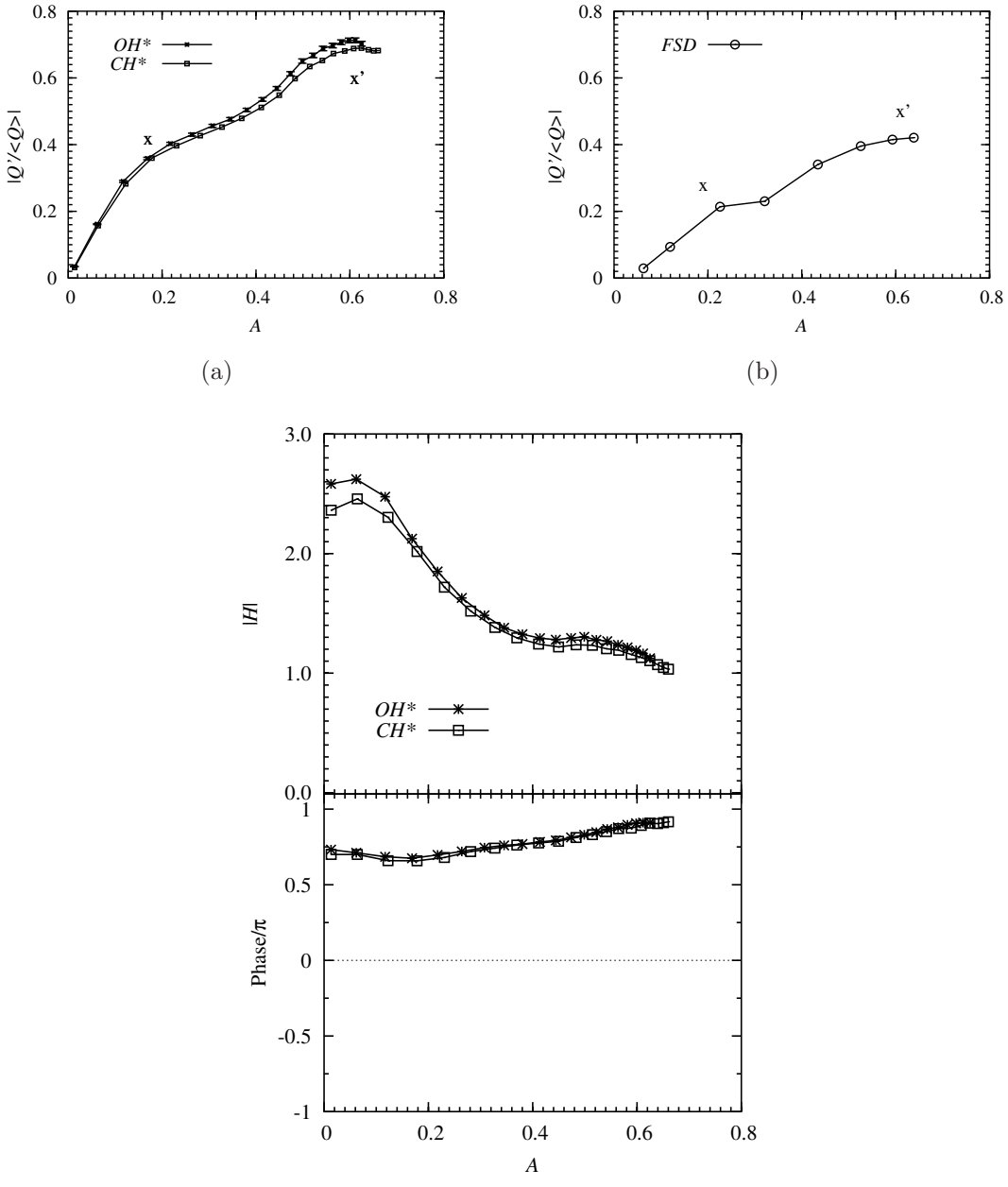

Figure 4.7: The dependence of normalised global heat release fluctuation upon the forcing velocity amplitude A for a forcing frequency $f = 160$ Hz, measured using OH* and CH* chemiluminescence (a) and evaluated using FSD (b). (c) The magnitude of the transfer function [Eq. 1.3] and its phase evaluated from the data of (a). (x and x' denote the points of saturation, discussed in detail in the text.)

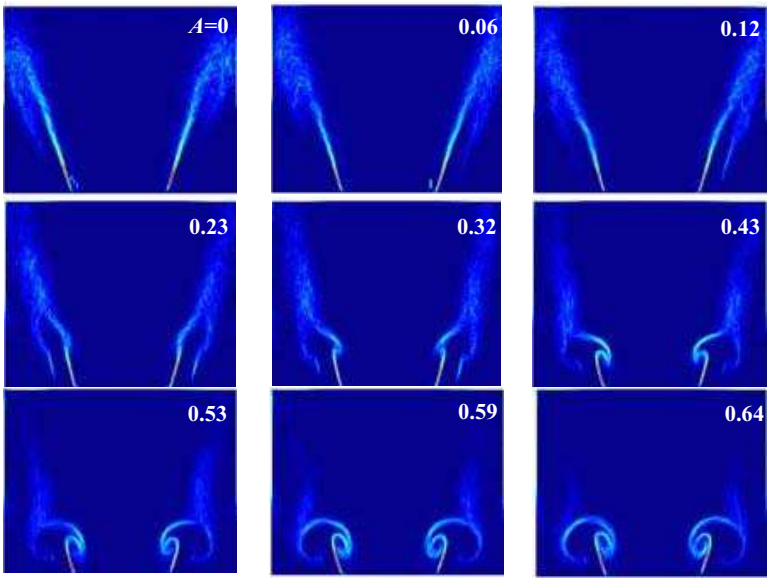

Figure 4.8: Phase-averaged FSD images at 120 degrees relative to the reference signal for different values of A. Conditions are: $\langle U \rangle$ = 9.9 m/s, ϕ = 0.55 and f = 160 Hz.

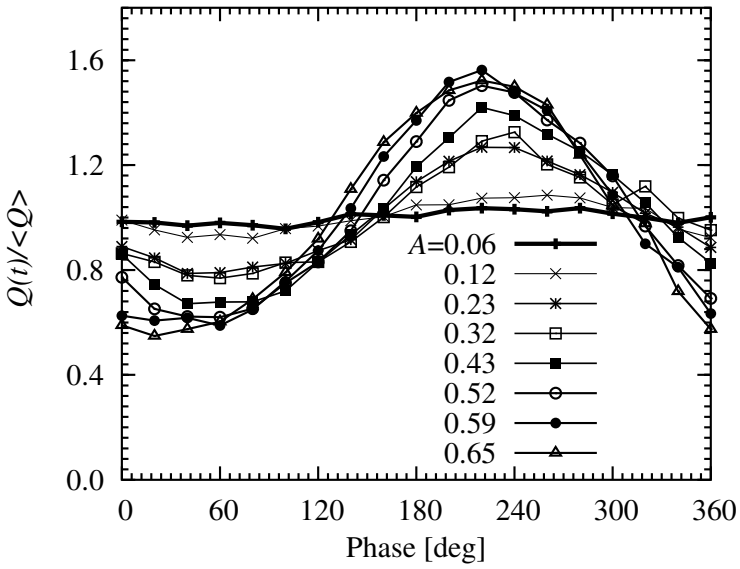

Figure 4.9: Cyclic variation of the heat release evaluated from phase-averaged FSD images for different forcing amplitudes, A: $\langle U \rangle = 9.9$ m/s, $f = 160$ Hz, $\phi = 0.55$.

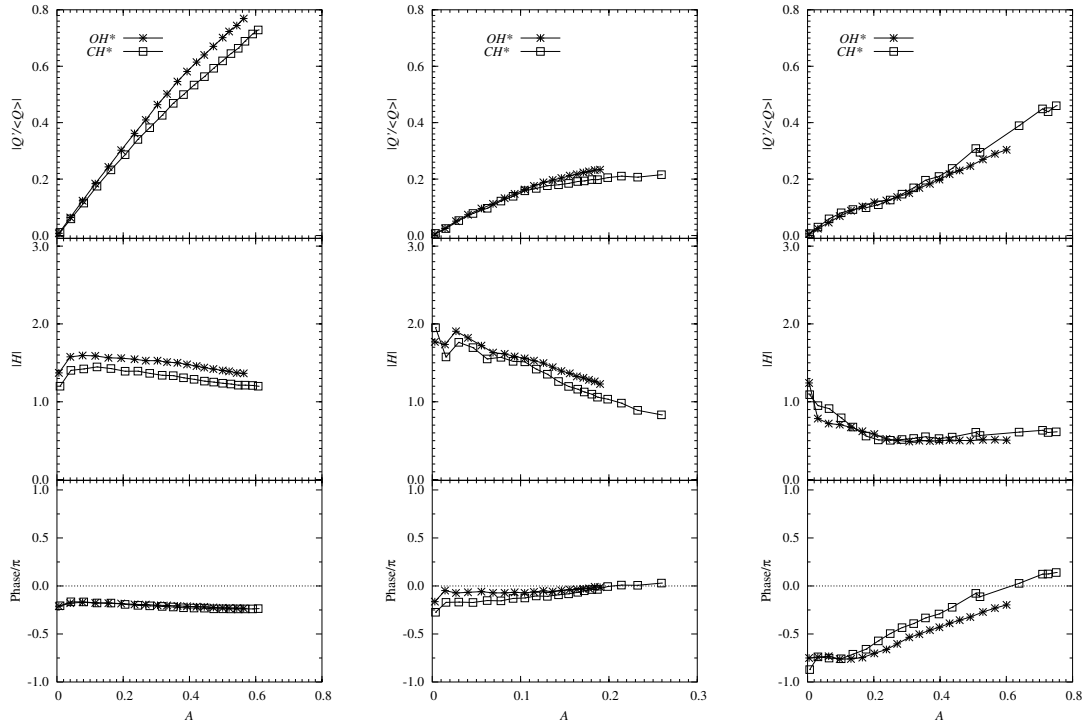

(a) (b) (c)

Figure 4.10: The dependence of normalised global heat release fluctuation upon the forcing velocity amplitude A, measured using OH* and CH* chemiluminescence and their corresponding transfer function and the phase relation for frequencies (a) 40 Hz (b) 240 Hz and (c) 310 Hz respectively. For all, $\langle U \rangle = 9.9$ m/s, $\phi = 0.55$.

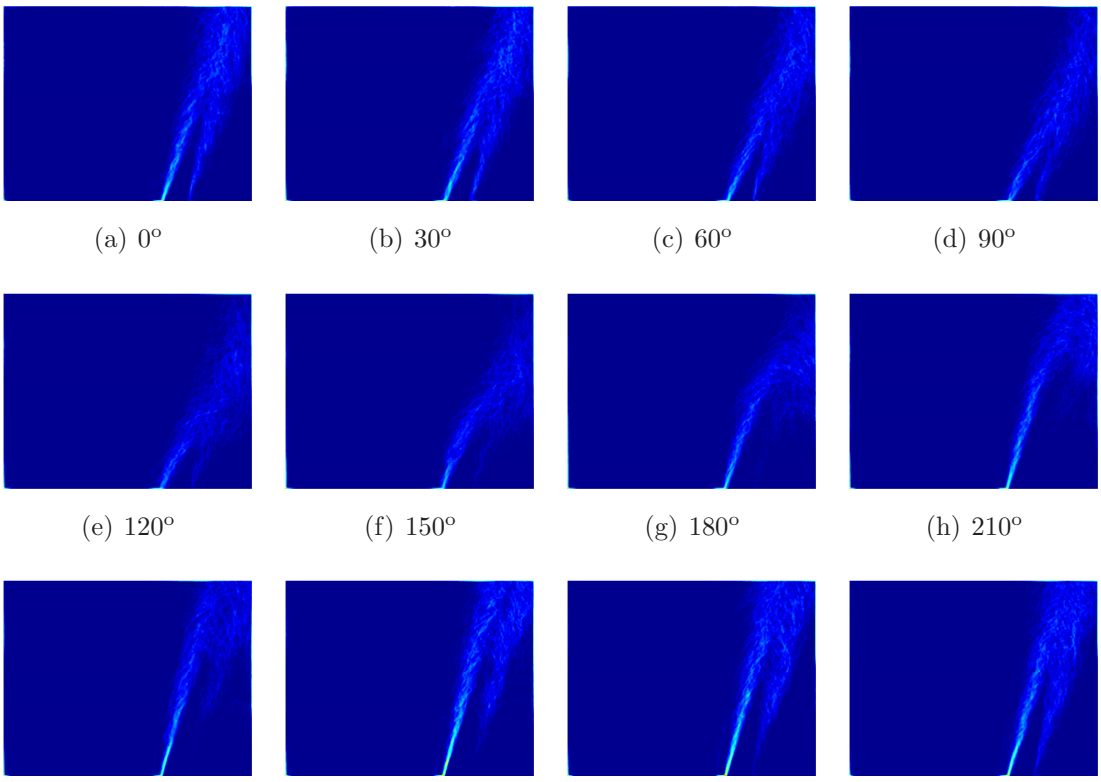

(a) 0° (b) 30° (c) 60° (d) 90°

(e) 120° (f) 150° (g) 180° (h) 210°

(i) 240° (j) 270° (k) 300° (l) 330°

Figure 4.11: Phase-averaged FSD image sequence of flame forced at $f = 40$ Hz: $\langle U \rangle = 9.9$ m/s, $A = 0.62$, $\phi = 0.55$.

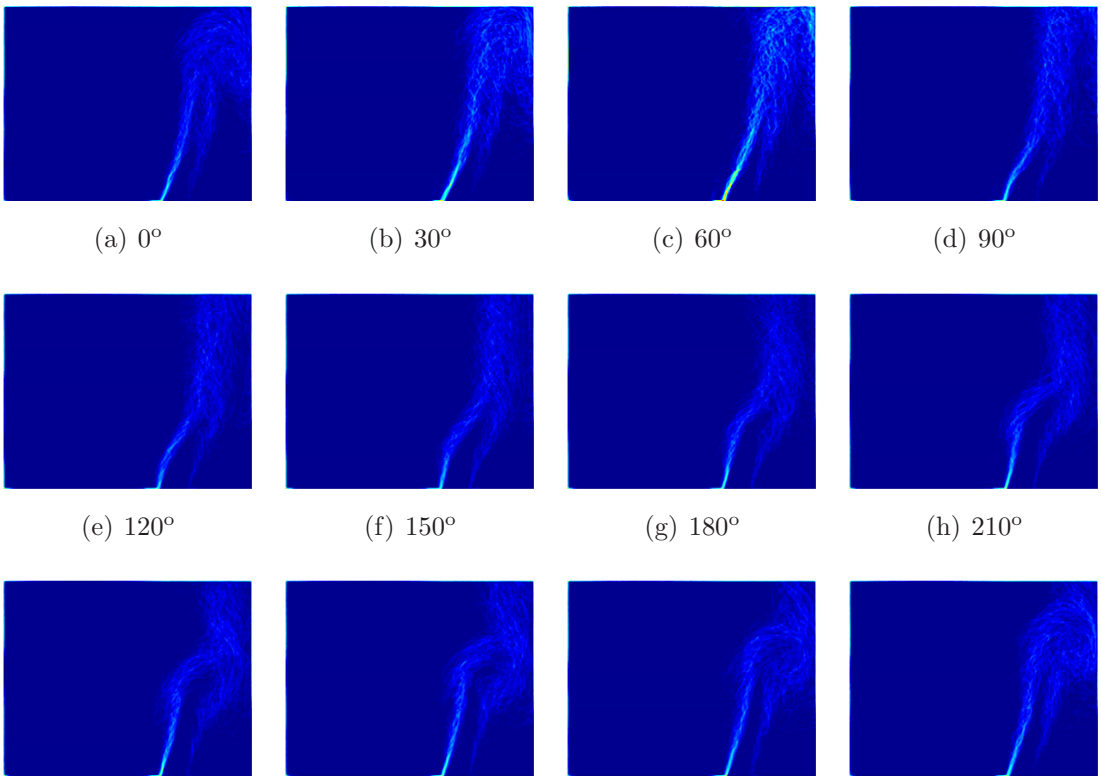

(a) 0° (b) 30° (c) 60° (d) 90°

(e) 120° (f) 150° (g) 180° (h) 210°

(i) 240° (j) 270° (k) 300° (l) 330°

Figure 4.12: Phase-averaged FSD image sequence of flame forced at $f = 240$ Hz: $\langle U \rangle = 9.9$ m/s, $A = 0.25$, $\phi = 0.55$.

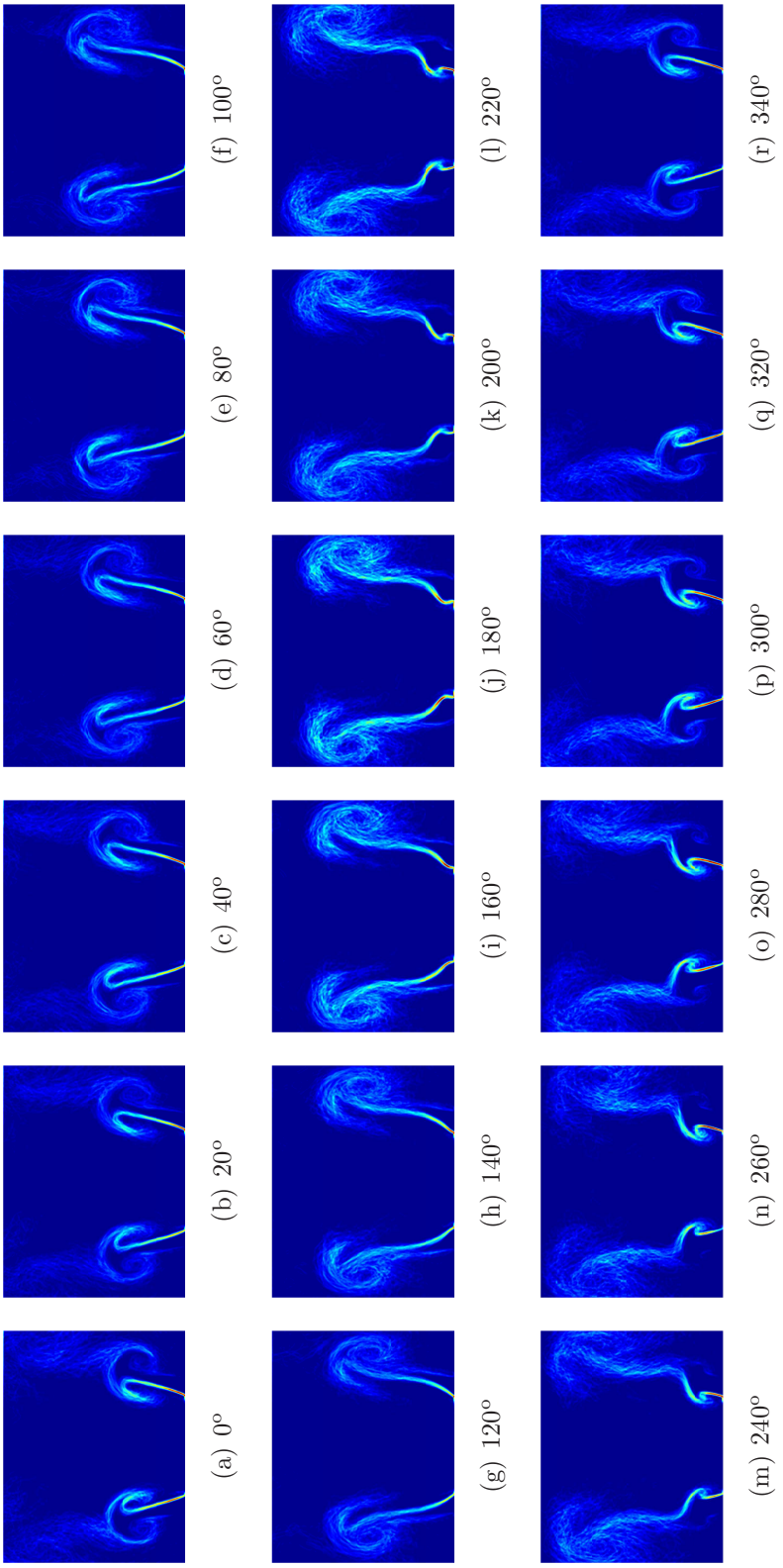

Figure 4.13: Phase-averaged FSD image sequence of flame forced at $f = 310$ Hz: $\langle U \rangle = 9.9$ m/s, $A = 0.62$, $\phi = 0.55$.

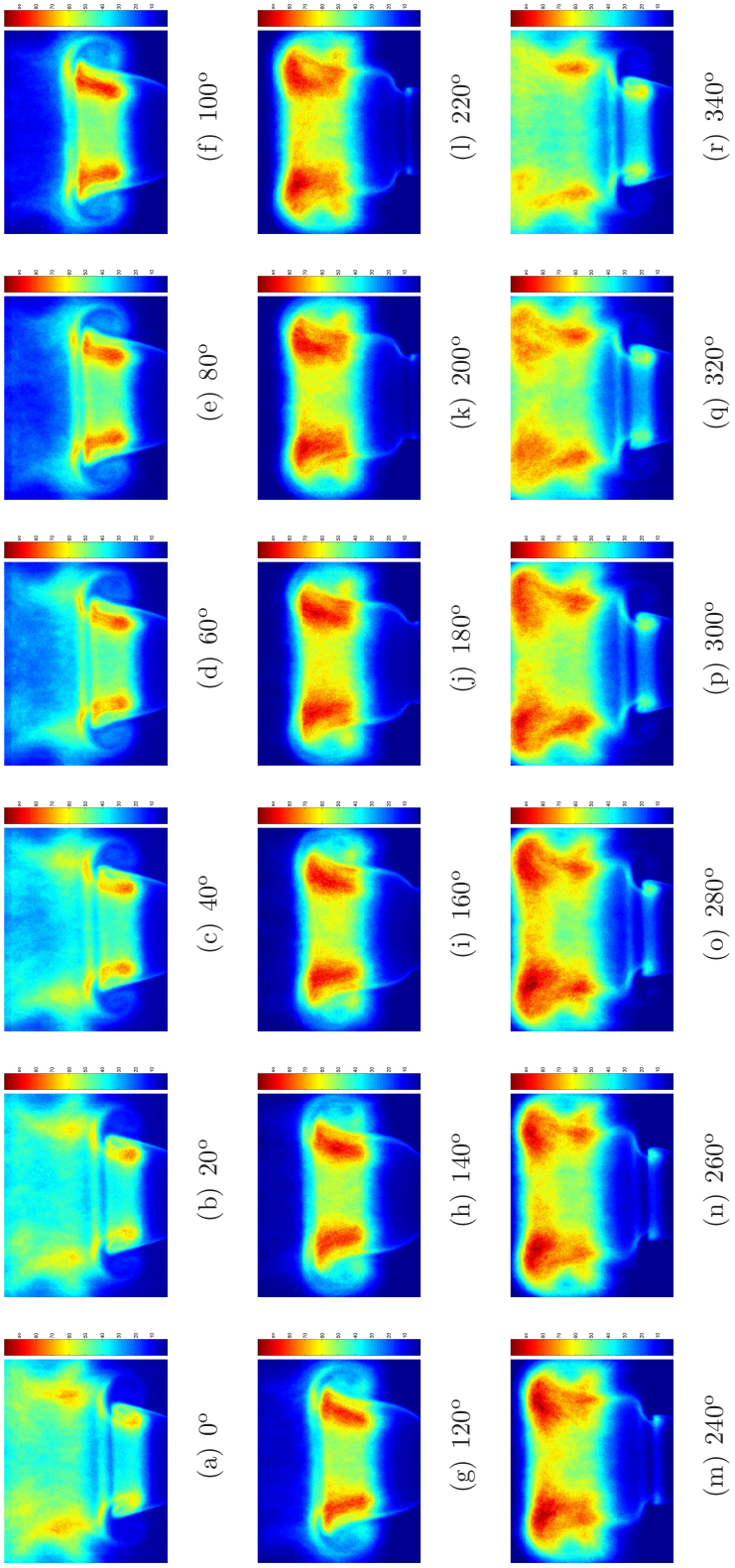

Figure 4.14: Phase-averaged OH* chemiluminescence image sequence of flame forced at $f = 310$ Hz, imaged simultaneously with OH PLIF for the case presented in Fig 4.13: $\langle U \rangle = 9.9$ m/s, $A = 0.62$, $\phi = 0.55$.

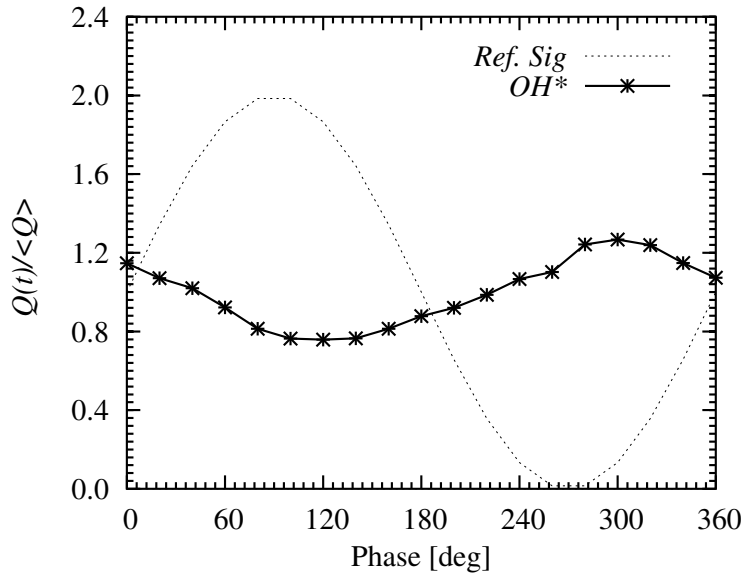

Figure 4.15: The global heat release evaluated from phase-averaged OH* chemiluminescence images presented in Figs. 4.14: $\langle U \rangle = 9.9$ m/s, $\phi = 0.55$, $f = 310$ Hz and $A = 0.62$.

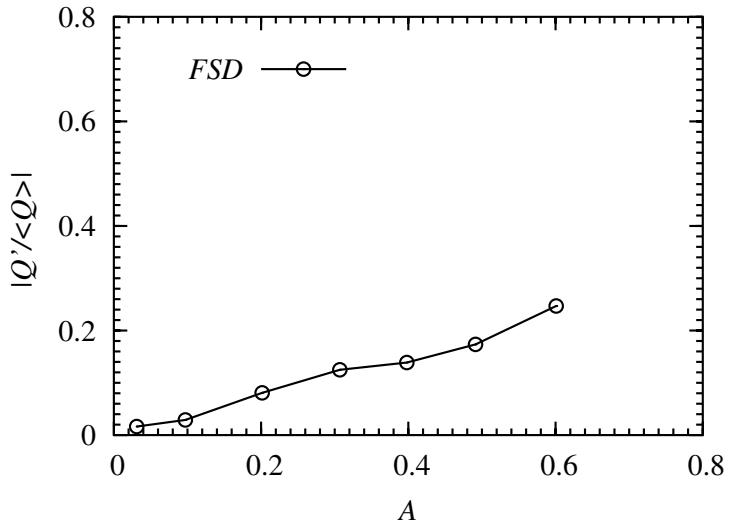

(a)

Figure 4.16: The dependence of normalized global heat release fluctuation upon the forcing velocity amplitude A for a forcing frequency $f = 310$ Hz, evaluated using FSD for the case presented in Fig. 4.10.

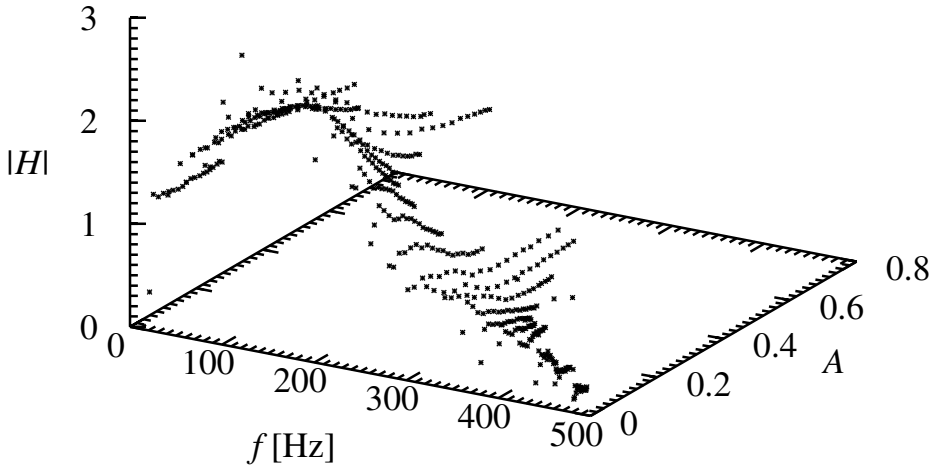

(a)

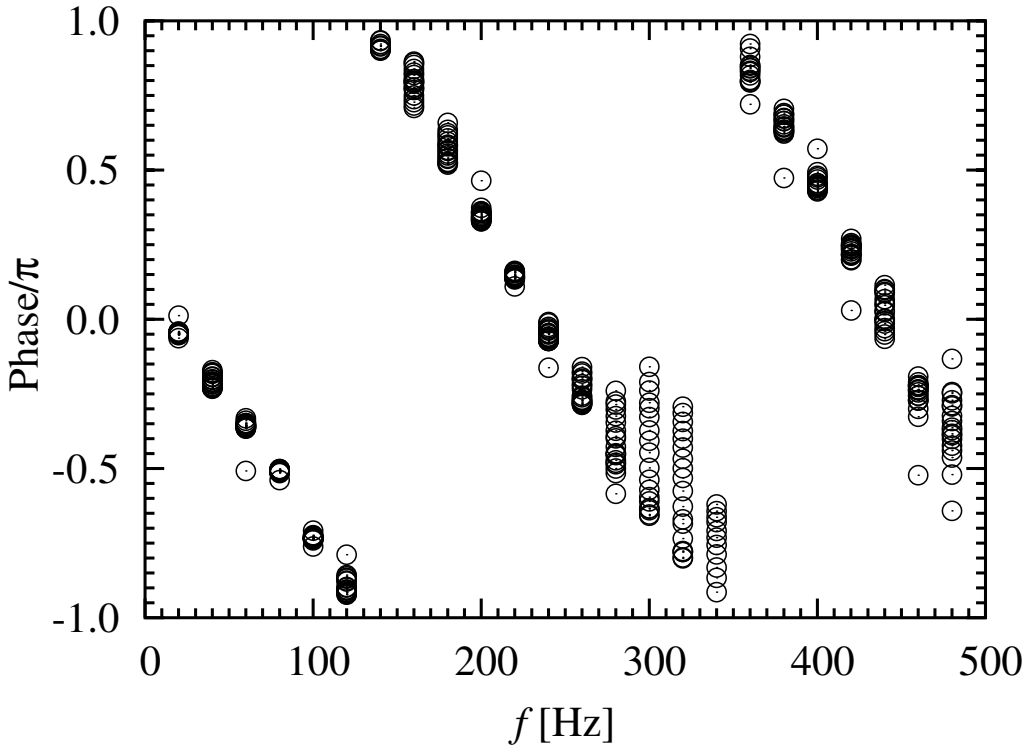

(b)

Figure 4.17: (a) Flame transfer function as a function of frequency and amplitude and (b) the relative phase relation. $\langle U \rangle \stackrel{123}{=} 9.9$ m/s, $\phi = 0.55$.

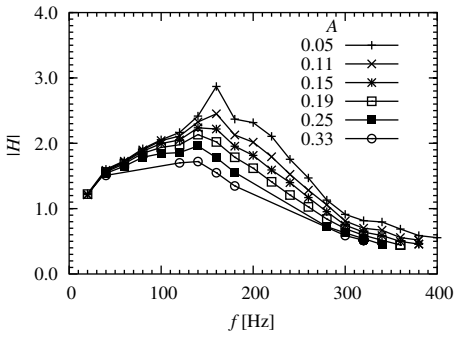

Figure 4.18: Transfer function evaluated from the data of Fig. 4.17 using binomial curve-fit as function of frequency for the indicated A.

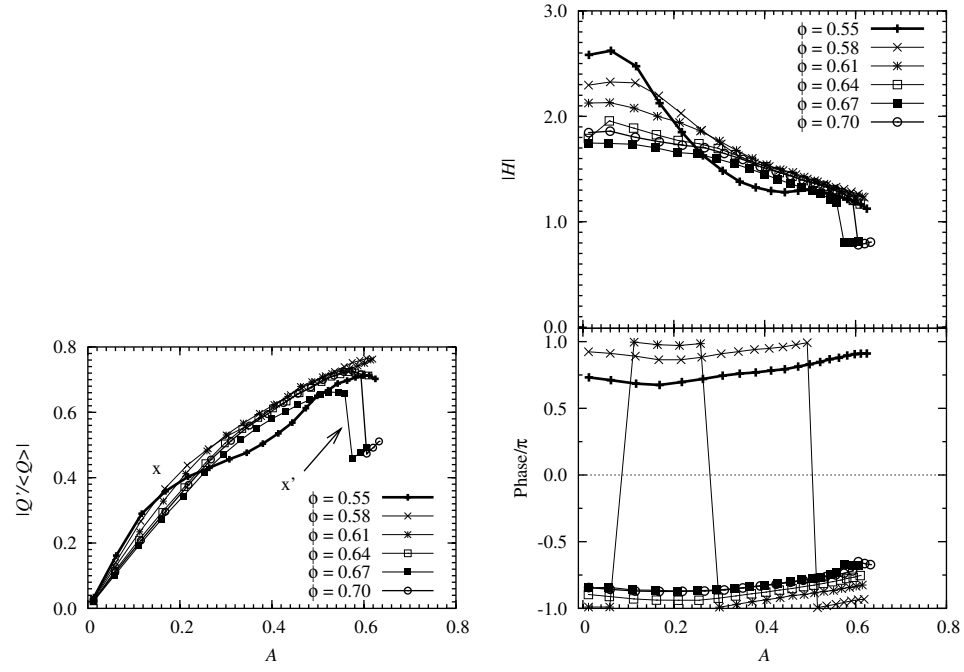

(a) (b)

Figure 4.19: (a) The normalised global heat release fluctuation measured as a function of A for various equivalence ratios, using OH* chemiluminescence. (b) The corresponding transfer function and the phase: $\langle U \rangle = 9.9$ m/s, $\phi = 0.55$ (x and x' are points of saturation, see text).

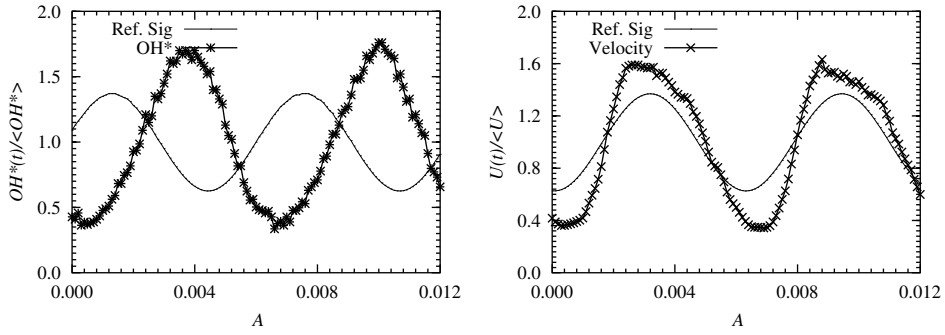

(a)

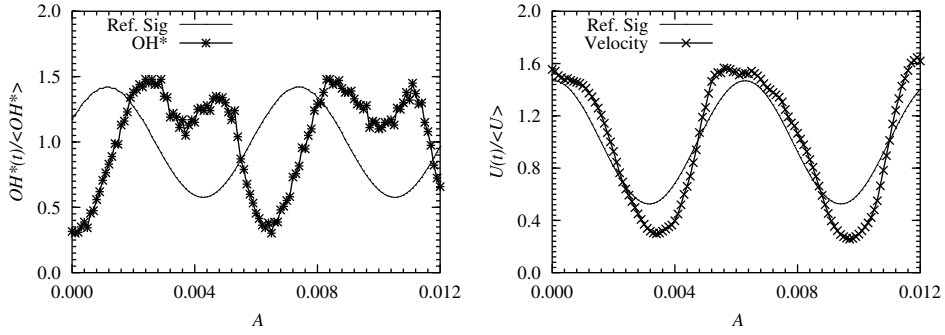

(b)

Figure 4.20: Time series of OH* chemiluminescence and the corresponding cold flow inlet velocity measurements (a) before and (b) after saturation noted as x' in Fig. 4.19 with A values 0.57 and 0.64 respectively. $\langle U \rangle = 9.9$ m/s, $\phi = 0.67$, $f = 160$ Hz.

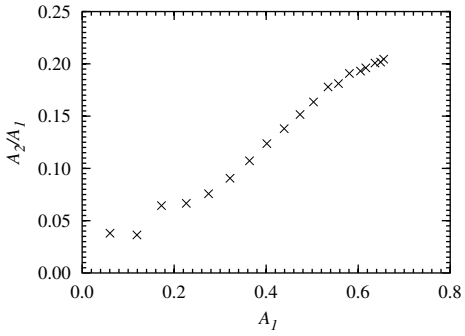

Figure 4.21: Variation of ratio of amplitude of inlet velocity fluctuation at first harmonic of the forcing frequency (320 Hz) A_2, to that at the forcing frequency (160 Hz), A_1 upon amplitude A_1. $\langle U \rangle = 9.9$ m/s.

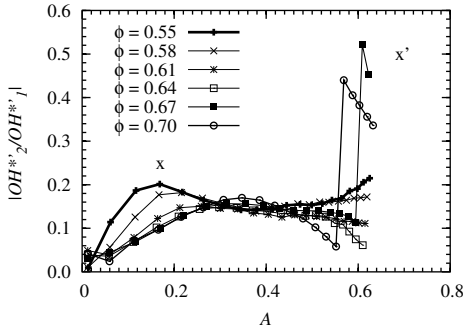

Figure 4.22: Variation of ratio of amplitude of heat release fluctuation at first harmonic of the forcing frequency (320 Hz) to that at the forcing frequency (160 Hz) upon amplitude A_1 over different equivalence ratio: $\langle U \rangle$ = 9.9 m/s (x and x' are points of saturation, marked in Fig. 4.20).

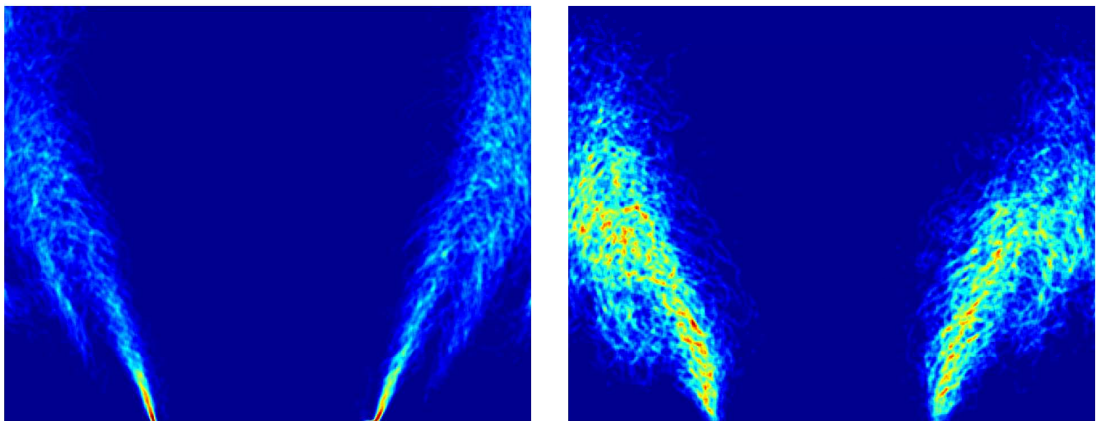

(a) (b)

Figure 4.23: Time-averaged FSD of flames with two different swirl conditions (a) moderate swirl, S1 and (b) high swirl, S2. $\langle U \rangle = 9.9$ m/s, $\phi = 0.52$.

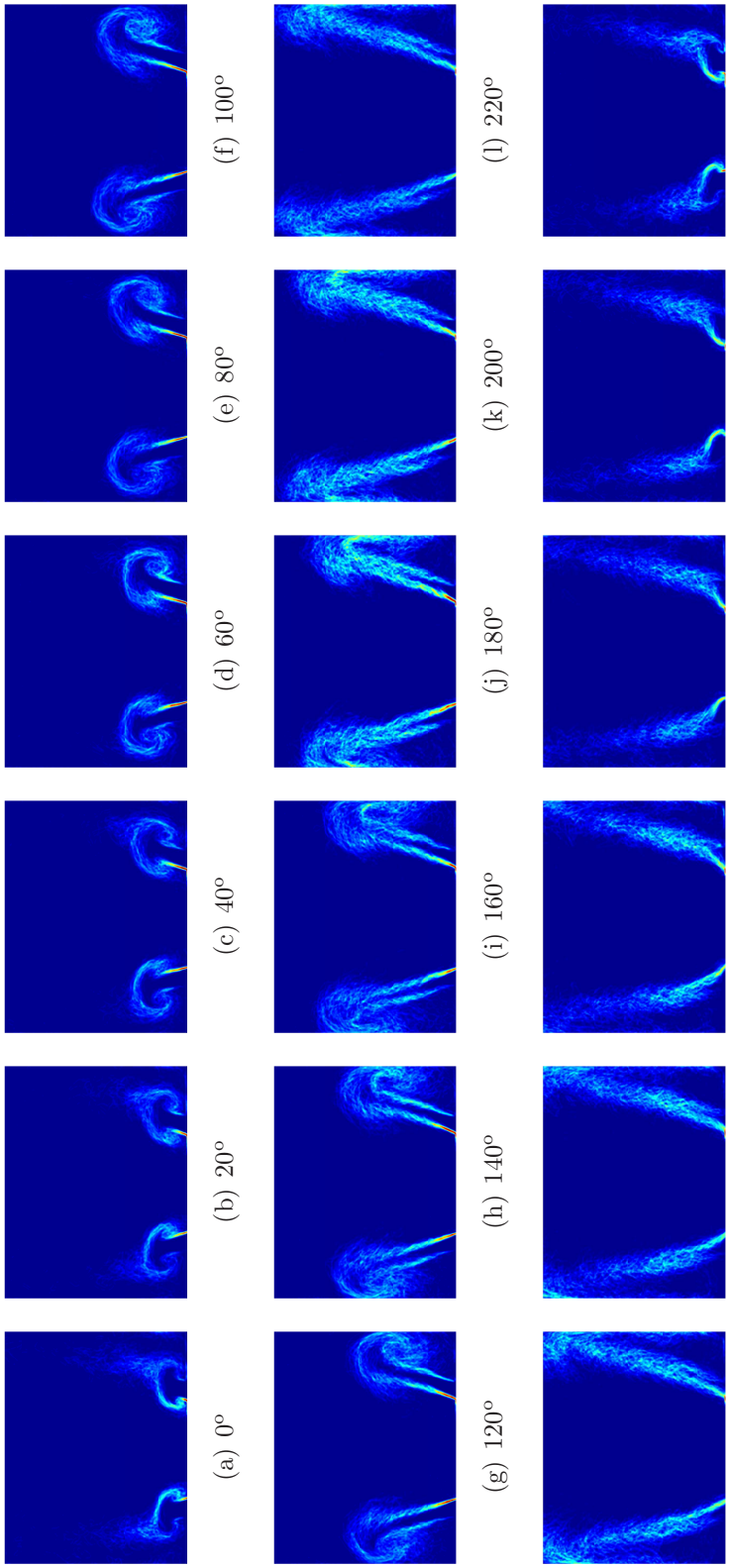

Figure 4.24: Phase-averaged FSD image sequence of swirl flame S1 forced at $f = 160$ Hz: $\langle U \rangle = 9.9$ m/s, $A = 0.58$, $\phi = 0.52$.

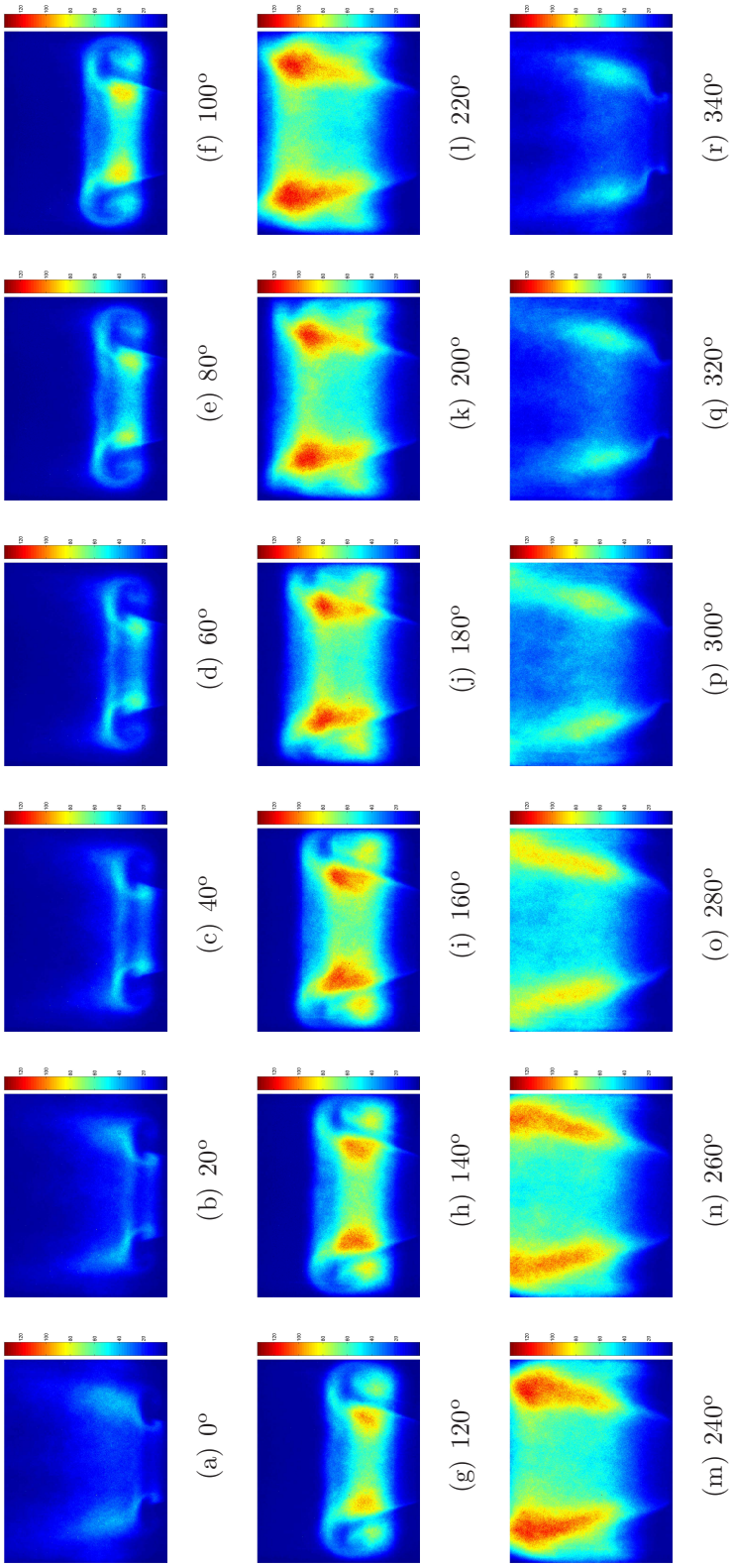

Figure 4.25: Phase-averaged OH* image sequence of swirl flame S1 forced at $f = 160$ Hz imaged along with data presented in Fig. 4.24: $\langle U \rangle = 9.9$ m/s, $A = 0.58$, $\phi = 0.52$.

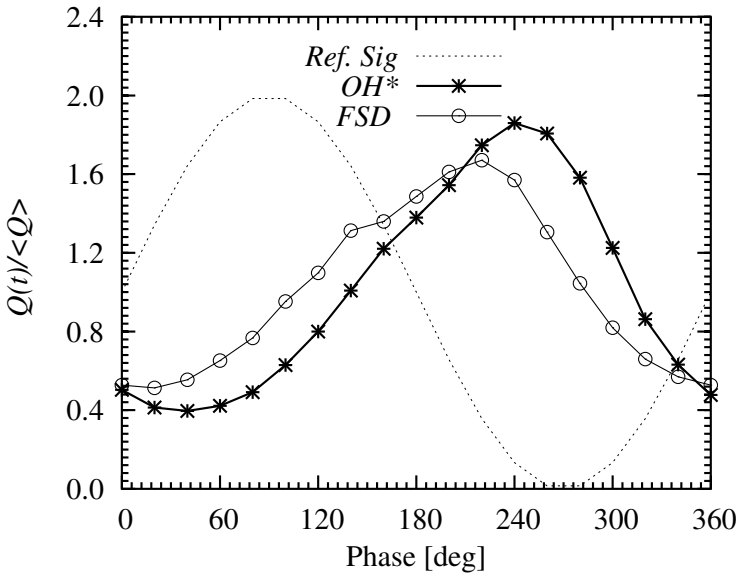

Figure 4.26: Comparison of the global heat release fluctuations evaluated from phase-averaged FSD and from OH* chemiluminescence images presented in Figs. 4.24 and 4.25: $\langle U \rangle = 9.9$ m/s, $\phi = 0.52$, $f = 160$ Hz and $A = 0.58$.

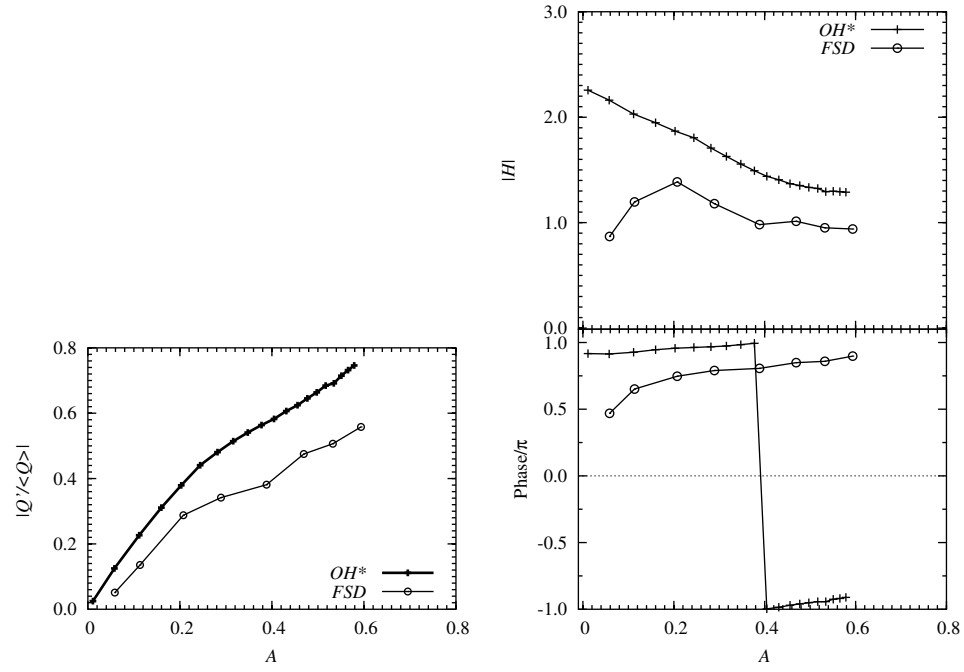

(a) (b)

Figure 4.27: (a) The normalized global heat release fluctuation of flame with swirl S1, measured as a function of A using OH* chemiluminescence and FSD. (b) The corresponding transfer function and the phase: $f = 160$ Hz, $\langle U \rangle = 9.9$ m/s, $\phi = 0.52$.

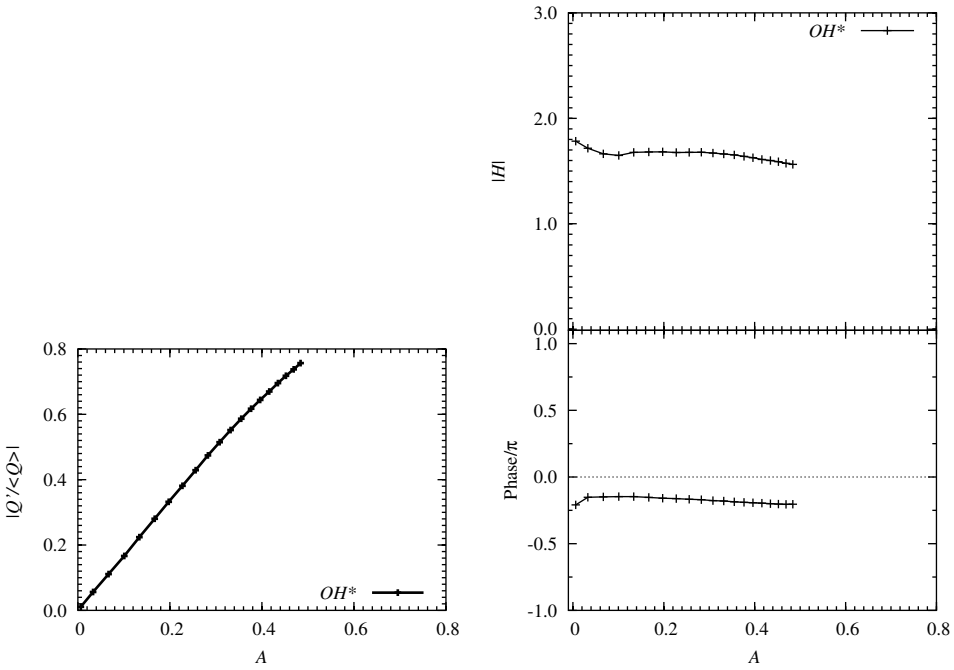

(a) (b)

Figure 4.28: (a) The normalized global heat release fluctuation of flame with swirl S1, measured as a function of A using OH* chemiluminescence. (b) The corresponding transfer function and the phase: $f = 40$ Hz, $\langle U \rangle = 9.9$ m/s, $\phi = 0.52$.

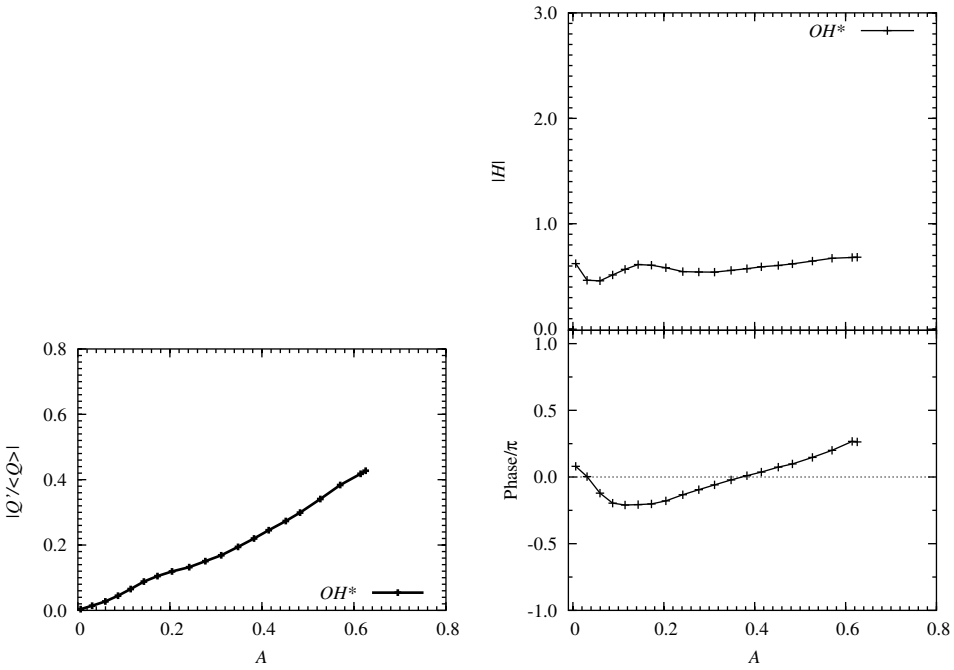

(a) (b)

Figure 4.29: (a) The normalized global heat release fluctuation of flame with swirl S1, measured as a function of A using OH* chemiluminescence. (b) The corresponding transfer function and the phase: $f = 330$ Hz, $\langle U \rangle = 9.9$ m/s, $\phi = 0.52$.

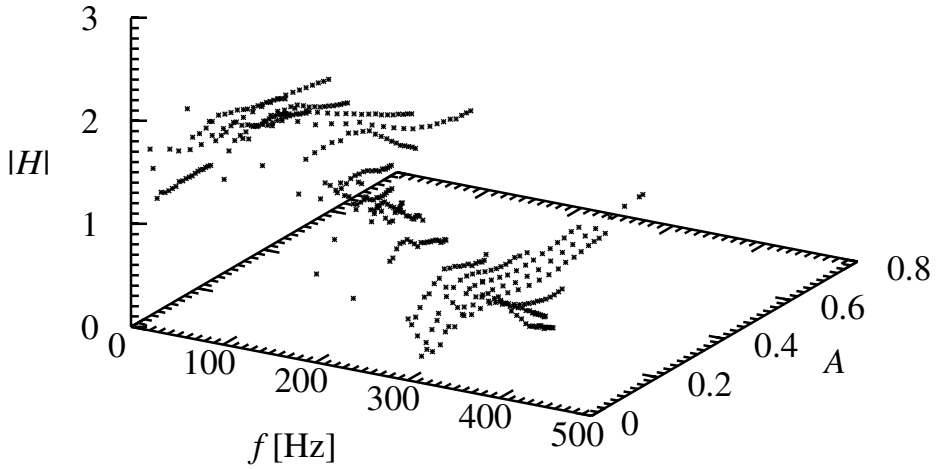

(a)

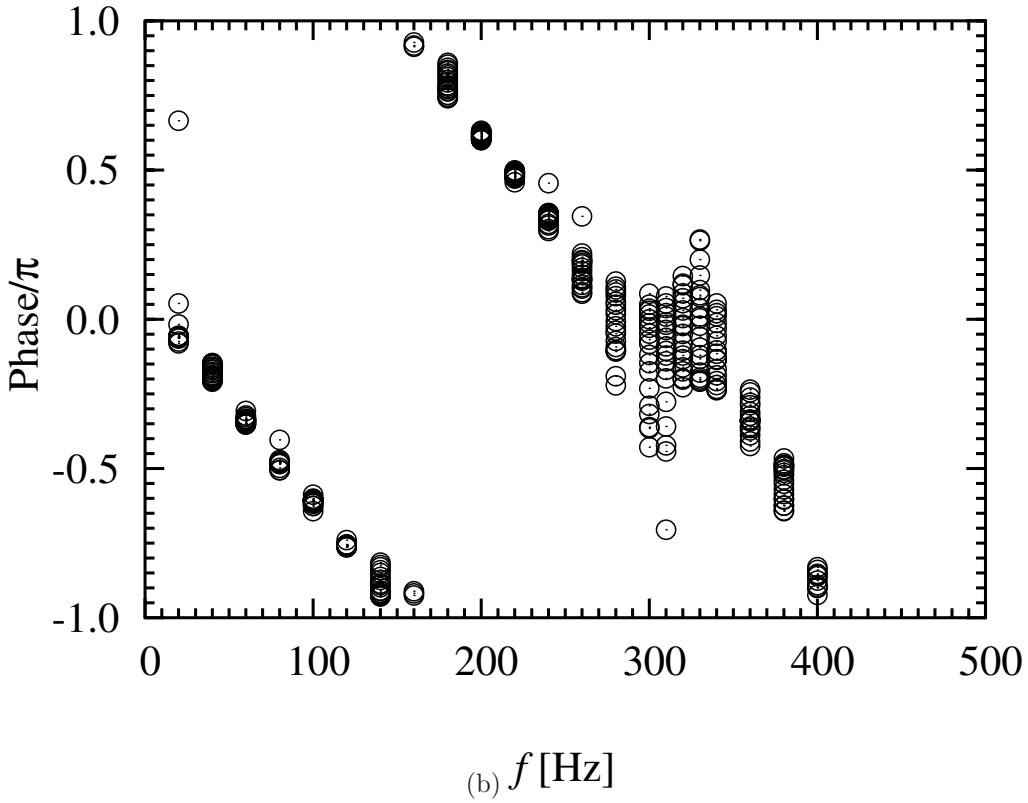

(b)

Figure 4.30: (a) Flame transfer function as a function of frequency and amplitude and (b) the relative phase relation. For swirl S1, $\langle U \rangle = 9.9$ m/s, $\phi = 0.52$.

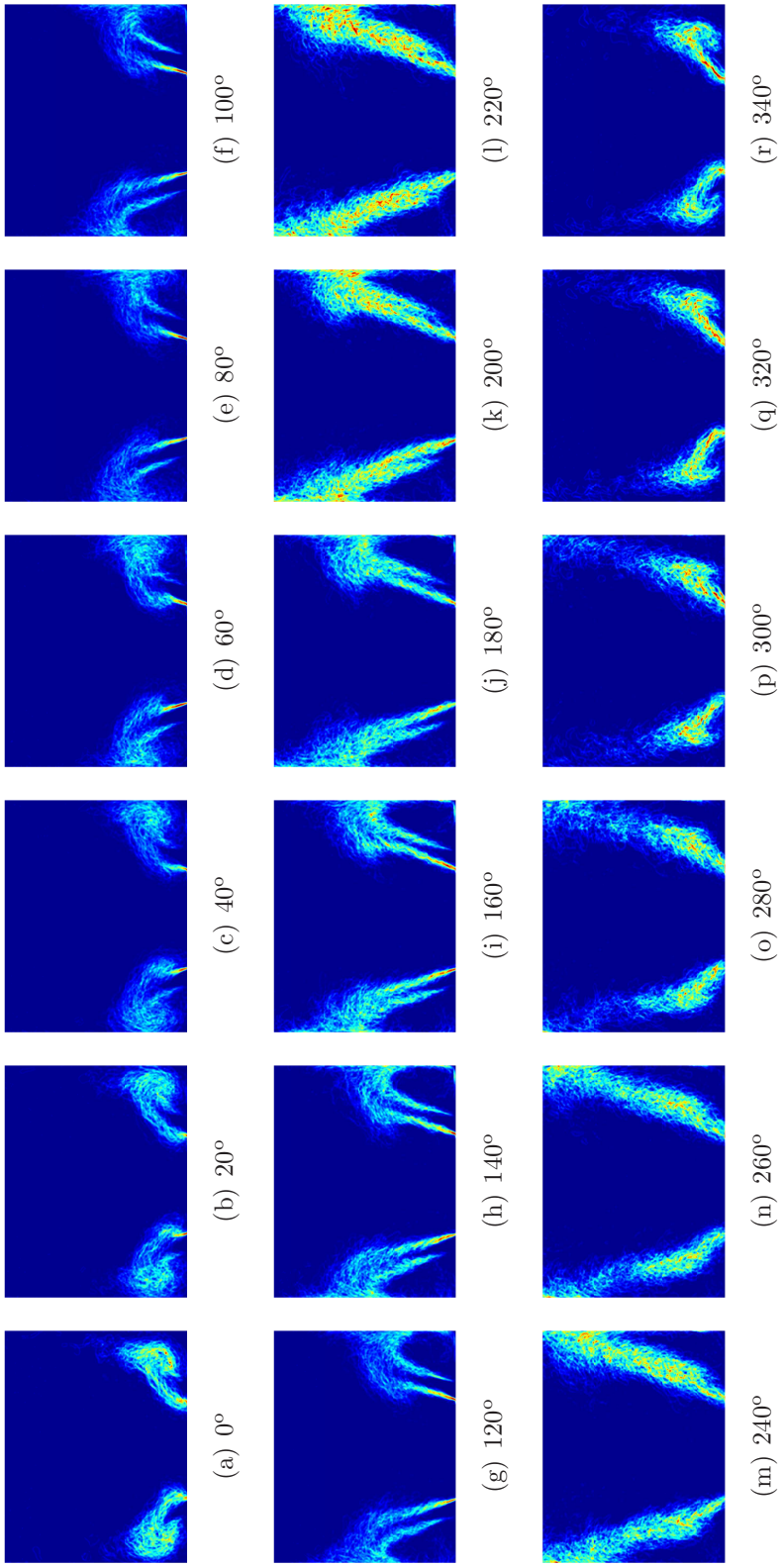

Figure 4.31: Phase-averaged FSD image sequence of swirl flame S2 forced at $f = 160$ Hz: $\langle U \rangle = 9.9$ m/s, $A = 0.55$, $\phi = 0.52$.

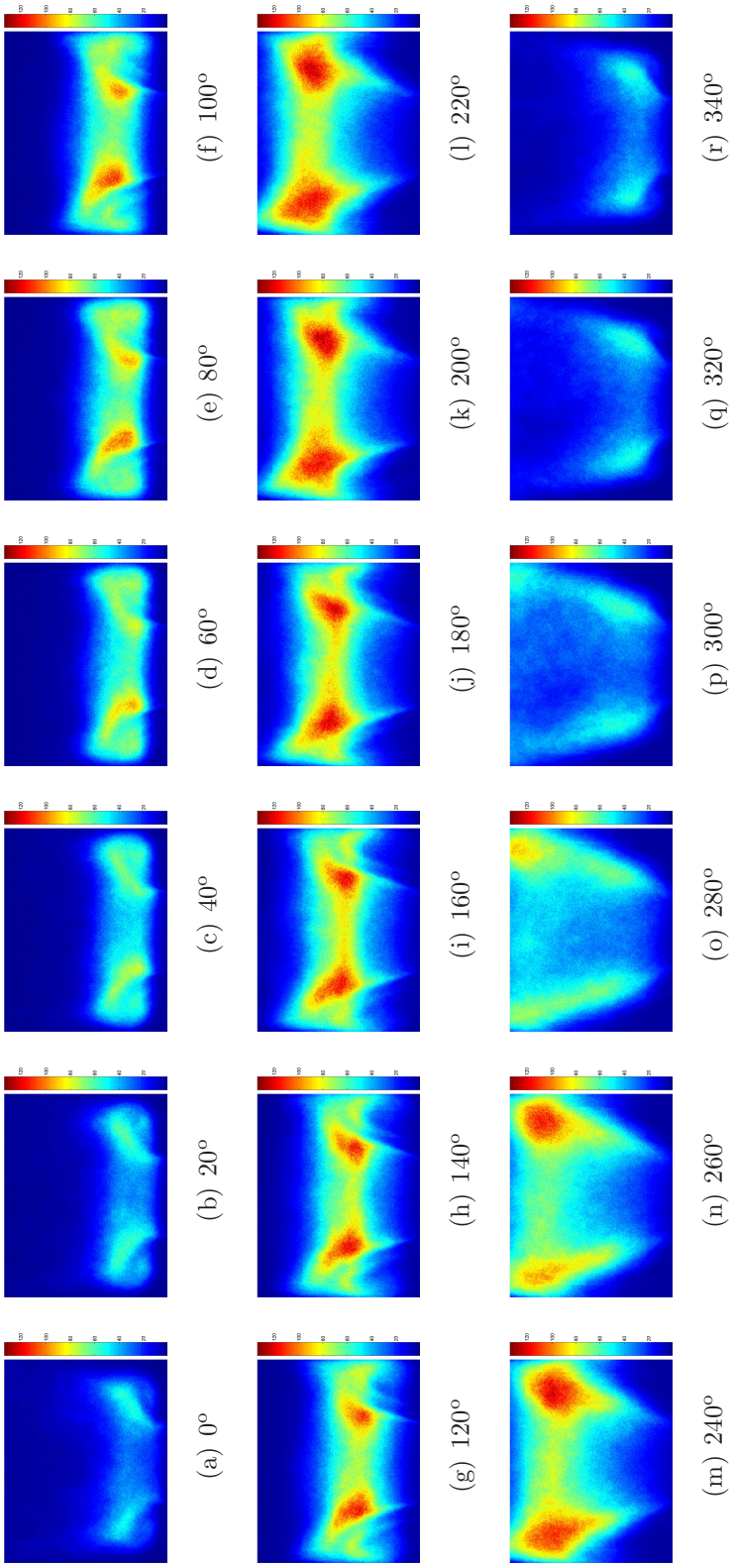

Figure 4.32: Phase-averaged OH* image sequence of swirl flame S2 forced at $f = 160$ Hz for the case presented in Fig. 4.31: $\langle U \rangle = 9.9$ m/s, $A = 0.55$, $\phi = 0.52$.

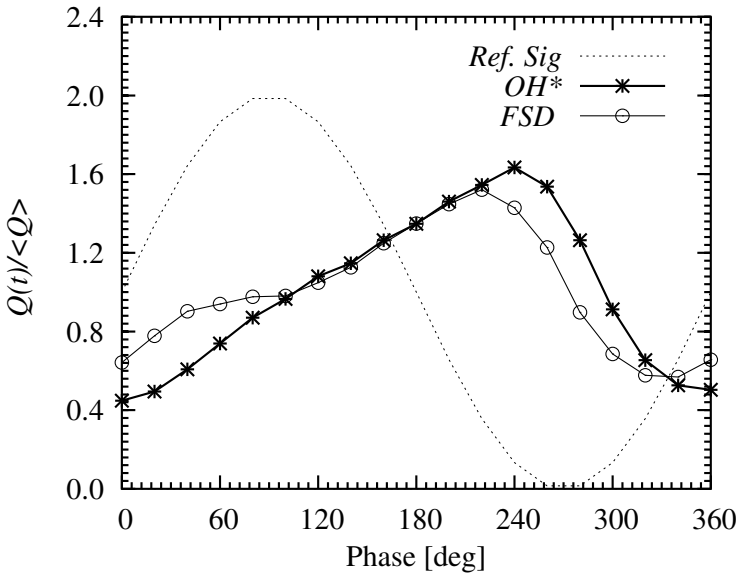

Figure 4.33: Comparison of the global heat release fluctuations evaluated from phase-averaged FSD and from OH* chemiluminescence images presented in Figs. 4.31 and 4.32: $\langle U \rangle = 9.9$ m/s, $\phi = 0.52$, $f = 160$ Hz and $A = 0.55$.

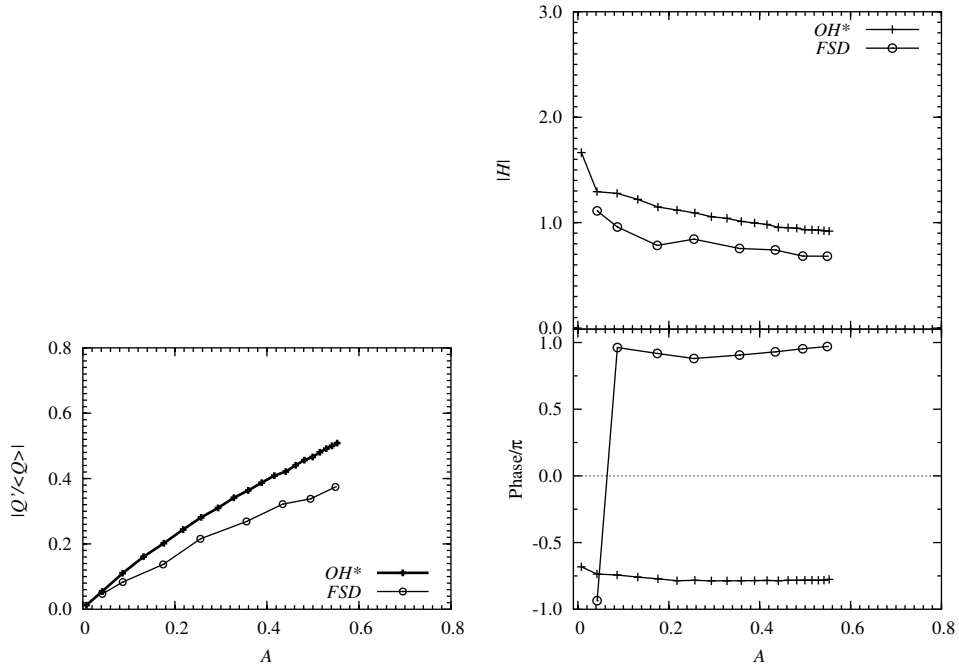

(a) (b)

Figure 4.34: (a) The normalized global heat release fluctuation of flame with swirl S2, measured as a function of A using OH* chemiluminescence and FSD. (b) The corresponding transfer function and the phase: $f = 160$ Hz, $\langle U \rangle = 9.9$ m/s, $\phi = 0.52$.

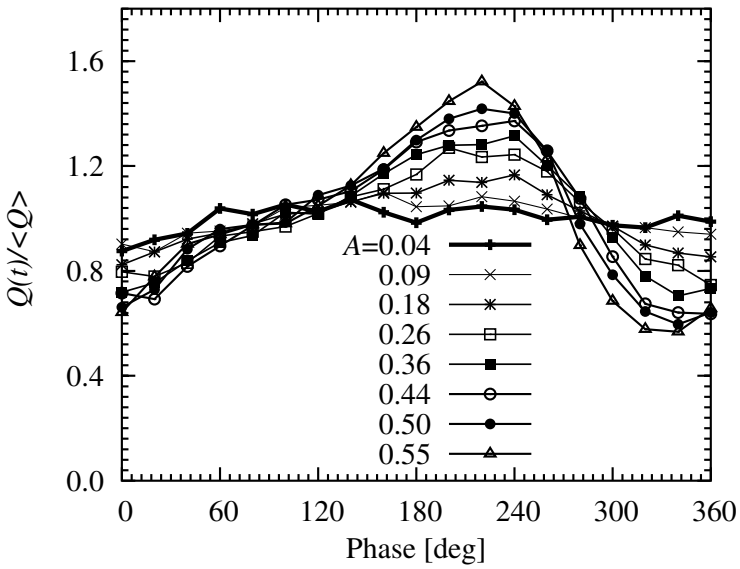

Figure 4.35: Cyclic variation of the heat release in swirl flame S2, evaluated from phase-averaged FSD images for different forcing amplitudes, A: $\langle U \rangle = 9.9$ m/s, $f = 160$ Hz, $\phi = 0.55$.

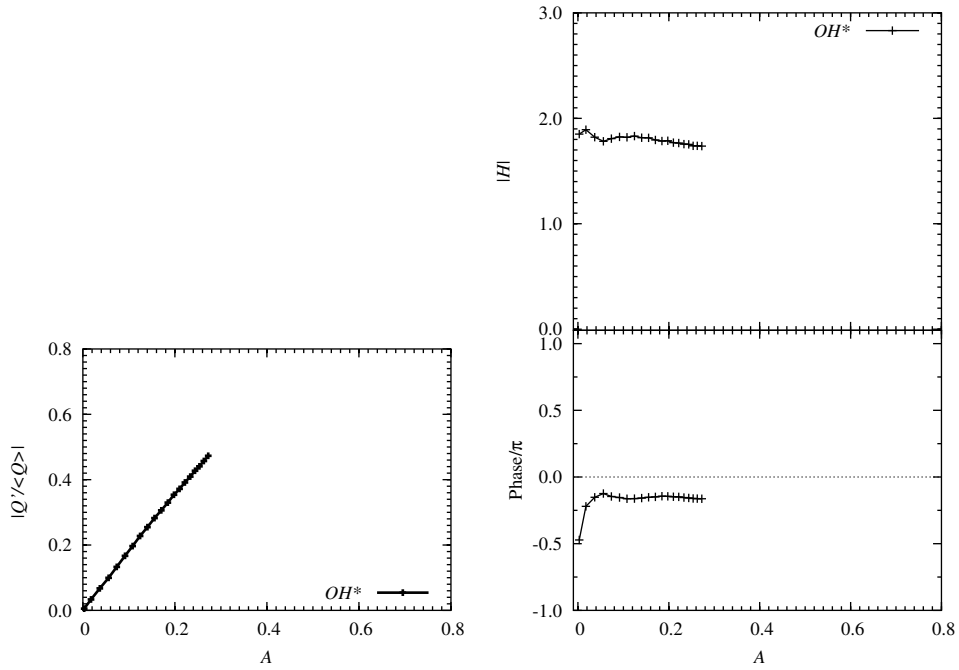

(a) (b)

Figure 4.36: (a) The normalized global heat release fluctuation of flame with swirl S2, measured as a function of A using OH* chemiluminescence and FSD. (b) The corresponding transfer function and the phase: $f = 40$ Hz, $\langle U \rangle = 9.9$ m/s, $\phi = 0.52$.

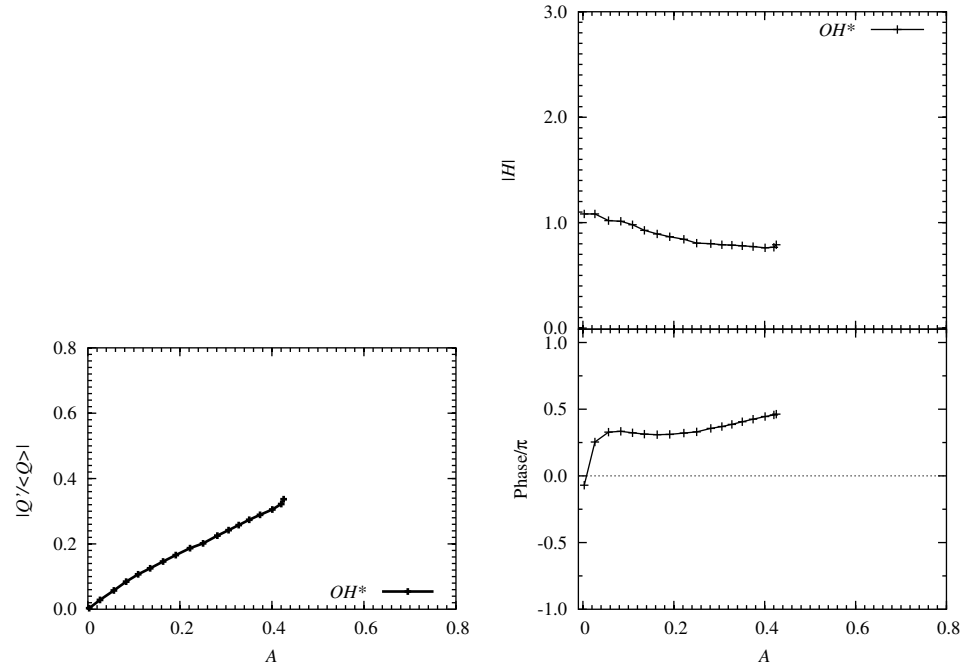

(a) (b)

Figure 4.37: (a) The normalized global heat release fluctuation of flame with swirl S2, measured as a function of A using OH* chemiluminescence and FSD. (b) The corresponding transfer function and the phase:$f = 330$ Hz, $\langle U \rangle = 9.9$ m/s, $\phi = 0.52$.

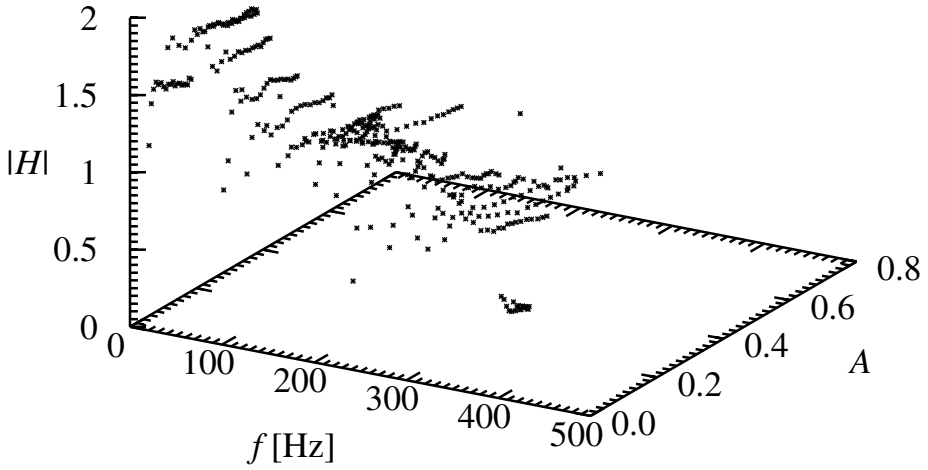

(a)

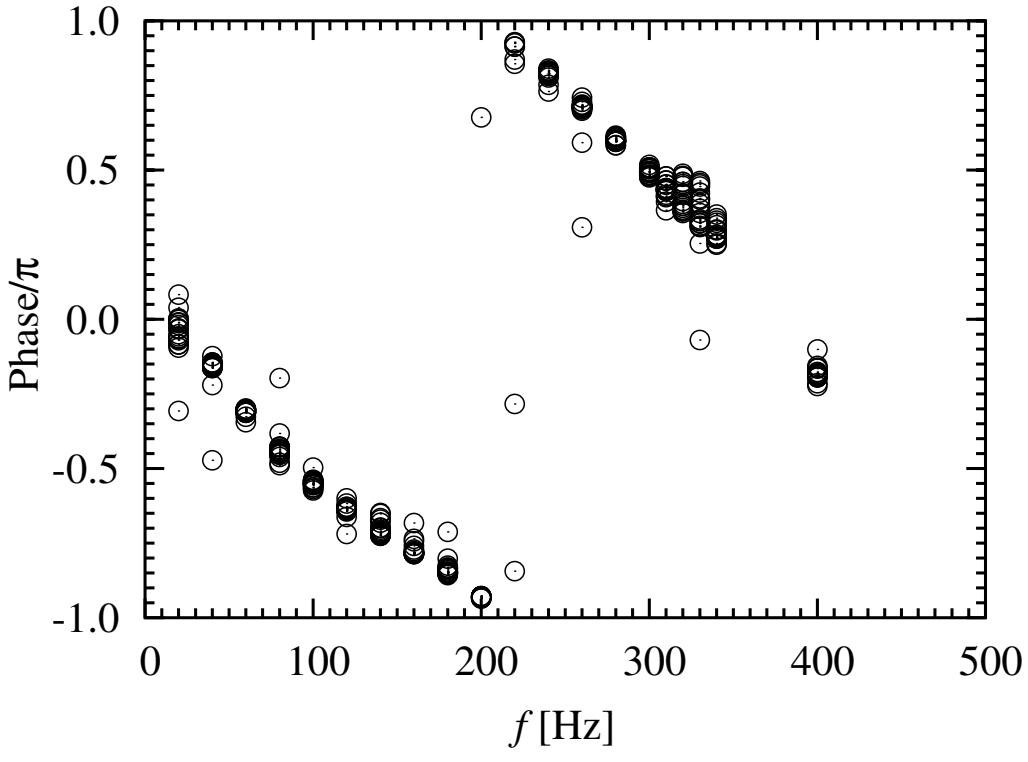

(b)

Figure 4.38: (a) Flame transfer function as a function of frequency and amplitude and (b) the relative phase relation. For case S2, $\langle U \rangle = 9.9$ m/s, $\phi = 0.52$.

(a) $A_1 = 0.03$ (b) 0.06 (c) 0.11 (d) 0.16

(e) 0.23 (f) 0.30 (g) 0.36 (h) 0.42

Figure 4.39: Time-series of simultaneously measured reference signal and OH* chemiluminescence with different level of forcing at the secondary frequency. The input peak-to-peak voltage (V_{p1}) at the primary frequency $f_1 = 160$ Hz was varied while keeping that of the forcing signal at the secondary frequency $f_2 = 320$ Hz to a constant value: S0, (non-swirling flame), $\langle U \rangle = 9.9$ m/s, A_2 =0.16, $\phi = 0.55$.

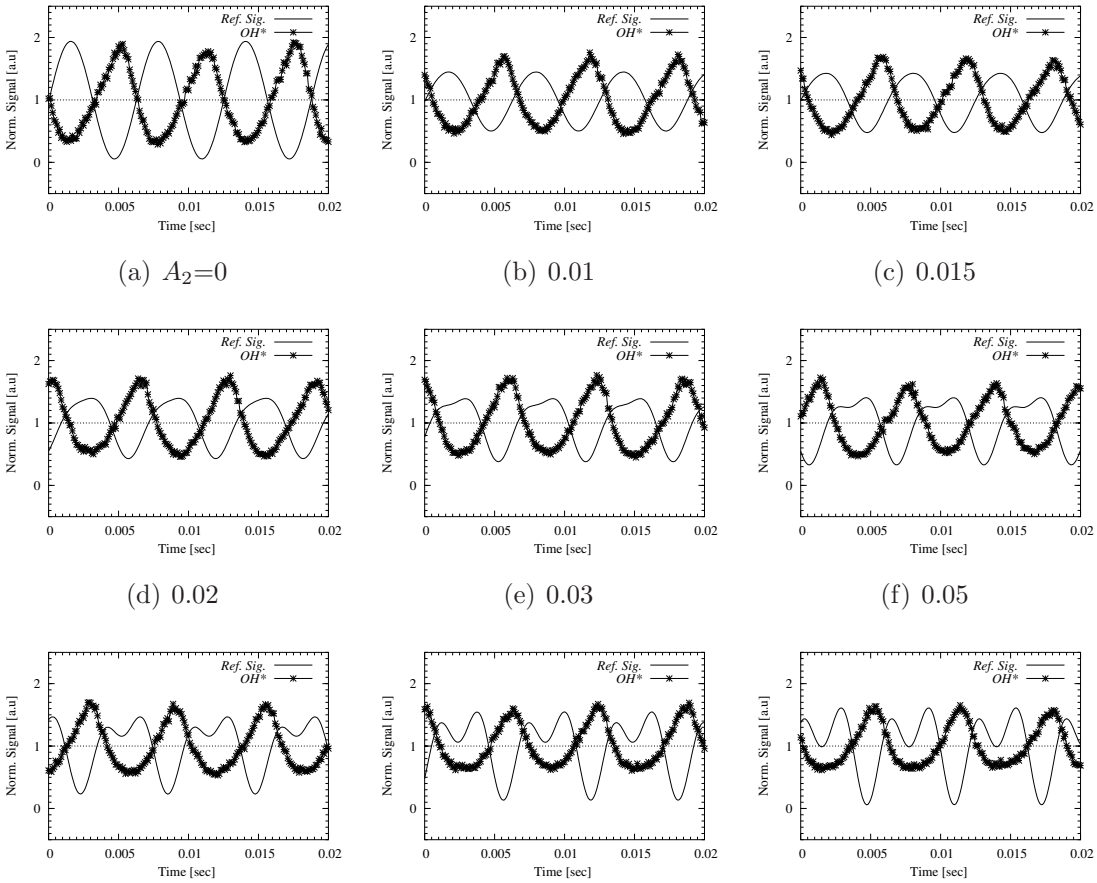

(a) A_2=0 (b) 0.01 (c) 0.015

(d) 0.02 (e) 0.03 (f) 0.05

(g) 0.09 (h) 0.12 (i) 0.16

Figure 4.40: Time-series of simultaneously measured reference signal and OH* chemiluminescence with different level of forcing at secondary frequency. The peak-to-peak voltage (V_{p1}) of the signal exciting the primary frequency $f_1 = 160$ Hz amplitude was kept to a constant value, while varying the input peak-to-peak voltage (V_{p2}) at the secondary (first harmonic) frequency $f_2 = 320$ Hz: S0, (no swirl flame), $\langle U \rangle = 9.9$ m/s, $A_1 = 0.42$, $\phi = 0.55$.

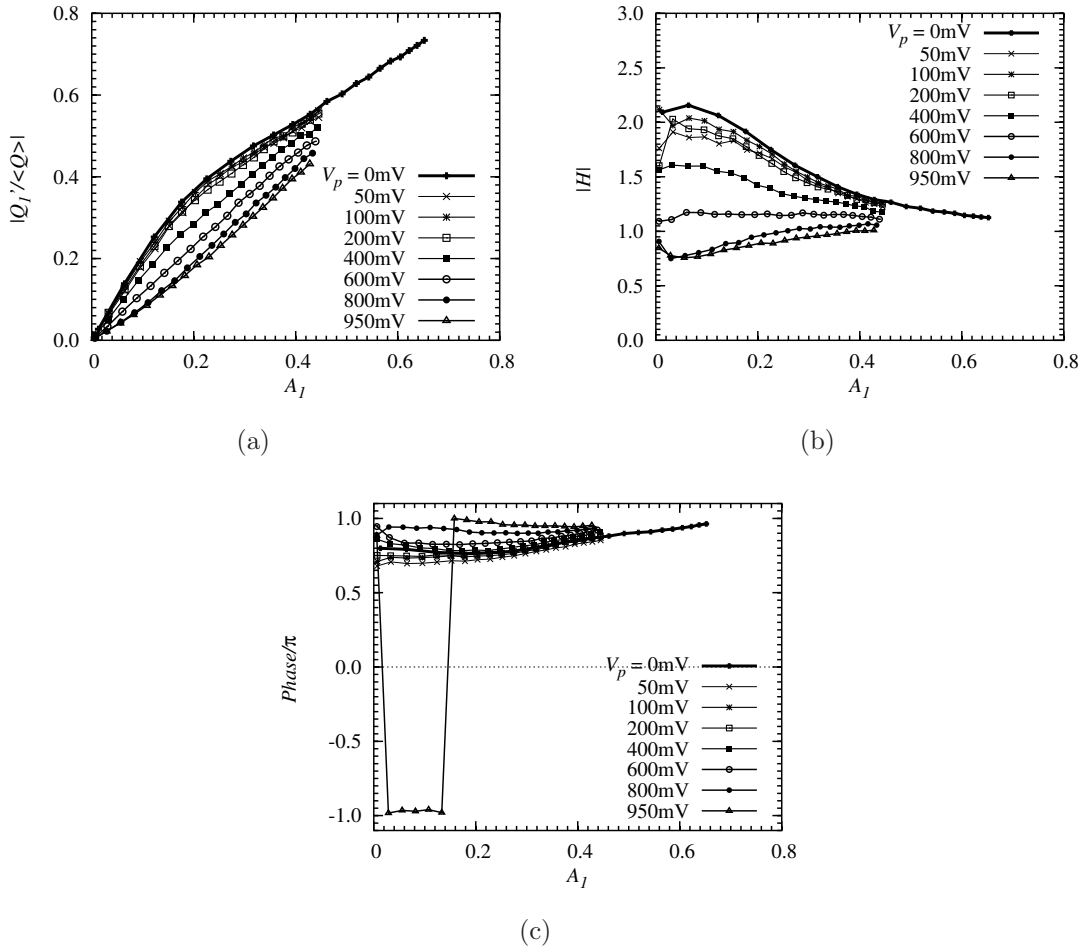

Figure 4.41: (a) The normalized global heat release fluctuation of flame, measured as a function of A using OH* chemiluminescence. (b) & (c) The corresponding transfer function and the phase: $f_1 = 160$ Hz, $f_2 = 320$ Hz, $\langle U \rangle = 9.9$ m/s, $\phi = 0.55$, Case S0.

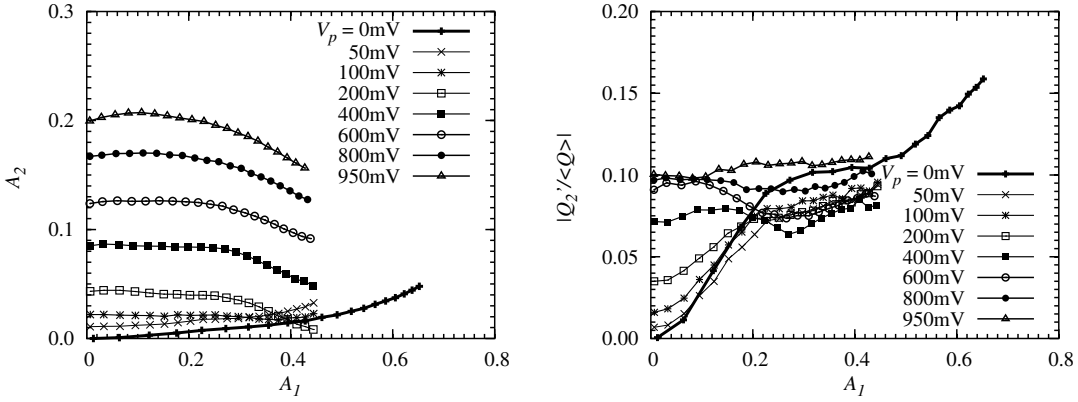

(a) (b)

Figure 4.42: (a) The variation of amplitude of velocity at secondary frequency f_2 as a function of A_1 (b) The corresponding heat release response to f_2, for the case presented in Fig. 4.40: $f_1 = 160$ Hz, $f_2 = 320$ Hz, $\langle U \rangle = 9.9$ m/s, $\phi = 0.55$, Case S0.

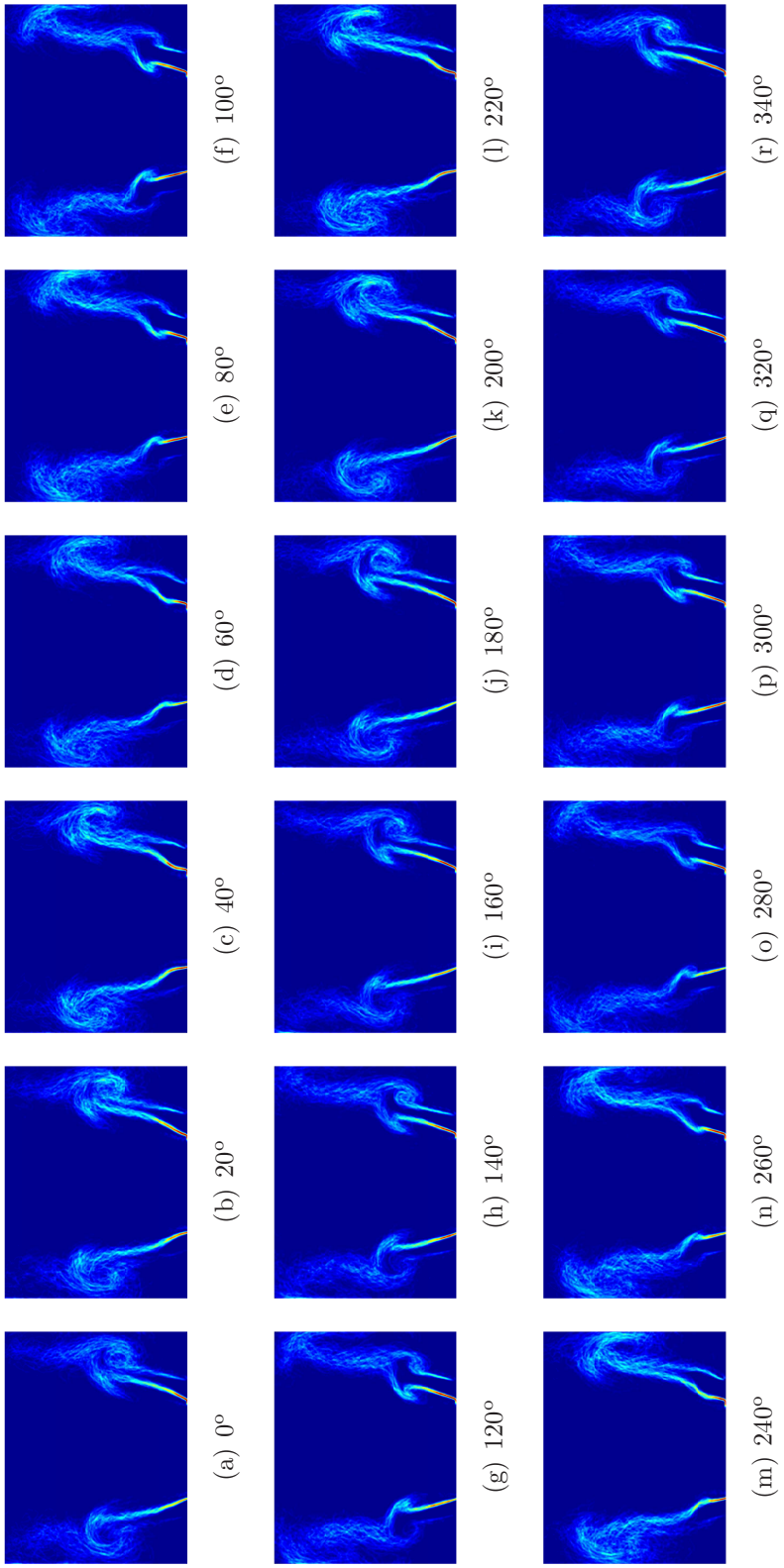

Figure 4.43: Phase-averaged FSD image sequence of non-swirling flame (S0) forced at two frequencies, $f_1 = 160$ Hz and $f_2 = 320$ Hz, with amplitude of input forcing/ reference signal at V_{p1}=50mV , V_{p2}=950mV , : $A_1 = 0.03$, A_2 =0.16, $\langle U \rangle = 9.9$ m/s, $\phi = 0.55$.

Figure 4.44: Phase-averaged FSD image sequence of non-swirling flame (S0) forced at two frequencies, $f_1 = 160$ Hz and $f_2 = 320$ Hz, with amplitudes of input forcing/ reference signal at V_{p1}=950mV, V_{p2}=950mV : $A_1 = 0.42$, A_2 =0.16, $\langle U \rangle = 9.9$ m/s, $\phi = 0.55$.

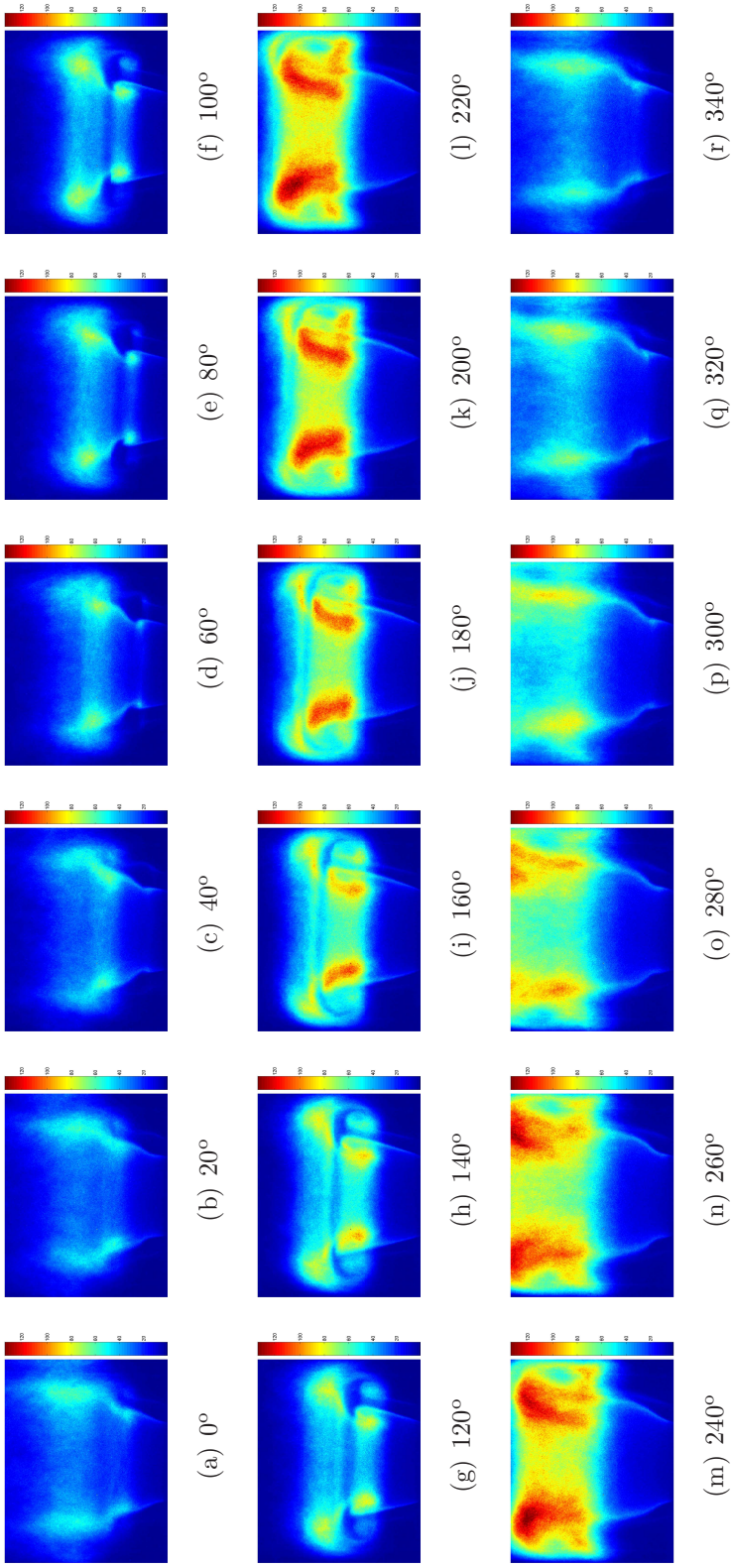

(a) 0° (b) 20° (c) 40° (d) 60° (e) 80° (f) 100°

(g) 120° (h) 140° (i) 160° (j) 180° (k) 200° (l) 220°

(m) 240° (n) 260° (o) 280° (p) 300° (q) 320° (r) 340°

Figure 4.45: Phase-averaged OH* image sequence of non-swirling flame (S0) forced at two frequencies for the case presented in Fig. 4.44, $f_1 = 160$ Hz and $f_2 = 320$ Hz, with amplitude of input forcing/ reference signal at V_{p1}=950mV, V_{p2}=950mV: $A_1 = 0.42$, A_2 =0.16, $\langle U \rangle = 9.9$ m/s, $\phi = 0.55$.

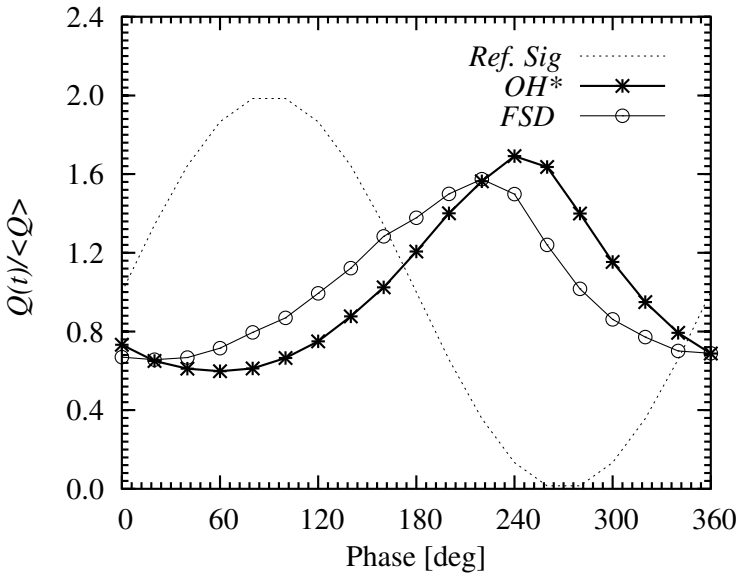

Figure 4.46: Comparison of the global heat release fluctuations evaluated from phase-averaged FSD and from OH* chemiluminescence images presented in Figs. 4.44 and 4.45.

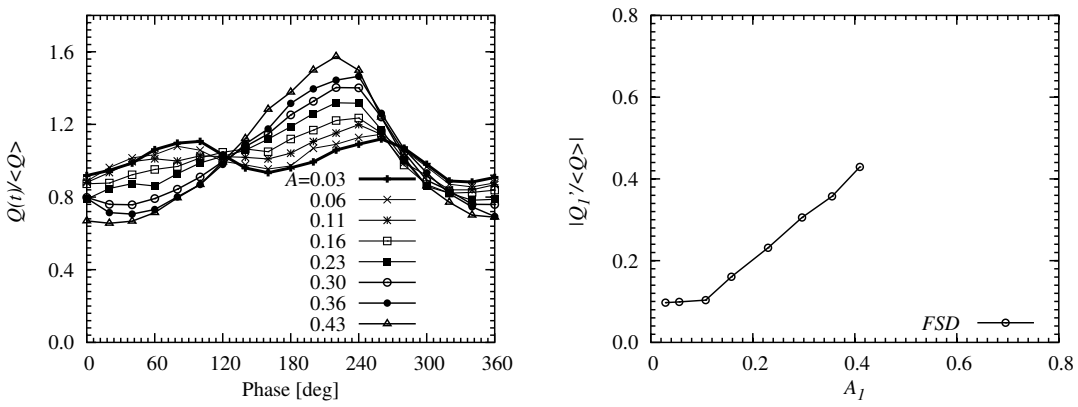

(a) (b)

Figure 4.47: (a) The cyclic variation of heat release from FSD measurements for a constant V_{p2}=950mV for different V_{p1} values. (b) The amplitude dependence of heat release response for V_{p2}=950mV: f_1 = 160 Hz, f_2 = 160 Hz,$\langle U \rangle$ = 9.9 m/s, ϕ = 0.55, Case S0.

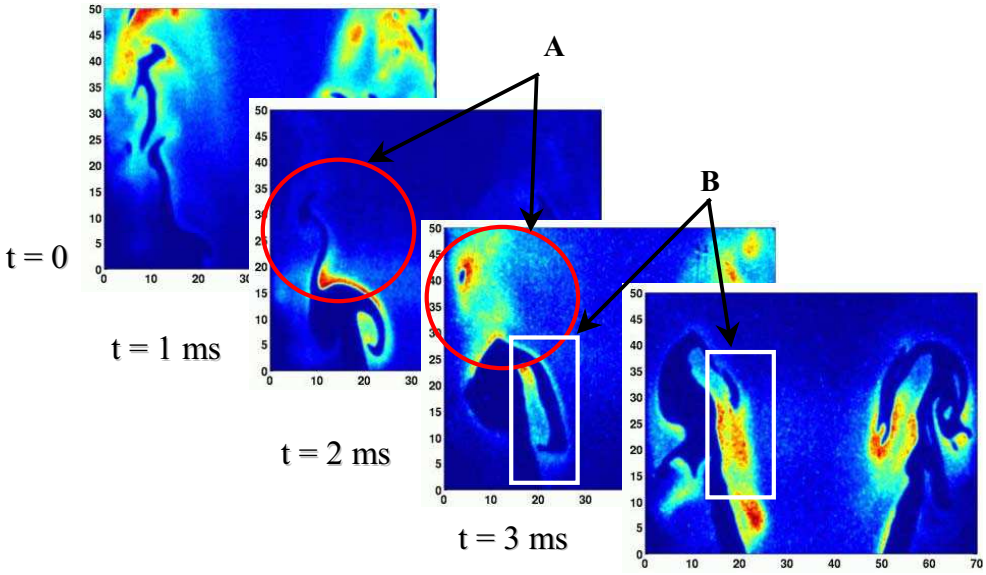

Figure 4.48: Time resolved OH PLIF images of a flame subjected to strong forcing showing flame annihilation events, A and B: $\langle U \rangle = 9.9$ m/s, $\phi = 0.55$, $f = 160$ Hz, $A \sim 0.5$.

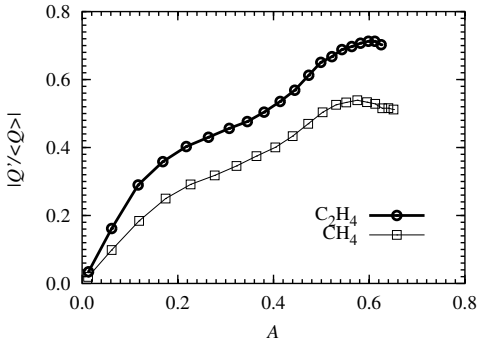

Figure 4.49: Comparison of response of ethylene and methane flames of equivalence ratio values $\phi = 0.55$ and 0.7 respectively. Measurements with OH*, and for both $\langle U \rangle = 9.9$ m/s, $f = 160$ Hz.

Chapter 5

Response of Imperfectly Premixed Flames

In this chapter, the results from the experiments investigating the response of the flames with initial spatial equivalence ratio variation (termed as 'imperfectly premixed flames') to inlet velocity and equivalence ratio oscillations are presented. Section 5.1 describes briefly the background for these experiments. The flow and acoustic conditions at which the experiments were performed are described in section 5.2. Section 5.3 presents the results and the discussions on the effect of different parameters such as amplitude & frequency of forcing, inlet swirl etc on the flame response. The role of time varying equivalence ratio and dynamics of coherent vortices on the nonlinear response of the imperfectly premixed flames is elucidated. The chapter closes with a summary about the mechanisms of saturation in these flames.

5.1 Background

The major cause for unsteady heat release in lean prevaporised-premixed (LPP) combustors are attributed to oscillations in equivalence ratio or initial premixedness (Dowling & Stow, 2003; Lieuwen & Zinn, 1998b). In the presence of high amplitude oscillations, along with variation in equivalence ratio, strong flame area variation due to coherent vortex formation and shedding may also exist (Menon, 1991), similar to the case of fully premixed flames of Chapter 4. Many theoretical

models for both linear and nonlinear behaviour have been developed considering the variation in equivalence ratio (Sattelmayer, 2000) and also with the kinematic contributions (Dowling & Stow, 2003); these models are used successfully in predicting the mode shapes and frequency information. In order to predict the limit cycle behaviour, information on amplitude and frequency dependence of the flame response are required. During the limit cycle oscillations, in practical combustion devices, either of the mechanisms afore mentioned could play a dominating role. Computational methods can be used to investigate the mechanism involved in saturation of the flame response resulting a limit cycle behaviour, but experiments to validate both simplified models and detailed computational studies are imperative. As described in previous chapters, many experimental techniques to measure heat release during these conditions have associated uncertainties and reservations. Hence, the results from such experiments need to be interpreted carefully. During this study, the experiments were performed with conventional chemiluminescence technique along with laser based measurements. The latter was used here to understand the response of the flame structure and the role of coherent vortices on the flame response, since obtaining a quantity that is proportional to heat release in the conditions with variation in equivalence ratio both spatially and temporally is ambiguous without simultaneous measurement of the fuel/air ratio.

Experiments were performed on simple flames with initial spatial variation in premixedness. The oscillations introduced at the inlet resulted in time varying velocity field and equivalence ratio, because the air mass flow was oscillating but the fuel mass flow rate was constant since the fuel was injected from choked holes. This simulated the conditions similar to that in LPP combustors. The objectives of this chapter are: i) to measure and understand the response of premixed flames (with initial spatial equivalence ratio variation) to time-varying equivalence ratio and velocity (introduced by strong acoustic forcing); ii) to clarify the role of equivalence ratio variation and that of flame surface modulation on the flame response; iii) to understand the effect of swirl on the flame response; and iv) to compare the results to that of fully premixed flames.

5.2 Experimental Conditions

The data presented in this section were performed on an imperfectly premixed flame using a configuration in which the fuel was injected through choked nozzles 55 mm upstream of the bluff body location (see chapter 2 for details). The flames of global equivalence ratios ϕ equal to 0.55 and 0.52 with the bulk velocity of 9.9m/s at the burner plane was commonly used in this section. Two swirler blocks with vane angles 45° and 60° were employed to introduce swirl to the flow. As in Chapter 4, the no-swirl, 45° and 60° cases are referred to as S0, S1 and S2 respectively. The amplitude and frequency velocity perturbation effected at the burner plane was varied; the frequencies from 20-400 Hz and amplitudes A up to 70% at resonant frequencies. (see Figure 3.1 that show the variation of maximum amplitude that could be excited for the selected flow condition).

5.3 Forced Imperfectly Premixed Flames

5.3.1 Dynamics of a Forced Imperfectly Premixed Flame

Figure 5.1 shows a typical time-averaged FSD image of an unforced imperfectly premixed flame. The image shows that the flame was primarily anchored at the shear layer generated by the bluff body, with some flame elements at the outer shear layer generated by the rearward facing step (dump plane) as in the case of fully premixed flames. When the reactant mixtures were forced with sufficiently large amplitude for certain frequencies, these shear layers roll up to form a counter rotating vortex pair. The flow field response at the cold conditions were presented in Chapter 3. As seen in the fully premixed flame case, the inner shear layer rolled inward and the outer shear layer rolled outwards. The shear layer rolled up as a result of acoustic forcing. Figure 5.2 shows the evolution of the flame using phase-averages of FSD when the flame was forced at 160 Hz with the value of forcing amplitude, A equal to 0.62. The 18 images presented in Fig. 5.2 show the flame surface evolution at every 20 degree phase angle. The image sequence shows clearly the deformation of the flame base and later resulting in roll up of the flame front stabilised at the inner shear layer radially inward and the flame stabilised

on the outer layer rolled up radially outward. It can be observed that the rolled up flame front grew in size and was convected with the flow and impinged on the wall. Once this disturbance moved out of the imaging region, a new vortex started forming at the base of the flame. This phenomenon was cyclic following the imposed velocity fluctuations. These observations were consistent with the fully premixed flame response presented in Chapter 4 and the response of the flow field to similar forcing conditions presented in Chapter 3.

Figure 5.3 shows the phase-averaged OH* chemiluminescence images taken simultaneously with the PLIF measurements for the case presented in Fig. 5.2. The roll up of the reacting shear and the dynamics of the vortex ring formed are found to be similar to the response of non-reacting shear layer to acoustics at the cold condition (see Fig. 3.5). The flame behaviour observed here is very similar that of the fully premixed flames.

As described earlier (in Chapter 4), the phase averaged FSD images obtained from the PLIF images were revolved around the burner central axis and were used to obtain the normalised cyclic heat release fluctuation and this was compared with the quantity obtained from OH* chemiluminescence imaging. Figure 5.4 shows the heat release variation evaluated from spatial integration of each of the phase-averaged FSD images in Fig. 5.2 and the OH* chemiluminescence images in Fig. 5.3 captured simultaneously during the experiments. It can be noticed that the heat release decreased with the beginning of the roll up (around 240 deg. relative to the forcing signal) and decreased further to attain the lowest value, which corresponded to the case where the flame surface area was at the lowest value due to the vortex roll up. The vortex while moving downstream towards the wall increased in size, increasing the flame area. The heat release evaluated from these measurements increased during this phase to attain a peak value, which corresponded to the highest flame surface area. The heat release due to the fine mixing between the reactants and hot products caused by the vortex is also evident from Fig. 5.3.

The time-series of OH* and CH* chemiluminescence measured using PMT and the phase-averaged FSD from OH PLIF were analyzed spectrally to obtain the complex amplitude of the fluctuation at the forcing frequency as described in Chapter 2. The acoustic velocity calculated from acoustic pressure measurement

using the two-microphone method was used to quantify the velocity amplitude at the inlet. The effects of various parameters affecting the response of imperfectly premixed flames are investigated in the following subsections.

5.3.2 Amplitude and Frequency Dependence of the Flame Response

Figure 5.5(a) shows the dependence of the OH* and CH* chemiluminescence upon the inlet forcing amplitude at a particular forcing frequency (160 Hz). Figure 5.5(b) shows the magnitude of the transfer function (i.e., the y-axis of Fig. 5.5(a) divided by A) and the corresponding phase information calculated from the data presented in Fig. 5.5(a). The results suggests that at this forcing frequency, the flame response was linearly dependent on the acoustic forcing amplitude A. It can be seen from Fig. 5.5(b) that the phase of the transfer function was nearly independent of the amplitude of forcing. From these results it is also clearly evident that the magnitude and phase of the heat release response measured by both the OH* and CH* chemiluminescence techniques are in good agreement as in the case of fully premixed flames.

The heat release response evaluated from FSD as a function of forcing amplitude is the same as that of OH* and CH* measurements (see Fig. 5.5(b)). These measurements suggest that for this flame the level of contribution from flame surface modulation to the total heat release response is significant and the flame area evolution is playing a key role in the observed amplitude dependence. The variation in burning speeds due to time-varying equivalence ratio does not seem to be significant for this flame at the reported forcing condition. The agreement between the magnitude and phase of the transfer function from different techniques, presented in Fig. 5.5(b) confirms the above fact that the flame surface modulation is important in this flame.

The finite amplitude response of the imperfectly premixed flame was investigated further for different forcing frequencies between 20-400 Hz. Figure 5.6 shows the amplitude dependence of heat release response of the flame at 40 Hz with the corresponding magnitude of transfer function and the phase information measured using OH* and CH* chemiluminescence. The figure suggest a highly

nonlinear amplitude dependence. The magnitude of the transfer function presented in 5.6(b) also suggests a very high response which is at the least two to three times higher than the magnitude of the response at 160 Hz. The phase of the transfer function measured seemed to be linearly dependent on the amplitude.

The time-series of OH* chemiluminescence for various forcing amplitudes (used to obtain data for Fig. 5.6) are presented in Fig. 5.7. The OH* chemiluminescence data was normalized using the time-mean of the signal and the reference signal was scaled (by a factor of 2) and offset (by a value of 1.0) for better presentation. The figures suggest that with increase in forcing amplitude, the peak-to-peak variation varied nonlinearly. It can be seen clearly that the increase in the heat release was much steeper than the decay of the signal. With an increase in amplitude, the region of the heat release cycle with low values reached values close to zero. The increase in peak value with the increase in forcing amplitude was first higher and after reaching the normalized values of about 4, the rate at which the heat release increased was low.

For comparison with the fully premixed flame response at 40 Hz, the time-series at the highest amplitude is presented in Fig. 5.7(h). It can be seen clearly from these figures and from results in Chapter 4 that the flame response at 40 Hz for imperfectly premixed was much greater (by a factor of 2) compared to the fully premixed flame response. The cold flow smoke visualization measurements at this forcing condition (presented in Fig. 3.7) suggested that there was no shear layer roll up, however there was a great change in the characteristic length and width of the recirculation. The response of the full premixed flame observed earlier in Chapter 4, in Fig. 4.10(a) also suggested a linear dependence throughout the forcing conditions. The FSD images presented in Fig. 4.11 also did not show shear layer roll up, and the flame area modulation was shown to be due to the oscillatory motion of the flame. These results suggest that for this forcing frequency, the response was not dominated by the flame surface modulation. It can be speculated that the steep increase in heat release values and the values approaching zero could be due to variation of the equivalence ratio. The low values in heat release rates could be due to the fact that the oscillation in equivalence ratio could have resulted in mixture concentration close to the extinction limits locally or even globally, resulting in much decreased heat release. At 40 Hz

forcing and for bulk velocity of 9.9m/s, the flame enclosed in a 80 mm long tube is very compact acoustically-convectively, meaning, the effect of cycle variation in equivalence ratio would affect greatly the global equivalence ratio and thus the heat release.

Figure 5.8 shows the phase-averaged OH* chemiluminescence for highest forcing presented in Figs. 5.6 and 5.7 and Fig. 5.9 shows the integrated heat release from the phase-averaged images. The phase-averaged images presented had individual colour scaling to show the flame shape. The figures suggest a strong variation in heat release and it can be seen clearly that the variation was not sinusoidal, with heat release remaining at lowest value for long and with steep rise in heat release followed by rapid decrease in heat release to low values again. From the figures, it can be seen that there was no vortex roll up, suggesting that the variation should be mainly due to variation in equivalence ratio. It should be noted here that the flame did not blow out completely during the cycle. The instantaneous OH* images suggested the presence of isolated flame regions. The results suggests that the heat release remained nonzero through out the cycle. Similar observations were made by Reuter *et al.* (1986) during their study, investigating the heat release variation in a pulse combustor.

In an effort to understand further the response of the flame to acoustic forcing, the transfer functions measured at different forcing frequencies for a range of amplitudes are consolidated in Fig. 5.10. Figure 5.10(a) shows the magnitude of the transfer function at different forcing frequencies for different amplitudes, Fig. 5.10(b) shows the data presented in Fig. 5.10(a) now presented just as a function of frequency and Fig. 5.10(c) shows the phase between the heat release and the velocity fluctuations. The magnitude of transfer function was found to decrease with increasing amplitude for low forcing frequencies (say around 40 Hz). With increase in frequency, the response of the flame decreased, which had a frequency dependence similar to studies presented in Armitage *et al.* (2004). The phase presented as function of frequency in Fig. 5.10(c) suggests a flame response with time delay.

The results presented from the experiments with flame with no swirl suggest that the flame response in imperfectly premixed flames are controlled by two mechanisms based on whether the flame is acoustically-convectively compact

or not. When the flame was compact (i.e. f was low) the heat release modulation were highly nonlinear and the saturation mechanism was dominated by equivalence ratio modulation. For the forcing conditions where the flame was not acoustically convectively compact (i.e. f was high), the flame response was dominated by the vortex roll up and shedding, i.e. by the flame area modulation.

5.3.3 Effect of Swirl

In this section, the results from the experiments on the response of the imperfectly premixed flames under different swirl conditions are presented. Figure 5.11 shows the unforced swirl imperfectly premixed flames with two swirl conditions, Fig. 5.11(a) corresponding to the moderate swirl S1, and Fig. 5.11(b) that of high swirl at the inlet, case S2; both the flames had same bulk velocity and same global equivalence ratio. When the moderately swirled flame was forced at 160 Hz with sufficiently large amplitude, the flame front rolled up into vortex ring as in the case of no swirl case. Figure 5.12 shows the evolution of the vortex ring in moderately swirled imperfectly premixed flame (swirl case S1). The phase-averaged OH* chemiluminescence images taken with the PLIF measurements are also presented in Fig. 5.13. These two figures 5.12 and 5.13 suggest that when the flame wrapped up by the vortex, in the region above the vortex, the flame elements were annihilated as in the case of completely premixed flames (Fig. 4.48). The variation of the heat release through the cycle evaluated from the data presented in Figs. 5.12 (FSD) and 5.13 (OH*), is presented in Fig. 5.14. The figure suggests that the magnitude of variation captured by the two methods are similar, but with a slight phase shift. These results suggest that the heat release modulation in this flame is through flame surface area modulation, as in the case of premixed flames.

The amplitude dependence of the normalized heat response and the transfer function evaluated from PMT measurements and that from FSD are presented in Fig. 5.15. The figures suggest that the flame saturation occurred for this particular flame for this frequency at A value around 0.4. The agreement in the trend by the FSD measurements both in magnitude and in phase, suggest that the saturation was dominated by the flame surface modulation. The spatial

variation in equivalence ratio in this case if it existed could be low and this could have resulted in the difference in the magnitude of the response measured by the two techniques.

The response of the moderately swirled (S1) flames to 40 Hz forcing is presented in Fig. 5.16. The amplitude dependence of the response suggests saturation at A around 0.25. The amplitude dependence of magnitude and phase of the transfer function presented in the Fig. 5.16(b) is very similar to that of the no-swirl case. The time series data of the OH* chemiluminescence used for evaluating some of the points in Fig. 5.16 are presented in Fig. 5.17. These figures also suggest that the flame response at this frequency is very similar to that of no-swirl case, implying that the response is dominated by equivalence ratio variation for this forcing frequency. The results presented for moderately swirl case also suggest that for low frequency (when the flame is compact) the response was due to equivalence ratio variation and at high frequencies it is due to flame surface area modulation. The response of the flame for different frequency and amplitude is presented in Fig. 5.18. These figures suggest that the flame response in the case of moderately swirled imperfectly premixed flame is very similar to (or same as) that of the no-swirl case.

Figure 5.19 shows the variation of flame structure using phase averaged FSD, when an imperfectly premixed, highly swirled flame was forced at 160 Hz. The simultaneously imaged phase-averaged OH* chemiluminescence is presented in Fig. 5.20. These images suggest the existence of vortex roll up and subsequent variation in flame heat release. However, the heat release evaluated from these images presented in Fig. 5.20 suggests that the two techniques did not agree well in the phase, which implies that the flame surface is not a true representation of the global heat release for these flames. This was further confirmed when the amplitude dependence of the response was compared (Fig. 5.22). Not only in magnitude, the phase also did not agree well between the techniques. The results in Fig. 5.22 suggest that the flame response was low for these flames and had a nearly linear dependence on the amplitude for this forcing condition. The response of the flame at 40 Hz had some nonlinearity (presented in Fig. 5.23). The time series of the OH* chemiluminescence in Fig. 5.24 for the case presented in Fig. 5.23 shows that the flame response for this flame was similar in trend but

low in magnitude. The graphs showing the amplitude and frequency dependence of the magnitude and phase of the transfer function is shown in Fig. 5.25. These graphs suggest that the frequency response of these highly swirled flames are very close to that of their counterparts with low swirl conditions.

5.4 Discussion

In this chapter, the chemiluminescence (from OH* and CH*) measured using PMT and by phase-averaged imaging using ICCD along with the FSD estimation from OH PLIF were used to investigate the response of imperfectly premixed to acoustic forcing. In non-swirling and low swirling flames, the FSD estimates agrees very well with the OH* and CH* chemiluminescence measurements. This suggest that FSD estimates in these flame, for these conditions could give a true estimate of heat release variation in these flames. The good agreement in FSD and the global chemiluminescence from OH* and CH* measurements suggest that the spatial variation in equivalence ratio (thus resulting in variation in flame speeds) if present, might have resulted in increased flame surface through wrinkling, which the FSD measurements could capture well. However, in the highly swirling flames, the FSD estimates did not agree well with the OH* chemiluminescence. This might be either due to increased wrinkling in the third dimension which is difficult to account for with planar measurements or due to difficulties in identifying the flame fronts using the current algorithm when the reactants and products mix thoroughly (as mentioned in Chapter 3).

As in the case of premixed flames, the flame response from the OH* and CH* measurements are in good agreement. Both the measurements were found to capture the non-linear flame response well. The agreement with the FSD during the high frequency forcing (160 Hz) suggests that the heat release modulations are mainly due to the flame surface modulations. It can be conjectured from these results that the flame kinematics plays a significant role in these high frequency forcing conditions. The results from the low frequency forcing experiments and in comparison with the fully premixed flame response (presented in Fig. 5.26) suggests that the flame response was very high at these conditions (factor of 3). The phase-averaged chemiluminescence images, the cold flow smoke visualization

experiments (Fig. 3.10) and the results fully premixed flames suggest that the role of flame kinematics could be very low. This implies that the equivalence ratio fluctuations could be very important during these experiments. The time series measurements presented for 40 Hz forcing for different flames in this chapter, suggest that the flame chemiluminescence reach values close to zero during the decay and the values increases steeply to achieve maximum values, suggesting possibilities of extinction. However it should be noted that in no part of the cycle, the values reached the zero fully. The OH* chemiluminescence images showed presence of pockets of reaction zones during these portions of cycles.

The frequency of forcing was normalized using the fuel convection time, and the transfer function as a function of this normalized frequency is presented in Fig. 5.26. The convection time for a non-swirling flame was obtained by dividing the length of the flame (L_f) with the bulk velocity ($\langle U \rangle$). This value was used to normalize the forcing frequency to obtain the reduced frequency. The figure suggests that the response of imperfectly premixed flames was high compared to the fully premixed case (by factor of 3) when the flame was compact (i.e. when the value of reduced frequency was much less than 1). The response of the flame decreased with increase in the reduced frequency, i.e. with decrease in compactness. The values of the response for fully premixed flames and imperfectly premixed flames are of comparable magnitude for reduced frequency values close to one and above, where the acoustic wavelengths are comparable to the flame lengths. This suggests that during low frequency forcing, the change in equivalence ratio at the flame front could be felt globally affecting the heat release, while during the high frequency forcing these effects are not comparable to the kinematic contributions. The balance of these two mechanisms and the phase between the two could be playing an important role in the nonlinear frequency response of the flames. The transfer function values reaching values close to zero for certain frequencies in between these two frequencies could be because the two mechanisms are balancing each other. The role of these two mechanisms did not change even when the flow was swirled. Detailed measurements of equivalence ratio are required to understand the role of temporal and spatial variation in equivalence ratio better.

These results imply that the heat release response in imperfectly premixed flames has contributions through two mechanisms: equivalence ratio fluctuations

and flame kinematics. The earlier dominates in saturation mechanism of the flame response when the flame is compact and the latter plays a significant role when the acoustic wavelengths and the flame length are of comparable magnitude.

5.5 Summary

Detailed experimental investigations were performed to investigate the response of lean imperfectly premixed turbulent bluff-body stabilised flames to imposed inlet velocity and equivalence ratio perturbations. Special attention was given to the amplitude and frequency dependence of the transfer function, which are relevant to the emergence of limit-cycle combustion-induced oscillations. The heat release measurements were performed using OH* and CH* chemiluminescence measured with photo-multiplier tubes and ICCD camera. The variation in local flame structure was investigated using flame surface density (FSD) based on OH PLIF.

Concerning the use of the above techniques for the flame response studies in imperfectly premixed flames, the following conclusions were reached. First, the global heat release evaluated from OH* and CH* chemiluminescence agreed very well both in magnitude and in phase during all forcing frequencies and amplitudes. Second, the magnitude of the heat release response captured by chemiluminescence measurements and by FSD showed a similar trend with forcing amplitude for the low swirling and non-swirling flames, when the flame was forced at 160 Hz with high amplitude ($A \sim 0.64$). This implies that the variation in local equivalence ratio affecting the burning velocity probably resulted in increased flame area through increased flame wrinkling, which could be captured well by FSD measurement approach. Hence the cyclic global heat release rate from the two measurements agreed well for this case. It can be concluded that the global heat release modulation during these forcing conditions had a greater contribution from the flame surface modulation as in the case of premixed flames. For the highly swirling flames, the FSD and OH* chemiluminescence did not agree. The difference in both phase and magnitude suggest that the FSD cannot be a true measure of heat release for these cases. This could be either due to the increased wrinkling in the third dimension or the equivalence ratio variation was

much greater resulting in strong variation in local heat release which could not be captured by the FSD technique.

Concerning the frequency and amplitude dependence of the flame response, the following conclusions were reached. The response of the imperfectly premixed flames was found to greatly depend on how well the flame was compact acoustically and convectively. When the overall length of the flame was comparable to or greater than the wavelength of the forced oscillations (ie. high f values), the heat release modulations were dominated by flame sheet kinematic and when the flame was compact (i.e. low f), the flame response was mainly due to temporal variations in the equivalence ratio. The comparison of transfer function values with the completely premixed flames suggests that the contribution from the flame sheet kinematics could be not be very important in the low frequency forcing. While the magnitude of the transfer function for premixed and imperfectly premixed flames were of same order at higher frequencies. The frequency when normalized with the fuel dispersion time (or the convection time or the residence time) corroborated the fact that these equivalence ratio modulations were important when the acoustic wavelengths are greater than flame lengths. The OH* chemiluminescence and FSD confirmed the role of flame sheet kinematics during the high frequency forcing.

The measurements of heat release response of swirl flames further clarified the role of flame area and equivalence ratio modulation. The amplitude dependence of response of moderately swirling flame was very similar to that of the no-swirl flame with saturation occurring from 25% forcing for 40 Hz forcing and from 40% of forcing amplitude for 160 Hz. For the highly swirling flames, the response was found to have a non linear dependence on the amplitude of the forcing, but the magnitude of response was low when compared to the low swirling flames. The phase variation in all the cases were found to depend on the amplitude only when the flame was not acoustically convectively compact.

The present results suggest that the amplitude and frequency response of the imperfectly premixed flames to acoustic forcing had two distinct regimes, during which either the equivalence ratio or flame sheet kinematics play the major role in the saturation mechanism, depending on how the flame is acoustically-convectively compact. These results apart from confirming the previous analytical

and experimental results showing the role of equivalence ratio fluctuations in heat release modulation, also suggest a criterion to identify the role played by it.

5.6 Figures for Chapter 5

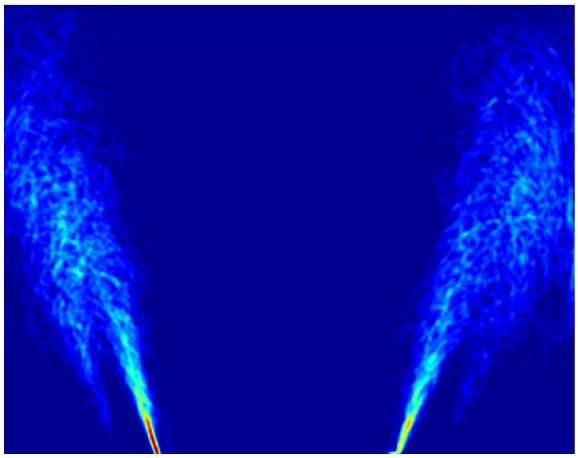

Figure 5.1: Time-averaged FSD image of an unforced imperfectly premixed flame. Conditions are: Global $\phi = 0.55$, $\langle U \rangle$ of 9.9 m/s. (The field of view is 70 mm x 55 mm, lower side of image is 0.5 mm above the bluff body.)

Figure 5.2: Phase-averaged FSD image sequence under strong acoustic forcing of the flame presented in Fig. 5.1: $\langle U \rangle = 9.9$ m/s, $f = 160$ Hz, $A = 0.65$, $\phi = 0.55$.

Figure 5.3: Phase-averaged OH* image sequence for the case presented in Fig. 5.2, taken simultaneously with OH PLIF: $\langle U \rangle = 9.9$ m/s, $f = 160$ Hz, $A = 0.65$, $\phi = 0.55$.

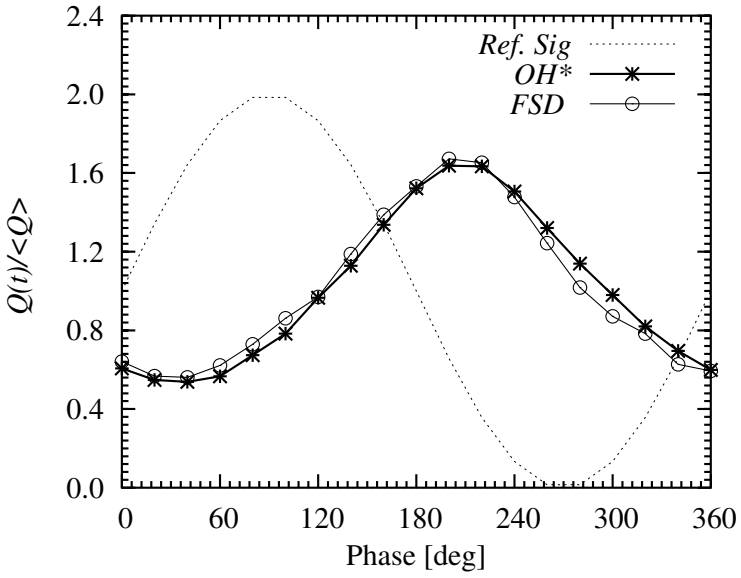

Figure 5.4: Comparison of the global heat release fluctuations evaluated from phase-averaged FSD and from OH* chemiluminescence images (data presented in Figs. 5.2 and 5.3 both imaged simultaneously): $\langle U \rangle = 9.9$ m/s, $\phi = 0.55$, $f = 160$ Hz and $A = 0.65$.

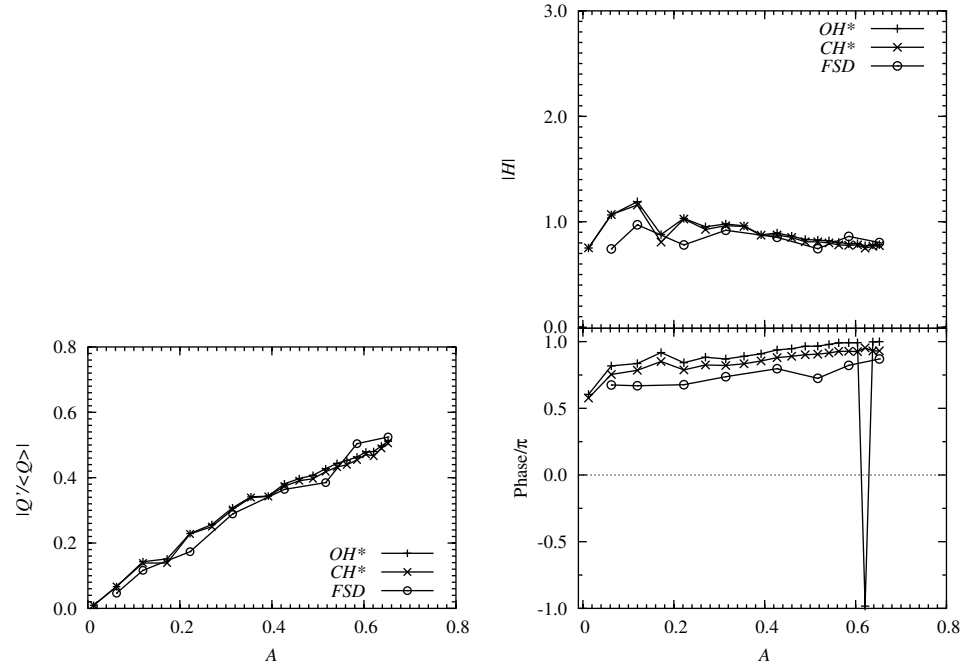

(a) (b)

Figure 5.5: (a) The normalised global heat release fluctuation of flame with swirl S0, measured as a function of A using OH* and CH* chemiluminescence and FSD. (b) The corresponding transfer function and the phase: $f = 160$ Hz, $\langle U \rangle = 9.9$ m/s, global $\phi = 0.55$.

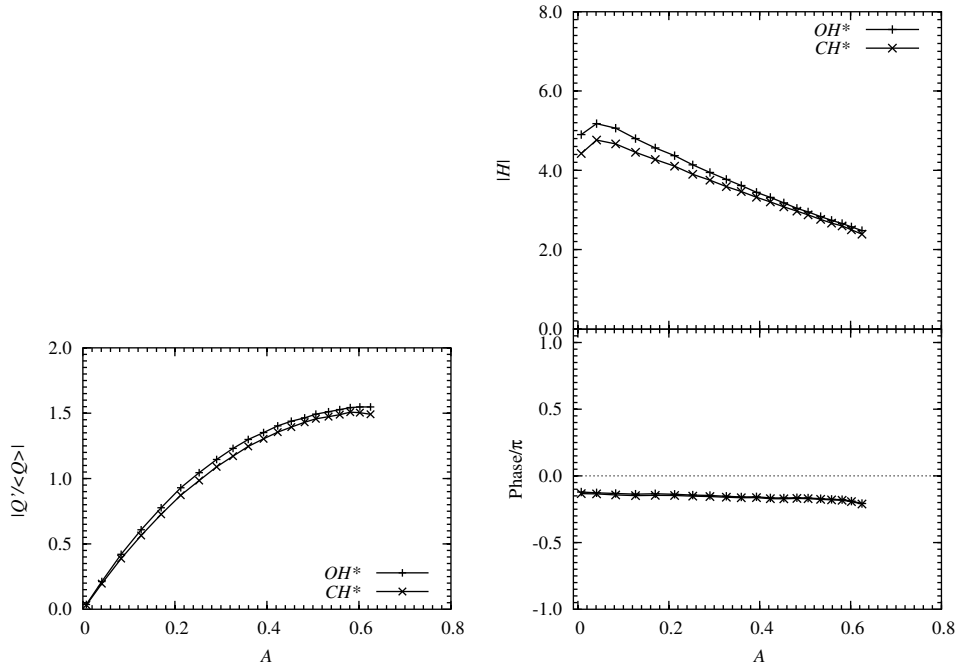

(a) (b)

Figure 5.6: (a) The normalized global heat release fluctuation of flame with swirl S0, measured as a function of A using OH* and CH* chemiluminescence (b) The corresponding transfer function and the phase: $f = 40$ Hz, $\langle U \rangle = 9.9$ m/s, global $\phi = 0.55$.

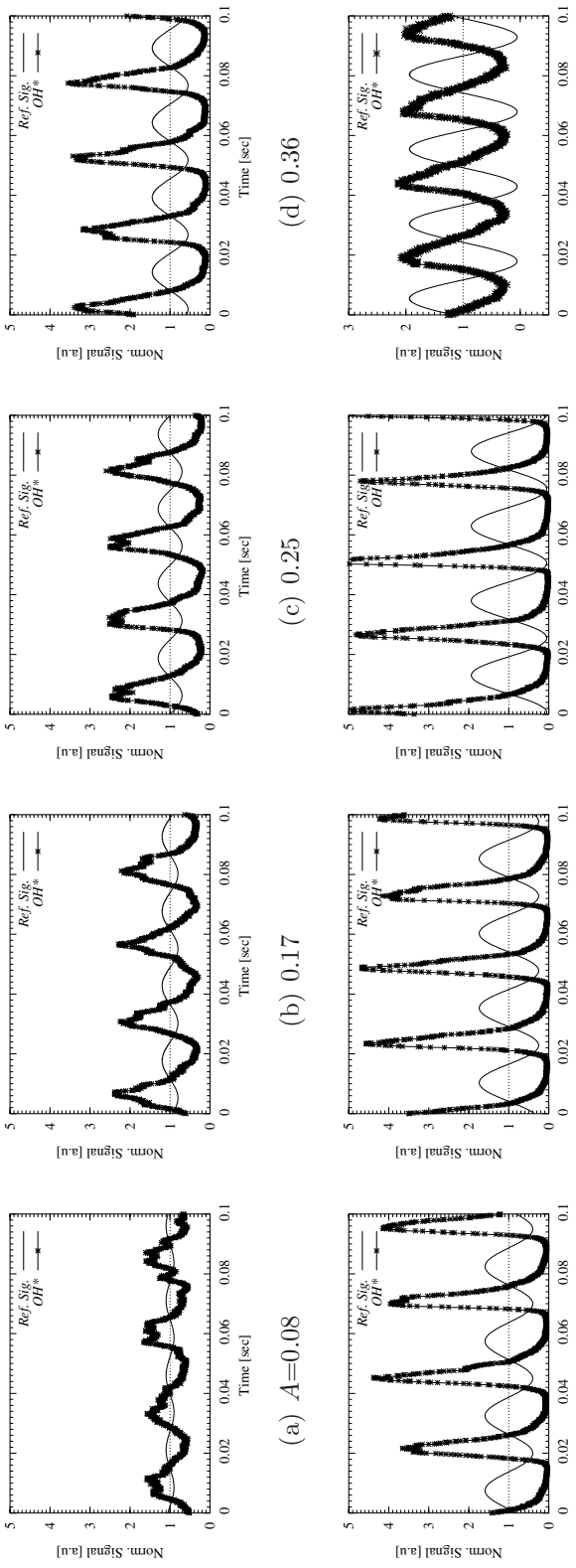

(a) A=0.08 (b) 0.17 (c) 0.25 (d) 0.36

(e) 0.45 (f) 0.54 (g) 0.63 (h) A=0.64, fully premixed

Figure 5.7: (a-g) Time-series of simultaneously measured reference signal and OH* chemiluminescence from imperfectly premixed flame with different levels of forcing (for the datapoints in 5.6) and (b) that of fully premixed flame at highest forcing amplitude : S0 (non-swirling flame), $\langle U \rangle = 9.9$ m/s, $\phi = 0.55$.

Figure 5.8: Phase-averaged OH* image sequence for the highest forcing case presented in Fig. 5.7: $\langle U \rangle = 9.9$ m/s, $f = 40$ Hz, $A = 0.63$, $\phi = 0.55$.

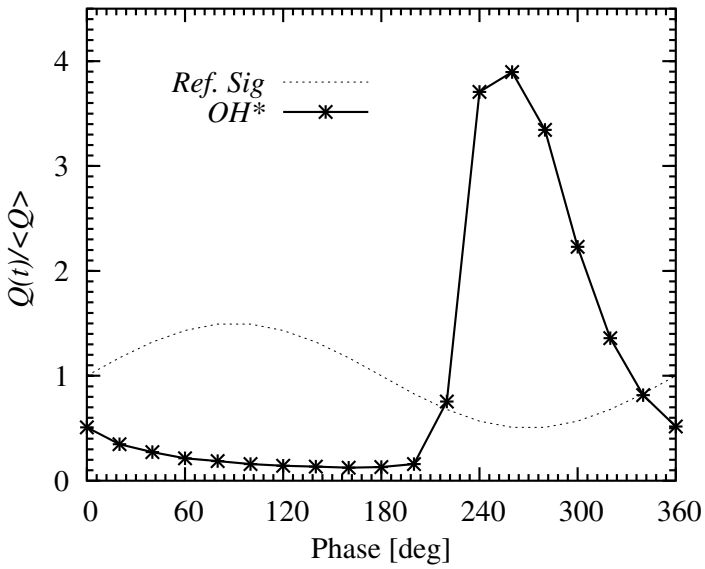

Figure 5.9: Cyclic variation of the heat release fluctuations of swirl flame S0, evaluated from phase-averaged OH* images of Fig. 5.8: $\langle U \rangle = 9.9$ m/s, $f = 40$ Hz, $\phi = 0.55$.

Figure 5.10: (a) Flame transfer function as a function of frequency and amplitude and (b) the magnitude of the transfer function in (a) presented as function of frequency and (c) the relative phase relation. Swirl S0, $\langle U \rangle = 9.9$ m/s, global $\phi = 0.55$.

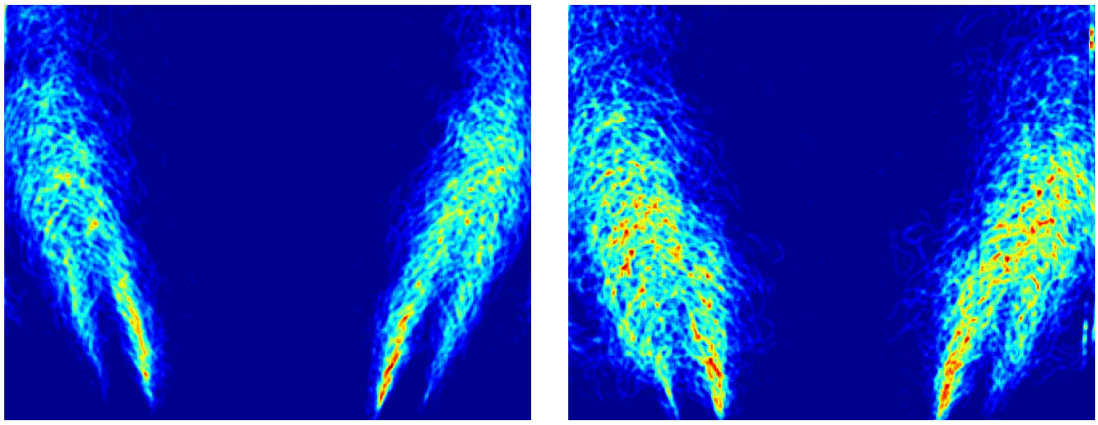

(a) (b)

Figure 5.11: Time-averaged FSD of imperfectly premixed flames with two different conditions (a) moderate swirl, S1 and (b) high swirl, S2. $\langle U \rangle = 9.9$ m/s, global $\phi = 0.52$.

Figure 5.12: Phase-averaged FSD image sequence under strong acoustic forcing of the flame presented in Fig. 5.11(a): Swirl S1, $\langle U \rangle = 9.9$ m/s, $f = 160$ Hz, $A = 0.60$, global $\phi = 0.52$.

Figure 5.13: Phase-averaged OH* image sequence for the case presented in Fig. 5.12, taken simultaneously with OH PLIF: Swirl S1, $\langle U \rangle = 9.9$ m/s, $f = 160$ Hz, $A = 0.60$, global $\phi = 0.52$.

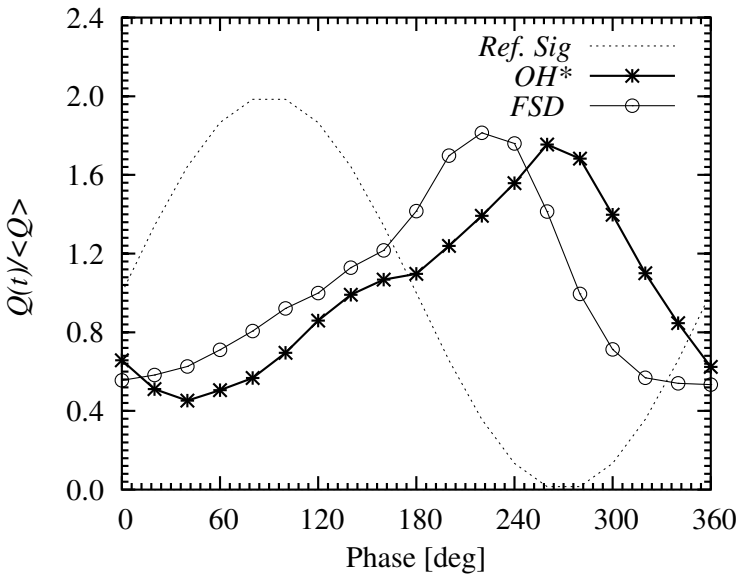

Figure 5.14: Comparison of the global heat release fluctuations evaluated from phase-averaged FSD and from OH* chemiluminescence images (data presented in Figs. 5.12 and 5.13 both imaged simultaneously): Swirl S1, $\langle U \rangle = 9.9$ m/s, global $\phi = 0.52$, $f = 160$ Hz and $A = 0.60$.

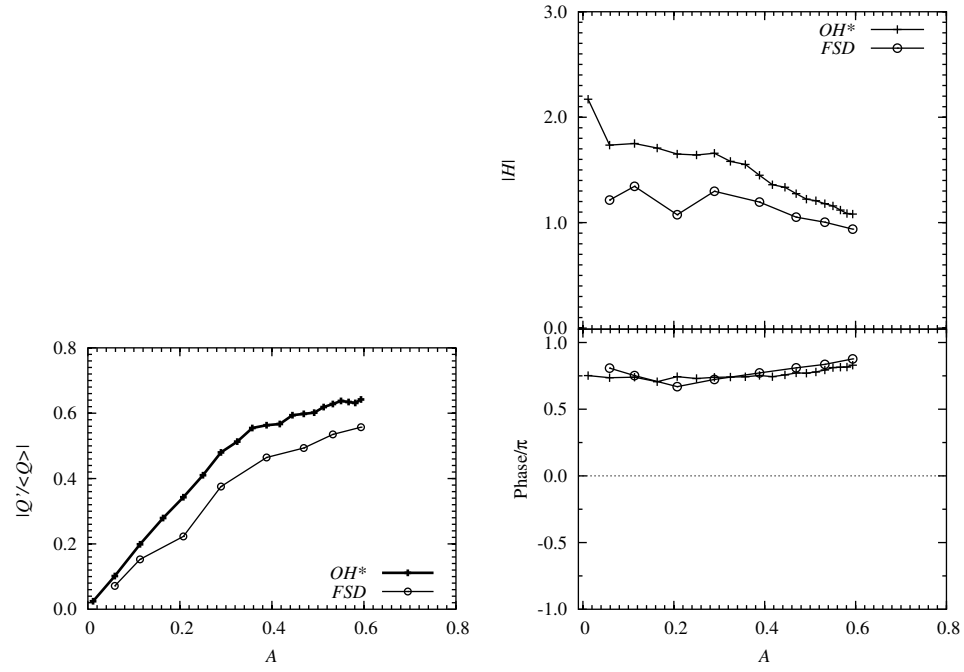

(a) (b)

Figure 5.15: (a) The normalized global heat release fluctuation of flame with swirl S1, measured as a function of A using OH* chemiluminescence and FSD. (b) The corresponding transfer function and the phase:f = 160 Hz, $\langle U \rangle$ = 9.9 m/s, global $\phi = 0.52$.

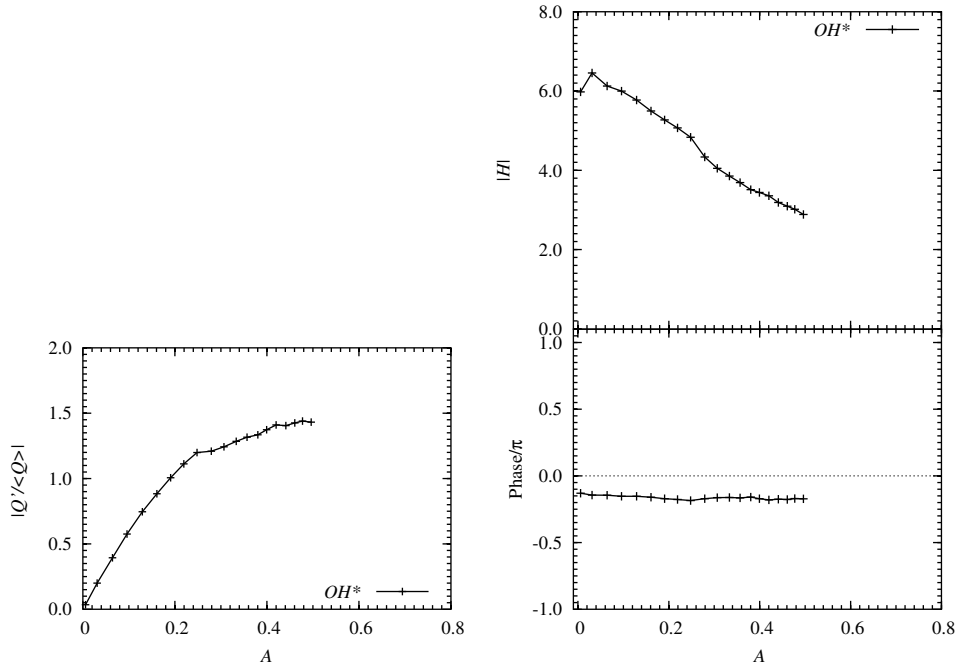

(a) (b)

Figure 5.16: (a) The normalised global heat release fluctuation of flame with swirl S1, measured as a function of A using OH* chemiluminescence (b) The corresponding transfer function and the phase:$f = 40$ Hz, $\langle U \rangle = 9.9$ m/s, global $\phi = 0.52$.

(a) A=0.06 (b) 0.19 (c) 0.28

(d) 0.36 (e) 0.42 (f) 0.49

Figure 5.17: Time-series of simultaneously measured reference signal and OH* chemiluminescence with different levels of forcing (for the data points in 5.16) : Swirl S1, $\langle U \rangle = 9.9$ m/s, A_2 =0.19, $\phi = 0.52$.

Figure 5.18: (a) Flame transfer function as a function of frequency and amplitude and (b) the magnitude of the transfer function in (a) presented as function of frequency and (c) the relative phase relation. Swirl S1, $\langle U \rangle = 9.9$ m/s, global $\phi = 0.52$.

Figure 5.19: Phase-averaged FSD image sequence under strong acoustic forcing of the flame presented in Fig. 5.11(b): Swirl S2, $\langle U \rangle = 9.9$ m/s, $f = 160$ Hz, $A = 0.55$, global $\phi = 0.52$.

Figure 5.20: Phase-averaged OH* image sequence for the case presented in Fig. 5.19, taken simultaneously with OH PLIF: Swirl S2, $\langle U \rangle = 9.9$ m/s, $f = 160$ Hz, $A = 0.55$, global $\phi = 0.52$.

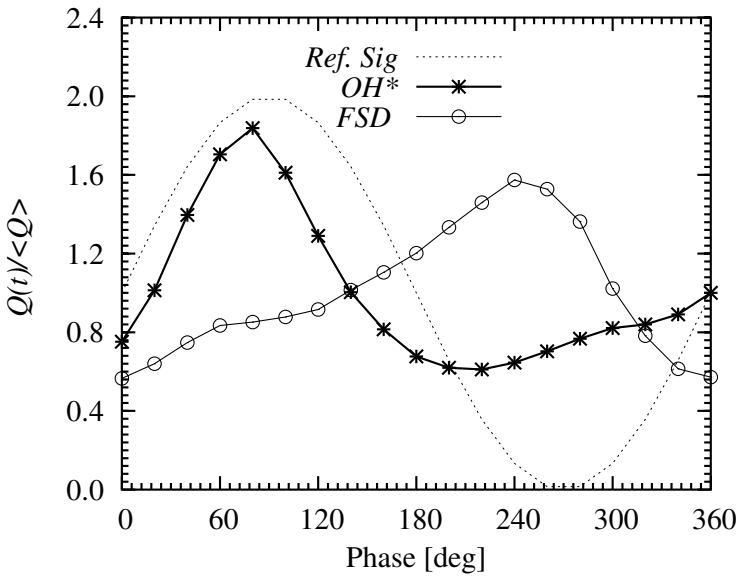

Figure 5.21: Comparison of the global heat release fluctuations evaluated from phase-averaged FSD and from OH* chemiluminescence images (data presented in Figs. 5.19 and 5.20 both imaged simultaneously): Swirl S2, $\langle U \rangle = 9.9$ m/s, global $\phi = 0.52$, $f = 160$ Hz and $A = 0.55$.

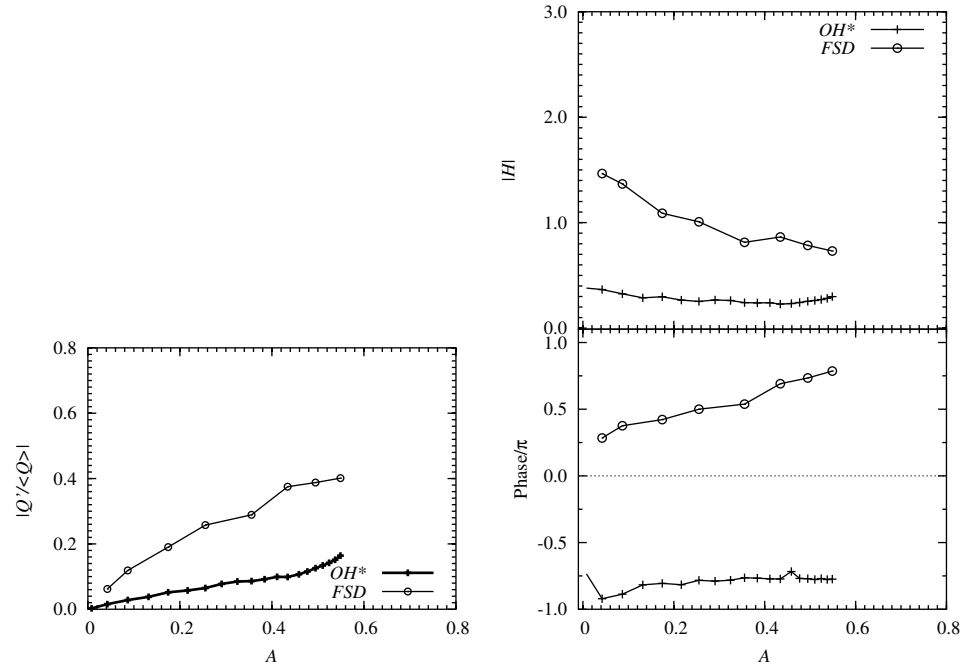

(a) (b)

Figure 5.22: (a) The normalized global heat release fluctuation of flame with swirl S2, measured as a function of A using OH* chemiluminescence and FSD. (b) The corresponding transfer function and the phase: $f = 160$ Hz, $\langle U \rangle = 9.9$ m/s, global $\phi = 0.52$.

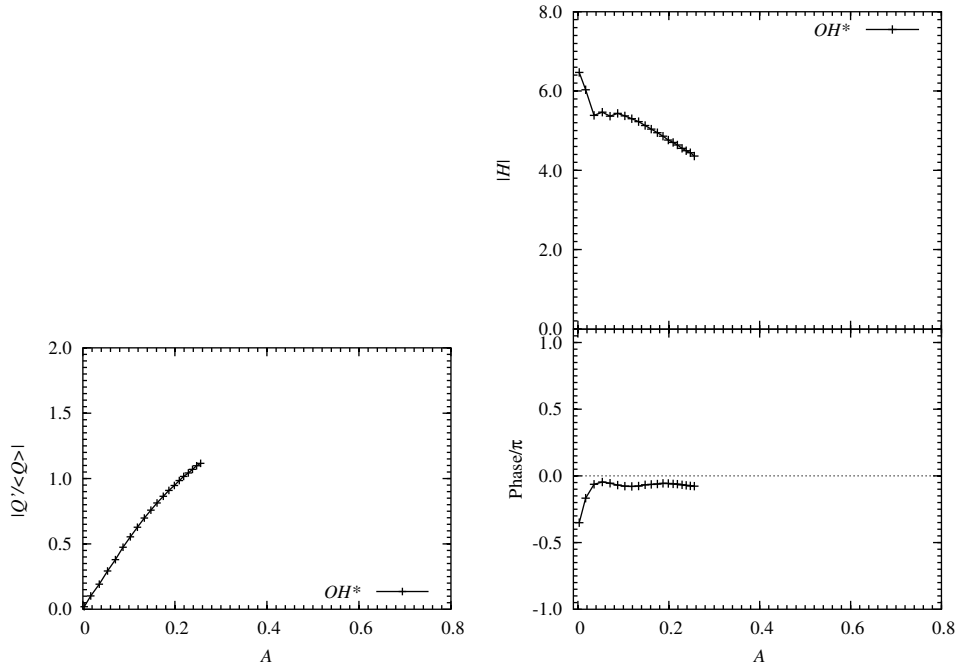

(a) (b)

Figure 5.23: (a) The normalized global heat release fluctuation of flame with swirl S2, measured as a function of A using OH* chemiluminescence (b) The corresponding transfer function and the phase: $f = 40$ Hz, $\langle U \rangle = 9.9$ m/s, global $\phi = 0.52$.

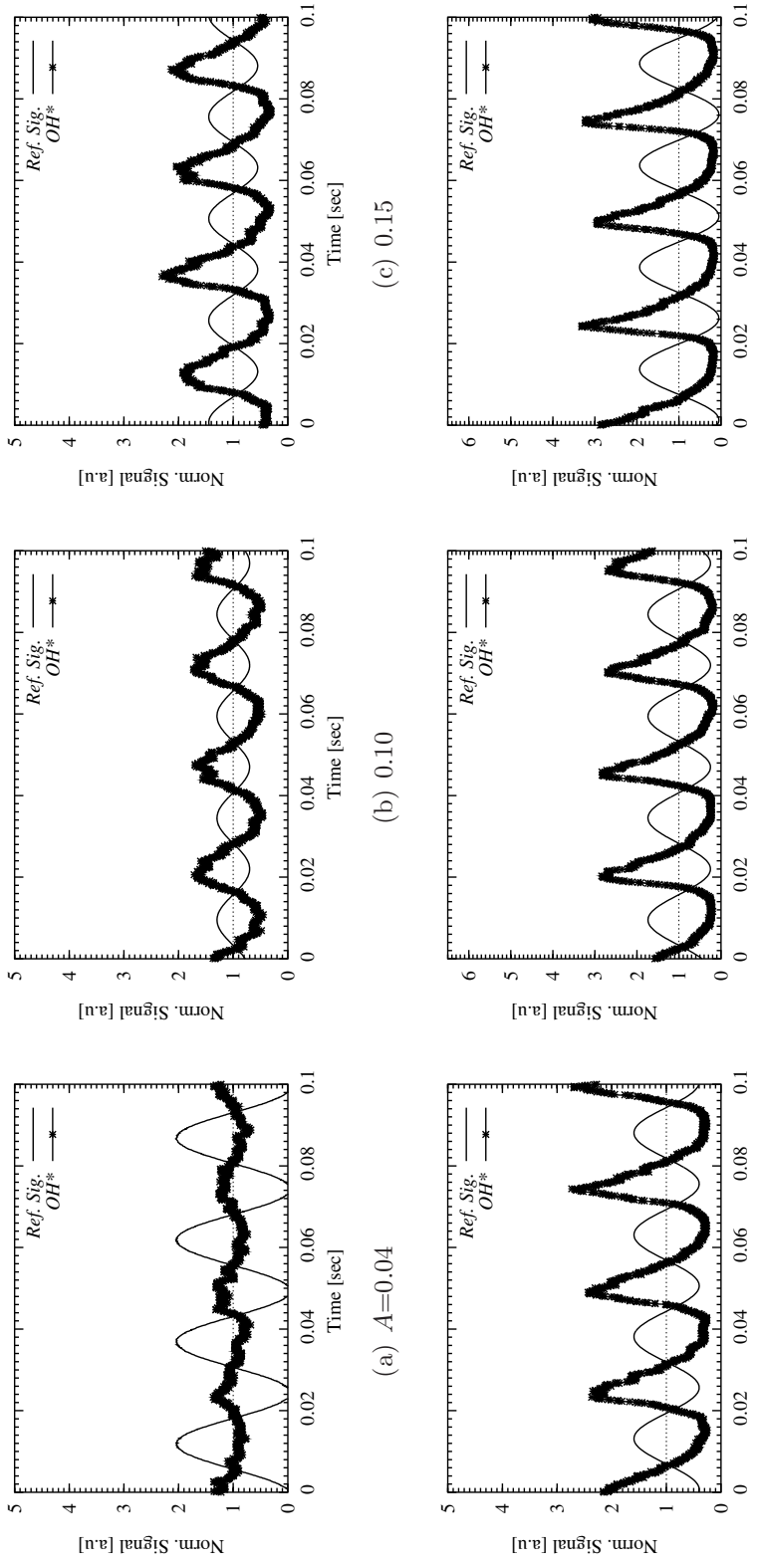

(a) A=0.04 (b) 0.10 (c) 0.15

(d) 0.19 (e) 0.22 (f) 0.26

Figure 5.24: Time-series of simultaneously measured Ref. Signal and OH* chemiluminescence with different level of forcing (for the data points in 5.23) : Swirl S2, $\langle U \rangle = 9.9$ m/s, $\phi = 0.52$.

Figure 5.25: (a) Flame transfer function as a function of frequency and amplitude and (b) the magnitude of the transfer function in (a) presented as function of frequency and (c) the relative phase relation. Swirl S2, $\langle U \rangle = 9.9$ m/s, global $\phi = 0.52$.

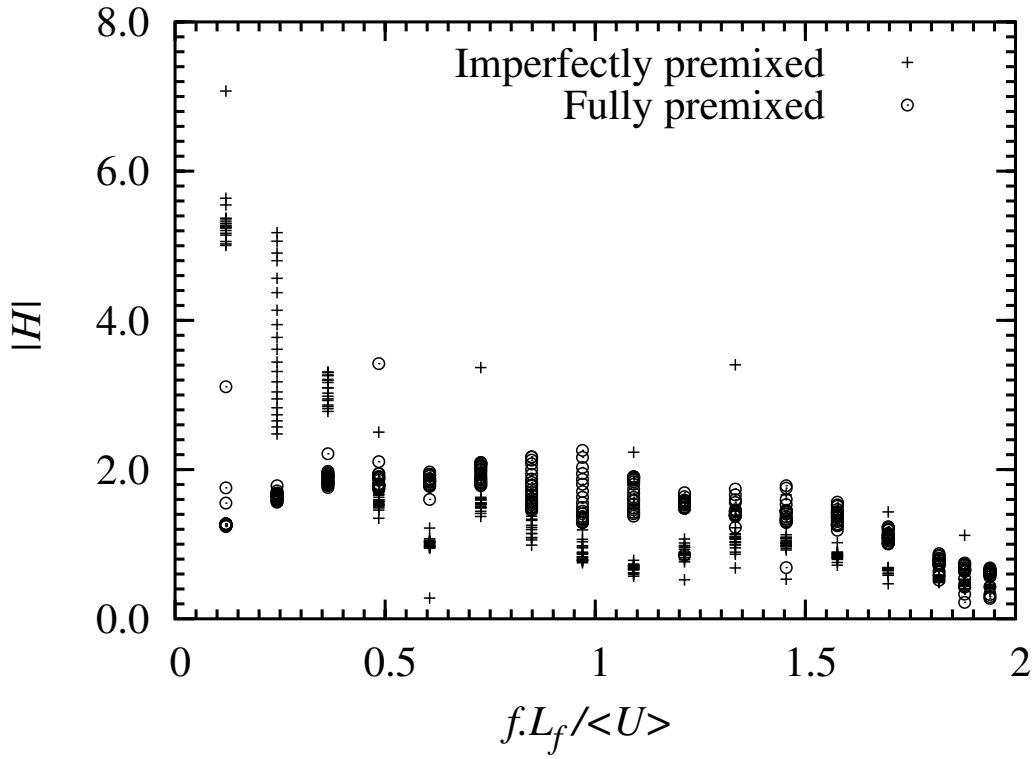

(a)

Figure 5.26: Comparison of flame transfer functions of imperfectly and fully premixed flames, the magnitude of which shown as a function of reduced frequency. Swirl S0, $\langle U \rangle = 9.9$ m/s, global $\phi = 0.55$.

Chapter 6

Self-excited Oscillations

In this chapter, the results from the experiments investigating the response of the imperfectly premixed flames (with initial spatial equivalence ratio variation) under self-excitation and the comparison with the forced response of the flame at the same flow conditions are described. The flow and acoustic conditions at which the experiments were performed are described in the section 6.2. Section 6.3 presents the results and discusses the qualitative comparison between the self and forced excitation cases. The chapter closes with a summary about the implication of the comparison between the forced and self-excitation cases on the mechanism of saturation in these imperfectly flames.

6.1 Introduction

Many experimental investigations on the forced response of the flame are available in the literature. However, there is no direct comparison of the results from these experiments to that of the self-excited cases. In this section, the results from the forced flames are compared to that of the self-excited cases. In the previous chapters (Chapter 4 and 5) of this thesis, the role of flame surface modulation and that of equivalence ratio modulation on nonlinear behaviour was presented. In order to clarify these results, the results from the experiments studying self-induced oscillations are presented in this chapter. There is a chance of flame flash back during such studies in the current experimental set-up if operated in premix mode and hence only the imperfectly premixed flames are considered.

6.2 Experimental Conditions

The data presented in this section were performed on an imperfectly premixed flame with enclosures of two different lengths. The self-excitation was achieved in a configuration, in which the length of the enclosure of the combustor was 350 mm. The forced response of the flames was studied with short combustor tube (80 mm). The acoustic characteristics of the combustor with the short and long enclosures have been presented in Figs. 3.2 and 3.3. During the forced study, the resonance of the enclosure was avoided while during the self-excitation the resonance was exploited. As in the previous chapters, the bulk velocity at the burner plane was 9.9 m/s. Two swirlers with vane angles 45^o and 60^o were employed to introduce swirl in the flow. As in previous chapters, the no-swirl, 45^o and 60^o cases are referred to as S0, S1 and S2.

The procedure used to obtain self-excitation in a configuration with long tube and with a particular swirler is described below. Firstly, bulk flow of the air was set to a particular value (here to a value which corresponded to 9.9m/s at the inlet plane) after which the fuel was introduced into the flow. The global equivalence ratio was kept to a value where the flame can just be ignited and stabilised. At low equivalence ratios, there was no strong self-induced oscillations observed. By slowly increasing the fuel flow rate, the global equivalence ratio of the flame was increased, until the self-induced oscillations are achieved. The spectral analysis of the OH* chemiluminescence signal from the flame was used to obtain the frequency of oscillation. This frequency of oscillation and the equivalence ratio at which self-excitation occurred was noted. The forced response of the flame was studied for these conditions, after changing the long enclosure with the short one. The flame chemiluminescence during these experiments were imaged with the high-speed CMOS camera with an UV-intensifier and an interference filter for OH* (centered at 307nm with 10nm bandwidth) fitted at the front (see Chapter 2).

6.3 Comparison with Forced Excitation

The power spectra of OH* chemiluminescence signal during the self excitation of flames with three swirl conditions S0, S1 and S2 are presented in Fig. 6.1(a-c). The dominant frequencies were found to be 348, 329 and 330 Hz respectively. The equivalence ratios at which the self-excitation was achieved for swirl conditions S0, S1 and S2 were 0.61, 0.55 and 0.56 respectively. The flame at the above mentioned equivalence ratio and swirl conditions was forced with the frequencies noted from the self-excited case. The highest amplitude of the forcing that could be achieved for these conditions was used to study the forced response of the flame. The power spectra of the OH* signal for these forced response studies are presented in Fig. 6.1(d-f). It can be seen from these figures, that during the self-excitation the response of the flame seemed to have broader frequency content around the dominant frequency, while during the forced cases, the response of the flame was mainly at the frequency of forcing.

The time-series of the global OH* chemiluminescence measured using photo-multiplier tubes (PMTs) for the cases presented in Fig. 6.1 are shown in Fig. 6.2. The instantaneous values presented here are normalized using the time-mean of the quantities. It can be seen from these figures, that the normalized response of the flame with swirl conditions S0 and S1 during the self-excitation was slightly higher than that of the forced case. For the highest swirl case (S2), the OH* chemiluminescence was similar in the forced and self-excited flames. The shape of the cyclic variation for all these cases were very similar. These results showing good comparison between the normalized heat release variations suggest that the flame behaviour during the self-excitation is very similar to that of the forced flame.

In order to further investigate and compare the dynamics of the flame during these experiments, the OH* chemiluminescence of the flame was imaged using an intensified high-speed camera. The images were grabbed at the rate of 3740 frames per second. The camera CMOS was exposed to the intensified signal for 200 μs. The camera was triggered using the input forcing signal during the forced response studies. During the self-excitation, the pressure signal from the pressure transducer mounted on the long enclosure was used to trigger the camera. The

pressure measurements from one of the transducers at the upstream locations measured during both the measurement cases, forced and self-excitation, was used as the reference for comparison.

Instantaneous OH* chemiluminescence images of the forced and self-excited flames with no swirl (S0) is presented in Fig. 6.3. The right hand side and left hand side of the images in Fig. 6.3 are from the forced and self-excitation experiments respectively. The color scale for the intensities are suitably normalized for the presentation. It is clearly evident from these images that the flame dynamics in both the flames are very similar. In both the cases, the flame was wrapped around by the vortex and the heat release modulation was governed by the dynamics of the vortex. As shown in previous chapter (Chapter 5), the heat release response at this frequency seemed to be controlled by the flame surface modulation.

Figure 6.4 shows the comparison of variation of flame structure through the cycle during forced and self-excitation of swirl flame S2, using instantaneous OH* images. As in the case of no-swirl case (S0), the flame dynamics seemed to be controlled by the vortex roll-up and shedding. However, the radial spreading was larger. The comparison of the heat release variation during the forced and self-excited cases evaluated from the high-speed OH* images are presented in Fig. 6.5, after integrating images such as those in Fig. 6.4 over space and normalizing using the time-averaged quantity. It can be seen clearly that the cyclic variation during the self-excitation is the same as that of the forced case. This suggests that the forced flame studies are a true representation of the self-excited cases in the present investigation. Therefore, the flame transfer functions and qualitative understanding developed in chapters 4 and 5 are probably applicable to self-induced oscillations as well.

It should be noted that in both the experimental conditions presented here (S0 and S2), the frequency of oscillations were above 320 Hz, the wavelength of which is comparable to the flame length. As discussed in Chapter 5, for these conditions, the role of kinematics should be more pronounced than the equivalence ratio fluctuations. The instantaneous OH* images presented in this chapter also suggest that the flame kinematics is very important in these cases, which is

consistent with our findings from the forced response experiments, presented in Chapter 5.

6.4 Summary

Experiments were performed to investigate the flame dynamics during self-excited oscillations in the imperfectly premixed flames. The forced experiments were also carried out on the flame with same equivalence ratio, with a forcing frequency close to the dominant frequency of oscillations measured during the self-excitation. The results from these experiments suggested that the flame behaviour during the limit cycle (self-excitation) is very similar to that of the forced cases. The good agreement in qualitative comparison of flame behaviour captured by OH* chemiluminescence imaging of the flame at equivalence ratio 0.6 (and with no swirl, S0) during self-excitation and forcing suggest that the mechanism of heat release variation in both the cases are very similar. The comparison heat release variation captured by OH* chemiluminescence images for a highly swirled flame (S2, and equivalence ratio of 0.56) during forced and self-excitation experiments agreed very well quantitatively, suggesting that the limit cycle behavior of the flame at this condition can be simulated well using external excitation experiments.

The present results suggest that the mechanism of heat release variation investigated in the forced response studies are close to the true limit cycle behavior of the flames. This further improves the confidence in the transfer function measurements presented in the earlier chapters and also in the understanding of the mechanisms involved in nonlinear heat release response of the flames from the external excitation experiments. The results from these experiments could be very useful in developing and validating acoustic (network) models for predicting the amplitude of oscillations during the limit-cycle operation.

6.5 Figures for Chapter 6

Figure 6.1: (a-c) Power spectra of OH* chemiluminescence during self-excited flames S0, S1, and S2 and (d-f) that of the forced excitation at the peak frequency chosen from (a-c) and with the highest possible external excitation amplitude for that case. $\langle U \rangle = 9.9$ m/s.

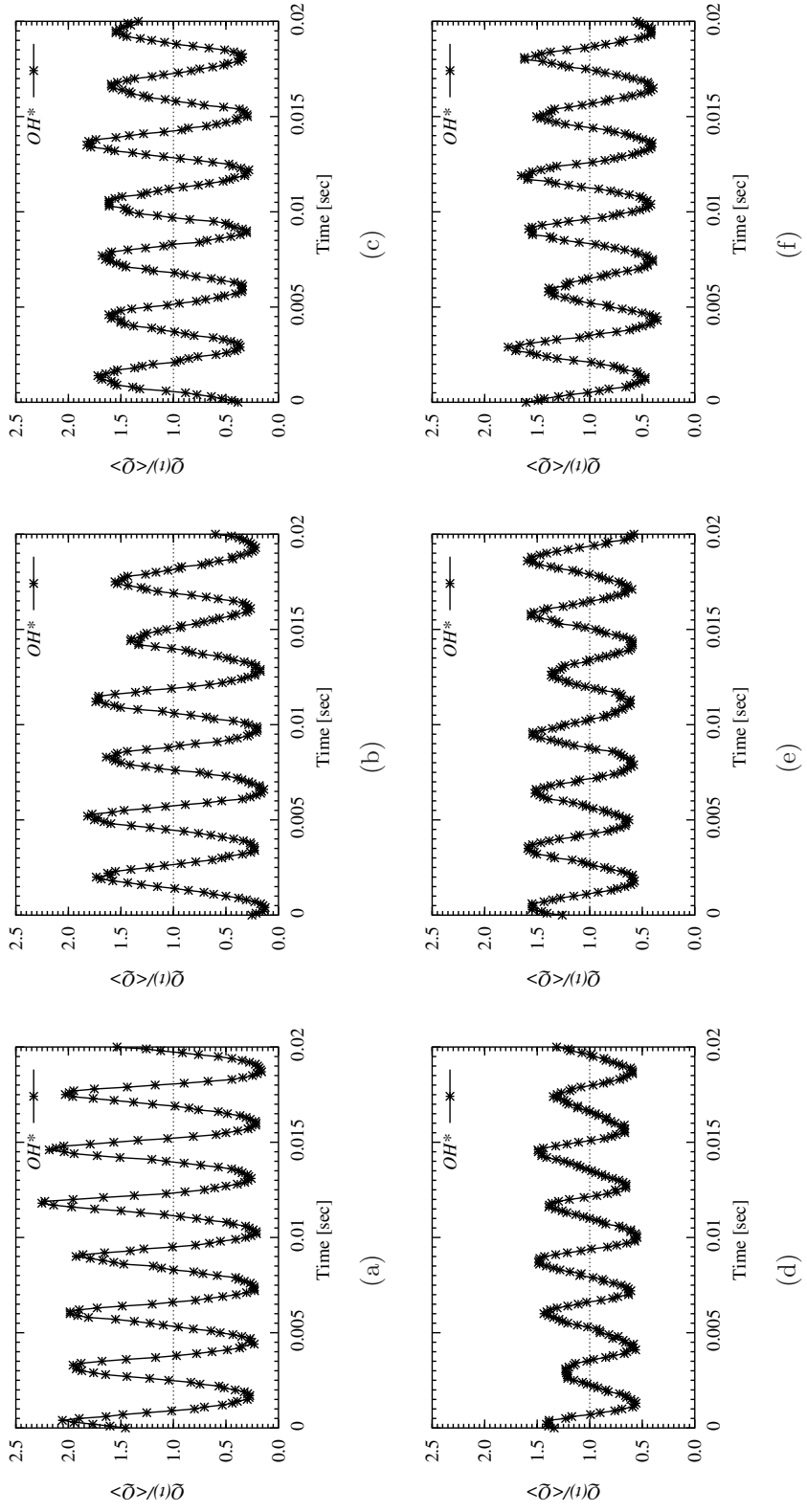

Figure 6.2: Time trace of OH* chemiluminescence signal measured for the case presented in Fig. 6.1 (a-c) self-excited of flames with swirls S0, S1, and S2 and (d-f) Forced excitation at the frequency chosen from (a-c) and with the highest possible external excitation amplitude for that case. $\langle U \rangle = 9.9$ m/s.

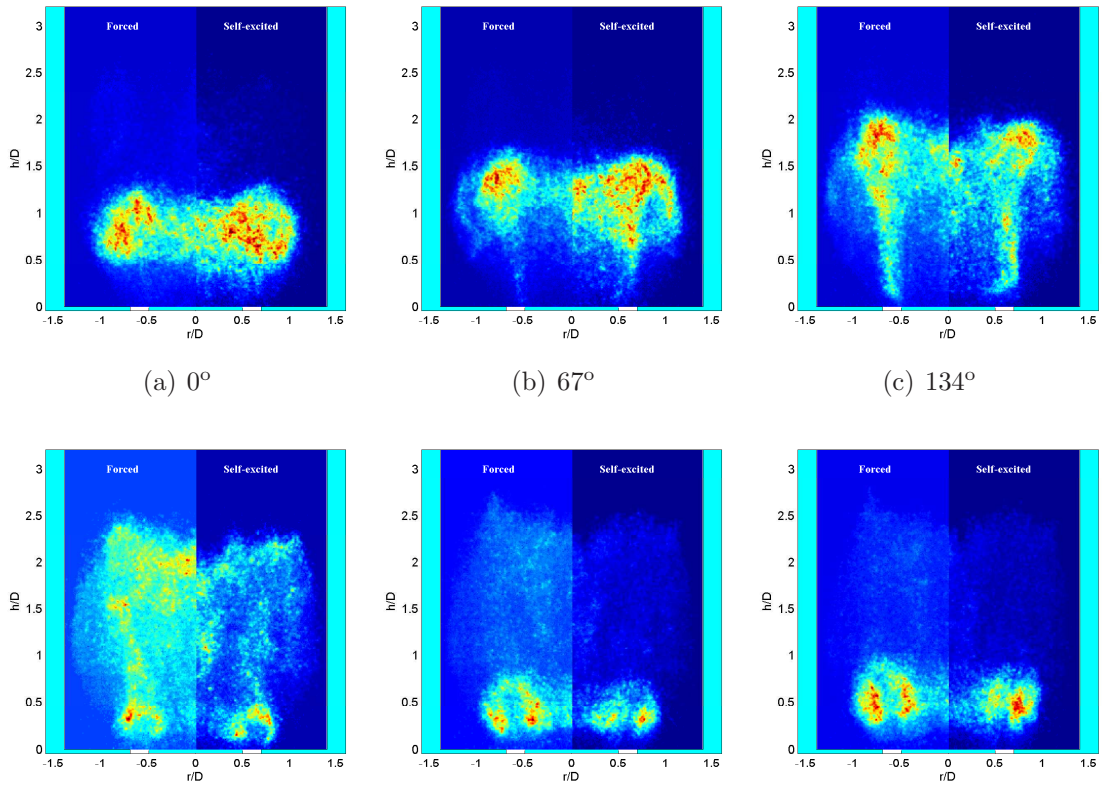

(a) 0° (b) 67° (c) 134°

(d) 201° (e) 268° (f) 301.5°

Figure 6.3: Time-sequence of instantaneous OH* image showing the flame dynamics of forced and self-excited flame: Swirl S0, $\langle U \rangle = 9.9$ m/s, $f = 348$ Hz, $\phi = 0.61$. Right hand side and left hand side of the image are forced and self-excited cases respectively.

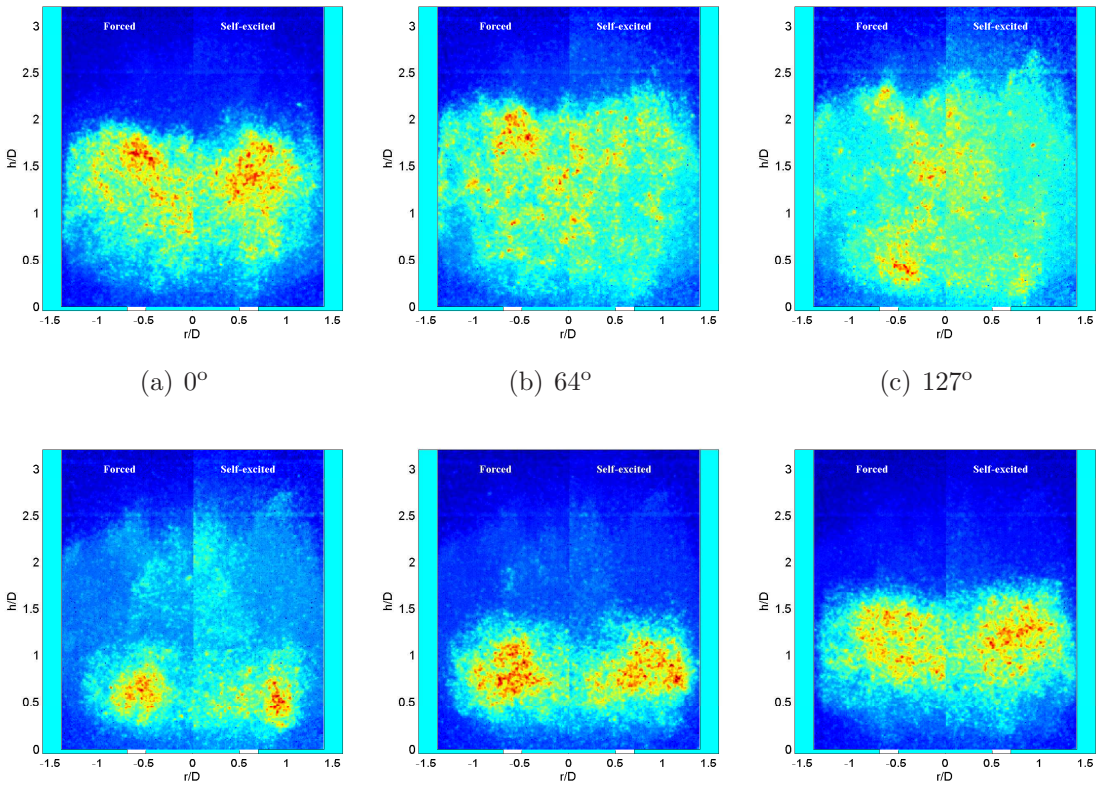

(a) 0° (b) 64° (c) 127°

(d) 191° (e) 254° (f) 318°

Figure 6.4: Time-sequence of instantaneous OH* image showing the flame dynamics of forced and self-excited flame: Swirl S2, $\langle U \rangle = 9.9$ m/s, $f = 330$ Hz, $\phi = 0.57$. Right hand side and left hand side of the image are forced and self-excited cases respectively.

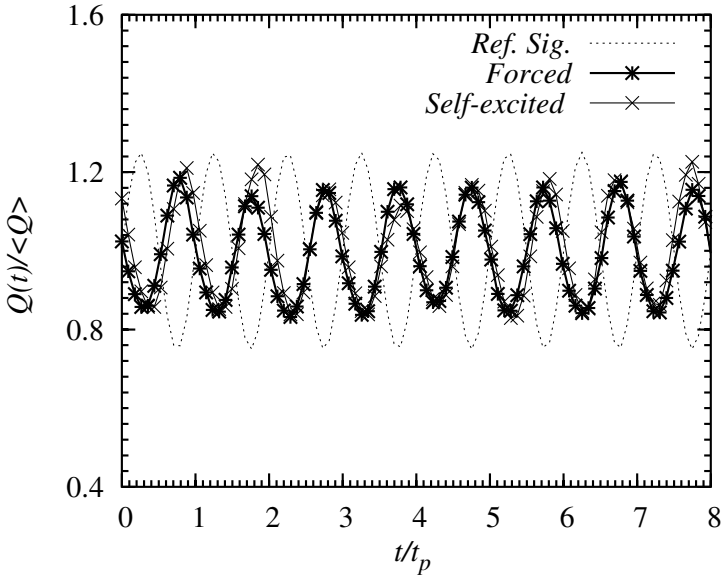

Figure 6.5: Comparison of the global heat release fluctuations evaluated from OH* instantaneous chemiluminescence images of forced and self-excited case presented in Fig. 6.4: $\langle U \rangle = 9.9$ m/s, $\phi = 0.57$, $f = 348$ Hz.

Chapter 7

Conclusions & Suggestions for Further Research

A laboratory scale bluff body combustor was developed to perform detailed experimental investigations to better understand the non-linear response of fully premixed and partially premixed (mixture with spatially non-uniform distribution) to strong acoustic excitation. The study also included experimental determination of cold flow acoustic and flow field characteristics and hot flow stability characteristics of the combustor. The facility was adapted to achieve self excitation and the results were compared with the forced response studies. A summary of the key conclusions from the work that were presented in previous chapters are consolidated in the following sections. Finally, this chapter closes with suggestions for further research.

7.1 Conclusions

7.1.1 Development of Bluff-body Combustor

The burner developed during this study is a generic, scaled gas burning combustor, which could be modified easily for various operating conditions. The burner was operated in a completely premixed mode where the fuel and air are mixed upstream of the flow and the flame was stabilised by the centrally located bluff body. This configuration was used to study the response of flames to velocity

perturbations. Various experimental methods were performed to measure heat release and their applicability in highly strained flows such as those in gas turbines during high amplitude self-excited oscillations, was evaluated during this study. The combustor was modified to operate in another configuration where fuel was injected upstream of the stabilization point. This resulted in spatially varying fuel distribution and when subjected to perturbations, resulted in time-varying equivalence ratio. This simulated the scenario similar to that during combustion instabilities in lean premixed prevaporized combustors. The careful design of this apparatus helped to achieve a well defined initial acoustic boundary conditions and the simplified design and the compact physical dimensions are quite an advantage for modelling purposes.

7.1.2 Characterization of the Combustor

The acoustic characteristics of the combustor under cold flow conditions revealed the resonant behaviour of the combustor with peak responses at the frequencies around 40 Hz, 160 and 320Hz. These peak responses were exploited to achieve high amplitude oscillations to understand the non-linear flow-acoustic interaction regime. A change in downstream length (used in some experiments to achieve self-excitation) affected the response at the highest frequency (320 Hz) and shifted the peak to 340 Hz at cold flow conditions. The cold flow high-speed smoke visualization measurements revealed the response of the shear layer and the change in the characteristics of the recirculation zones to acoustic forcing. During the low frequency forcing, the shear layer modulation was by oscillatory motion and even at the highest forcing amplitudes there was no shear layer roll-up. During the experiments with high frequencies (160 Hz and 320 Hz), the low amplitude forcing resulted in oscillatory motion of the shear layer, while the shear layer started to roll-up to form a vortex ring with increase in amplitude of forcing. In order to obtain further insight into the formation of vortex rings in this geometry and to get generalized criteria of this phenomenon, further detailed investigations of velocity field are required.

7.1.3 Acoustic Response of Fully Premixed Flames

Important conclusions from the detailed experimental investigations performed to measure the response of lean fully premixed turbulent bluff-body stabilised flames subjected to inlet velocity perturbations are summarized here. The conclusions reached on the amplitude dependence of the transfer function, and the flame response to high amplitudes are relevant to the emergence of limit-cycle combustion-induced oscillations.

On experimental methods: Three different heat release measurement approaches were followed during the present work, namely OH* and CH* chemiluminescence using photo-multiplier tubes and ICCD, flame surface density (FSD) based on OH PLIF, and local heat release (RX) rate evaluated from simultaneous OH and CH_2O PLIF measurements. Time-resolved measurements of OH PLIF resulted in a sequence of four OH PLIF images separated by 1 ms, which assisted in showing the time evolution of the flame front during the forcing cycle.

Concerning a comparison of the above techniques used to evaluate the flame transfer function in fully premixed flames, the following conclusions were reached.

- The global heat release evaluated from OH* and CH* chemiluminescence agreed very well both in magnitude and in phase.
- the magnitude of the heat release response captured by chemiluminescence measurements and by FSD showed a similar trend with forcing amplitude in all measurement conditions.
- The local heat release evaluated from high resolution reaction rate imaging was higher than that estimated from the FSD measurement by 10-20% in magnitude and the latter had a phase lag of about 40 degrees.
- These results show that the heat release estimation through measurement of the flame surface density is adequate for flame instability studies, despite the large amplitudes of forcing used here.

- This implies that the local effects of strain and curvature in reducing the burning velocity probably do not cause large variations in the global heat release rate.

On the flame response: Concerning the detailed flame response with forcing amplitude, it was found that the heat release increased non-linearly after inlet velocity amplitudes of around 15% for flames without swirl, a value that depended on the forcing frequency and the equivalence ratio. This non-linearity was found to occur when the reacting shear layers rolled-up into vortices and was captured with all heat release measurement techniques. The vortices induced by the inlet velocity fluctuations not only generated flame area when the flame wrapped around them, but also caused cusps and even large-scale flame annihilation events, as observed in time-resolved OH-PLIF images, when parts of the flame stabilised on the inner shear layer close to the recirculation zone collapsed on parts of the flame stabilised on the outer recirculation zone, a phenomenon that was made more prominent with increasing forcing amplitude. A further non-linearity occurred at high amplitudes and at some equivalent ratios, where a significant leakage of energy to higher harmonics was observed, despite the fact that the inlet velocity fluctuation had a correspondingly small content at the harmonic frequency.

On the effect of harmonics in the inlet oscillations: The measurement concerning the presence of harmonics suggest that the transfer function measurement are unaffected only up to a level of presence of harmonics, above which the transfer function values were greatly affected. The results suggest that the interpretation of the transfer function measured in any system should be done carefully based on the amount of other harmonics present in the flow at the inlet. The reduced flame response by introduction of secondary frequency also suggest the possibility of active control of the instability by carefully chosen external excitation.

On the effect of swirl: The measurements of heat release response of swirl flames further proved the role of flame area modulation. With moderate swirl

(produced by 45° swirl vane), the flame response was very similar to the no-swirl flame with saturation occurring from 20% forcing. However, for high swirl (produced by 60° swirl vane), the response was found to have a nearly linear dependence on the amplitude of the forcing. The phase variation in all the cases studied were found to depend on the amplitude only when the flame was not acoustically convectively compact.

Short Summary: The present results suggest that the flame sheet kinematics play the major role in the saturation mechanism of lean completely premixed flame response. These results extend the previous experimental and analytical results on the significance of the role played by flame sheet kinematics in nonlinear flame response, from laminar flames to turbulent flames. Heat release fluctuations due to local fluctuations of strain rate and curvature had a smaller effect, while no localised extinction has been observed even at large forcing amplitudes.

7.1.4 Acoustic Response of Imperfectly Premixed Flames

The important conclusions from the detailed experimental investigations carried out to investigate the response of lean imperfectly premixed turbulent bluff-body stabilised flames to imposed inlet velocity and equivalence ratio perturbations are presented here. During the study, a special attention was given to the amplitude and frequency dependence of the transfer function, which is relevant to the understanding the limit-cycle behaviour of combustion-induced oscillations.

On experimental methods: To investigate the global heat release in the imperfectly premixed flames, OH* and CH* chemiluminescence were used and to understand the variation in local flame structure flame surface density (FSD) based on OH PLIF was employed. Concerning the use of the above techniques for the flame response studies in imperfectly premixed flames, the following conclusions were reached. First, the global heat release evaluated from OH* and CH* chemiluminescence agreed very well both in magnitude and in phase during all forcing frequencies and amplitudes. Second, the magnitude of the heat release response captured by chemiluminescence measurements and by FSD showed a

similar trend with forcing amplitude for the low swirling flames, when the flame was forced at 160 Hz. This suggests that the global heat release modulation during these forcing conditions had the greatest contribution from the flame surface modulation. However, in the case of highly swirling flames, the flame surface modulation was out of phase with the global heat release captured suggesting that there could be limitations in the FSD measurement method in estimating a quantity proportional to heat release rate in this scenario.

On the flame response: Concerning the frequency and amplitude dependence of the flame response following conclusions were reached. The response of the imperfectly premixed flames were found to greatly depend on how well the flame was compact acoustically and convectively. When the overall length of the flame was comparable or greater than the wavelength of the forced oscillations, the heat release modulation was dominated by flame sheet kinematics and when the flame was compact, the flame response was mainly due to variations in the equivalence ratio distribution. The transfer function values compared with the completely premixed flames suggest that the contribution from the flame sheet kinematics could not be very important in the low frequency forcing, while the magnitude of the transfer function for premixed and imperfectly premixed flames were of same order at higher frequencies. The plot of the transfer function against the frequency when normalized for the fuel dispersion time (or the convection time/the residence time) corroborated the fact that these equivalence ratio modulations were important when the acoustic wavelengths are greater than flame lengths. While OH* images at low frequencies suggested the absence of vortex ring formation, suggesting that the contribution from equivalence ratio is higher than the surface modulation, which was only the oscillatory motion of the flame. The OH* chemiluminescence and FSD confirmed the dominating role of flame sheet kinematics during the high frequency forcing.

On the effect of swirl: The measurements of heat release response of swirl flames further proved the existence of two regimes in frequencies where the role of flame area and equivalence ratio modulation could be different. With moderate

swirl, the amplitude dependence of flame response was very similar to the no-swirl flame with saturation occurring from 40% forcing at 160 Hz dominated by flame kinematics and the saturation started at 25% of forcing at 40 Hz with time varying equivalence ratio playing a major role. The response of the highly swirled flames was also found to depend non linearly on the amplitude and frequency of the forcing, however, the magnitude of the response was low when compared to that of the low swirling flames.

Short Summary: The present results suggest that the amplitude and frequency response of the imperfectly premixed flames to acoustic forcing had two distinct frequency regimes, in which either the equivalence ratio or flame sheet kinematics play the major role in the saturation mechanism, depending on how the flame is acoustically-convectively compact. These results apart from confirming the previous analytical and experimental results showing the role of equivalence ratio fluctuations in heat release modulation, also suggest a possibility to determine a criteria to identify the role played by these mechanisms, which would greatly enhance the prediction capabilities.

7.1.5 Comparison with Self-excited Oscillations

It was shown from the experiments investigating the flame dynamics of self-excited oscillations in the imperfectly premixed flames, when compared with the results of the forced response experiments on the flame (with same equivalence ratio) and with a forcing frequency close to the dominant frequency of oscillations measured during the self-excitation, that the flame behaviour during the limit cycle (self-excitation) is very similar to that of the forced cases. The results presented in this thesis suggest that the mechanism of heat release variation investigated in the forced response studies are close to the true limit cycle behavior of the flames. This further improves the confidence in the transfer function measurements presented in the earlier chapters and also in the understanding of the mechanisms involved in nonlinear heat release response of the flames from the forced excitation experiments. Furthermore, the good comparison between the forced response in this combustor with the self-excited cases suggest that

these studies can serve as a validation case for development of computational and predictive tools for combustion instability studies.

7.2 Suggestions for Further Research

The extensive database produced from this work on the response of premixed and imperfectly premixed flames for different conditions can serve as a bench mark database for validation of computational and acoustic based network models. Further detailed velocity measurements along with the present database would improve not only the understanding of the existing data, but would also help the modelers to verify the input and other boundary conditions better.

Although this thesis has discussed in detail instability mechanisms in premixed and imperfectly premixed flames in a laboratory scale burner, the results from these studies could be compared with studies from more realistic geometries.

In this thesis, it has been pointed out that the flame response in partially premixed flames are essentially due to balance of two different mechanisms, namely, the equivalence ratio fluctuations and the flame sheet kinematics depending on the compactness of the flame to acoustics. More detailed investigation on this could result in better modelling approaches. Albeit the fact that these studies are focused on the forced responses, a detailed comparison with self-excited oscillations in different frequency regimes (essentially resulting with different flame compactness to acoustic waves), including the comparison of the amplitudes of oscillations at the inlet would improve the current prediction capacities.

It has to be noted that, in the case of imperfectly premixed flames, the information on the premixedness and also on the time varying equivalence ratio distribution is very important to understand further the non-linear responses of flames especially for the case when the flame is acoustically convectively compact. Experiments to measure the time and space resolved equivalence ratios could help a great deal in improving the current understanding of the nonlinear flame response.

Appendix A

List of Publications

Some portions of the work from this thesis are published and presented. They are:

- R. Balachandran, B.O. Ayoola, C. F. Kaminski, A. P. Dowling, E. Mastorakos (2005), "Experimental investigation of the non-linear response of turbulent premixed flames to imposed inlet velocity oscillations", Combustion and Flame [in press].
- B.O. Ayoola, R. Balachandran, J. H. Frank, E. Mastorakos, C. F. Kaminski (2005), "Spatially resolved heat release rate measurements in turbulent premixed flames", Combustion and Flame [in press].
- C. A. Armitage, R. Balachandran, E. Mastorakos, R. S. Cant (2005), "Numerical investigation of the non-linear response of turbulent premixed flames to imposed inlet velocity osicllations", Combustion and Flame [submitted].
- R. Balachandran, A. P. Dowling, E. Mastorakos (2005), "Non-linear response of premixed flames to superimposed harmonic inlet velocity fluctuations of multiple frequencies", 41st AIAA/ASME/SAE/ASEE Joint Propulsion Conference & Exhibit, 10-13 July, Tucson, Arizona, USA.

- R. Balachandran, A. P. Dowling, E. Mastorakos (2005), "Response of turbulent premixed flame subjected to inlet velocity and equivalence ratio perturbations", European Combustion Meeting, Belgium (Hosted by the Belgium section of the Combustion Institute).

- B.O. Ayoola, R. Balachandran, C.F. Kaminski, E. Mastorakos (2005), "Measurements of local heat release rates in a turbulent premixed bluff body stabilized flames with acoustic forcing", European Combustion Meeting, Belgium.

- B.O. Ayoola, R Balachandran, E Mastorakos, C.F. Kaminski (2005), "Heat release rate measurement in turbulent flames", Seventh World Congress of Chemical Engineering , Glasgow, Scotland.

- B. O. Ayoola, R. Balachandran, J. H. Frank, E. Mastorakos, C. F. Kaminski (2004), "Heat release imaging of acoustically forced turbulent flames", Laser Applications to Chemical and Environmental Analysis, Annapolis, Maryland, USA.

Bibliography

Anning, G.H.G. (1999). *The effect of fuel injector geometry on the flow structure of a swirl stabilised gas turbine combustor*. Master's thesis, Department of Aerospace Engineering and Engineering Mechanics, College of Engineering, University of Cincinnati.

Armitage, C.A., Riley, A.J., Cant, R.S., Dowling, A.P. & Stow, S.R. (2004). Flame transfer function for swirled lpp combustion from experiments and CFD. *Proceedings of ASME Turbo Expo*, 1–11.

Ayoola, B.O., Balachandran, R., Frank, J.H., Mastorakos, E. & Kaminski, C.F. (2005). Spatially-resolved heat release measurements in turbulent premixed flames. *Combustion and Flame*, in press.

Baillot, F., Durox, D. & Prud'homme, R. (1992). Experimental and theoretical study of a premixed vibrating flame. *Combustion and Flame*, **88**, 149–152.

Baillot, F., Durox, D., Ducruix, S., Searby, G. & Boyer, L. (1999). Parametric response of a conical flame to acoustic waves. *Combustion Science and Technology*, **142**, 91–109.

Balachandran, R., Ayoola, B.O., Kaminski, C.F., Dowling, A.P. & Mastorakos, E. (2005). Experimental investigation of the non-linear response of turbulent premixed flames to imposed inlet velocity oscillations. *Combustion and Flame*, to appear.

Barr, P.K., Keller, J.O., Bramlette, T.T., Westbrook, C.K. & Dec, J.E. (1990). Pulse combustor modeling demonstration of the importance of characteristic times. *Combustion and Flame*, **82**, 252–269.

Bellows, B.D. & Lieuwen, T. (2004). Nonlinear response of a premixed combustor to forced acoustic oscillations. *42nd Aerospace Science Meeting and Exhibit, Reno, NV, USA*.

Bellows, B.D., Zhang, Q., Neumeier, Y., Lieuwen, T. & Zinn, B.T. (2003). Forced response studies of a premixed flame to flow disturbances in a gas turbine combustor. *41st AIAA Aerospace and Science Meeting and Exhibit, Reno, NV, USA*.

Bernier, D., Ducruix, S., Lacas, F. & Candel, S. (2003). Transfer function measurements in a model combustor: Application to adaptive instability control. *Combustion Science and Technology*, **175**, 993–1013.

Bloxsidge, C.J., Dowling, A.P. & Langhorne, P.J. (1988). Reheat buzz: an acoustically coupled combustion instability. part 2. theory. *Journal of Fluid Mechanics*, **193**, 445–473.

Böckle, S., Kazenwadel, J., Kunzelmann, T., Shin, D.I., Schultz, C. & Wolfrum, J. (2000). Simultaneous single-shot laser-based imaging of formaldehyde, oh, and temperature in turbulent flames. *Proceedings of the Combustion Institute*, **28**, 279–286.

Bourehla, A. & Baillot, F. (1998). Appearance and stability of a laminar conical premixed flame subjected to an acoustic perturbation. *Combustion and Flame*, **114**, 303–318.

Brookes, S.J., Cant, R.S., Dupere, I.D.J. & Dowling, A.P. (2001). Computational modeling of self-excited combustion instabilities. *Journal of Engineering for Gas Turbines and Power*, **123**, 322–326.

Cala, C.E.C., Fernandes, E.C. & Heitor, M.V. (2002). Analysis of oscillating shear layer. *Symposium on Application of Laser Techniques and Fluid Mehanics LISBOA Portugal*, **11**.

Candel, S. (2002). Combustion dynamics and control: Progress and challenges. *Proceedings of the Combustion Institute*, **29**, 1–28.

Cheung, W.S., Sims, G.J.M., Copplestone, R.W., Tilston, J.R., Wilson, C.W., Stow, S.R. & Dowling, A.P. (2003). Measurement and analysis of flame transfer function in a sector combustor under high pressure conditions. *Proceedings of ASME TURBO EXPO 2003, Atlanta, Georgia, USA*, 1–8.

Chew, T.C., Bray, K.N.C. & Britter, R.E. (1990). Spatially resolved flamelet statistics for reaction rate modeling. *Combustion and Flame*, **80**, 65–82.

Cho, S.K., Yoo, J.Y. & Choi, H. (1998). Vortex pairing in an axisymmetric jet using two-frequency acoustic forcing at low to moderate strouhal numbers. *Experiments in Fluids*, **25**, 305–315.

Clark, W.H. & Humphrey, J.W. (1986). Identification of longitudinal acoustic modes associated with pressure oscillations in ramjets. *Journal of Propulsion*, **2**, 199–205.

Crosley, D. (1993). Collisional effects on laser-induced fluorescence flame measurements. *Optical Engineering*, **20**.

Crump, J.E., Schadow, K.C., Yang, V. & Culick, F.E.C. (1986). Longitudinal combustion instabilities in ramjet engines : Identification of acoustic modes. *Journal of Propulsion*, **2**, 105–109.

Culick, F.E.C. (2002). Combustion instabilities in liquid rocket engines: Fundamentals and control. Tech. rep., California Insitute of Technology.

Dec, J.E. & Keller, J.O. (1989). Pulse combustor tail-pipe heat-transfer dependence on frequency, amplitude, and mean flow rate. *Combustion and Flame*, **77**, 359–374.

Dec, J.E. & Keller, J.O. (1990). Time-resolved gas temperatures in the oscillating turbulent flow of a pulse combustor tail pipe. *Combustion and Flame*, **80**, 358–370.

Descamps, B.M., Smallwood, G.J., Prieur, J., Snelling, D.R. & Gulder, O.L. (1996). Surface density measurements of turbulent premixed flames in a spark-ignition engine and an bunsen-type burner using planar laser induced fluorescence. *Proceedings of the Combustion Institute*, **26**, 427–435.

Donbar, J.M., Driscoll, J.F. & Carter, C.D. (2000). Reaction zone structure in turbulent nonpremixed jet flamesfrom ch-oh plif images. *Combustion and Flame*, **122**, 1–19.

Dowling, A.P. (1995). The calculation of thermoacoustic oscillations. *Journal of Sound and Vibration*, **180**, 557–581.

Dowling, A.P. (1997). Nonlinear self-excited oscillations of a ducted flame. *Journal of Fluid Mehanics*, **346**, 271–290.

Dowling, A.P. (1999). A kinematic model of ducted flame. *Journal of Fluid Mechanics*, **394**, 51–72.

Dowling, A.P. & Hubbard, S. (2000). Instability in lean premixed combustors. *Proceedings of Institute of Mechanical Engineers*, **214**, 317–332.

Dowling, A.P. & Stow, S.R. (2003). Acoustic analysis of gas turbine combustors. *Journal of Propulsion and Power*, **19**, 751–764.

Ducruix, S., Durox, D. & Candel, S. (2000). Theoretical and experimental determinations of the transfer function of a laminar premixed flame. *Proceedings of the Combustion Institute*, **28**, 765–773.

Durox, D., Ducruix, S. & Baillot, F. (1998). Strong acoustic forcing on conical premixed flames. *Proceedings of the Combustion Institute*, **27**, 883–889.

Esquiva-Dano, I., Nguyen, H.T. & Escudie, D. (2001). Influence of bluff-body shape on the stabilization regime of non-premixed flames. *Combustion and Flame*, **127**, 2167–2180.

Fayoux, A., Zähringer, K., Gicquel, O. & Rolon, J.C. (2005). Experimental and numerical determination of heat release in counterflow premixed laminar flames. *Proceedings of the Combustion Institute*, **30**, 251–257.

Fleifl, M., Annasamy, A.M., Ghoneim, Z.A. & Ghoniem, A.F. (1996). Response of a laminar premixed flame to flow oscillations: A kinematic model and thermoacoustic instability results. *Combustion and Flame*, **106**, 487–510.

Giezendanner, R., Keck, O., Weignand, P., Meier, W., Meier, U., Stricker, W. & Aigner, M. (2003). Periodic combustion instabilities in a swirl burner studied by phase-locked planar laser-induced fluorescence. *Combustion Science and Technology*, **175**, 721–741.

Gutmark, E., Parr, T.P., Parr, D.M. & Schadow, K.C. (1989). Planar imaging of vortex dynamics in flames. *Transcation of ASME, Journal of Heat Transfer*, **111**, 148–155.

Gutmark, E., Schadow, K.C., Sivasegaram, S. & Whitelaw, J.H. (1991). Interaction between fluid-dynamic and acoustic instabilities in combusting flows within ducts. *Combustion Science and Technology*, **79**, 161–166.

Haber, L.C. (2000). *An investigation into the origin, measurement and application of chemiluminescence light emissions from premixed flames*. Ph.D. thesis, Virginia Polytechnic Institute and State University, Blacksburg, Virginia, USA.

Haq, M.Z., Sheppard, C.G.W., Woolley, R., Greenhalgh, D.A. & Lockett, R.D. (2002). Wrinkling and curvature of laminar and turbulent premixed flames. *Combustion and Flame*, **131**, 1–15.

Hardalupas, Y. & Orian, M. (2004). Local measurements of the time-dependent heat release rate and equivalence ratio using chemiluminescent emission from a flame. *Combustion and Flame*, **139**, 188–207.

Hardalupas, Y. & Selbach, A. (2002). Imposed oscillations and non-premixed flames. *Progress in Energy and Combustion Science*, **28**, 75–104.

Hegde, U.G., Reuter, D., Daniel, B.R. & Zinn, B.T. (1987). Flame driving of longitudinal instabilities in dump type ramjet combustors. *Combustion Science and Technology*, **55**, 125–138.

Heiser, W.H., McClure, W.B. & Wood, C.W. (1996). Simulating heat addition via mass addition in variable area compressible flow. *AIAA Journal*, **34**, 1076–1077.

Hornak, J.P., ed. (2002). *Encyclopedia of Imaging Science and Technology*, 390. John Wiley and Sons, New York, U.S.A.

Huang, Y. & Yang, V. (2004). Bifurcation of flame structure in a lean-premixed swirl-stabilized combustor: transition from stable to unstable flame. *Combustion and Flame*, **136**, 383–389.

Hubbard, S. & Dowling, A.P. (2001). Response of a laminar premixed flame to flow oscillations: A kinematic model and thermoacoustic instability results. *ASME Journal of Engineering for Gas Turbines and Power*, **123**, 766–773.

Joos, F. & Vortmeyer, D. (1986). Self-excited oscillations in combustion chambers with premixed flames and several frequencies. *Combustion and Flame*, **65**, 253–262.

Kaminski, C.F., Hult, J., Alden, M., Lindenmaier, S., Dreizler, A., Mass, U. & Baum, M. (2000). Spark ignition of turbulent methane/air mixtures revealed by time-resolved planar laser induced fluorescence and direct numerical stimulations. *Proceedings of the Combustion Institute*, **28**, 399–405.

Keller, J.O., Bramlette, T.T., Dec, J.E. & Westbrook, C.K. (1989). Pulse combustion: The importance of characteristic times. *Combustion and Flame*, **75**, 33–44.

Keller, J.O., Barr, P.K. & Gemmen, R.S. (1994). Premixed combustion in a periodic flow field. part i: Experimental investigation. *Combustion and Flame*, **99**, 29–30.

Klein, S.A. (2000). *On the acoustics of turbulent non-premixed flames*. Ph.D. thesis, University of Twentee.

Knikker, R., Veynante, D. & Meneveau, C. (2002). A priori testing of a similarity model for large eddy simulations of turbulent premixed combustion. *Proceedings of the Combustion Institute*, **29**, 2105–2111.

Külsheimer, C. & Büchner, H. (2002). Combustion dynamics of turbulent swirling flames. *Combustion and Flame*, **131**, 70–84.

Kushari, A., Rosen, J.L., Jagoda, J.I. & Zinn, B. (1996). The effect of heat content and composition of fuel on pulse combustor performance. *Twenty-Sixth Symposium on Combustion / The Combustion Institute*, 3363 – 3368.

Lang, W. (1991). Harmonic frequency generation by oscillating flames. *Combustion and Flame*, **83**, 253–262.

Langhorne, P.J. (1988). Reheat buzz: an acoustically coupled combustion instability. part 1. experiments. *Journal of Fluid Mechanics*, **193**, 417–443.

Lawn, C.J. (2000). Distributions of instantaneous heat release by the cross-correlation of chemiluminescent emissions. *Combustion and Flame*, **123**, 227–240.

Lawn, C.J. & Polifke, W. (2004). A model for the thermoacoustic response of a permixed swirl burner, part ii: The flame response. *Combustion Science and Technology*, **176**, 1359–1390.

Lawn, C.J., Evesque, S. & Polifke, W. (2004). A model for the thermoacoustic response of a premixed swirl burner, part i: Acoustic aspects. *Combustion Science and Technology*, **176**, 1331–1358.

Lee, J.G. & Santavicca, D.A. (2003). Experimental diagnostics for the study of combustion instabilities in lean premixed combustors. *Journal of Propulsion and Power*, **19**, 735–750.

Lee, S.Y., Seo, S., Broad, J.C., Pal, S. & Santoro, R.J. (2000). An experimental estimation of mean reaction rate and flame structure during combustion instability in a lean premixed gas turbine combustor. *Proceedings of the Combustion Institute*, **28**, 775–782.

Lieuwen, T. (2003). Modeling premixed combustion-acoustic wave interaction: A review. *Journal of Propulsion and Power*, **19**, 765–781.

Lieuwen, T. & Neumeier, Y. (2002). Nonlinear pressure-heat release transfer function measurements in a premixed combustor. *Proceedings of the Combustion Institute*, **29**, 99–105.

Lieuwen, T. & Zinn, B. (1998a). The role of equivalence ratio oscillations in driving combustion instabilities in low nox gas turbines. *Twenty-Seventh Symposium on Combustion/The Combustion Institute,*, 1809 – 1816.

Lieuwen, T. & Zinn, B.T. (1998b). Theoretical investigation of combustion instability mechanisms in lean premixed gas turbines. *36th Aerospace Sciences Meeting & Exhibit, January 12-15, 1998, Reno, NV*.

Macquisten, M.A. & Dowling, A.P. (1993). Low-frequency combustion oscillations in a model afterburner. *Combustion and Flame*, **94**, 253–264.

Macquisten, M.A. & Dowling, A.P. (1995). Combustion oscillations in a twin-stream afterburner. *Journal of Sound and Vibration*, **188**, 545–560.

Marsano, S., Bowen, P.J. & O'Doherty, T. (1998). Cyclic modulation characteristics of pulse combustors. *Twenty-Seventh Symposium on Combustion / The Combustion Institute*, 3155 – 3162.

Mastui, Y. (1981). An experimental study on pyro-acoustic amplification of premixed laminar flames. *Combustion and Flame*, **43**, 199–209.

McManus, K.R., Vandsburger, U. & Bowman, C.T. (1990). Combustor performance enhancement through direct shear layer excitation. *Combustion and Flame*, **82**, 75–92.

Menon, S. (1991). Large-eddy simulations of combustion instability in an axisymmetric ramjet combustor. *Combustion Science and Technology*, **75**, 53–72.

Merk, H.J. (1956). An analysis of unstable combustion of premixed gases. *Sixth Symposium (International) on Combustion/The Combustion Institute*, 500–511.

Merzkirch, W. (1987). *Flow Visualization Second Edition*. Academic Press, Inc., Orlando, Florida.

Mizomoto, M. & Yoshida, H. (1987). Effects of lewis number on the burning intensity of bunsen flames. *Combustion and Flame*, **70**, 47–60.

Mueller, C.J., Driscoll, J.F., Reuss, D.L., Drake, M.C. & Rosalik, M.E. (1998). Vorticity generation and attenuation as vortices convect through a premixed flame. *Combustion and Flame*, **112**, 342–346.

Najm, H.N., Knio, O.M., Paul, P.H. & Wyckoff, P.S. (1998a). A study of flame observables in premixed methane - air flames. *Combustion Science and Technology*, **140**, 369–403.

Najm, H.N., Paul, P.H., Mueller, C.J. & Wyckoff, P.S. (1998b). On the adequacy of certain experimental observables as measurements of flame burning rate. *Combustion and Flame*, **113**, 312–332.

Najm, H.N., Paul, P.H., Mcilroy, A. & Knio, O.M. (2001). A numerical and experimental investigation of premixed methane-air flame transient response. *Combustion and Flame*, **125**, 879–892.

Neumeier, Y. & Zinn, B.T. (1996). Experimental demonstration of active control of combustion instabilities using real-time modes observation and secondary fuel injection. *Proceedings of the Combustion Institute*, **26**, 2811–2818.

Nguyen, Q.V. & Paul, P.H. (1996). The time evolution of a vortex-flame interaction obtained via planar imaging of ch and oh. *Proceedings of the Combustion Institute*, **26**, 357–364.

Paschereit, C., Gutmark, E. & Weisenstein, W. (1998). Flow-acoustic interactions as a driving mechanism for thermoacoustic instabilities. *AIAA Paper*.

Paschereit, C.O., Schuermans, B., Polifke, W. & Mattson, O. (2002). Measurement of transfer matrices and source terms of premixed flames. *ASME Journal of Engineering For Gas Turbines and Power*, **124**, 239–247.

Paul, P.H. & Najm, H.N. (1998). Planar laser-induced fluorescence imaging of flame heat release rate. *Proceedings of the Combustion Institute*, **27**, 43–50.

Poinsot, T.J., Trouve, A.C., Veynante, D.P., Candel, S. & Esposito, E. (1987). Vortex-driven acoustically coupled combusiton instabilities. *Journal of Fluid Mechanics*, **177**, 265–292.

Preetham & Lieuwen, T. (2004). Nonlinear flame-flow transfer function calculations: Flow disturbance celerity effects. *40th AIAA/ASME/SAE/ASEE Joint Propulsion Conference and Exhibit, Fort Lauderdale, Florida, USA*, 1–15.

Price, R., Hurle, I. & Sugden, T. (1968). Optical stuides of the generation of noise in turbulent flames. *Twelfth Symposium (International) on Combustion/The Combustion Institute*, 1093–1102.

Pun, W. (2001). *Measurments of Thermo-Acoustic Coupling*. Ph.D. thesis, California Institute of Technology, Pasadena, California, USA.

Pun, W., Palm, S.L. & Culick, F.E.C. (2003). Combustion dynamics of an acoustically forced flame. *Combustion Science and Technology*, **175**, 499–521.

Putnam, A.A. & Dennis, W.R. (1953). A study of oscillations of the organ-pipe type. *Transcations of ASME*, 15–18.

Ratner, A., Pun, W., Palm, S.L. & Culick, F.E.C. (2002). Phase-resolved no planar laser-induced fluorescence of a jet flame in an acoustic chamber with excitation at frequencies ¡ 60 hz. *Proceedings of the Combustion Institute*, **29**, 85–90.

Rayleigh (1945). *Theory of Sound*, vol. 2. Dover Publications, New York, USA.

Renard, P.H., Thevenin, D., Rolon, J.C. & Candel, S. (2000). Dynamics of flame/vortex interactions. *Progress in Energy and Combustion Science*, **26**, 225–282.

Reuter, D., Daniel, B.R., Jagoda, J. & Zinn, B.T. (1986). Periodic mixing and combustion processes in gas fired pulsating combustors. *Combustion and Flame*, **65**, 281–290.

Rook, R., de Goey, L.P.H., Somers, L.M.T., Schreel, K.R.A.M. & Parchen, R. (2002). Response of burner-stabilized flat flames to acoustic perturbations. *Combustion Theory and Modelling*, **6**, 233–242.

Rutland, C.J. & Trouve, A. (1993). Direct simulations of premixed turbulent flames with nonunity lewis numbers. *Combustion and Flame*, **94**, 41–57.

Samaniego, J., Egolfopoulos, F. & Bowman, C. (1995). Co2 chemiluminescence in premixed flames. *Combustion Science and Technology*, **109**, 183–203.

Samaniego, J.M. & Mantel, T. (1999). Fundamental mechanisms in premixed turbulent flame propagation via flamevortex interactions: Part i: experiment. *Combustion and Flame*, **118**, 537–556.

Sankar, S.V., Jagoda, J.I. & Zinn., B.T. (1990). Oscillatory velocity response of premixed flat flames stabilized in axial acoustic field. *combustion and flame*, **80**, 371–384.

Sattelmayer, T. (2000). Influence of the combustor aerodynamics on combustion instabilities from equivalence ratio fluctuations. *Proceedings of ASME TURBOEXPO, Munich, Germany*.

Savin, A.V. (1996). On mechanism of self-oscillatory interaction of plane subsonic jet with acoustic resonator. *Experimental Thermal and Fluid Science*, **12**, 388–398.

Schadow, K.C. & Gutmark, E. (1992). Combustion instability related to vortex shedding in dump combustors and their passive control. *Progress in Engery and Combustion Science*, **18**, 117–132.

Schimmer, H. & Vortmeyer, D. (1977). Acoustical oscillation in a combustion system with a flat flame. *Combustion and Flame*, **28**, 17–24.

Schuller, T., Durox, D. & Candel, S. (2002). Dynamics of and noise radiated by a perturbed impinging premixed jet flame. *Combustion and Flame*, **128**, 88–110.

Schuller, T., Durox, D. & Candel, S. (2003a). Self-induced combustion oscillations of laminar premixed flames stabilized on annular burners. *Combustion and Flame*, **135**, 525–537.

Schuller, T., Durox, D. & Candel, S. (2003b). A unified model for the prediction of laminar flame transfer functions: comparisons between conical and v-flame dynamics. *Combustion and Flame*, **134**, 21–34.

Seybert, A.F. & Ross, D.F. (1977). Experimental determination of acoustic properties using a two-microphone random excitation technique. *Journal of Acoustic Society of America*, **61**, 1362–1370.

Shepherd, I.G. (1996). Flame surface density and burning rate in premixed turbulent flames. *Proceedings of the Combustion Institute*, **26**, 373–379.

Sohn, C.H., Chung, S.H., Kim, J.S. & Williams, F.A. (1996). Acoustic response of droplet flames to pressure oscillations. *AIAA Journal*, **34**, 1847–1854.

Tang, Y.M., Waldherr, G., Jagoda, J.I. & Zinn, B.T. (1995). Heat release timing in a nonpremixed helmholtz pulse combustor. *Combustion and Flame*, **100**, 251–261.

Torres, H., Lieuwen, T., C.Johnson, Daniel, B.R. & Zinn, B.T. (1999). Experimental investigation of combustion instabilities in a gas turbine combustor simulator. *37th AIAA Aerospace Sciences Meeting and Exhibit, Reno, NV*.

Truffin, K. & Poinsot, T. (2005). Comparison and extension of methods for acoustic identification of burners. *Combustion and Flame*.

Veynante, D., Duclos, J.M. & Piana, J. (1994). Experimental analysis of flamelet models for premixed turbulent combustion. *Proceedings of the Combustion Institute*, **25**, 1249–1256.

Wu, X., Wang, M. & Moin, P. (2001). Combustion instability due to the nonlinear interaction between sound and flame. *Annual Research Briefs, Center for Turbulence Research*.

Yang, V. & Culick, F.E.C. (1986). Analysis of low frequency combustion instabilities in a laboratory ramjet combustor. *Combustion Science and Technology*, **45**, 1–25.

Yu, K.H., Trouve, A. & Daily, J.W. (1991). Low-frequency pressure oscillations in a model ramjet combustor. *Journal of Fluid Mechanics*, **232**, 47–72.

Yu, K.H., Parr, T.P., Wilson, K.J., C.Schadow, K. & Gutmark, E.J. (1996). Active control of liquid-fueled combustion using periodic vortex-droplet interaction. *Twenty Sixth Symposium (International) on Combustion/The Combustion Institute*, 2843–2850.

Zähringer, K., Durox, D. & Lacas, F. (2003). Helmholtz behavior and transfer function of an industrial fuel swirl burner used in heating systems. *International Journal of Heat and Mass Transfer*, **46**, 3539–3548.

Zelinski, J.J., III, L.J.M., Falk, F. & Bagnall, E.C. (1960). The design of combustors for ramjet engines. *Combustion and Flame*, **4**, 343 – 353.

Zhou, M. & Wyganski, I. (2001). The response of a mixing layer formed between parallel streams to a concomitant excitation at two frequencies. *Journal of Fluid Mechanics*, **441**, 139–168.

Zhu, M., Dowling, A.P. & Bray, K.N.C. (2001). Self-excited oscillations in combustors with spray atmoizers. *Journal of Engineering for Gas Turbine and Power*, **123**, 779–786.

Zinn, B.T. & Narayanaswami, L. (1982). Application of the impedance tube technique in the measurement of the driving provided by solid propellants during combustion instabilities. *Acta Acoustica*, **9**, 303–315.